InN and In-rich InGaN Nanocolumns

by Molecular Beam Epitaxy

Dissertation

zur Erlangung des mathematisch-naturwissenschaftlichen Doktorgrades

"Dr. rerum naturalium"

an der Georg-August-Universität Göttingen

vorgelegt von

Christian Denker
aus Oldenburg (Oldb)

Göttingen, 2011

.

D7
Referentin: Frau Prof. Dr. A. Rizzi
Koreferent: Herr Prof. Dr. A. Krost
Tag der mündlichen Prüfung: 8.11.2011

Contents

1 Introduction **1**

2 InN and InGaN - Physical properties **3**
2.1 Structural properties . . . 3
2.2 Electronic properties . . . 7
2.3 Nanostructures: confinement, surface induced properties . . . 12
2.4 Possible applications III-N nanowires . . . 13

3 Growth of InN and InGaN **15**
3.1 Synthesis of III-N semiconductors . . . 15
3.2 Substrates for heteroepitaxy . . . 16
3.3 Miscibility of $In_{1-x}Ga_xN$ . . . 16

4 Molecular beam epitaxy of III-N semiconductors **19**
4.1 Metastable growth . . . 19
4.2 Growth temperature . . . 19
4.3 Difference of chemical potential in metastable growth . . . 21
4.4 Controlling and measuring growth conditions . . . 23
4.4.1 Substrate temperature . . . 23
4.4.2 Deposition rate, beam equivalent pressure . . . 25
4.4.3 Nitrogen supply . . . 28

5 Nanowire growth **31**
5.1 III-N nanowires by molecular beam epitaxy . . . 31
5.2 Equilibrium shape of crystals . . . 32
5.3 Nucleation . . . 38
5.4 III:N ratio and preferential growth direction . . . 40
5.5 Kinetics of diffusion-controlled wire growth . . . 41
5.6 Conclusion . . . 45

6 InN layers as a reference **47**
6.1 Stoichiometry and influence of III:V ratio in InN growth . . . 47
6.2 Morphology on sapphire and GaN templates . . . 47
6.3 Structural and optical properties . . . 49
6.4 Interval growth . . . 52
6.4.1 RHEED of InN . . . 53
6.4.2 RHEED-controlled interval growth . . . 53
6.5 Conclusion . . . 58

7 Properties of InN nanocolumns **61**
7.1 Self-organized growth of InN nanowires . . . 61
7.2 Transmission electron microscopy (TEM) . . . 63

7.3 Surface oxidation of InN probed by XPS 64
7.4 Electrical measurements on single nanowires 66
7.4.1 Contacting single nanowires 66
7.4.2 Electrostatic discharge, grid induced voltage peak-protection and bonding . . 72
7.4.3 Measurement geometries 75
7.4.4 Measurements 79
7.4.4.1 Measurement setups 79
7.4.4.2 Contact resistance 79
7.4.4.3 Influence of the radius on conductivity 81
7.4.4.4 Temperature dependence 84
7.4.5 Conclusion 84
7.5 Optical characterization of InN nanocolumns 85
7.5.1 Qualitative evidence of electron accumulation by Raman-spectroscopy 85
7.5.2 First quantitative analysis based on Photoluminescence (PL) 87
7.5.3 Quantitative analysis based on photoluminescence excitation spectroscopy (PLE) 91
7.5.4 Conclusion 94
7.6 Discussion 94
7.7 Conclusion 95

8 InGaN nanocolumns 97
8.1 Experimental conditions 97
8.2 $In_{1-x}Ga_xN$ nanowires with x_{supply}=0.60 98
8.3 $In_{1-x}Ga_xN$ nanowires with x_{supply}=0.07, 0.13, 0.26 98
8.3.1 Growth rate model 103
8.4 Discussion 105
8.5 Conclusion 106

9 Growth rate monitoring with markers 107
9.1 Growth of InN nanowires with $In_{1-x}Ga_xN$ markers 107
9.1.1 Influence of the markers on morphology and size 107
9.2 Marker detection by transmission electron microscopy 109
9.3 Length-time dependence 109
9.4 Conclusion 111

10 Selective area growth: A way to control nucleation and growth 113
10.1 General aspects of selective area growth 113
10.1.1 Mechanisms of SAG in the mask approach 115
10.1.2 InN - SAG: Choice of mask material and growth conditions 116
10.2 Selective area nucleation by carbon masks 117
10.3 Selective area growth by Molybdenum and Titanium masks 117
10.4 Conclusion 123

11 Conclusion 125

A List of abbreviations 129

B List of experimental setups 131

C InGaN nanowire morphologies 133

D Equilibrium nucleation **135**
D.1 Nucleation rate with desorption 135
D.2 Nucleation rate without desorption 136

E Nitrogen spectra **139**

F Curriculum vitae **141**

G List of publications **143**

1. Introduction

The continuous development of semiconductor light emitting devices during the past 5 decades is based on progress in growth of III-V semiconductors. In the first decades, III-arsenides and III-phosphides enabled the exploration of the infrared to yellow-red spectral range, but their emission is more or less limited to this range. Therefore, the alloy $In_{1-x}Ga_xN$ gained more attention, since it is predestined for optoelectronic applications over the whole visible range due to its direct band gap tunable from infrared to ultraviolet. Since the 1990s, improvements on growth of III-nitrides allowed for the production of blue and ultraviolet light emitting diodes (LED) and laser diodes (LD). Due to their versatility, III-nitrides are nowadays the technologically most important semiconductor aside from silicon. White LEDs based on Ga-rich $In_{1-x}Ga_xN$ and phosphor coating for down-converting of the emitted blue light are about to revolutionize the lighting industry and are already available in supermarkets. At present, however, there is an efficiency reduction of LEDs and LDs with higher In content emitting at longer wavelengths. Therefore, III-N alloys with higher In content are currently intensively studied for lighting in the whole visible range to close the gap in the green emission range. Due to progress on the growth of this alloy, green laser diodes for low power projectors are almost market-ready and will capture a new market for small size and low power-consumption projectors. This demonstrates the importance of InGaN for energy to light conversion. In addition, it is also promising for the opposite process of light to energy conversion in detectors and high efficiency multi-junction solar cells. The use in solar cells would require material with higher In content and an adequate solution for the interconnection of the subcells.

Single crystalline bulk material of silicon, germanium or gallium arsenide are grown from a melt with high quality. However, this growth process is challenging or even impossible for III-nitrides due to their high nitrogen vapor pressure. Bulk GaN substrates have been available for several years, but are still rare and expensive. Therefore, the III-nitrides are typically grown by metalorganic chemical vapor deposition (MOCVD) or molecular beam epitaxy (MBE) as thin films on foreign substrates. The lack of lattice-matched substrates typically induces a high dislocation density. This and the limited miscibility of InGaN, as well as the lattice mismatch within this material system are currently the main challenges for longer wavelength applications, such as solar cells and LEDs for the red to green spectral range.

Despite their technological importance and great potential, many fundamental questions concerning InN and InGaN still remain unsolved. Up to the beginning of this decade, the most fundamental property of semiconductors, the band gap, of InN was still under debate. Now, a band gap of about 0.7 eV for InN is widely accepted and has been confirmed by several studies. However, further fundamental properties need to be explored, such as the mobility of charge carriers and their effective mass, as well as the electrical properties of surfaces and interfaces. Furthermore, a reliable knowledge of the electrical properties of dopants, as well as their incorporation and inter-crystal diffusion behavior is mandatory for device fabrication.

Within the last 10-15 years, nanowires have gained high attention due their outstanding properties and the resulting enormous potential in various fields of material science and semiconductor physics. Nanowires show essential advantages over thin films in basic research experiments and open up new possibilities. Nanowires usually show a low density of defects and therefore high crystal quality. The small diameter facilitates strain relaxation and defect reduction in heteroepitaxy. Also, the high surface-to-volume makes nanowires ideally suited for chemical sensing and enables novel device geometries, e.g. field effect transistors with wrap-around gate. Presumably, their status is going

to change from “promising and interesting for basic research“ to “useful for industrial products” in the near future. The focus of recent research on nanowires has been on their physical properties and suitability for devices, as well as growth. In particular, research on growth has aimed to gain an understanding of the processes of nanowire formation and on the growth of ordered arrays and heterostructures.

The focus of this thesis is on InN and InGaN nanowires. This combines the two highly interesting research fields of the III-nitride material system and nanowires. The aim of this thesis is to gain a deeper understanding of the electronic properties of InN nanowires and the growth mechanisms of InN and InGaN nanowires. First, the knowledge of basic properties of the material system is reviewed, as well as the theoretical background of growth in general, and of nanowires in particular. Subsequently, the electrical properties of InN nanowires are analyzed with focus on the influence of the native oxide formed at their surfaces. Moreover, the growth of InGaN nanowires and in particular of the In-rich part of this alloy is demonstrated and analyzed. The In and Ga incorporation are controlled by the growth mechanism. Thus, InGaN markers are introduced into InN nanowires to monitor their growth rate as a function of time and to draw conclusions about nucleation and growth of these wires. The control over nucleation by a mask approach on selective area growth of InN nanowires is studied, with the aim of growing ordered nanowire arrays.

2. InN and InGaN - Physical properties

InN is a semiconductor with direct band gap of about 0.7 eV at 0 K. $In_{1-x}Ga_xN$ is the alloy of InN with GaN. This alloy has a tunable direct band gap from 0.7 eV to 3.4 eV, which makes it appealing for optoelectronic applications. The Ga-rich part of this alloy has been intensively studied, but is still an interesting research field. However, the InN and In-rich part of this alloy are less studied, even though they are interesting for many applications. Therefore, the focus of this thesis is on InN and In-rich InGaN.

The high electron drift velocity and electron mobility of InN make it interesting for high frequency applications. High quality InN is challenging to synthesize due to the lack of bulk material or suitable substrates. Another difficulty arises from the fact that oxygen and hydrogen form shallow donors in InN. Since both elements are always present in the growth environment, InN discussed in literature is highly n-doped or degenerate. Due to increasing progress in the growth of high quality InN, it is possible to analyze nearly intrinsic material, instead of completely defect controlled. Furthermore, a high kinetic barrier for formation and decomposition, as well as its high nitrogen vapor pressure, impede also measurements of its thermal properties. Thus, the lattice and its parameters are well known, as well the direct nature of its band gap, whereby its value now seems to be reliably determined. But most of further properties of InN have are not yet been reliably determined and are therefore the subject of recent research. For applications, p-type material is mandatory in the majority of cases, but reports are still rare.

In this section, the important structural and electronic properties of InN and the InGaN material system are briefly reviewed.

2.1. Structural properties

In this paragraph, an overview of the crystal structure and some relevant chemical characteristics is given.

Crystal structure

The stable phase under standard conditions of all III-nitrides is the wurzite α-phase. The zincblende β-phase is metastable. These two phases differ only in the stacking order if one compares the (0001) and (111) orientation, as shown in figure 2.1.1. The first phase has an AB stacking sequence, while the latter has ABC.

The wurzite structure is described by two lattice parameters a and c, the zincblende structure by one. The zincblende β-phase of III-N is metastable and not relevant to this thesis. But, substrates with zincblende structure are interesting due to the similarity in the (0001) and (111) directions of the two structures. This allows for the growth of wurzite crystals in the (0001) direction on zincblende (111) substrates. The corresponding lattice parameter a^* can be deduced by simple geometric considerations.

The lattice parameters for wurzite InN, GaN and AlN are listed in table 2.1.1. According to the Vegard's law-approximation, the lattice parameter for an $A_{1-x}B_xN$ alloy are linearly related on the concentration x:

$$g_{A_{1-x}B_x\mathrm{N}} \approx (1-x)g_{\mathrm{AN}} + x\, g_{\mathrm{BN}} \tag{2.1.1}$$

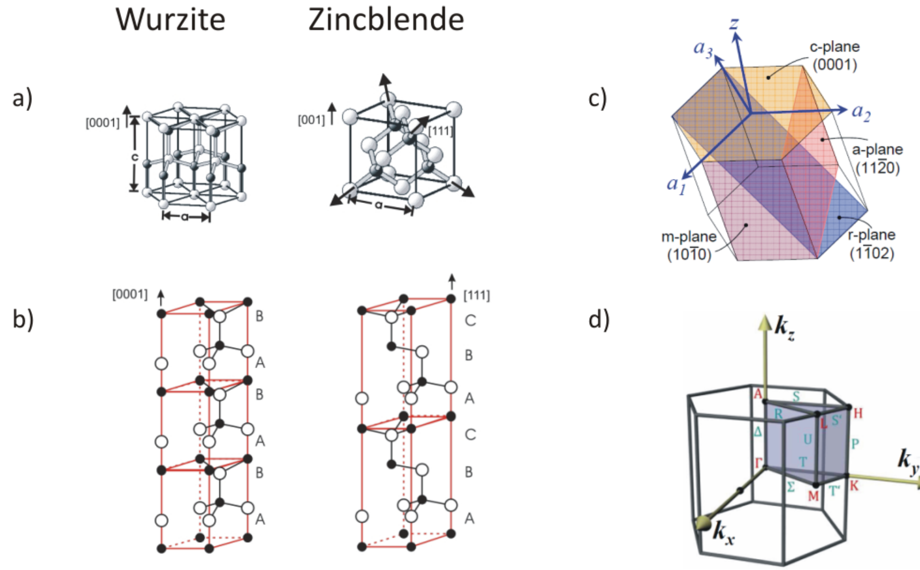

Figure 2.1.1.: *Comparison of zincblende and wurzite crystal structure. a) Unit cells, b) stacking sequences of wurzite structure in the (0001) direction and zincblende in the (111) direction, c) wurzite unit cell with important planes, d) first Brillouin zone for wurzite crystals showing points of high-symmetry and directions according to the Koster notation. Figures c) and d) are taken from Segura-Ruiz (2009).*

Material	lattice constant a [nm]	lattice constant c [nm]
InN	0.3563	0.57039
GaN	0.3189	0.5185
AlN	0.311	0.4982

Table 2.1.1.: *Lattice constants of III-nitrides (Morkoc, 2008).*

The deviation from this approximation should be below 1% of the lattice constant according to theoretical calculations of Caetano *et al.* (2006).

The energy difference between the zincblende and wurzite crystal structure is relatively low for AlN, GaN and InN with values of 43.7, 8.4, 21.4 meV, respectively per anion-cation pair (Stampfl & Van de Walle, 1999). In wurzite III-nitrides, the appearance of zincblende stacking sequences called stacking faults is more likely than zincblende inclusions. The energies for the stacking fault with the lowest formation energy per anion-cation pair for AlN, GaN and InN are 24, 5, 11 meV, respectively (Wright, 1997).

Phonons and Raman scattering spectroscopy of InN and InGaN

This paragraph provides a brief introduction to phonons and coupled plasmon-LO-phonon (PLP) modes, as well as their detection by Raman scattering spectroscopy.

In Raman scattering spectroscopy (Raman spectroscopy), the specimen is illuminated with monochromatic light and the energy of scattered light is detected. Raman scattering is based on the fact that some of the scattered photons interact in scattering processes with phonons. In this process, a phonon is created or annihilated and the energy of the scattered photon is decreased or increased by the energy of the phonon. The analysis of the scattered light allows one then to draw conclusions about the phonons inside the crystal.

Material	E_{2l}	A_1(TO)	E_1(TO)	E_{2h}	A_1(LO)	E_1(LO)
InN	87	447	476	490.1	585.4	593
GaN	144.0	531.8	558.8	567.6	734.0	741.0
AlN	248.6	611.0	670.8	657.4	890.0	912.0

Table 2.1.2.: *Phonon modes of AlN, GaN, and InN (in cm^{-1}) without the silent B_1 modes (Cantarero* et al. *(2011), Garro* et al. *(2008) and Segura-Ruiz* et al. *(2009)).*

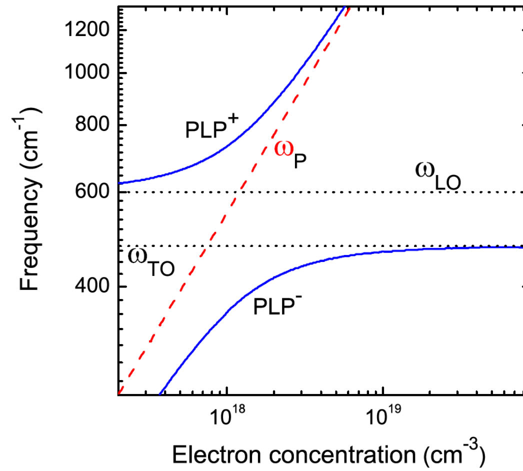

Figure 2.1.2.: *Calculated frequencies of the $PLP^{\pm}$ modes in InN as function of electron concentration (Segura-Ruiz, 2009 and Lazic, 2008).*

Six of the phonons in wurzite crystals can be probed by Raman spectroscopy and their wavelengths are listed in table 2.1.2. The polarization of the lattice vibrations and incident light leads to selection rules for the observation of the different phonons depending on the direction of the incident and detected scattered light and their polarizations. In this thesis, only Raman spectroscopy results obtained in backscattering geometry with incident light in [0001] and detected $[000\bar{1}]$ without a certain polarization are shown. In this case, the so-called allowed modes are the A_1(LO), E_{2l} and E_{2h} modes.

Since phonons are lattice vibrations, their energy changes, if the lattice is strained. Therefore, a shift of phonon modes indicates strain. The E_{2h} mode is usually used to analyze possible strain. Furthermore, a high density of crystal defects, each causing local strain, leads to variations of the energy of the E_{2h} mode and therefore to a broadening of the E_{2h} signal.

In addition to the phonon modes, coupled modes of collective electron excitations (plasmons) and phonons are observed by Raman spectroscopy. In the case of III-nitrides, the phonon-LO-plasmon coupled modes are of special interest because their energy depends on the electron concentration. The dependence of the frequency of the PLP^- and PLP^+ modes on electron concentration is shown in figure 2.1.2. See e.g. Segura-Ruiz *et al.* (2010) for further details.

Furthermore, the frequencies of the phonon modes shift linearly with the mole fraction of In in $In_{1-x}Ga_xN$ alloys according to Grille *et al.* (2000) and enable the determination of the In mole fraction.

Chemical bonds and stability

The properties mentioned within this paragraph are still under debate, so the given values can only be regarded as a guide for general trends (Saitoh *et al.*, 2008). The binding energies and formation enthalpies for InN, GaN and AlN are listed in table 2.1.3. Both values increase from InN to GaN

Material	Binding energy E_B [eV/per anion-cation pair]	Formation enthalpy H_f [eV/per anion-cation pair]	Energy difference ΔE_{WZ-ZB} [meV/per atom]
InN	-7.97	-0.21	-11.44
GaN	-9.06	-1.08	-9.88
AlN	-11.67	-3.13	-18.41

Table 2.1.3.: *Comparison of binding energies and formation enthalpies of InN, GaN and AlN (Lax, 1967; Stampfl & Van de Walle, 1999, and references therein), as well as calculated energy differences between wurzite and zincblende phases ΔE_{wz-zb} (Yeh* et al.*, 1992).*

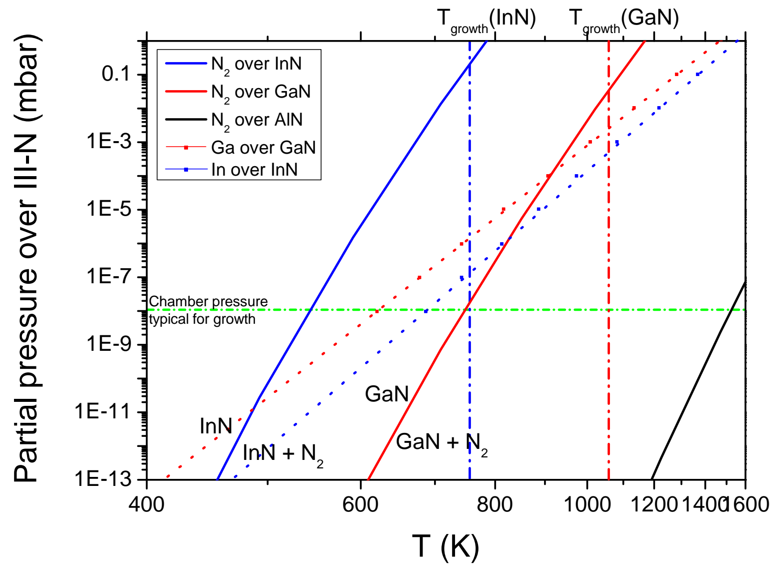

Figure 2.1.3.: *Equilibrium vapor pressure of nitrogen and metals over III-N semiconductors (adapted from Wang & Yoshikawa (2004)). Vertical and horizontal lines indicate typical nitrogen pressures and growth temperatures used in MBE.*

and further to AlN. Taking the equilibrium vapor pressures into account (see fig. 2.1.3), it is obvious that InN is the most unstable among III-nitrides. The difference in Pauling electronegativity for In-N, Ga-N and Al-N of 1.26, 1.23, 1.61 indicate a predominantly covalent character of bonds, since the transition to ionic bonds takes place at about 1.7 (Drago, 2006).

Regarding stability in vacuum, noticeable decomposition takes place at about 430-470°C, 770-800°C and >900°C in the case of InN, GaN and AlN, respectively (Morkoc, 2008). On the one hand, a large kinetic barrier for crystallization and decomposition processes in combination with a high nitrogen vapor pressure impede the determination of the phase stability line of InN and GaN. On the other hand, the large kinetic barrier allows meta-stable growth at the low pressures typical for molecular beam epitaxy (Newman, 1997). This means that the large kinetic barrier hampers decomposition under growth conditions where the material is thermodynamically unstable (see figure 2.1.3). Another interesting point is the stability under normal ambient conditions. As shown by experiment, the surface starts to oxidize in atmosphere. The surface oxidation of InN is investigated in more detail in section 7.3.

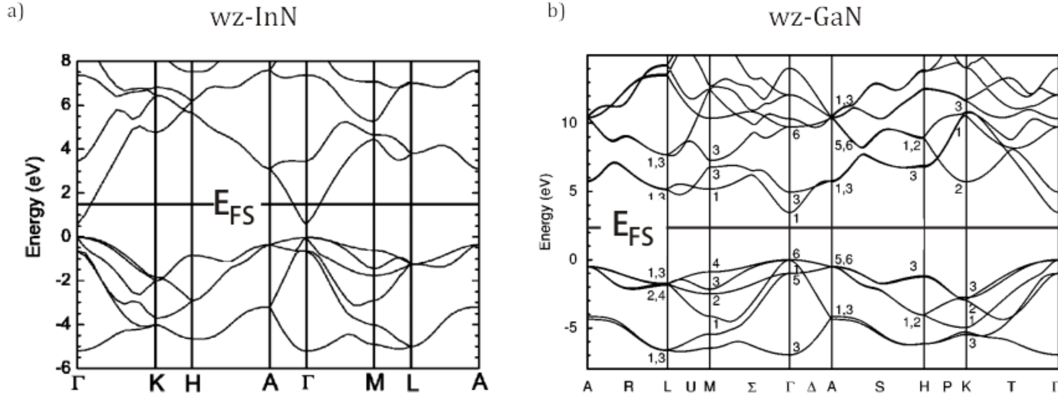

Figure 2.2.1.: *Calculated band structures of a) InN (Mahboob* et al., *2004) and b) GaN (Fritsch* et al., *2003). E_{FS} denotes the Fermi-level stabilization energy.*

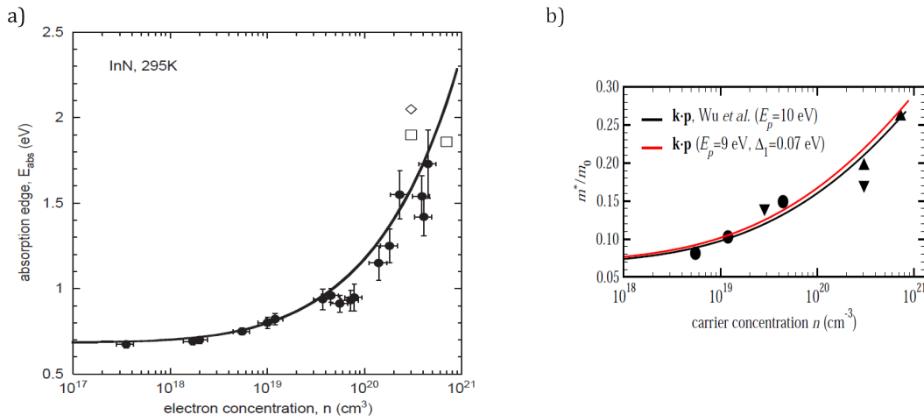

Figure 2.2.2.: *a) Burstein-Moss-shift (Walukiewicz* et al.*, 2004) and b) increase of effective mass with electron concentration (Rinke* et al.*, 2009) for InN (Symbols represent experimental data and solid lines calculations).*

2.2. Electronic properties

As mentioned previously, InN and GaN are semiconductors with a direct band gap of 0.7 eV and 3.4 eV. The formerly assumed band gap of InN of about 2 eV has now been assigned to poor material quality resulting in a large Burstein-Moss-shift. In the following paragraphs some general electronic properties of InN and GaN are presented, such as band structure, charge carrier mobilities and charge neutrality level. The temperature dependence of the band gap of InN as well as its dependence on electron density is shown, as well as the change of band gap for $In_{1-x}Ga_xN$ alloys. In addition, recent knowledge about the electronic properties of InN and GaN surfaces is reviewed. An introduction to doping of InN is given at the end of this section.

Band structure and band gap

In contrast to GaN, InN is a narrow gap semiconductor. Figure 2.2.1 shows calculated band structures of the two materials. The point of lowest energy difference between the valence and conduction band is in both cases at the Γ point. Ab-initio calculations predict a band gap of 0.7eV, if density-functional theory (DFT) is combined with sufficient corrections to compensate for the underestimation of the band gap by standard DFT calculations. This was shown by Rinke *et al.* (2009) using the following

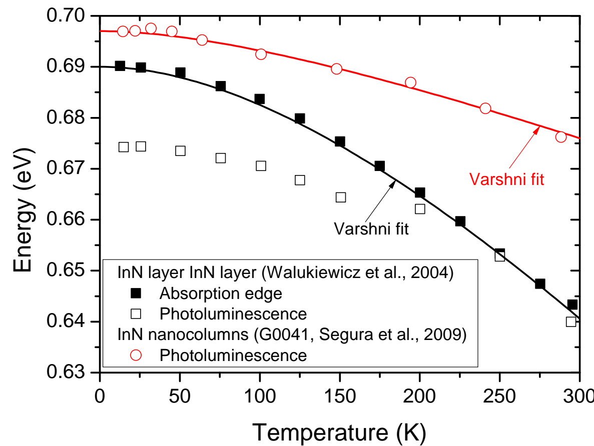

Figure 2.2.3.: *Temperature dependence of InN band gap as reflected in the absorption edge and photoluminescence of a thick layer (7.5 µm) layer and photoluminescence of nanocolumns.*

corrections: many-body perturbation theory in the G_0W_0 approximation and applying G_0W_0 corrections to the exact-exchange optimized effective potential approach (OEPx) ground state calculations.

InN exhibits a low density of states near the conduction band minimum (CBM). Due to this, the charge neutrality level or Fermi stabilization energy E_{FS} is at about 1.8 eV above the valence band maximum (VBM) and therefore 1.1 eV above the CBM. This explains the tendency of InN to be n-type (Wu *et al.*, 2004). If the electron concentration reaches a certain level, the Fermi-level is in the conduction band. The critical concentrations for InN were calculated by Moret *et al.* (2009) to be 1.05 $\times 10^{15}$, 2.32 $\times 10^{16}$, and 1.81 $\times 10^{17}$ cm^{-3} at 10, 80, and 300 K, respectively. If the electron concentration exceeds these levels, the optical properties are mainly determined by band filling effects. Free states in the conduction band are needed for absorption processes. The absorption edge is equal to the energy difference of the VBM and the energy of the lowest free states in the conduction band. Therefore, the absorption edge shifts to higher energies with increasing electron concentration, i.e. increasing band-filling. Figure 2.2.2 shows the change of the absorption edge with electron concentration for InN layers. Also, the emission in luminescence experiments is affected by this band filling. In the case of an unpopulated conduction band, the excited electron and holes relax to their band extrema. Then electrons and holes from the band extrema recombine. But if the conduction band is partially filled, the electrons cannot relax to the CBM. But holes can recombine with electrons at higher energy levels than the CBM. This leads to a blue shift and broadening of the emission peak in luminescence spectra with increasing band filling. Due to this correlation, low energy and narrow photoluminescence peaks are often used as indicators for material quality with a low donor concentration. The temperature, at which these spectra are recorded, as well as the excitation intensity, influence the observed results. Figure 2.2.3 shows this temperature dependence for the absorption edge, as well as for the peak energy in photoluminescence (PL) experiments for a layer. In addition, the temperature behavior of the PL emission for a nanowire sample is shown for comparison.

The tendency of InN for n-type conductivity and to be degenerated is similar to InAs (Vilkotskii *et al.*, 1979), InSb (Moss, 1985) and InP (Bugajski & Lewandowski, 1985). The change in absorption and photoluminescence due to band-filling effects is also known as the Burstein-Moss-effect.

In contrast, the charge neutrality level of GaN is in the gap, 2.20–2.50 eV above the valance band maximum (King *et al.*, 2008). In the case of GaN, the width of the peaks in emission spectra broaden first of all with carrier concentration.

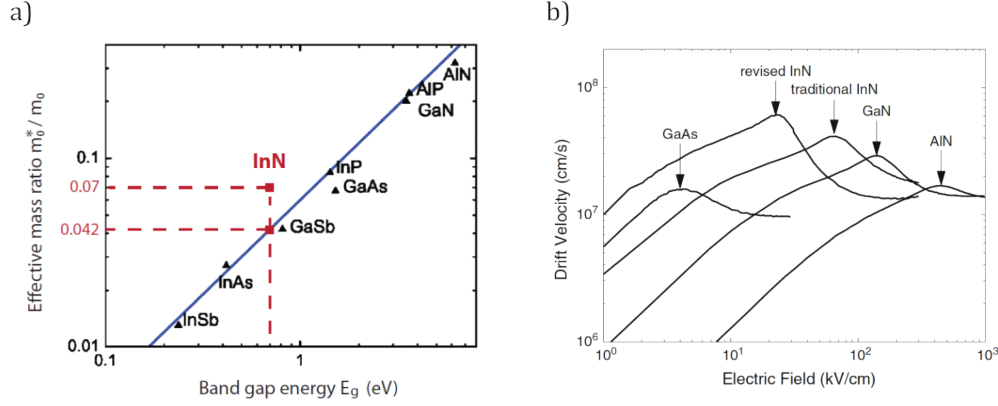

Figure 2.2.4.: *a) The empirical rule $m_e^* = 0.06\ E_g$ for several semiconductors (adapted from Nag (2003)). b) The simulated electron drift velocity depending on electric field. For "InN revised", $E_g = 0.75\ eV$ and $m_e^* = 0.045\ m_e$ were used and for "InN traditional", $E_g = 1.9\ eV$ and $m_e^* = 0.11\ m_e$ (O'Leary* et al., *2010).*

The value of the effective electron mass m_e^* for InN is controversially discussed and varies between 0.04 m_e and 0.11 m_e. From $k * p$ theory, the relation $m_e^* \approx 0.06\ E_g$ is deduced (Nag, 2003), which is true for most compound semiconductors, as shown in figure 2.2.4 a). For InN with a band gap of 0.69 eV, this leads to $m_e^* \approx 0.041\ m_e$, which is in agreement with the m_e values reported by Hofmann *et al.* (2006). Higher values of effective electron mass can also be assigned to band filling effects. Figure 2.2.2 b) shows the increase of effective mass with carrier concentration, demonstrating a significant increase at typical carrier concentrations of about $10^{18}\ cm^{-3}$ for unintentionally doped material. The effective mass is $m_e^* \approx 0.2\ m_e$ for GaN (Morkoc, 2008) (compare to figure 2.2.4). For the holes in both cases, three bands are present: heavy hole (hh), light hole (lh) and split-off (so) band. The effective hole masses for InN are 0.5(hh), 0.27(lh) and about 0.1(so) in contrast to GaN, with 1.4 (hh), 0.3 (lh) and 0.6 (so) m_e (Morkoc, 2008). Nevertheless, the reliability of the values for InN is questionable, since p-type material is rare and the same reference book for III-N (Morkoc, 2008) also gives outdated values for the better known effective electron mass. Due to the low effective electron mass, high electron drift velocities are predicted for InN (see figure 2.2.4). This is in accordance with measured mobilities of 3750 cm²/Vs at 300 K (Fehlberg *et al.*, 2007) for the bulk contribution. The surface contribution is subtracted by means of quantitative mobility spectrum analysis (QMSA) on multiple magnetic field Hall effect measurements. Electron mobilities $\leq$ 1000 cm²/Vs at 300 K (Morkoc, 2008) are typical for InN layers. As shown in figure 2.2.4 b), the electron drift velocity of InN is higher than in GaN and GaAs, which are used for high frequency applications nowadays.

For $In_{1-x}Ga_xN$ alloys, the change of band gap E_g with Ga fraction x can be described by the following equation (Walukiewicz *et al.*, 2004) (see figure 2.2.5):

$$E_g^{In_{1-x}Ga_xN} = x\ E_g^{InN} + (1-x)\ E_g^{GaN} - b\ x(1-x) \tag{2.2.1}$$

using a bowing parameter b of 1.4 eV which is in accordance with the universal rule:

$$b = \beta |E_g^{GaN} - E_g^{InN}| \tag{2.2.2}$$

with $\beta\ \approx 0.45$ (Walukiewicz *et al.*, 2004). In addition, figure 2.2.5 shows calculated band offsets, which always correspond to type I heterojunctions.

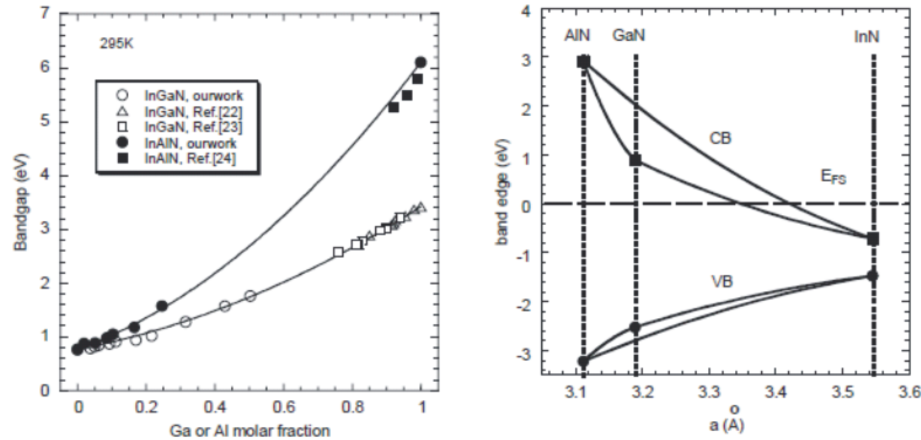

Figure 2.2.5.: *On the left, the dependence of the band gap on In concentration in AlInN and InGaN alloys is shown. On the right, the band offset for these alloys are shown as deduced from a valence band offset for InN/GaN of 1eV (taken from Walukiewicz* et al. *(2004)).*

Surface properties

Theoretical and experimental results (Van de Walle *et al.*, 2010) are in agreement and state that the polar surfaces of InN show a surface Fermi-level-pinning in the conduction band leading to an electron accumulation at the surface. In contrast, GaN has a surface Fermi-level pinning in the gap, which leads to a surface-depletion of electrons at all surfaces (Segev & van de Walle, 2006), as illustrated in figure 2.2.6.

In the case of non-polar surfaces, theoretical calculations by Segev & van de Walle, 2006 and Segev & Van de Walle, 2007 predict the absence of Fermi-level pinning in the conduction band (compare figure 2.2.6), unless a metallic adlayer exists. Experimental results on this issue must be handled with care since surface contamination or reactions with atmosphere change the surface properties. Non-polar surfaces exposed to atmosphere generally show a Fermi-level pinning above CBM. Wu *et al.* (2008) and Ebert *et al.* (2011) observed no electron accumulation at a-planes, if they were obtained by cleaving under ultra-high-vacuum conditions. Due minor quality of the cleaved surfaces, the origin of these observations is not completely clear. It seems that once the surface is exposed to atmosphere, it is irrevocably changed and shows a Fermi-level pinning above the CBM. This could be explained by oxygen contamination or by an unstoichiometric surface after cleaning (Wang *et al.* (2011), Segev & Van de Walle (2007)). Furthermore, a higher nitrogen vacancy density close to the surface would lead to an electron accumulation at the surface (Terentjevs *et al.*, 2010). This issue of surface electron accumulation will be treated in detail in section 7.3 and 7.5.

Doping behavior

Due to the fact, that the electronic properties of InN are analyzed in this thesis, the following paragraph is focused on the doping behavior of InN.

According to the Amphoteric Defect Model (Walukiewicz, 1989), the character of defects is determined by the position of the Fermi Stabilization Energy E_{FS}. The Fermi Level E_F tends to be equal to E_{FS} by increasing the amount of native defects in a material due to their amphoteric character (Walukiewicz, 2001). Samples without intentional dopants show n-type conductivity with electron concentrations of $\geq 10^{17} cm^{-3}$. p-doping is challenging because the E_{FS} is in the conduction band for InN or in the upper part of the band gap for GaN.

Recent knowledge about conductivity in InN was summarized by van de Walle in his comprehen-

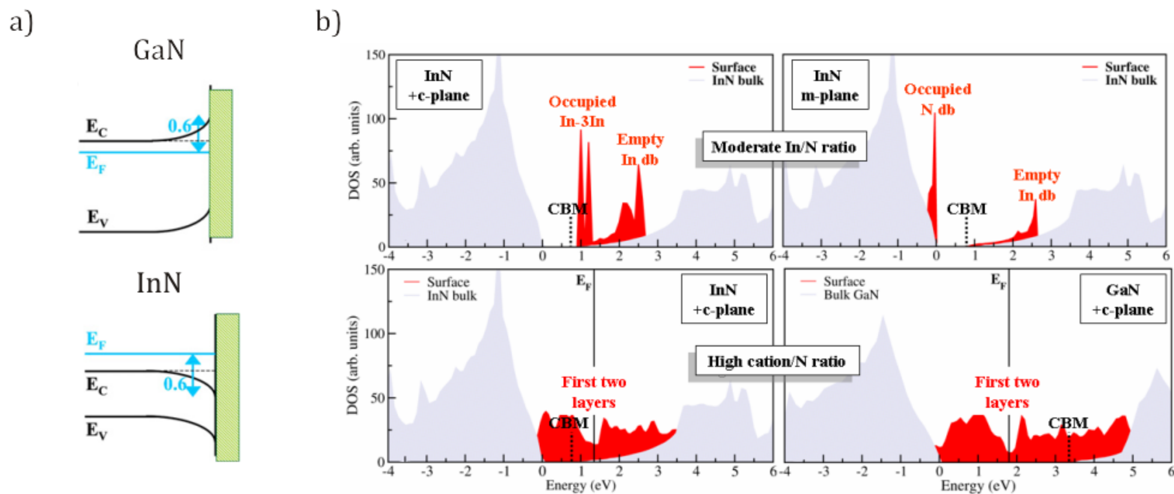

Figure 2.2.6.: *a) Sketch of the observed band bending at the c-plane surfaces for n-type InN and GaN. b) The calculated density of states of bulk and surface of polar and non-polar surfaces (Segev & van de Walle (2006) and Segev & Van de Walle (2007)).*

sive review article. Therefore, information shown in this section is taken from Van de Walle *et al.* (2010) and references therein, unless otherwise indicated. The probability of finding a defect in a crystal depends on its formation energy. This formation energy is composed of a contribution due to crystal deformation and a contribution due to its charge state, leading to a dependence on the Fermi-level.

In InN, the intrinsic defect with lowest formation energy for all positions of the Fermi-level is the nitrogen vacancy V_N. It is an amphoteric defect with a (3+/+) transition at 0.24 eV above the VBM and a (+/-) transition 1.85 eV above the VBM. The latter coincides roughly with E_{FS}. The 2+, as well as its neutral charge state, are unstable. The concentration under typical growth conditions is assumed to be in the $10^{15}cm^{-3}$ range. The indium vacancy is an acceptor with transitions (0/-), (-/2-), (2-/3-) located 0.25, 0.53, 0.92 eV above the VBM, but its formation energy is very high, leading to concentrations of at least less than $6 \times 10^{16}cm^{-3}$. Among interstitials and antisites, only indium interstitials have reasonably low formation energy. But their formation energy is still significantly higher than that of nitrogen vacancies. Therefore, the concentration of these defects should be negligible. The density of dislocations was found not to correlate with carrier concentration and thus it is assumed that they play a minor role in unintentional doping (Gallinat *et al.*, 2009). Accordingly, intrinsic defects are not responsible for the high unintentional n-doping, typically in the $10^{17} - 10^{18}cm^{-3}$ range.

Typical unintentional impurities in as grown samples are hydrogen and oxygen, because they cannot be completely avoided in the growth environment. Both elements are donors with low formation energies. Furthermore, hydrogen does not have the feature of being an amphoteric compensating defect in InN, as in most other semiconductors. Hydrogen can be found as an interstitial as well as on a nitrogen site, but the interstitial site is energetically more favorable by 1.14 eV. Interestingly, hydrogen impurities are under all considered Fermi-level conditions in a 1+ charge state. It is noteworthy to mention that hydrogen is a fast diffuser and is still mobile at temperatures of about 100 °C. But the surface electron accumulation layer impedes outdiffusion of these positively charged impurities. Annealing under nitrogen atmosphere leads to a reduction of H concentration whereas annealing in ammonia leads to an increase of H concentration. On the energetically favorable nitrogen site, oxygen is a shallow donor. Since it is known that the III-nitrides form a thin surface oxide, the surface accumulation of electron could also originate from oxygen incorporation or doping at the surface and not from surface states of clean InN.

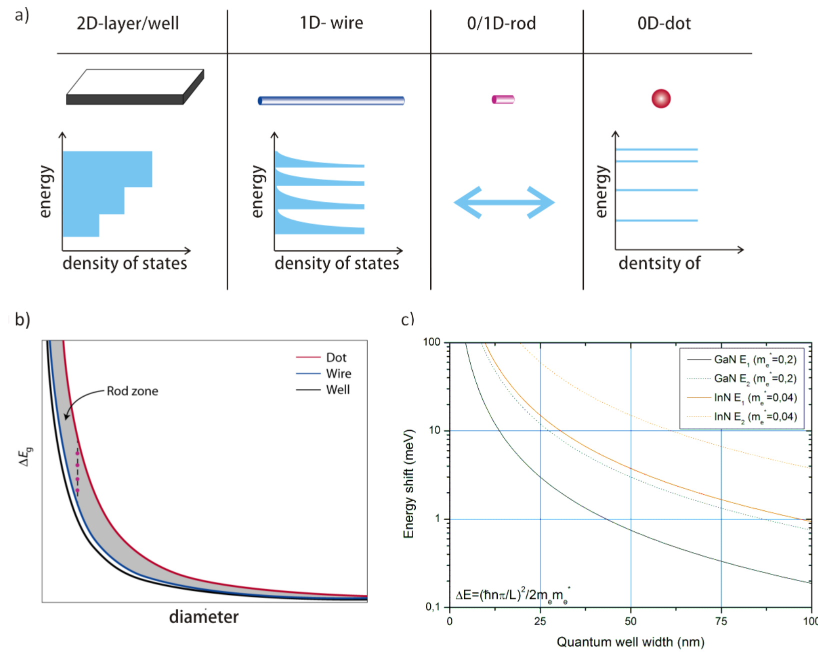

Figure 2.3.1.: *a) Overview of quantum structures and their density of states (Buhro & Colvin (2003); Waser (2003)), b) Sketch of increase of band gap with diameter (Buhro & Colvin, 2003), c) Calculated increase of lowest quantized energy level in a quantum well with infinite barrier height depending on its thickness (Compare also Denker (2007)).*

The typical intentional n- and p-dopants, Si and Mg, have sufficient solubility. Silicon is a shallow donor and easily enables an increase in electron concentration. Mg on an In site has a lower formation energy than in GaN, so solubility is relatively high. Compensation by other impurities or nitrogen vacancies is a problem in achieving p-type material. In addition, an inversion layer at the surface caused by Fermi-level pinning in the conduction band at the surface always introduces a n-type conduction channel. Up to now, reports of successful p-doping are rare. Jones *et al.* (2006) and Wang *et al.* (2008) reported p-type material under a n-type inversion layer at the surface characterized by capacitance voltage measurements. In addition, Anderson *et al.* (2006) reliably proved successful p-type doping by conductance channel separation (QMSA). However, the samples still show an overall n-type behavior due to the inversion layer at the surface. Very recently Nguyen *et al.* (2011) realized InN nanocolumns with a very low background doping. Hence, they were able to fabricate axial p-i-n diodes. The position of the Mg acceptor level (0/-) is calculated to be about 200 meV above the VBM. Very little is known about other possible acceptors.

2.3. Nanostructures: confinement, surface induced properties

Starting from three dimensional crystals, dimensionality can be reduced step by step. Reduction by one dimension leads to planes, by two dimensions to lines and by three to points. Infinite reduction of expansion is physically impossible, but quasi-2D-films or wells, quasi-1D-wires and quasi-0D dots can be realized. An approximate size for the onset of quantum-confinement effects is the Bohr radius of excitons. All structures with a size in the nm range are called nanostructures, but they are called quantum structures only if they show confinement effects. By quantum confinement, a quantization of energy and a shift of the lowest energy state are introduced. This is sketched in figure 2.3.1.

The growth of nanowires is usually limited to diameters bigger than 15-20 nm. Due to this, III-N

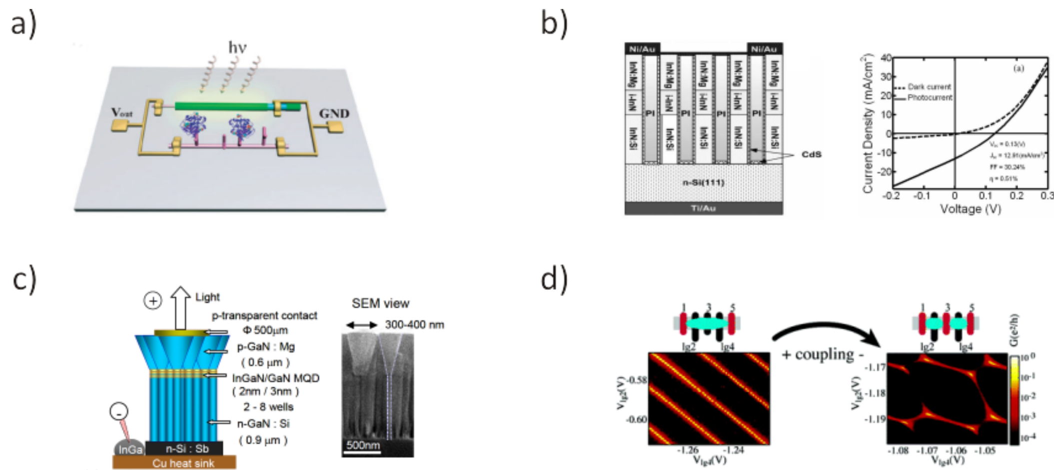

Figure 2.4.1.: *a) Nanowire solar cell and sensor on one chip (Tian* et al.*, 2009), b) InN nanowire p-i-n solar cell on silicon (Nguyen* et al.*, 2011), c) InGaN nanowire LEDs on silicon (Kikuchi* et al.*, 2004) , d) tunable quantum dots made of InAs nanowires (Fasth* et al.*, 2005).*

nanowires usually show no or only very little confinement effects, if no extra barriers are introduced. This can be realized by axial or radial heterostructures. At this point, their small size and large surface facilitate strain relaxation before defect formation, resulting in the opportunity to combine materials with larger lattice mismatch at high crystal quality. Their large surface-to-volume ratio also increases the impact of surface effects.

2.4. Possible applications III-N nanowires

In general, every kind of semiconductor device can be made of nanowires. Nanowires stand out due to their small size, high surface-to-volume ratio and typically high crystal quality. Their high surface-to-volume ratio makes them very appealing for gas sensing applications. In this case, the strong influence of surface properties is fully utilized , which increases sensitivity (e.g. Pearton *et al.* (2008); Koley & Zhihua (2008) and Koley & Zhihua (2008)). Furthermore, this is interesting for dye sensitized solar cells and batteries, and wherever a high surface-to-volume ratio is desirable.

The typically high crystal quality, independent of substrate, has great potential for materials, for which suitable substrates are expensive or not available, as in the case of III-nitrides. Therefore, a lot of research activity has been taken place in the field of InGaN nanowire-LEDs (e.g. Kikuchi *et al.* (2004); Hersee *et al.* (2009); Mi & Chang (2009); Guo *et al.* (2010), see figure 2.4.1 c)). Gradečak *et al.* (2005) have even showed optically pumped lasing was shown for GaN nanowires. Additionally, nanowires are also highly interesting for light to electrical energy conversion in the way of pure inorganic (e.g. Nguyen *et al.* (2011), see figure 2.4.1 b)), organic-inorganic (e.g. Lai *et al.* (2010)) and dye sensitized solar cells (i.e. Law *et al.* (2005)). Their efficiency is considerably low at present but may increase noticeably by an appropriate surface passivation. The combination of nanosized sensors and solar cells can be used for nanosized sensing devices without external energy supply (Tian *et al.* (2007), see figure 2.4.1a)).

An interesting example for basic research on nanowires are tunable quantum dots, whereby confinement is introduced by electric fields. Here, barrier heights as well as potentials in the dots can be tuned by external voltages (see figure 2.4.1 d)).

Even though there are plenty of promising applications for nanowires, up to now, there is no existing nanowire-based commercially available product. Most of the applications are just in a proof

of principle stage. The major drawback is that most applications are based on handling of single wires. Up to now handling of single wires is very time consuming, expensive and not capable of being integrated in standard processing for layer based devices.

3. Growth of InN and InGaN

Typically, single crystalline bulk material of high quality is obtained by growth from a melt, as in the case of silicon, germanium or gallium arsenide. This is up to now challenging or even impossible for III-nitrides due their high nitrogen vapor pressure. Bulk GaN substrates are available since several years, but still rare and expensive. Due to this, III-nitrides are usually grown by vapor deposition techniques as thin films on foreign substrates, aside some alternative attempts (i.e. Sardar *et al.* (2005)). A general problem in realization of green light emitting diodes or laser diodes is the immiscibility of InN and GaN.

Therefore, a brief overview is given concerning the methods, as well as possible substrates, for crystal growth of III-nitrides and the miscibility of InGaN.

3.1. Synthesis of III-N semiconductors

InN and GaN melt under high temperatures (> 1700 and > 2000 K) and high pressures ($> 4 * 10^4$ bar). This fact makes growth from a melt technologically challenging. For GaN growth from a melt was demonstrated with high crystalline quality, but at high costs and only for small pieces of about 1x1 cm². Samples grown by this technique are commercially available from TopGaN Ltd., Poland.

Vapor phase deposition techniques are mostly applied to grow InN and GaN due to the lower costs. Since a direct reaction of the metal with N_2 does not take place at low pressures, nitrogen has to be supplied as nitrogen radicals, in an excited state or by other molecules with a higher reactivity. Nitrogen radials and excited nitrogen can be generated by plasma excitation. Ammonia, which dissociates at elevated temperatures is widely used to supply nitrogen by molecules with higher reactivity. Also, different ways exist to supply the metal. It can be supplied directly by effusion cells or indirectly by gas sources for precursor molecules which release metal atoms at the substrate. All combinations of supplying the constituents are possible. Depending on the way how the constituents are supplied, they can be assigned to chemical or physical vapor deposition methods. In the following, a short overview is given over the most commonly used methods which are suitable for synthesis of high quality material.

Typical chemical vapor deposition (CVD) techniques for the growth of III-nitrides are metal-organic vapor phase epitaxy (MOCVD), chemical beam epitaxy (CBE) and hydride vapor phase epitaxy (HVPE). All of these methods use ammonia as precursors for nitrogen supply. MOCVD and CBE use metal-organic compounds like trimethyl-indium as metal supply, whereas in HVPE III-trichloride as metal precursor is used. MOCVD and HVPE takes place at about atmospheric pressure, whereas CBE at pressures below $\lesssim 10^{-5}$ mbar and therefore in the high or ultra-high vacuum range. HVPE stands out due to high deposition rates of more than 100 µm per hour, whereas for MOCVD deposition rates of several µm per hour and for CBE of about one µm per hour are typical. For the sake of completeness, it has to be mentioned that evaporation of indium or indium oxide is sometimes used to supply metal for growth of nanowires in CVD systems (e.g. Lan *et al.* (2004)).

Typical physical vapor deposition techniques for III-nitrides are MBE and sputter deposition. The latter is nowadays rarely used due to the low material quality which was realized by this method. MBE takes place in a ultra high vacuum, similar to CBE. In MBE effusion cells are used to supply the metal. Nitrogen can be provided by plasma sources or ammonia gas sources. The advantage of plasma assisted MBE is that both constituents are directly supplied as beams. Thus, the supply rates are only controlled by the cell and do not depend on substrate temperature. In addition, the residual

gas in the reactor chamber does only contain In, Ga and nitrogen, aside from a very little background, which pressure is at least 5 orders of magnitude lower. The use of precursors harbors the risks of contamination with parts of the precursor, which are not used for growth. An additional advantage of plasma assisted MBE is that no toxic chemicals are used.

In general, beam based vacuum techniques, MBE and CBE, provide exact control over deposition thickness in the order 1 monolayer, whereas the gas in the furnace for HVPE and MOCVD may lead to retardation effects. Therefore, MBE and CBE are perfectly suitable for thin layer heterostructures. Their main drawbacks are low deposition rates, the lack of possibility for parallel processing and that any maintenance causes long down times. These causes lead to high costs per sample. Hence, these techniques are mostly used in scientific research, in contrast to MOCVD and HVPE which are used in research and production.

3.2. Substrates for heteroepitaxy

Substrates have to fulfill several requirements for deposition of single crystalline films with high quality. First of all, a comparable crystal structure with a low lattice mismatch and similar temperature expansion coefficients is required. Furthermore, the chemical stability under growth conditions and UHV compatibility are needed. Beside this, it must be possible to prepare flat and clean surfaces in the desired orientation. Finally, the substrate itself must be available at a reasonable price and quality. Table 2.1.1 provides a list of possible substrates for III-N heteroepitaxy including lattice parameters and lattice mismatch to InN and GaN.

In the case of lattice mismatched growth, there is a critical island size above which strain is compensated by dislocations. If the material is grown in the form of nanowires, the quality is less sensitive to lattice mismatch. This is due to the small cross-section of the nanowires. No dislocations are introduced at hetero-interfaces, if the cross-section is smaller than the critical size of islands. Additionally, the high surface-to-volume ratio facilitates the reduction of dislocations at the sidewalls close to the substrate, if the cross-section is larger than the critical one and dislocations have formed. Hence, nanowires show only few dislocations.

The commonly used traditional substrates for InN layers are sapphire and GaN on sapphire. These substrate have a high lattice mismatch to InN of about 12% or 25%, respectively, which lead to formation of crystal defects. To reach lower defect densities in InN layers, the approach using yttrium stabilized zyrconia (YSZ) (111) with a lattice mismatch of -2.24 % is auspicious (i.e. Honke *et al.* (2004) or Swartz *et al.* (2008)).

Moreover, it has to be regarded that most semiconductor technology is based on silicon and integration of III-nitrides into silicon technology is of great interest. Therefore, this study concentrates on the deposition of InN and InGaN on silicon and on sapphire without or with GaN buffer layer, even though approaches on substrates, like YSZ, ZnO, γ-$LiAlO_2$ or $LiGaO_2$ are promising.

Growth of InN and GaN on Si suffers from a general problem. The bond of In or Ga to nitrogen is weaker than the one of Si to nitrogen. The plasma excited nitrogen reacts with the Si surface. This leads to the formation of a thin amorphous inter-layer of SiN (Galopin *et al.*, 2011). Due to this, direct deposition of InN on Si does not result in epitaxial films. In the case of nanowires, the formation of an amorphous interlayer leads less alignment of the wires, a missing epitaxial relation in the basal plane among the wires and growth free of strain from the substrate lattice. The epitaxial relation can be maintained by the introduction of an thin AlN buffer layer.

3.3. Miscibility of $In_{1-x}Ga_xN$

The $In_{1-x}Ga_xN$ alloy exhibits a large immiscibility gap. Ho & Stringfellow (1996) calculated the thermodynamical stability as function of In mole fraction and temperature. The results are shown in

Material	Lattice constants a / b / c [Å]	a or a*(direction) [Å]	Mismatch InN / GaN [%]
InN (hexagonal)	3.563 /-/ 5.704	3.563	0 / -10.50
GaN (hexagonal)	3.189 /-/ 5.175	3.189	11.73 / 0
AlN (hexagonal)	3.104 /-/ 4.966	3.104	14.79 / 2.74
Al_2O_3(rhombohedral)	4.759 /-/ 12.991	4,759 (2.747**)	-25.13/-32.99 (39.63/ 16.09)**
Si (cubic)	5.4301 /-/-	3.840*	-7.21/-16.95
Ge (cubic)	5.658 /-/-	4.000*	-10.93 / -20.28
ZnO (hexagonal)	3.250 /-/ 5.207	3.250	9.63 / -1.88
γ-$LiAlO_2$ (tetragonal)	5.169 / - / 6.268	3.134**	13.69 / 1.75
$LiGaO_2$ (hexagonal)	5.402 / 6.372 / 5.407	6.372*0.5	11.83 / 0.09
GaAs (cubic)	5.653 /-/-	3.997*	-10.86 / -20.22
InAs (cubic)	6.058 /-/-	4.284*	-16.83 / -25.56
6H SiC (hexagonal)	3.082 /-/ 15.112	3.082	15.61 / 3.47
Yttrium stabilized Zyrconia (cubic)	5.154 /-/-	3.645*	-2.24 / -12.50

Table 3.2.1.: *Lattice parameter and mismatch of possible substrates for InN and GaN in (0001) direction. The mismatch calculated by* $f = (a_{Layer} - a_{substrate})/a_{substrate}$. *Constants from Morkoc (2008); Chen* et al. *(2002). (* a* is the corresponding lattice constant to the a lattice constant of the wurzite structure; ** see Morkoc (2008) for details).*

figure 3.3.1. The solid line indicates the theoretical transition from conditions, under which the alloy is stable, to conditions under which the alloy is unstable. Above the dashed line there is a barrier for phase separation, whereas below there is none. Therefore, this curve marks the transition from spinodal to binodal phase separation. At temperatures above 1200°C, the alloy should be stable over the whole compositional range. But decomposition impedes growth at these temperatures. In the case of strained growth, the thermodynamically stable region can be expanded (i.e. Karpov (1998) and Tabata *et al.* (2002)), but the film thickness is limited in this case. For the standard growth direction, the c-direction, the strain induces piezoelectric fields, which lead to a spatial separation of electrons and holes. This spatial separation causes a reduction of radiative recombination and is mainly responsible for the low efficiency of green $In_{1-x}Ga_xN$ quantum well LEDs grown in the c-direction. Due to the technological importance, there is an impressively high research activity on growth in semi- and non-polar directions to reduce the spatial separation of electrons and holes. An overview of the actual progress and challenges on this topic is given in Schwarz & Scholz (2011).

According to Ho & Stringfellow (1996), binodal phase separation should occur at temperatures of about 400-800°C used for InN and GaN MBE growth, if $x \geq 0.18$-0.22. At temperatures of 700-920°C, Stringfellow (2010) found a good agreement between theoretical calculation and experimental data. In contrast, Kuykendall *et al.* (2007) demonstrated the successful growth of $In_{1-x}Ga_xN$ nanowires for the whole compositional range by Halide-CVD. Kuykendall *et al.* believe, that the low growth temperature of about 550°C and a high growth rate promote the growth of the non-thermodynamically-stable alloy.

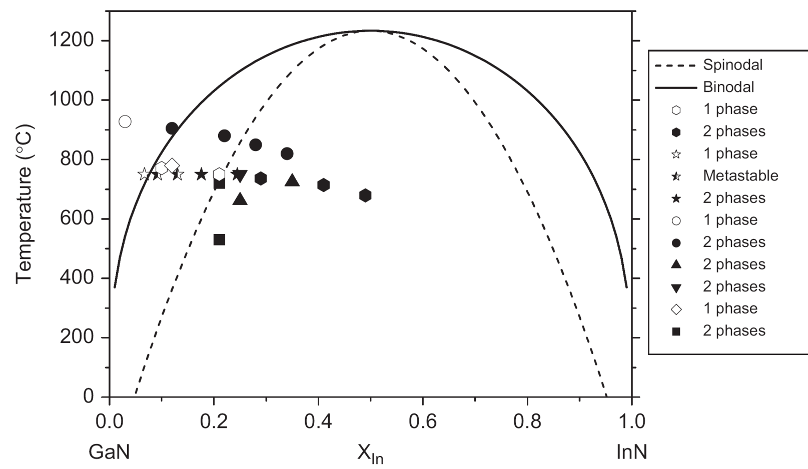

Figure 3.3.1.: *Calculated phase diagram compared to experimental data. The solid line indicates the binodal curve and the dashed one the spinodal (Stringfellow, 2010).*

4. Molecular beam epitaxy of III-N semiconductors

Molecular beam epitaxy is a physical vapor deposition method, as mentioned in section 3.1. The constituents are directly supplied as molecular beams to a heated substrate in an ultra high vacuum chamber. The low residual background pressure of about 10^{-10} mbar in combination with ultra high purity source materials enable growth of material with low impurity concentrations. For this study, a "Veeco Gen II" MBE system, shown in figure 4.0.1, was used. This system is equipped with effusion cells for metal supply and a Veeco "UNI-Bulb RF" plasma source for nitrogen. The fluxes of metal are controlled by their cell temperature and the nitrogen flux is controlled by the operating parameters of the plasma source. The temperatures and plasma condition cannot be changed instantaneously and fast "on" and "off"-switching of the fluxes is realized by shutters in front of the cells.

In the following, aspects of the MBE growth, which are relevant for this thesis, are considered in detail. Based on considerations about metastable growth of III-nitrides in MBE, it is discussed, how the concept of difference of chemical potential could be transferred to this type of growth based on rate equations. At the end of this section, relevant technical aspects of controlling and monitoring growth conditions are discussed.

4.1. Metastable growth

In thermodynamics, the phase stability line indicates the conditions under which different phases are equally favorable. The MBE process of III-As is one of the best known and takes place near the phase stability line. Crystal growth takes place if the pressure of the gas phase is higher than the equilibrium one and the solid sublimates if the pressure is lower. The driving forces can be expressed by differences of chemical potentials.

For MBE growth of III-nitrides the situation is supposed to be different (Newman, 1997). The window for plasma assisted MBE is at pressures several orders lower than the stability line for phase equilibrium according to the pressure-temperature phase diagram of the Ga(l)+N_2(g)$\rightleftharpoons$GaN(s) reaction in figure 4.1.1. At these conditions, liquid Ga and gaseous nitrogen are thermodynamically stable. This is in agreement with the observation, that no growth occurs at typical MBE conditions, if N_2 is supplied in its ground state. Growth is only observed if excited nitrogen is supplied. The additional energy due to the excitation facilitates overcoming of the kinetic barrier for forward reaction, whereas the barrier still hampers backward reaction, decomposition (Compare figure 4.1.1). This situation is called metastable growth.

4.2. Growth temperature

High quality thin film growth is usually obtained at about $\sim \frac{1}{2}$ to $\frac{2}{3}$ of melting temperature. But the equilibrium pressure, i.e. the decomposition rates, of III-nitrides would be too high to be compensated by cells used in MBE. Furthermore, also the pressure would be too high to allow MBE. The growth temperatures of III-nitrides are low as 1070 K (GaN) and 800 K (InN), which corresponds to about $\frac{1}{3}$ of melting temperature (Newman, 1997). At these temperatures, the mobility of the surface atoms or molecules is usually too low for high quality thin films growth. Metal rich conditions are used for high quality thin film MBE growth of III-nitrides. In this case, a metal adlayer forms which

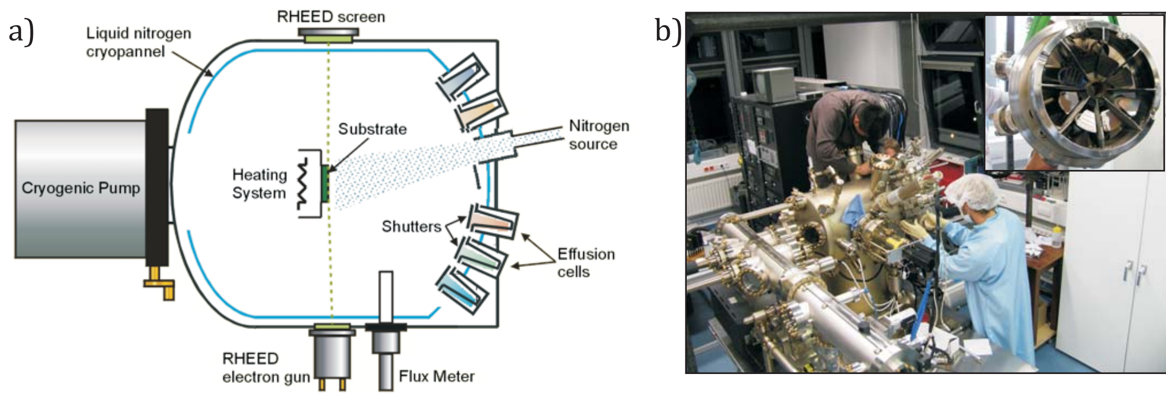

Figure 4.0.1.: *a) Sketch of an MBE system. b) Image of the "Veeco GEN II" MBE system, in the inset the source flange with cryo shield, cells and shutters is shown.*

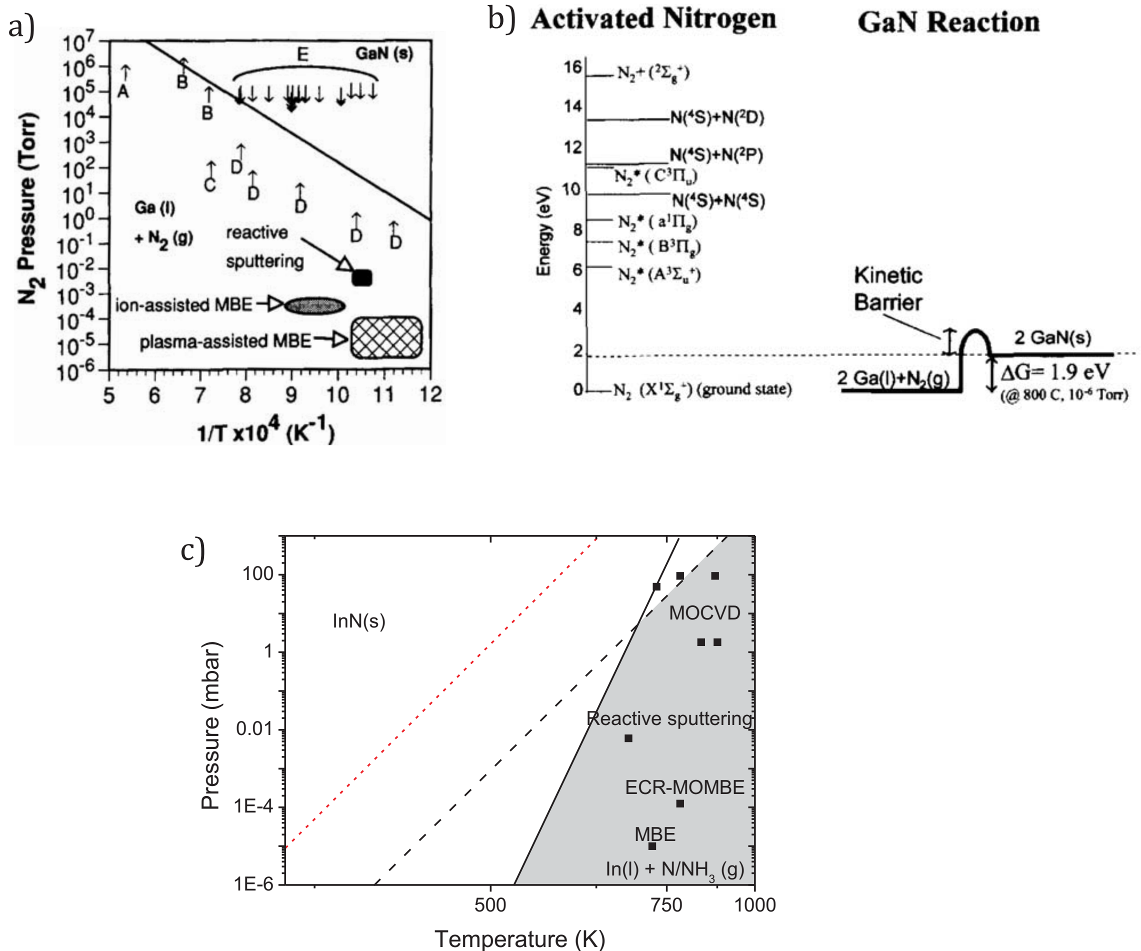

Figure 4.1.1.: *p-T phase diagram of a) GaN Newman (1997), b) sketch of metastable growth model of Newman (1997) and c) InN with marked MBE window. The grey area indicates the conditions, under which InN is unstable according to Newman (1997) and Onderka* et al. *(2002).*

is supposed to lower the kinetic barrier for movement of surface atoms and thereby increase their mobility (Broxtermann, 2011). Furthermore, the metal adlayer increases the diffusion length of nitrogen (Neugebauer *et al.*, 2003). This indicates, that plasma assisted MBE growth III-N is different from standard thin film growth. It has to be mentioned that N-rich conditions III-N can lead also to high quality material at similar substrate temperatures, but the resulting columnar structures do not form a closed layer.

4.3. Difference of chemical potential in metastable growth

The state of a system with constant pressure p and temperature T is determined by the Gibbs free energy. The knowledge of the Gibbs free energy of a given system and the environment conditions enable the calculation of the observable phases and their ratios by minimizing its Gibbs free energy. If a system is not in equilibrium, the chemical potentials are not equal anymore. The difference of the chemical potentials $\Delta\mu_i$ from their equilibrium value are a measure of the driving force to push the system back to equilibrium.

The chemical potential μ is defined as the derivative of the Gibbs free energy of phase j with respect to the amount of a component N_i. Therefore, the chemical potential is defined for each phase and each of its components separately.

$$\mu_i^j = \frac{d}{dN_i} G^j(p,T,N_1,\ldots,N_n) \tag{4.3.1}$$

with μ_i^j the chemical potential of component i and phase j.

In equilibrium, all chemical potentials of the different phases for each component are equal:

$$\forall i,j: \ \mu_i^j = \mu_{ie}(p,T,N_1,\ldots,N_n) \tag{4.3.2}$$

with μ_{ie} the equilibrium chemical potential for component i.

Any system out of equilibrium can be regarded as a system with a pressure or temperature deviating from equilibrium. The reference to the equilibrium pressure at the same temperature or equilibrium temperature at the same pressure allows for the calculation of the difference in chemical potential $\Delta\mu$. Both possibilities are in general equivalent. A situation of a higher pressure than equilibrium is called supersaturation and a situation of lower temperature than equilibrium undercooling.

The solid phase of III-N systems is a binary phase with III:N ratio of 1:1. Therefore, the deviation of the system from equilibrium can be generally divided into nitrogen-rich, metal-rich and stoichiometric. In the N-rich case, there is excess of nitrogen and possible growth of a crystal is limited by the metal supply. In the metal-rich case, there is excess of metal and possible growth of a crystal is limited by the nitrogen supply. Therefore, it is convenient to reduce the system to a quasi one component system by treating the excess component as environmental parameter and regarding only the limiting species. In the metal-rich case, the environmental conditions can either be described by the metal flux or the corresponding amount of metal on the sample surface. In the stoichiometric case metal and nitrogen are supplied in a way that both constituents limit possible growth in the same way. However, this case is not considered here due to its minor interest for this study.

Supersaturation

Under the assumption of an ideal gas and an incompressible solid, the difference in the chemical potential $\Delta\mu^{vs}$ for a one component vapor-solid system is

$$\Delta\mu^{vs}(T,p) \approx k_B T \ \ln\frac{p}{p_e} \tag{4.3.3}$$

with p_e the equilibrium pressure and k_B the Boltzmann constant (e.g. Markov, 1995).

The question arises, how these can be adapted to the case of a metastable growth in MBE. In standard systems pressure is isotropic and the impingement rate on a surface F is given under the assumption of an ideal gas by

$$F = p/\sqrt{2\pi m k_B T} \tag{4.3.4}$$

with m the mass of the molecule and T the temperature.

MBE can be described as an open system. The impingement rates are given directly by the fluxes from the sources. Desorbing atoms or molecules are not given back to system and are directly pumped or stick to the walls of the MBE chamber. Therefore, the difference of chemical potential does not depend on the pressure in the chamber, but on the fluxes of the supply and the desorption rates.

Accordingly, the ratio of pressures has to be replaced by the ratio of fluxes using equation 4.3.4. Under the assumption of equal temperatures and equal masses for impinging and desorbing molecules, it follows:

$$\frac{p}{p_e} = \frac{F}{F_e} \tag{4.3.5}$$

with F the impinging flux and F_e desorption rate.

In the metal rich case, i.e. excess of metal, the system is in equilibrium if the amount of escaping nitrogen (due to decomposition) is compensated by incorporation of impinging nitrogen F_N. The nitrogen flux needed to keep the amount of III-N constant is the equilibrium flux F_{eN} at a certain metal coverage σ_{metal} depending on the metal flux F_{metal}. Accordingly, the difference of chemical potential $\Delta\mu^{vs}_{III-rich}$ can be approximated by

$$\Delta\mu^{vs}_{III-rich}(F_N, \sigma_{metal}, T) \approx k_B T \ \ln \frac{F_N}{F_{eN}(T, \sigma_{metal})} \tag{4.3.6}$$

with $F_{eN}(T, \sigma_{metal})$ equal to the decomposition rate at temperature T. The metal coverage σ_{metal} can change the surface reactions (i.e. decomposition and incorporation rates) and its influence must be regarded.

In the N-rich case, the limiting constituent is the metal. Its stable phase can be either gaseous or liquid. The considerations about a desorption flux is only useful, if the limiting component desorbs, i.e. its stable phase is gaseous. This is the case for InN at temperatures above 470°C according to Gallinat *et al.* (2007). At these conditions, excited nitrogen is needed to stabilize the InN and the impinging nitrogen reduces the decomposition rate $F_{e\ metal}$. In this case, the nitrogen flux F_N has be considered as an environmental parameter and the difference of chemical potential $\Delta\mu^{vs}_{N-rich}$ can be approximated similar to the III-rich case by:

$$\Delta\mu^{vs}_{N-rich}(F_{metal}, F_N, T) \approx k_B T \ \ln \frac{F_{In}}{F_{e\ metal}(F_N, T)} \tag{4.3.7}$$

Undercooling

For a one component liquid-solid system, the first approximation of the difference in chemical potential $\Delta\mu^{ls}$ is given by

$$\Delta\mu^{ls} \approx \frac{\Delta s_m}{T_e}(T - T_e) \tag{4.3.8}$$

with T_e the equilibrium temperature and Δs_m the melting enthalpy (e.g. Markov, 1995). This equation can also be applied for the case of an undercooled gas, if the melting enthalpy is replaced by the sublimation enthalpy. For the different cases of MBE growth, this enthalpy must be replaced by the enthalpy of the corresponding transition. In the N-rich case the equilibrium temperature T_e can be determined by heating the sample under active nitrogen flux. At temperatures, at which no

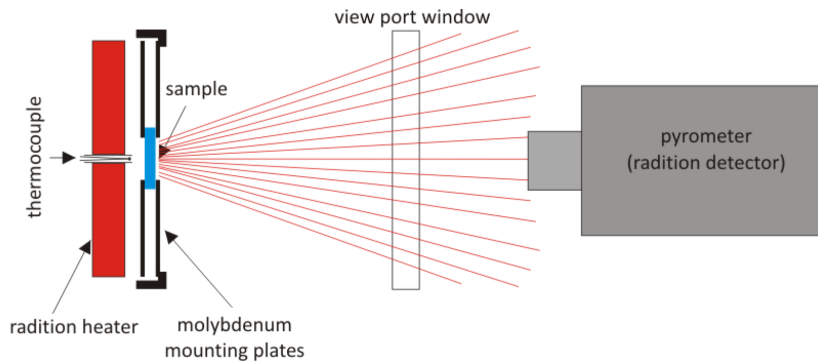

Figure 4.4.1.: *Sketch of sample holder and heater with thermocouple and pyrometer for temperature measurement.*

metal desorption occurs, the transition temperature between no metal adlayer and a metal adlayer is T_e. At temperatures at which metal desorbtion occurs, the metal desorbtion must be compensated by additional metal supply. For the metal-rich case, T_e is temperature at which a present metal adlayer starts to reduce. It has to be kept in mind, that the presence of metal can increase the decomposition rate and by this lower T_e.

In conclusion, it was shown how the difference of chemical potential can in principle be determined for the metastable growth of III-N MBE by regarding MBE as an open system, where pressures are replaced by fluxes. However, these considerations neglect that during growth the type of surfaces, as well as their area may change, which would affect the decomposition rates.

4.4. Controlling and measuring growth conditions

For any growth study, the growth conditions must be controlled. For design and interpretation of such studies, knowledge about the way how growth conditions are controlled, including their accuracy and reliability, are mandatory. Therefore, the principles and control of the substrate heater, metal sources and nitrogen source are briefly discussed.

4.4.1. Substrate temperature

Temperature control and measurement under vacuum conditions is challenging. Thermocouples in contact with the samples are critical because the thermocouple will influence temperature homogeneity. Solid heat conducting blocks behind the sample decrease the influence of the thermocouple on the temperature, but increase the thermal response time. Additionally, the reproducibility of the heat contact between sample and thermocouple is critical. In the used "Veeco Gen II" system, the samples are heated from the backside by a radiation heater, which mainly emits in the infra-red to red spectral range. A thermocouple in the center of the heater is used to control the temperature by proportional–integral–derivative (PID)-controllers. This concept avoids any problems related to heat conduction, but the temperature of the thermocouple of the heater and of the sample differ and the relation between thermocouple and substrate temperature must be measured. Furthermore, this relation varies for samples of different material or geometry since the amount of reflected and adsorbed radiation varies.

The substrate temperature can be monitored by pyrometry (see figure 4.4.1). The pyrometer measures the radiation intensity of the sample in a certain energy band in comparison with the radiation intensity of a black body. The difference from black body is considered by a simple prefactor called emissivity ε and enables the calculation of the substrate temperature. Furthermore, the pyrometer can only monitor the samples through a window, which also adsorbs certain percentage of the radiation.

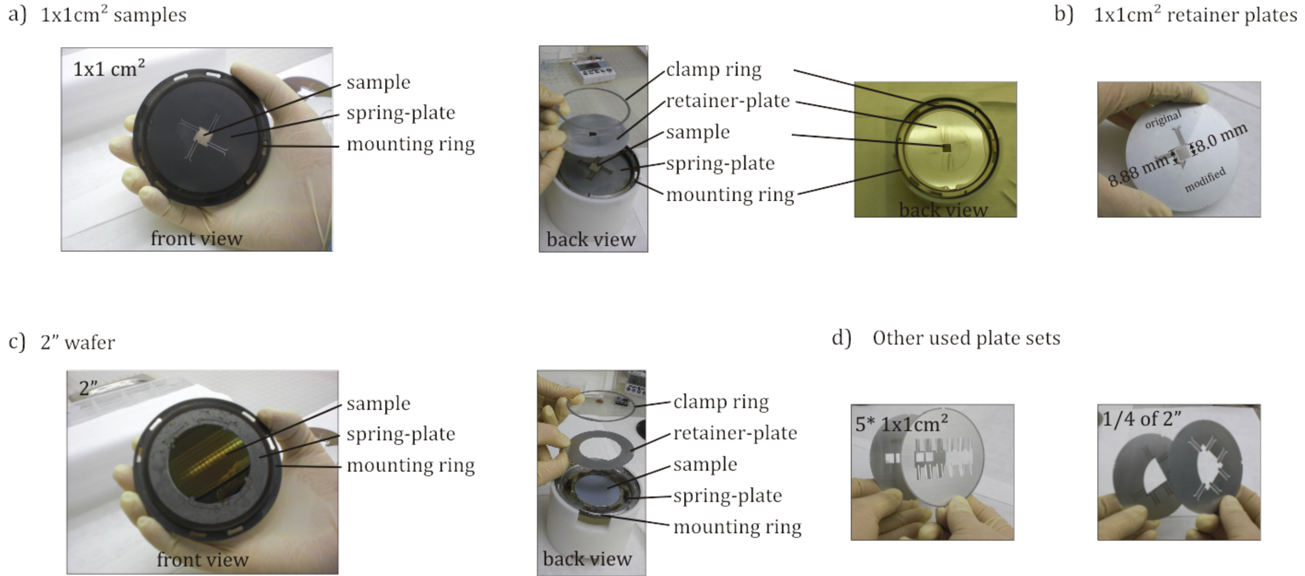

Figure 4.4.2.: *a) and c) Assembly of the sample holder for 1x1cm² and 2" samples, b) difference between a original retainer plate from Veeco and the home build one, d) mounting plates for five 1x1cm² samples and one 1/4 of 2" sample.*

Its influence is considered by an additional prefactor τ. According to this, the dependence of radiation intensity I and sample temperature T_{sample} is given by following equation:

$$I \propto \varepsilon \tau T_{sample}^4 \tag{4.4.1}$$

The energy band of the pyrometer must be chosen depending on the substrate material because the substrate must be opaque for this band and its emissivity must be independent of temperature. For silicon, this is the case for wavelengths of about 1 µm (Irc, 1997). Unfortunately, these conditions are met for sapphire at wavelength of about 12 µm at which the mounted window is opaque. Therefore, the absolute temperatures will be given for Si substrates. For sapphire substrate, the absolute substrate temperature is unknown and only the temperature of the thermocouple can be given as reference.

A general drawback of this type of temperature measurement for hetero-epitaxy is that the surface changes during growth and due to this its emissivity. Therefore, pyrometry is not suitable for monitoring the sample temperature T_{sample} during heteroepitaxial growth of thin layers. Furthermore, the absolute accuracy and reproducibility is limited. The manufacturer of the used "Ircon Modline 3" pyrometers specifies the accuracy to 0.6% of reading +1°C or at least 3°C (<4°C@450°C) and the repeatability to 0.1% of fullscale temperature +1°C (<3C @ 450°C) (Irc, 1997). This does not take into account stray light from other hot parts in the chamber which increases the uncertainty of the temperature. As a rule of thumb, the relative accuracy is estimated to be about 5°C and the absolute to be about 10-20°C. Higher reliability could be obtained monitoring the adsorption edge, which changes with temperature, but an adequate measurement setup was not available for this study. It was found during experiments that the highest reproducibility of sample temperature is obtained by the thermocouple. However, even small changes in geometry have a relatively strong influence on the radiation characteristics, which leads to different relations between temperatures, as measured by thermocouple and pyrometer. Therefore, a closer look at the heater and sample holder follows.

The substrates are mounted to a ring of molybdenum with a molybdenum-tungsten clamp ring. Substrates smaller than three inch are clamped between two molybdenum plates of three inch diameter to fit into the ring. The back side plate (called retainer plate) supports the sample from the back side

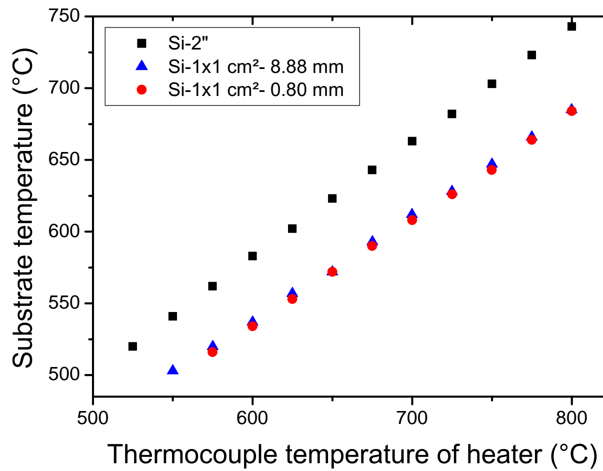

Figure 4.4.3.: *Substrate temperature measured by a "Ircon modline 3" 3V-13C10 as a function of the thermocouple temperature.*

and has an opening for radiation to enter the substrate. The front plate (called spring plate) presses the samples with its molybdenum fingers against the retainer plate. The used sets of spring and retainer plate for different sample sizes are shown in figure 4.4.2. Different relations of substrate temperature, as measured by thermocouple and pyrometer, were obtained for different sample sizes and sets of mounting plates, as shown in figure 4.4.3. The difference can be up to 60°C. Most surprising was the temperature shift for sapphire substrates if the only the retainer plate for 1x1 cm² samples was changed. In this case, the difference can be about 30-50°C at equal thermocouple temperatures if a custom build retainer plate with a 8×8 mm² opening is used instead of a original one from Veeco with an opening of 8.88×8.88 mm².

Furthermore, the sample temperature reaches its equilibrium value up to half an hour latter than the thermocouple because the heater is controlled by the temperature of the thermocouple instead of the sample. See figure 4.4.4. Due to this, the heater was set to the growth temperature at least half an hour prior to growth. In addition, the heat radiation of the beam sources influences the measurement by pyrometers and changes the temperature of the sample. This change may vary for different sample sizes and the substrate temperature during growth could be different even if the substrate temperature is equal prior to the growth.

4.4.2. Deposition rate, beam equivalent pressure

As mentioned, effusion cell sources are used for metal supply in MBE systems. In the used "Veeco GenII" MBE system, a conical crucible is mounted in the In cell, whereas in the Ga cell a SUMO®-crucible. The SUMO®-crucible is more similar to Knudsen cells and the flux is more stable. In principle, it is possible to calculate the beam fluxes for both types of cells including their angular distribution under full knowledge of cell and substrate geometry, as shown in Herman & Sitter (1996); Curless (1985) and Yamashita *et al.* (1987). Since the actual fill level, as well as wetting of the crucible sidewalls, are not accurately known and change with time, it is more convenient to measure the fluxes. This can be done directly by deposition of material or in a much faster way by measuring the so called beam equivalent pressure (BEP) and temperature.

It has to be regarded how pressure under vaccum conditions typical for MBE chambers of 10^{-5} – 10^{-10} mbar is measured. For this pressure range, hot cathode ion gauges are the right choice. These are open triodes in the sensed gas. A current heated filament emits electrons by thermionic emission.

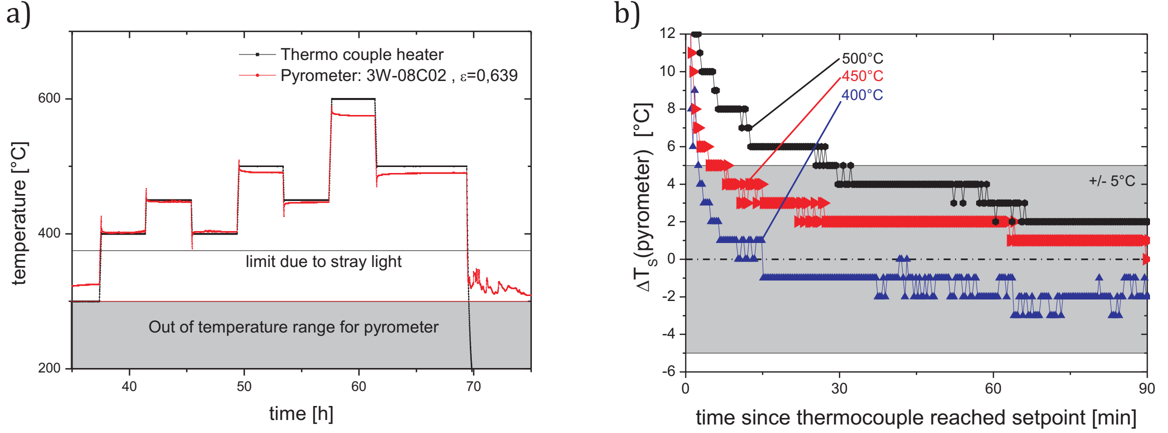

Figure 4.4.4.: *a) Thermocouple and substrate temperature as a function of time for a two inch silicon substrate with a clear over shot of the substrate temperature if the thermocouple temperature is changed , b) deviation of substrate temperature from the equilibrium value as a function of time for cooling down to a thermocouple temperature of 400, 450, 500°C with 10°C/min. (The temperature was measured by a "Ircon Modline 3, 3W-08C02" pyrometer).*

These electrons ionize molecules in the gas which are accelerated by a voltage between a grid and a collector towards the collector. The resulting collector current $I_{collector}$ is in the range of picoamps and proportional to the molecule density of the gas and its specific ionization probability. Therefore, ion gauges do not sense pressure, but a mixture of molecule density and ionization probability (Joyce & Bullough, 1993). If the gas consists of just one species, the collector current depends linearly on the pressure. This leads to the fact, that ion gauges can only be calibrated to one gas species. In the present case the gauges are calibrated to molecular nitrogen. In any case, the displayed pressure $P_{display}$ corresponds linearly to the collector current $I_{collector}$. This Leads to the following relation:

$$P_{diplay} \propto I_{collector} = k_{geometry} \sum_i c_i n_i \tag{4.4.2}$$

with $k_{geometry}$ a geometry depending constant and c_i the ionization probability and n_i the density of the i-th component in the gas. If the collector current is caused by only one species, it leads to:

$$P_{display} \propto n \tag{4.4.3}$$

The deposition rate D_i is a multiplication of the gas density and its average velocity $\bar{v}$, which is $\bar{v} = \sqrt{\frac{3k_b}{m}}\sqrt{T}$ under the assumption of an ideal gas and that the molecules have the temperature of their cell T_{cell}. In conclusion this leads to:

$$D_i = C_i P_{display} \sqrt{T_{cell}} \tag{4.4.4}$$

with a material and ion gauge geometry specific constant C_i. The assumption, that ion gauges would directly measure pressure, as one might think since they are used for pressure measurement, would lead to a significantly different dependency of $D_i \propto \sqrt{T_{cell}}^{-1}$.

For calibration purpose, samples were grown and the amounts of deposited material were measured in height and weight. Indium and aluminum were deposited directly to a cold sample (<100°C), because in this case all impinging atoms remain on the sample and form compact solid In layer. In

	C_{In} $\left[\frac{1}{mbar\ cm^2\ s\ \sqrt{K}}\right]$	C_{Ga} $\left[\frac{1}{mbar\ cm^2\ s\ \sqrt{K}}\right]$
By weight	5.19(4) * 10^{19}	4,16(8) * 10^{19}
By thickness	5.44(74) * 10^{19}	5.65(4) * 10^{19}
RHEED oscillations	-	ca. 5 * 10^{19}

Table 4.4.1.: *Material and ion gauge geometry specific constant C_i from calibration samples for deposition rate calculation from beam flux monitor ion gauge pressure $P_{display}$ and cell temperature T_{cell}. The values in brackets refer to standard deviation of the measurements. The constant C_{Ga} from thickness measurements is overestimated due to the porous structure of the GaN grown under cold and nitrogen rich conditions*

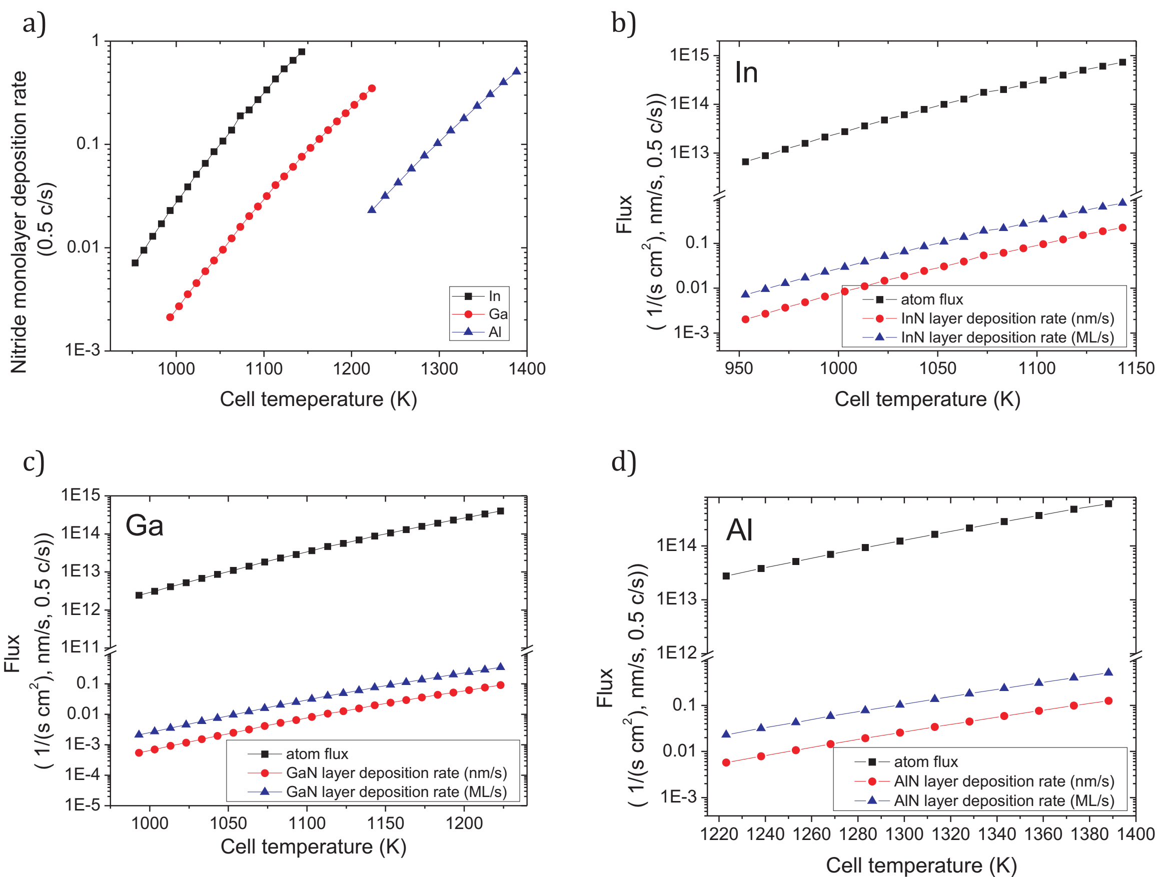

Figure 4.4.5.: *Flux of the effusion cells: a) Flux from In, Ga and Al cells in monolayers (ML) (half c-lattice spacing) per second, if all metal incorporated into a compact III-nitride layer, b-d) Flux in $\frac{1}{cm^2\ s}$, $\frac{nm}{s}$ and $\frac{c}{s} = \frac{ML}{s}$ for b) In, c) Ga and d) Al (data from January the 11th to 13th, 2011)*

contrast, Ga was deposited with additional supply of activated nitrogen under nitrogen rich conditions to obtain a compact solid GaN layer. Ga would be liquid and form droplets, which would complicate the height determination. The height of the grown samples were measured by a DEKTAK stylus profiler. The weights of the deposited material of about 300 µg was measured by a Satorius 4503 Micro scale and the deposition rate was calculated regarding the size of the coated area and the molecular weights. In addition, oscillations in intensity of reflective high energy electron diffraction are used for Ga as comparison. The results are summarized in table 4.4.1 and visualized in figure 4.4.5. The accuracy of fluxes is at least in the 5-10% range. Growth of nanowires takes place under highly nitrogen rich conditions. Hence, small changes in the flux only lead to a change in the total amount of deposited material and an exact control over the III-flux is not so crucial. However, if nanowires of the ternary alloy $In_{1-x}Ga_xN$ are grown, this uncertainty in determining the metal fluxes has to be regarded for the interpretation of the growth results. For layers, the precise control of the N:III ratio is very essential, since growth takes place under metal-rich conditions close to stoichiometry and slight change in the metal flux have strong influence on the growth. In this case, reflective high energy electron diffraction (RHEED) can be used to probe the state of the surface directly to achieve higher accuracy in determination of the V:III ratio.

4.4.3. Nitrogen supply

As mentioned in section 4.1, nitrogen must be excited for the metastable growth mode of III-nitrides. In this study, a Veeco "UNI-bulb" radio frequency (RF) plasma source, which supplies a mixture of excited N_2, N_2 ions and N radicals, was used for excitation.

The source consists of a poly-boron nitride tube with a gas inlet at the outer part and an aperture plate covered outlet directing to the sample (see fig.4.4.6). The amount of nitrogen introduced into the MBE chamber is controlled by a "MKS Instruments" mass flow controller. The amount of nitrogen pumped out of the camber is given by the pumping power. The control parameters are the flow rate of nitrogen (F_N) and power for exciting the plasma (P_N). The plasma is generated by coupling a RF signal of 13.6 MHz into a water cooled coaxial dual-coil around the PBN tube. The alternating electromagnetic field causes acceleration and collision of enclosed ions nitrogen and thereby an excitation into a plasma state. This plasma is only stable in a certain range of conditions. The used plasma source is capable of working in two different plasma regimes, called "high brightness" and "low brightness" mode. A special design of the aperture plate with 254 holes of about 100 µm diameter should ensure homogeneous supply of activated nitrogen at samples of up to 3 inch of size. The small holes should also reduce the amount of ions in the supplied nitrogen.

The state of the plasma can be monitored via a view port. It is easy to distinguish by the eye between "no plasma", "low brightness" and "high brightness" modes. Figure 4.4.6 d) shows a typical spectrum of light emission for the high brightness mode. The contributions in this plasma source can be mainly divided into atomic nitrogen and excited N_2. To monitor their intensities, a simple two channel "spectrometer" was designed and build in collaboration with Florian Werner and Emanuel Franke. With this unit emission intensity of both species can be monitored quantitatively. Their ratio and intensities allow to draw conclusions about the composition of the plasma inside the source. This is still not what is coming out of the source, but enables the monitoring of qualitative changes and long term stability.

The PBN tube and aperture plate degenerate with time under the exposure to nitrogen plasma. Due to this, small flakes in the size up to several mm² detach from time to time from the sidewalls. This disturbs the flow inside the plasma tube and changes the plasma condition. Additionally, the aperture plate itself degenerates. This degeneration can hinder or even block flow through the holes and changes the plasma conditions. The plasma usually starts to become unstable at high nitrogen supply rates. The aperture plate has to be changed about every second year. Every time this done, the flakes from the sidewalls should also be mechanically removed. After many years of usage, the tube

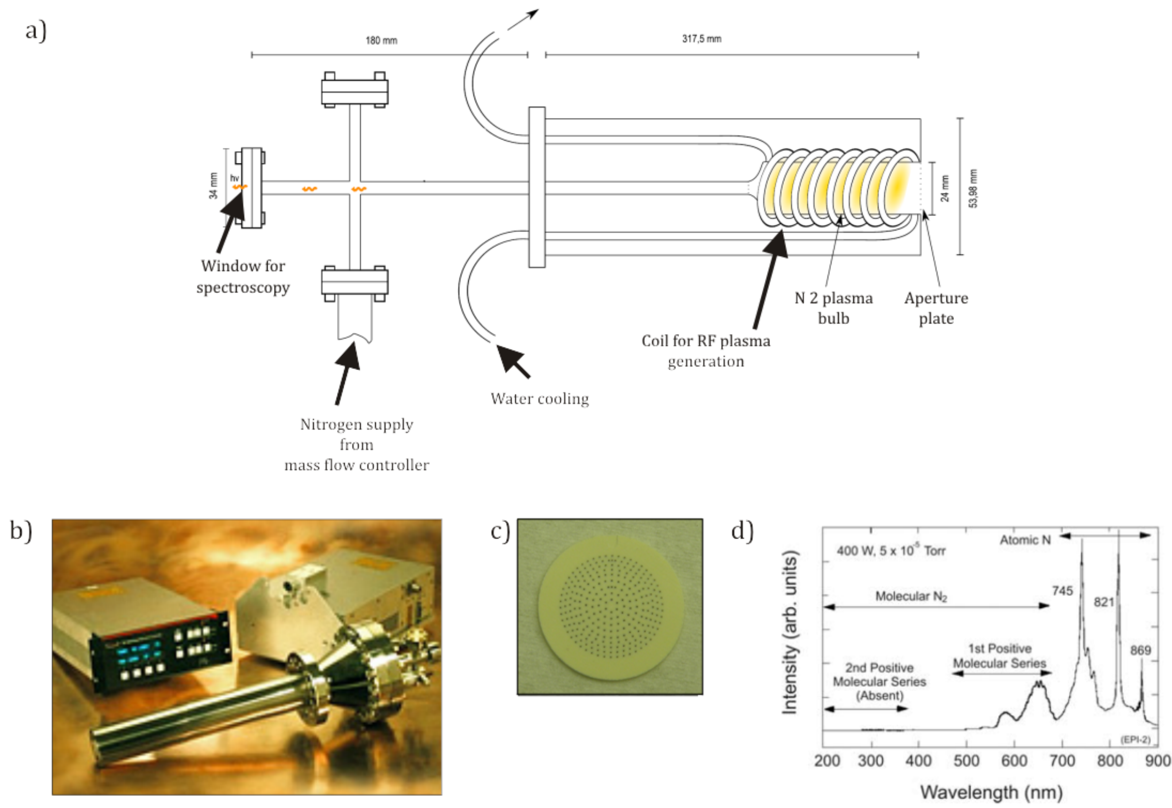

Figure 4.4.6.: *a) Sketch of nitrogen plasma source (adapted from Franke (2009)), b) Image of a Veeco "UNI-Bulb RF" plasma source with matching unit and power supply (Veeco, 2009) , c) Picture of an aperture plate, d) Typical optical emission spectrum of an Veeco "UNI-Bulb RF" plasma source (Veeco, 2009)*

must be exchanged as well.

The operation range and growth rates depending on plasma conditions were studied in the bachelor thesis of Franke (2009) and Hollermann (2010).

5. Nanowire growth

During the last five years, a lot of progress took place in the research field of formation and growth mechanisms of nanowires. The description of the formation of nanowires is usually divided into two stages. The first one is the formation of initial nuclei and the second is the growth of the nanowires.

The nucleation can be roughly described by theoretical models (see i.e. Markov (1995)) and the growth of single separated nanowires can be explained by theoretical descriptions of diffusion induced growth by Ruth & Hirth (1964) and supersaturation of droplets or particles (Givargizov, 1975). The theoretical models of growth were combined and refined (see i.e. Dubrovskii *et al.* (2009b)). Important experimental steps were monitoring of the growth rate evolution in single wires with markers (Harmand *et al.* (2010) and Songmuang *et al.* (2010)) and investigation of the evolution of initial nuclei of GaN nanowires (Songmuang *et al.* (2007) and Consonni *et al.* (2011)). However, some fundamental questions are still unanswered. A consistent model for all processes of self-organized growth of III-N nanowires is still lacking and the cause for the anisotropy of the growth rate for III-nitrides under N-rich conditions is unclear.

The aim of this section is to provide a brief overview on these topics. Therefore, different methods to grow nanowires by MBE as well as basic models of nucleation and crystal growth are briefly reviewed. In particular, it is investigated if the InN and GaN nanowire formation can be related to the equilibrium shape of crystals. This is followed by considerations about the preferential growth directions depending on the growth conditions with regard to the chemical potential for adatoms on different surfaces and incorporation probabilities. Furthermore, the diffusion growth model is reviewed and its possible application for the description of InN nanowire growth is discussed.

5.1. III-N nanowires by molecular beam epitaxy

Several ways exist to obtain nanowires. It is common for all of them that starting points for the nanowire growth have to be predefined or must form in a self-organized process. Once, these starting points have formed, anisotropic growth rates must favor axial growth.

The most famous method to obtain nanowires is vapor-liquid-solid (VLS) growth. For VLS-growth, droplets of an inert liquid material, usually gold, are deposited on the substrate. The droplets supersaturate and favor crystal growth beneath them, as already shown for silicon by Wagner & Ellis in 1965 for CVD growth. By this technique nanowires with length of up to several 100 µm and constant diameters of down to 20-30 nm can be grown. This concept is not limited to liquid droplets and CVD, as demonstrated for GaN nanocolumns by MBE using solid particles (Geelhaar *et al.* (2007) and Chèze *et al.* (2010)).

However, III-N nanowires by MBE are usually grown without any growth rate enhancing droplet or particle. The first reports on III-N nanocolumns by MBE by Sanchez-Garcia *et al.* (1998) and by Yoshizawa *et al.* (1998) on Si(111) and sapphire substrates, respectively, did not used any droplets or particles. N-rich growth conditions are sufficient to lead to columnar growth. In this case, nanowires grow probably by direct crystallization from the vapor phase. The detailed mechanisms of starting point formation and growth mechanism are still under investigation (Songmuang *et al.* (2007), Landré *et al.* (2009) and Consonni *et al.* (2011)). The formation of islands in heteroepitaxy is known (e.g. Markov (1995)). These islands can act as starting points for nanowire growth. On amorphous surfaces, like Si(111) with an amorphous top-layer, this is due to surface and interface energies. On crystalline substrates, lattice mismatch introduces additionally strain leading to island formation

known as Stranski-Kranstanov growth. However, aspect ratios predicted by this approach can depend on the size, but are in any case independent of time and the mechanism favoring axial growth of III-N nanowires under the N-rich growth conditions is unclear.

Beside these self-organized approaches, also growth of nanocolumns with ordered predefined starting points for nanowire growth was demonstrated. Araki *et al.* (2009) defined nucleation spots by holes and showed successfully position controlled growth of single InN nanowires. Furthermore, Kishino *et al.* (2009), Bertness *et al.* (2010) and Schumann *et al.* (2011) demonstrated position controlled growth of GaN nanowires using different masks, which inhibit nucleation.

5.2. Equilibrium shape of crystals

The following paragraphs will clarify if the nanowire shape and, in particular, its high aspect ratio, can be related to the equilibrium shape of the crystals. Therefore, a simple approach is used to deduce the Wulff rule. Based on this rule and the few data, which known about surface energies of InN and GaN, the equilibrium shapes for III-N nanowires is estimated in two dimensional projections of the nanowires in c-direction and perpendicular to it.

The Gibbs-Curie-Wulff Theorem

The Gibbs-Curie-Wulff theorem can be deduced by minimizing the surface energy of a crystal for a given volume, as already shown by Gibbs and Curie in the 19th century. The following deduction is adapted from Markov (1995).

Minimizing the Helmholtz free energy F of a closed system with constant volume V_c at constant temperature includes the minimization of surface energy, therefore

$$dF = 0 \ \wedge \ dV_c = 0 \tag{5.2.1}$$

The crystal is considered to be a polyhedron limited by oriented flat surfaces O_n with discrete values of the specific surface energies σ_n . This leads to:

$$dF = -(P_c - P_v)dV_c + \sum \sigma_n dO_n = 0 \tag{5.2.2}$$

with P_c the inner pressure of the crystal phase and P_v the pressure of the vapor phase, as defined in Markov (1995).

Due to the fact that the crystal is a polyhedron, it can be divided into pyramids with the heights h_n and a common apex. This enables the calculation of the crystal volume by:

$$V_c = \frac{1}{3}\sum_n h_n O_n \tag{5.2.3}$$

and its differential

$$dV_c = \frac{1}{3}\sum (O_n dh_n + h_n dO_n) \tag{5.2.4}$$

Furthermore, the change in volume with an accuracy of infinitesimals of second order is equal to a shift of the surface by a distance dh_n. This leads to

$$dV_c = \sum_n O_n dh_n \tag{5.2.5}$$

in combination with

$$dV_c = \frac{1}{2}\sum_n h_n dO_n \tag{5.2.6}$$

Using the equation 5.2.6 in 5.2.2, it follows:

$$\sum_n (\sigma_n - \frac{1}{2}(P_c - P_v)h_n)dO_n = 0 \tag{5.2.7}$$

Because the terms in the brackets are independent of dO_n, each single term in the brackets must be zero. This leads to:

$$2\frac{\sigma_n}{h_n} = P_c - P_V \tag{5.2.8}$$

with the definition of supersaturation $\Delta\mu = (P_c - P_V)v_c$ with $v_c = V_c/n_c$, it is deduced:

$$\frac{\sigma_n}{h_n} = \frac{\Delta\mu}{2v_c} = const \tag{5.2.9}$$

The relation "$\forall n : \frac{\sigma_n}{h_n} = const$" is known as Wulff rule or Gibbs-Curie-Wulff theorem. The rule enables the deduction of the equilibrium shape of crystals. For each possible surface, a vector points to a plane normal to it. The length of the vector is proportional to the specific surface energy and the direction corresponds to the orientation of the surface. The inner hull formed by the plane is the equilibrium shape. Beside the rule for the ratios, equation 5.2.9 implies that the size of the crystals should scale linearly with the inverse of the supersaturation $\Delta\mu$.

Furthermore, this model can be easily expended to crystals on a foreign substrate by considering interfaces as other possible surfaces. For this purpose planes and vectors according to their orientation and interface energy have to be added to the Wulff construction. In the strain free case, as for InN on Si(111) with an amorphous top-layer, the interface energy is size independent. Therefore, only the strain free case is treated in the following.

In the case of no adhesion between crystal and substrate, the interface energy is equal to the specific energy of the free surface and the equilibrium shape is equal to the one of a free crystal. In the case of repulsion, the crystal is not in contact with the substrate. This situation is called "complete nonwetting" and unlikely for MBE since the crystals need a connection to the substrate. In the case, that adhesion compensates or overcompensates the sum of the specific surface energies, it is energetically favorable for the crystal to cover the whole substrate before expanding its size in other directions. This case called "complete wetting". For the condition that the specific adhesion energy is bigger than 0, but smaller than the sum of specific energies of the free surfaces, the substrate will be partially covered by crystals. As a consequence, the equilibrium aspect ratio of a crystal on a substrate decreases with decreasing interface energy, as illustrated in figure 5.2.1. In contrast to liquids, the wetting angles of crystals are restricted to discrete values. It is noteworthy that a higher interface energy than the one of a free surface would increase the aspect ratio, but is not related to equilibrium anymore.

This model offers a first approach to the equilibrium shape of crystals, but neglects any phenomena taking place at the corners where the different planes are in contact. Furthermore, any effects, which appear, if the crystal size is comparable to its building units, are also not regarded.

For a quantitative evaluation of this model the specific surface energies are needed. One simple theoretical approach is to count the number of broken bonds per unit area. This would also enable the determination the specific surface energy of vicinal surfaces and thereby the application more detailed models. However, DFT calculations showed that this approach is too simple for the III-N system, because the surface energy is significantly changed by surface reconstructions (e.g. Northrup & Neugebauer (1996)).

The crystal surface is composed of c, a, m-planes if the nanowires show a clear faceting, as shown

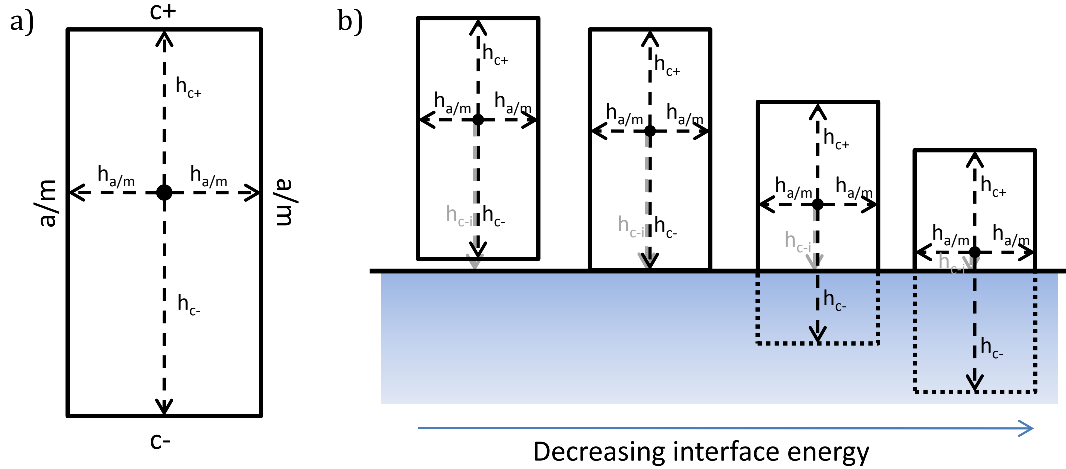

Figure 5.2.1.: *a) Illustration of the Wulff construction for the aspect ratio of free III-nitrides nanowires, b) the effect of increasing interface energy on the equilibrium shape for crystals on a foreign substrate.*

in section 7.2. Due to this and the lack knowledge concerning energies of other surfaces or step and edge energies, only these three surfaces are considered and all other effects are neglected in the following deduction of equilibrium shapes.

Equilibrium shape of InN and GaN - cross section

Northrup & Neugebauer (1996) calculated the stability of different surface reconstructions on a- and m-planes of GaN within a DFT approach. The results are shown in figure 5.2.2. According to these calculations, the most stable surfaces under N-rich conditions consists of unreconstructed GaN dimers. The specific surface energy is 118 meV/$\mathring{A}^2$ for the m-plane and 123 meV/$\mathring{A}^2$ for the a-plane. The resulting equilibrium shape is shown in figure 5.2.3. Assuming the given calculated values, a ratio of about 2.4 for the lengths of m-plane facets and the a-plane facets is deduced.

For InN, the same kinds of surfaces are predicted for the non-polar planes by Segev & Van de Walle (2007). Within the nanolicht project G. Cicero, A. Terentjevs, A Aliano and A. Catellani calculated with a DFT approach the specific surface energies to be 1.5 J/m² $\approx$ 94 meV/ for the m-plane and 1.59 J/m² $\approx$ 99 meV/ for the a-plane. The corresponding equilibrium shape (figure 5.2.4) has a ratio of the lengths of m-plane facets and a-planes facets of about 1.8.

To illustrate the influence of possible relative errors of the ratio of specific surface energies, the ratio of the facet lengths for given ratios of the specific surface energies are numerically calculated and plotted in figure 5.2.5. In the case of $\sigma_{m-plane}/\sigma_{a-plane} < 0.867$, the a-plane facets will completely disappear. If the energy ratio is overestimated by only 5-6%, the length ratio would dramatically increase to 6.5-9.6. This demonstrates the dramatic effect of relative errors of the energy ratio on the length ratio. Experimentally, a- and m-planes were observed on the nanowires and the tendency, that the m-planes are usually larger than the a-planes, could be confirmed, but no fixed a- to m-plane lengths ratio was found (see section 7.1). These results indicate, that the cross-section is close the cross section predicted by the Wulff rule, but the shape cannot be completely determined the surface energy minimization, since this would imply fixed lengths ratios.

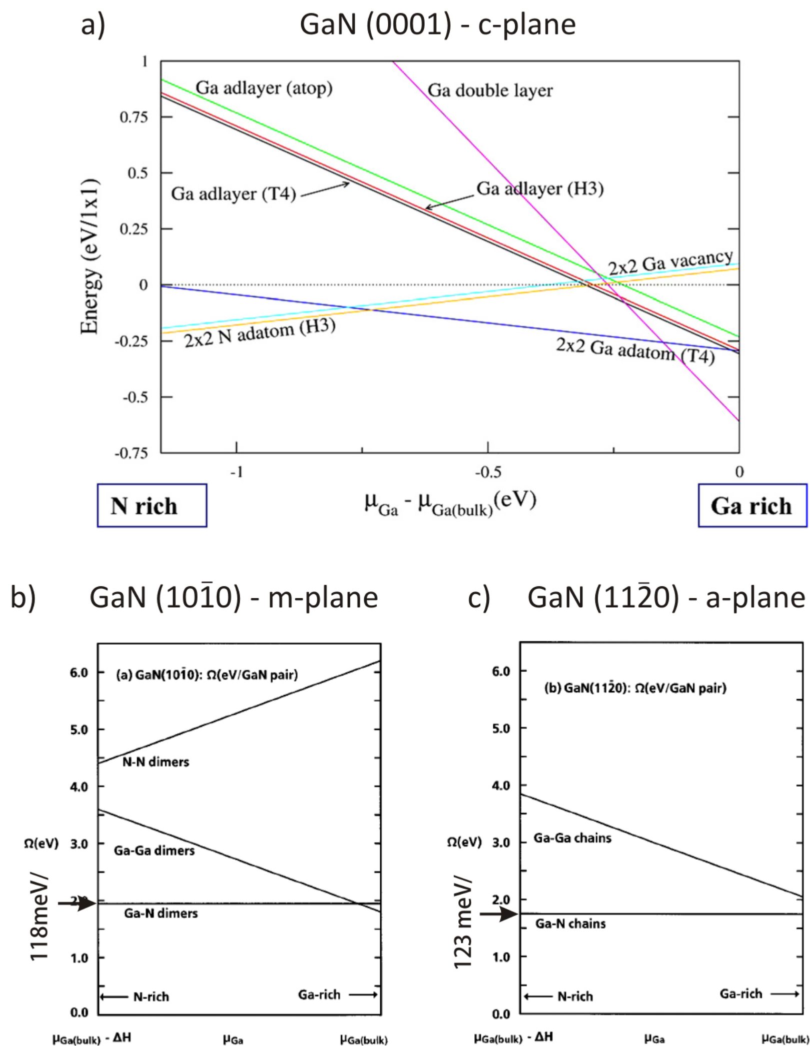

Figure 5.2.2.: *Surface energy calculations for GaN a) (0001), b) (10$\bar{1}$0) and c) (11$\bar{2}$0) from Segev & Van de Walle (2007) and Northrup & Neugebauer (1996)*

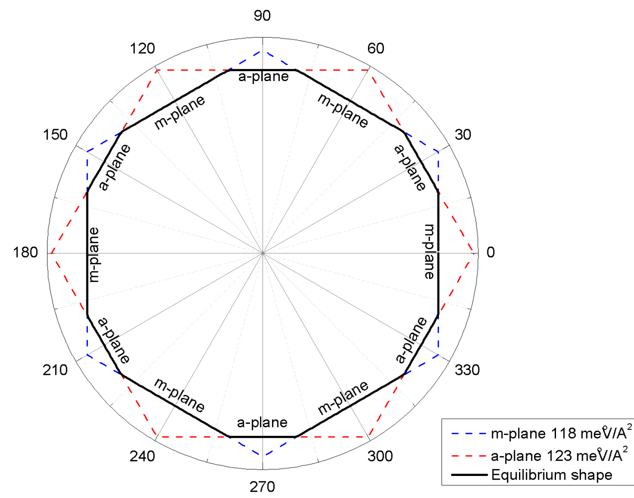

Figure 5.2.3.: *Equilibrium cross section of GaN nanowires in c-direction deduced by the Wulff rule.*

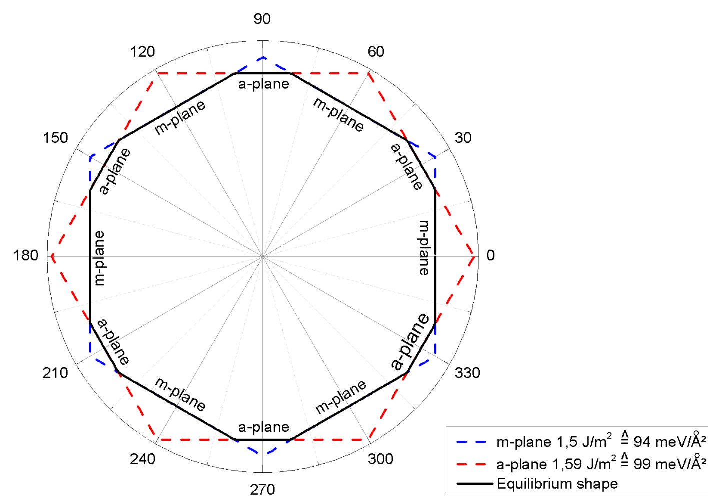

Figure 5.2.4.: *Equilibrium cross section of InN nanowires in c-direction deduced by the Wulff rule.*

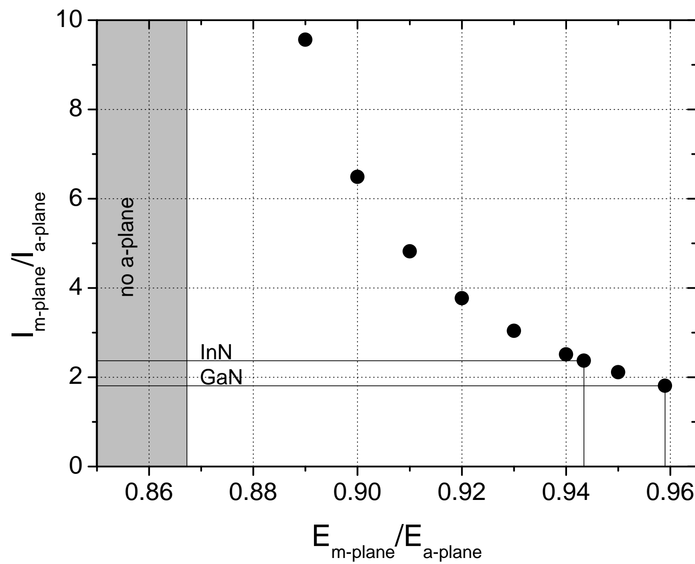

Figure 5.2.5.: *Ratios of the m- and a-plane facet lengths for the equilibrium cross section for wurzite nanowires growing in c-direction deduced by the Wulff rule as a function of the specific surface energy ratio. The equilibrium conditions given by Wulff rule were numerically calculated for some discrete values.*

Equilibrium shape of InN and GaN - side view

It is difficult to get reliable values for the specific surface energies for the c-planes and they differ for the (0001) and (000$\overline{1}$) direction. The only absolute value in literature is given by Elsner *et al.* (1998) with about 200 meV/Å^2 for GaN. Beyond this, no data exists for SiN-III-N interface. Due to this poor knowledge of the required surface energies for Wulff rule, only a proof of principle consideration can follow here.

Experimentally, wires with an aspect ratio of ≥ 10 for GaN and InN are typically obtained by MBE growth. The m-plane is the surface with the lowest energy of planes perpendicular to the growth direction which is the c-direction. Thus, the highest aspect ratio is obtained for wires consisting of m- and c- planes. Then, the aspect ratio is:

$$\frac{\overline{\sigma_c}}{\sigma_m} = \frac{\overline{hc}}{h_m} = \frac{L}{d} \tag{5.2.10}$$

with $\overline{\sigma_c}$ the average specific surface energy for the (0001) and (000$\overline{1}$) surface and $\overline{h_c}$ the corresponding height of the pyramid.

A reasonable value for the specific surface energy of the m-planes of $\sigma_m \approx 100$ meV/Å^2 and a moderate aspect ratio of 5 would already correspond to a surface energy of $\overline{\sigma_c} \geq 500$ meV/Å^2 for the averaged specific surface energy of the c-planes. Changes on the surface energy by surface reconstructions are in the order of some 10 meV/Å^2 and are therefore negligible in this rough estimation. Foreign substrates lower the surface tension and due this the aspect ratio. The non equilibrium case of a strong repulsion between substrate and crystal could increase aspect ratio, but is not related to any kind of equilibrium. Thus, it is unlikely that the high aspect ratio is given the minimization of surface total energy.

In conclusion, the obtained nanowires show a cross section close to the equilibrium one predicted

by the simple Wulff rule, but the ratios of the facets vary, see figure 7.2.1 and cannot be strictly determined by the minimization of surface energy. Furthermore, the high aspect ratios of nanowires cannot be explained by this model.

5.3. Nucleation

Nucleation is the first process of a phase transition of first order, i.e. it describes the formation of particle of new phase. This paragraph treats the most simple case of nucleation in a steady state approximation.

If a nucleus grows, the gain of energy linearly increases with the atoms n joining the nucleus by transferring atoms from the unstable to stable phase and the energy, which is needed to from the surface, only increases with $n^{2/3}$. This leads to an energy barrier for the formation of nuclei: the nucleation barrier. In the following, a simple model for nucleation is used to deduce an equilibrium nucleation rate for a system, where the atoms of a nucleus are given back to the system, when nucleus becomes stable, as shown in e.g. Markov (1995).

Equilibrium nucleation rate

In this model, the growth conditions are characterized by the supersaturation $\Delta\mu$, temperature T and impinging flux F. The substrate is described by the diffusion barrier E_{diff}, desorption barrier E_{des}, vibration frequency of adatoms $\nu_{\perp} \approx \nu_{=} \approx \nu$ and distance of adsorption sites a_{diff}. Finally, the surface properties of the nuclei are taken into account by specific surface and interface energies σ_m, $\sigma_{c+} + \sigma_{ci}$.

Under the assumption that nuclei that overcome the nucleation barrier ΔG_{cr} are given back to system as single atoms, the steady state nucleation rate J_0 for a system with a nucleation barrier is generally given by

$$J_0 = \omega_{cr}\Gamma N_{cr} \tag{5.3.1}$$

with ω_{cr} the frequency of atoms attaching to a nucleus of critical size, Γ the Zeldovich factor and N_{cr} the equilibrium concentration of critical nuclei. N_{cr} is given by

$$N_{cr} = N_1 e^{-\frac{\Delta G_{cr}}{k_B T}} \tag{5.3.2}$$

with N_1 the concentration of adatoms and k_B the Boltzmann constant.

This equation can be understood quite intuitively. The rate of nuclei that overcome the critical size depends linearly on the number of nuclei of critical size. Furthermore, it is obvious that it should be proportional to rate of atoms attaching to a nucleus of critical size. The barrier height is regarded by ΔG_{cr}, the barrier width by the Zeldovich factor Γ. Because nucleation is a thermally activated process, the effective barrier width is the interval, in which the Gibbs free energy differs by $k_B T$ or less from the energy maximum. Therefore, this factor is defined by interval Δn^* for the size where the change in ΔG is less than $k_B T$ compared to ΔG_{cr} the Gibbs free energy of the critical nucleus size. With a prefactor this reads:

$$\Gamma := \frac{2}{\sqrt{\pi}}\frac{1}{\Delta n^*} \tag{5.3.3}$$

Therefore, the Zeldovich factor corresponds to the inverse of the barrier widths.

The Gibbs free energy $\Delta G(n)$ is given by

$$\Delta G = -n\Delta\mu + \sum_{n'} O_{n'} \tag{5.3.4}$$

with $\sum_{n'} O_{n'}$ the sum of surface and interface energies. To calculate this sum, assumptions for the shape of the nuclei are needed. In this case, it is convenient to assume the equilibrium shape. The equilibrium shape for III-nitrides is a dodecagonal prism, which is characterized by the aspect ratios. For simplicity, a hexagonal prism with an edge length-to-height ratio c is assumed here.

The sidewall surface area A_m of prisms with hexagonal cross section is given by

$$A_m(a,h) = 6ah \Rightarrow A_m(n,c) = 2\sqrt[3]{4}(nv_c)^{2/3}c^{1/3} \tag{5.3.5}$$

with height h and edge length a, a given ratio $\frac{h}{a} = c$, n the number of molecules in the prism and v_c their volume.

And similar for the top or bottom facet area A_c:

$$A_c(a) = \frac{3}{2}\sqrt{3}a^2 \Rightarrow A_c(n,c) = \sqrt[3]{\frac{1}{6}}\left(\frac{nv_c}{c}\right)^{2/3} \tag{5.3.6}$$

Therefore, $\Delta G(n)$ is given by:

$$\Delta G(n) = -n\Delta\mu + k_{surf}n^{2/3} \tag{5.3.7}$$

with $k_{surf} = \left(6\sqrt[3]{\frac{2}{3\sqrt{3}}} + \sqrt[3]{\frac{2}{3}\sqrt{3}}\right)\sqrt[3]{v_c^2\sigma_m^2\left(\sigma_{ci+}\sigma_{c+}\right)}$.

Now, it is possible to calculate the maximum of ΔG at n_{cr}:

$$\frac{d\Delta G}{dn} = -\Delta\mu + \frac{2}{3}k_{surf}n_{cr}^{-1/3} = 0 \tag{5.3.8}$$

$$\Rightarrow \Delta\mu = \frac{2}{3}k_{surf}n_{cr}^{-1/3} \tag{5.3.9}$$

$$\Rightarrow n_{cr} = \left(\frac{2}{3}\frac{k_{surf}}{\Delta\mu}\right)^3 \tag{5.3.10}$$

This leads to the following expression for ΔG_{cr}

$$\Delta G_{cr} = \frac{4}{27}\frac{k_{surf}^3}{\Delta\mu^2} \tag{5.3.11}$$

Using equation 5.3.9 and 5.3.11, $\Delta G(n)$ can expressed by:

$$\Delta G(n) = \Delta G_{cr}\left(3\left(\frac{n}{n_{cr}}\right)^{2/3} - 2\frac{n}{n_{cr}}\right) \tag{5.3.12}$$

The Zeldovich factor is well approximated according to Markov (1995) by using a Taylor series of $\Delta G(n)$ at n_{cr} :

$$\Gamma \approx \sqrt{\frac{\Delta G_{cr}}{3\pi k_B T}}\frac{1}{n_{cr}} \tag{5.3.13}$$

and using equation 5.3.10 and 5.3.11 the Zeldovich factor is approximated by:

$$\Rightarrow \Gamma \approx \frac{3}{4}\sqrt{\frac{1}{\pi k_B T}}\frac{\Delta\mu^2}{k_{surf}^{3/2}} \tag{5.3.14}$$

Finally, an expression for the impingement rate of building units to a nucleus of critical size must be found to calculate the nucleation rate. As shown in e.g. Markov (1995), the adatom life time τ_s of

an adatom is given by

$$\tau_s = \frac{1}{\nu} e^{E_{des}/k_B T} \tag{5.3.15}$$

(F- the impingement rate to the substrate, E_{des} - the desorption barrier, $\nu \approx \nu_\perp \approx \nu_=$ - the vibration frequency of adatoms) and the density of adatoms N_1 can be approximated by

$$N_1 \approx F\tau_s = \frac{F}{\nu} e^{E_{des}/k_B T} \tag{5.3.16}$$

Assuming a diffusion towards the nuclei of $j_S = D_S \nabla N_1 \approx D_s \frac{N_1}{a} = Fae^{(E_{des}-E_{diff})/k_B T}$ with the diffusion constant $D_S = a^2 \nu e^{E_{diff}/k_B T}$ and accounting only for the diffusive impingement to the critical nuclei, the impingement rate of atoms towards a nuclei of critical size is given by

$$\omega_{cr} = \underbrace{6a_{edge\ cr}}_{\text{periphery of footprint}} \underbrace{Fae^{(E_{des}-E_{diff})/k_B T}}_{\text{diffusion flux to nuclei}} \tag{5.3.17}$$

with

$$a_{edge\ cr} = \frac{2}{3} \sqrt[3]{\frac{2}{3\sqrt{3}}} \sqrt[3]{\frac{\sigma_m}{\sigma_{c+} + \sigma_{ci}}} \sqrt[3]{v_C} \left(\frac{k_{surf}}{\Delta\mu} \right) \tag{5.3.18}$$

As shown in the appendix D.2 and D.1, the nucleation as function of the variables of growth (nitrogen flux, metal flux and substrate temperature) for growth with and without desorption is complex and many of the required constants are unknown. In addition, it would only describe the nucleation behavior approximately for the very beginning of growth, when no stable nuclei or nanowire have formed. This shows, that the theoretical description of nucleation is challenging. This simple approach cannot be used to predict the nucleation behavior of III-nanowires, but it enables a better insight into the physical processes of nucleation.

5.4. III:N ratio and preferential growth direction

For MBE growth, it is experimentally observed that N-rich conditions favor the growth in c-direction. Under N-rich conditions, nanocolumns form on substrates for growth in c-direction.

In the case of III-nitrides, the formation energies of surfaces depend on the V:III ratio of the growth environment. For GaN the formation energies of different facets and surface reconstructions were calculated by Elsner *et al.* (1998) and Northrup & Neugebauer (1996), see figure 5.2.2. Accordingly, c-plane facets are more favorable under Ga-rich conditions and a- and m-planes are more favorable under N-rich conditions. However, the different formation energies of the planes and the corresponding equilibrium shapes cannot explain the high anisotropy of growth rates for III-N nanowires, as shown in section 5.2.

Another cause for the anisotropy can be kinetic effects. The incorporation probability on a lattice site increases proportional to the density of adatoms in the low density adatom approximation ($\ll$ 1 ML) and decreases exponentially with the height of the reaction or formation barrier. In the case of III-N compound semiconductors, the probability that a group III and group V atoms are present for incorporation at one site must also be regarded.

In the low adatom density approximation, the chemical potential of adatoms is determined by ratio of the density of adatoms and adsorption sites n/N_{sites}, temperature and the potential energy μ_0 of adatoms on these sites (compare Dubrovskii *et al.* (2009a)):

$$\mu_{adatom} = k_B T \ln \frac{n}{N_{sites}} + \mu_0 \tag{5.4.1}$$

with k_B the Boltzmann constant. If the chemical potential for adatoms is higher on certain planes

than on others, the density of adatoms on the planes with the higher chemical potential reduces either by desorption or diffusion. This implies a reduction of the growth rate on the plane with the higher chemical potential, if the temperature is high enough that adatoms can desorb or are mobile and can reach positions of lower chemical potential.

The growth rates of III-N nanowires by MBE are significantly higher than expected if all supplied metal would form a compact III-N layer (see section 8). This indicates that metal adatoms diffuse from the substrate and nanowire sidewalls towards the nanowire tops and a higher incorporation probability on this planes maintains the difference in chemical potential.

DFT calculations predict for GaN under highly N-rich conditions a nitrogen adlayer on the c-plane and for InN an In adlayer (Segev & Van de Walle, 2007). The calculated stable surface reconstructions under N-rich conditions agree with the experimentally observed 2×1 reconstruction on c-plane GaN and 1×1 reconstruction on c-plane In probed by reflection high energy electron diffraction (RHEED). The formation of adlayers implies a lower chemical potential for these atoms on the c-planes since adatoms should be energetically favorable. For the a- and m-planes neither a nitrogen nor a metal adlayer is predicted under these conditions for both materials (Northrup & Neugebauer (1996) and Segev & Van de Walle (2007)). The formation of a metal adlayer is only predicted for m-planes under highly metal-rich conditions. Therefore, the high formation energies for adlayers indicate that adatoms are energetically unfavorable on a- and m-planes.

Accordingly, the following explanation for the high anisotropy of the growth rate for GaN under N-rich conditions is proposed. The N-rich conditions lead to the formation of a nitrogen adlayer on the c-planes, whereas the a-and m-planes are terminated by III-N dimers, i.e. nearly free of adatoms. The excess of nitrogen on the c-planes facilitates the incorporation of the metal atoms. Due to the lack of nitrogen and the high potential for metal adatoms, the incorporation of metal atoms is hampered on the a- and m-planes. Furthermore, the higher chemical potential for metal adatoms on the a-and m-planes than on the c-planes causes a diffusion flux towards the c-planes. The higher incorporation rate impedes the accumulation of metal on the c-planes. This leads to a continuous diffusion flux to the c-planes and explains the high anisotropy of growth rates under N-rich conditions.

For InN, the situation should be similar. Instead of a N-adlayer, an In adlayer should form on the c-planes according to Segev & Van de Walle (2007) and the chemical potential for In adatoms on the c-planes should be lower than on a- and m-planes. Thus, the growth rate increases due to the fact that the incorporation of nitrogen is more likely on a surface covered by In.

5.5. Kinetics of diffusion-controlled wire growth

In the case of nanowires, not only direct impingement to the nanowire top can contribute to the axial growth. After the atoms are adsorbed at a surface, they migrate by diffusion until they reevaporate or incorporate into a crystal. If the nanowire top attracts adatoms from the sidewall and/or substrate, they can incorporate on the top-facet and increase the axial grow rate of the nanowires. This was mathematically described already in 1964 by Ruth & Hirth. Since 2004, this idea was further developed mainly by Dubrovskii and coworkers, who combined the model of Ruth & Hirth with the model for VLS growth of Givargizov (1975). Since, there is no indication for VLS growth for III-N nanowires in MBE (Meijers, 2007), any effects caused by droplet at the nanowire top are neglected here. Thus, the growth model of Ruth and Hirth with some modifications is presented in the following.

Common for these models is that the system is divided into three areas:

- Nanowire top - A
- Nanowire sidewall - B
- Substrate - C

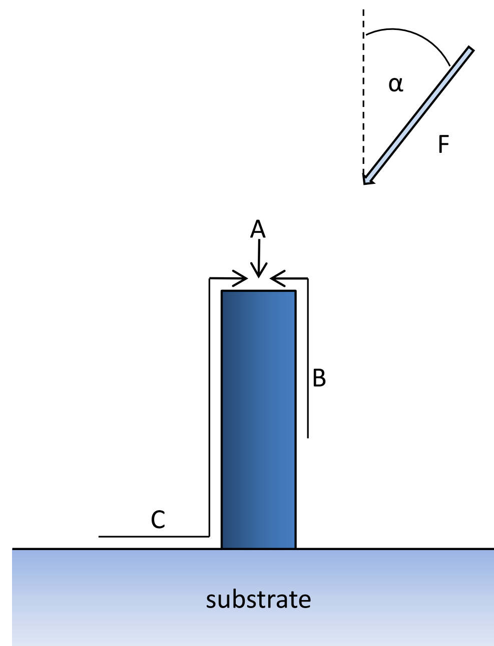

Figure 5.5.1.: *Illustration of the geometry and the different contributions for nanowire growth by MBE.*

The impingement rates for the different areas depend on the growth method and geometry. The top is considered as a sink with a certain chemical potential μ_{top}. For the other two sections diffusion equations are used to describe the fluxes of adatoms. The diffusion equations are differential equations of second order, thus four integration constants are needed from boundary conditions. Three of the four needed boundary conditions are deduced from continuity of mass and chemical potentials at the transition of the different sections. For the fourth, it is assumed the wire are separated or are located in an equal distance from each other. In this case, the adatom concentration is constant in certain distance from the wire. Therefore, the model does not describe the case of nanowires, which exchange adatoms or are so dense that shadowing from surrounding nanowires has to be taken into account.

Assumptions and boundary conditions

First of all, only the limiting constituent (i.e. only the metal atoms) is regarded for simplicity. In the case of MBE, the metal atoms impinge with a certain angle α to the substrate normal onto the nanowire top, nanowire sidewalls and the substrate. This leads to three contributions to the nanowire growth, direct impingement (A), the sidewall (B) and substrate (C) contribution. For the mathematical description, radial symmetry is assumed and the wire is described by its radius R_{wire} and its height H_{wire}.

In the model of Ruth & Hirth, the nanowire top is considered as a sink for adatoms and every atom arriving the top is incorporated there. A detailed knowledge of the effects at the growing top-facet is not required, but can be integrated into the model to explain effects of the droplet size (Dubrovskii *et al.*, 2009a). In addition, radial growth is typically neglected. However, parasitic layer growth due to limited diffusion and desorption the substrate is regarded. Due to diffusive transport on the substrate and the sidewalls, the adatom density varies with position. Since radial symmetry is assumed, the

sidewall adatom density n_{side} is a function of the coordinate z, the distance from the initial substrate surface, and the adatom density on the substrate n_{sub} is a function of r, the distance from the center of the nanowire. Now, the diffusion equations can be formulated for given impingement rates to the sidewall F_{side} and substrate F_{sub}, as well as the adatom live times τ_{side} and τ_{sub}.

1. For the substrate
$$\underbrace{D_{sub}\nabla n_{sub}(r)}_{diffusion} + \underbrace{F_{sub}}_{source} - \underbrace{\frac{n_{sub}(r)}{\tau_{sub}}}_{sink} = 0 \tag{5.5.1}$$
with ∇ the two-dimensional 2D Laplace operator in the substrate plane and D_{sub} the diffusion coefficient on the substrate

2. For the sidewall
$$\underbrace{D_{side}\frac{d^2}{dz^2}n_{side}(z)}_{diffusion} + \underbrace{F_{side}}_{source} - \underbrace{\frac{n_{side}(z)}{\tau_{side}}}_{sink} = 0 \tag{5.5.2}$$
with D_{side} the diffusion coefficient on the nanowire sidewalls

The impingement rate for the sidewall is given by $F_{side} = F_0 \sin\alpha$ and for the substrate and nanowire top by $F_{sub} = F_{top} = F_0 \cos\alpha$ with F_0 the flux at $\alpha = 0$. The four required integration constants are determined by four boundary conditions. The conservation of mass at the interface of nanowire and substrate leads to

$$D_{sub}\left.\frac{dn_{sub}}{dr}\right|_{r=R_{wire}} = -D_{side}\left.\frac{dn_{side}}{dz}\right|_{z=0}$$

The continuity for chemical potential at the base of the nanowire and its top lead to

$$\mu_{sub}(r = R_{wire}) = \mu_{side}(0) \tag{5.5.3}$$

$$\mu_{side}(z = H_{wire}) = \mu_{top} \tag{5.5.4}$$

where the chemical potential μ_i for adatoms is calculated under the assumption of low adatom density by

$$\mu_i = k_B T \ln\frac{n_i}{N_0} \tag{5.5.5}$$

with N_0 the density of adsorption sites and n_i the density of adatoms. For separated wires the density of adatoms is constant in a certain distance from the wire $R_{feeding}$. This is usually the fourth boundary condition

$$\left.\frac{dn_{sub}}{dr}\right|_{r=R_{feeding}} = 0 \tag{5.5.6}$$

Now the diffusion equations can be solved to calculate the flux from the sidewall and the substrate to the top. The nanowire growth rate is the flux of adatoms arriving at the nanowire top multiplied by the crystal volume per III-N pair and divided by the nanowire cross section. The following solution of the equation system neglects radial growth and non-stationary effects. The shown solution here is taken from Harmand *et al.* (2010), who rewrote the solution of Dubrovskii *et al.* (2009b). The formulation of Harmand *et al.* (2010) was chosen, since its content is equal to the one of Dubrovskii *et al.* (2009b), but it is easier to interpret from an experimental point of view due to the fact that Harmand *et al.* (2010) described the properties of the nanowires only by diffusion lengths and differences of chemical potentials. The diffusion length is simply given by $\lambda_i = \sqrt{D_i \tau_i}$.

The total growth rate, i.e. the growth rate relative to the initial substrate surface, of the nanowires

$\frac{dH_{total}(t)}{dt}$ is given by

$$\frac{dH_{total}(t)}{dt} = \frac{v_c}{\pi R_{wire}^2}(A+B+C) \tag{5.5.7}$$

with v_c the volume of a III-N dimer in the III-N crystal, A the contribution of direct impingement to the top-facet, B the contribution from the nanowire sidewalls and C the contribution of the substrate. The growth rate of the parasitic 2D layer $\frac{dH_{2D}(t)}{dt}$ is simply equal to the impinging flux to the substrate minus the contribution to the nanowire growth.

$$\frac{dH_{2D}(t)}{dt} = \frac{v_c}{L^2 - \pi R_{wire}^2}\left(T - (A+B+C)\right) \approx F_{sub} - \frac{\pi R^2}{L^2}\frac{dH_{total}(t)}{dt} \tag{5.5.8}$$

with L the unit area. The approximation is adapted from Harmand *et al.* (2010).

The wire growth rate is then given by

$$\frac{dH_{wire}(t)}{dt} = \frac{dH_{total}(t)}{dt}\left(1 + \frac{\pi R_{wire}^2}{L^2}\right) - F_{sub} \tag{5.5.9}$$

$$A = F_0 \cos\alpha \tag{5.5.10}$$

$$B = F_0 \frac{2\lambda_{side}}{\pi R_{wire}} \frac{U\left(\frac{H_w(t)}{\lambda_{side}}\right)}{U'\left(\frac{H_w(t)}{\lambda_{side}}\right)} \left(1 - e^{-\frac{\Delta\mu_{side-top}}{k_B T}}\right)\sin\alpha \tag{5.5.11}$$

$$C = F_0 \frac{2\lambda_{sub}}{R_{wire}} \frac{1}{U'\left(\frac{H_{wire}(t)}{\lambda_{side}}\right)} \left(1 - e^{-\frac{\Delta\mu_{sub-top}}{k_B T}}\right)\cos\alpha \tag{5.5.12}$$

with

$$U(x) = \sinh x + \delta \frac{\lambda_{sub}}{\lambda_{side}} \frac{\pi}{\tan\alpha} e^{\frac{\Delta\mu_{side-top} - \Delta\mu_{sub-top}}{k_B T}} \cosh(x-1) \tag{5.5.13}$$

$$U'(x) = \cosh x + \delta \frac{\lambda_{sub}}{\lambda_{side}} \frac{\pi}{\tan\alpha} e^{\frac{\Delta\mu_{side-top} - \Delta\mu_{sub-top}}{k_B T}} \sinh(x-1) \tag{5.5.14}$$

with K_i the Bessel function of second kind and order i (Harmand *et al.*, 2010).

For a better understanding of the meaning of this equation, some simple cases are now discussed. For simplicity, the influence of direct impingement of the nanowire top will be neglected, since it adds only positive constant to the growth rate. If the wire length is much longer than the diffusion length on the wire sidewall ($H_{wire} \gg \lambda_{side}$), the area from which adatoms can diffuse to the top is independent of the nanowire length. Therefore, the wire growth rate is constant. The next simple scenario is to assume no contribution from the substrate ($\lambda_{sub} = 0$) and a diffusion length on the sidewall which is much longer than the wire length ($\lambda_{side} \gg H_{wire}$). In this case, the wire growth rate increases linearly with the wire length .

If substrate diffusion is allowed ($\lambda_{sub} > 0$), the interplay of substrate and sidewall contribution has to be considered. Both contributions can be positive or negative depending on the difference of chemical potentials. Assuming a much longer sidewall diffusion length than wire length ($\lambda_{side} \gg H_{wire}$), the following four case are possible. If $\Delta\mu_{side-top}$ and $\Delta\mu_{sub-top}$ are positive, both contributions have to be added. The substrate contribution is constant and the sidewall contribution increases linearly with the nanowire length. If both differences of chemical potential are negative, no wire growth is possible. The third case is that the substrate contribution is positive and the contribution of the sidewalls is negative ($\Delta\mu_{sub-top} > 0$ and $\Delta\mu_{side-top} < 0$). The negative contribution of the sidewalls linearly increases with the length of the wire. Due to this, the positive substrate contribution will lead to nanowire growth, until it is completely consumed by the negative sidewall contribution, and

the length of the wires is limited. The fourth scenario is a negative substrate contribution and positive sidewall contribution ($\Delta\mu_{sub-top} < 0$ and $\Delta\mu_{side-top} > 0$). If the nanowires are long enough, the positive sidewall contribution is larger than the negative substrate contribution and the wires grow. If the nanowires are too short, all adatoms are consumed by the substrate and no nanowire growth is observed. A more detailed analysis can be found in Dubrovskii *et al.* (2009b).

In summary, this model explains many situations of nanowire growth and offers the opportunity to add more effects like radial growth in dependence of the adatom density on the sidewalls. However, it does not provide any origin for anisotropic growth.

InN nanowires

Up to now, this model is limited to the case of separated wires or wires with equal spacing and diameter with no shadowing of the impinging beam by the nanowires. InN nanowires are neither equal in size nor have equal spacing, the close spacing leads to shadowing and the density of nanowires is not constant during growth. Furthermore, InN nanowire growth by MBE is limited to a certain length, which is probably due to decomposition of at the bottom of the wire, as discussed in section 8.4.

Therefore, this model is useful to understand the principles of diffusion induced nanowire growth, but it is insufficient to describe the self-organized formation of InN nanowires on silicon. This problem is probably too complex for an analytical treatment and numerical simulations based on this diffusion model and a model for nucleation are required.

5.6. Conclusion

Considerations on the equilibrium shape of InN and GaN crystals showed that the high aspect ratio of the nanowires and the nearly completely suppressed radial growth cannot originate from minimization of surface energies. The nanowire cross section is close to the one predicted by the Wulff rule but due to the variation in the size ratios on single wires cannot only originate from the minimization of surface energy, too. Since, equilibrium shapes cannot explain the anisotropic growth rates under N-rich conditions, the adatom kinetics were discussed. A high potential for adatoms or surface adlayers on the nanowire sidewalls (a- and m-planes) is predicted, whereas on the top-facets (c-planes) the formation of adlayers is favored. Therefore, it is assumed, that the sidewalls are nearly free of adatoms and the radial growth rate is drastically lowered due to this. Furthermore, it is proposed to perform numerical simulations to combine the models for nucleation and diffusion induced nanowire growth to describe the formation and growth of InN nanowires.

6. InN layers as a reference

The aim of this section is to determine the growth rate limits given by the nitrogen supply (i.e. stoichiometry) for the growth conditions used for InN nanowire growth. Furthermore, layers are grown on the typical standard substrates for InN and characterized to obtain a reference for the properties of the wires.

6.1. Stoichiometry and influence of III:V ratio in InN growth

At low In supply, growth is limited by In and the growth rate increases proportional to the In supply. Under these nitrogen rich conditions, the grown material is porous or columnar. At high In supply, the growth rate is limited by nitrogen and the layers are closed and smooth. Contrary to excess nitrogen, excess Indium does not re-evaporate and contributes to the growth rate with the volume metallic In. Due to this fact, the growth rate increases under nitrogen-limited growth conditions no longer proportional to the crystal volume of In in InN, but to the one of In in its metallic phase. A series of samples on c-plane sapphire was grown to determine the stoichiometry in InN growth and to study the influence of the III:V ratio on the growth rate as well as on morphology. Growth duration and substrate temperature were kept constant, as well as the nitrogen conditions. The growth duration of one hour was chosen to obtain a layer thickness measurable with the Dektak surface profiler. The growth temperature was set to a relatively low value of T_{thermo} = 450°C to avoid any influence of decomposition or desorption. The nitrogen plasma conditions are equal to the ones used for nanowire growth ($F_N = 1.5$ sccm and P_N = 450 W). Furthermore, a second series of layers was grown on GaN templates under stoichiometric and In-rich conditions to investigate the influence of reduced lattice mismatch.

The height was measured by a Dektak surface profiler. Thus, the amount of grown material for porous (i.e. N-rich) samples was overestimated. This is obvious in figure 6.1.1, because the measured growth rate was higher than expected by the supplied amount of In. The point at which the slope changes is the stoichiometric point. To determine this point, the obtained growth rates in nm/min were plotted against the In supply in nm of InN/min in figure 6.1.1. The point where the slope changes, can be estimated by visual inspection to be between 7.5 nm and 10 nm of InN/min supply. The observed growth rate is almost equal to the In supply of around 9.5 nm/min. Therefore, it is supposed that this is the stoichiometric point. To estimate the uncertainty of this value, the growth rate for In-rich samples was extrapolated for samples on sapphire and GaN in figure 6.1.1. The intersections of the linear curve with a slope of one and the most extreme slopes for the growth rates limit the possible range for stoichiometry. The upper limit is given by 9.75 nm of InN/min from the samples on sapphire. The lower limit is given by 8.3 nm of InN/min from the samples on GaN. It was observed in these two series that In droplets form on the surface if the In supply increased to ca. 12.5 nm of InN/min or more.

6.2. Morphology on sapphire and GaN templates

The morphology of the samples was investigated using optical, scanning electron and atomic force microscopy. As mentioned before, N-rich conditions lead to porous morphology. Under several conditions, even nanocolumns were observed on sapphire. Closed layers were observed, if the In flux

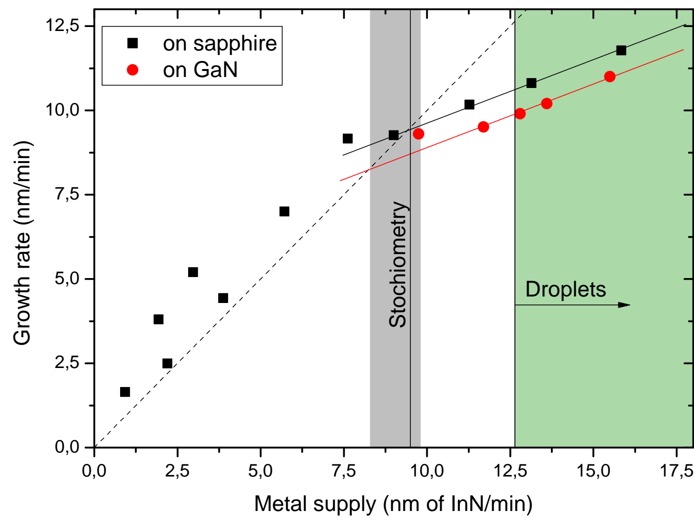

Figure 6.1.1.: *Growth rate of InN as function of Indium supply under nitrogen flux of 1.5 sccm and activation power of 450 W. The black dashed line has a slope of one. The growth rate under nitrogen rich conditions is increased due to the porosity of the grown material. The red and black lines are visual guidelines for the increment of the growth rate as a function of metal supply under metal rich conditions. The intersection of the dashed line and the straight lines enable estimation of the stoichiometric point. The stoichiometry was determined to be at ca. 9.5 nm/min In supply. Its estimated uncertainty is indicated by the gray area. InN droplet formation is observed on samples grown with a metal higher than ca. 12.5 nm/min, indicated by the green area. The 1x1 cm² samples were grown using the original Veeco 1x1 cm² holder at a heater temperature of* T_{thermo} *= 450°C.*

was increased to 9.0 nm of InN/min or higher. Further increase in the metal flux led to smoother layers, but if the In flux exceeded 12.5 nm of InN/min, In droplets formed at the surface during growth.

Figure 6.2.1 shows images of a set of representative samples in the first series grown on sapphire substrate for N-rich, stoichiometric, In-rich and highly In-rich conditions. Under highly In-rich conditions, the forming In droplets are visible under the optical microscope. The metallic character of these droplets was confirmed by etching experiments in fuming hydrochloric acid, during which the droplets disappeared within less than one minute. Further details were difficult to visualize by optical microscopy, therefore scanning electron microscopy was used to investigate the morphology at the nanoscale. The porous character of the samples under N-rich conditions is obvious and the observed morphologies differed from sample to sample. Depending on the growth conditions, nanocolumns, porous layers or layers with nanocolumns were found. The diameter of the nanocolumns was less than 100 nm. The more the In supply increased, the more the morphology changed to closed layers. At about stoichiometric conditions, the layers are closed. Their surfaces showed a grainy structure with a "grain" size of about 100-300 nm. The feature size was increased by increasing the In flux even more. At the highest applied In flux, the grains had a diameter of about 1 µm and were more or less hexagonal. Their top-facet was a little bit tilted with respect to the substrate surface, which becomes visible in the AFM images. The root-mean-square (rms) surface roughness, which is commonly used to compare the surface roughness, was about 3-5 nm for the In-rich samples and 10-13 nm for the highly In-rich samples. The high rms value at the highly In-rich sample was mainly due to the tilted top-facets of the grains. In conclusion, the more the In-flux is increased, the more the samples showed closed layers. Further increase of the In flux under In-rich conditions led to bigger grains with a smoother faceted structure.

The second series was grown on GaN templates to investigate influence of a lower lattice mismatch. The focus of this series was only on the layers, i.e. metal-rich growth conditions. Under stoichiometric and In-rich conditions, a similar behavior concerning morphology was observed. Stoichiometric growth conditions resulted in rms values of 6-9 nm. In contrast, samples grown under In-rich or highly In-rich conditions show a rms surface roughness of about 3.5 nm.

In conclusion, smooth layers were only obtained under growth conditions leading to unwanted In droplet formation. To combine smooth and droplet-free surface, an interval growth mode must be used, similar to the one often used for GaN (e.g. Broxtermann 2011). But since In does not evaporate, it must be converted by active nitrogen to InN. This method is well known and is usually used to flatten rough GaN for RHEED experiments. Recently, this method gained more attention and was investigated in detail for InN by Yamaguchi & Nanishi (2009).

6.3. Structural and optical properties

XRD with the Cu-K_α line at room temperature (RT) was used to analyze the crystal structure of the InN and its orientations. The spectra of the N-rich and In-rich grown samples showed peaks of the sapphire substrate and the InN epi-layer. The XRD $\Theta - 2\Theta$ scans presented in figure 6.3.1 d) showed that the grown InN was purely wurzite. The rocking curves indicated a parallel alignment of the c-axes. This in combination with RHEED experiments with rotating sample suggested that the InN grew epitaxially. The In-rich grown samples were treated with HCl to remove the metal on top. The signals of metal in the XRD completely disappeared after removing the metal on top and it is proven that the layers were free of metal inclusions. . The rocking curve of the InN(0002) peak of the N-rich grown sample was very broad with a full width at half maximum (FWHM) of about 25000 arcsec, in contrast to the In-rich grown sample, which was less broad with a FWHM of about 8000 arcsec. This indicates that In-rich growth conditions led to better alignment of the deposited material.

By changing the substrate from sapphire to GaN, the FWHM of the rocking curve of the (0002) peak was with 1080 arcsec about 8 times smaller than on sapphire and only twice the value of the

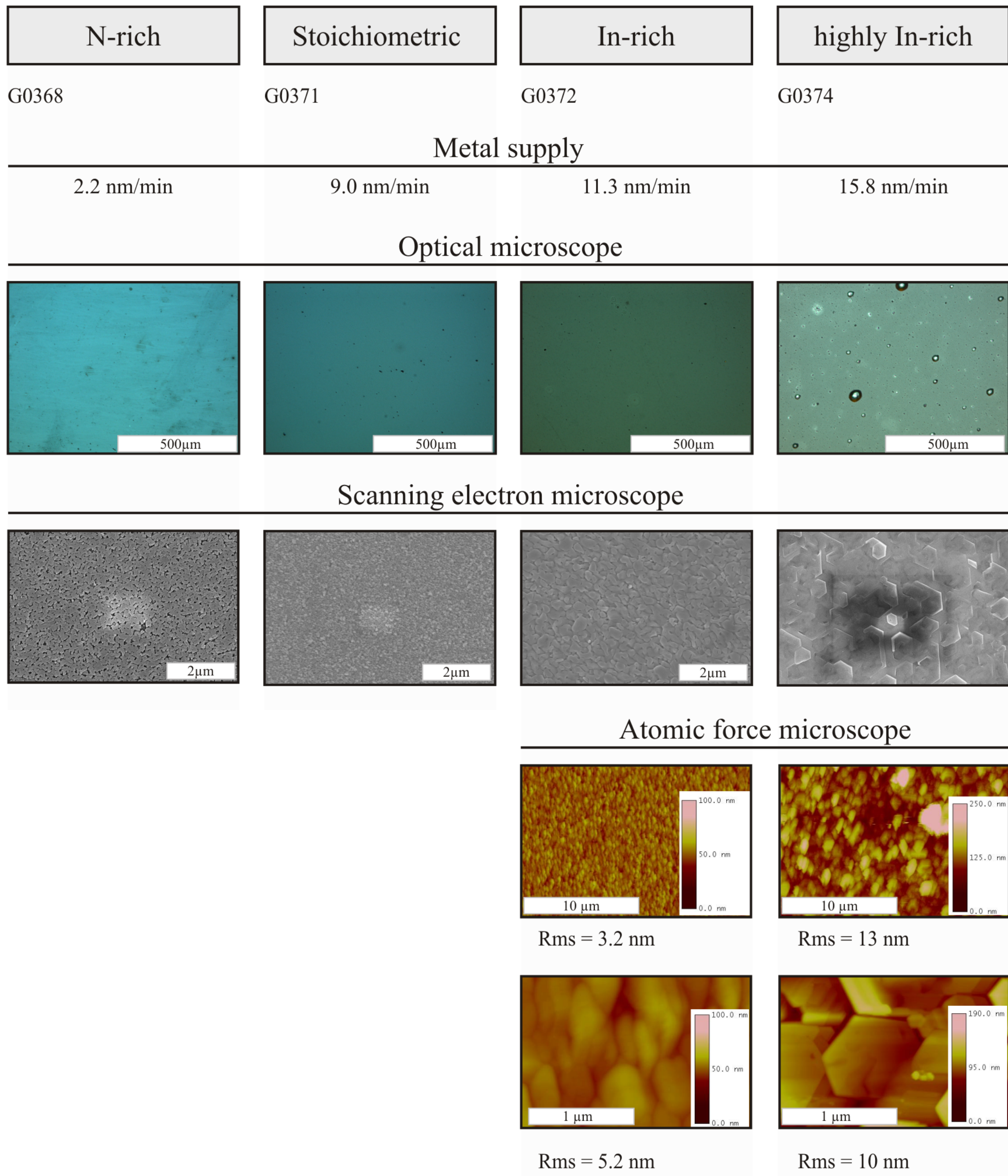

t=1 h, $T_{S\text{-heater}}$=450°C, F_N=9.5 nm/min (F_N=1.5 sccm, P_N=450 W)

Figure 6.2.1.: *Surface morphology of InN samples grown on sapphire under different III:V ratios. The images show representative results of optical, scanning electron and atomic force microscopy. AFM measurements of G0368 and G0371 were not carried out because no meaningful results could be observed due to high porosity.*

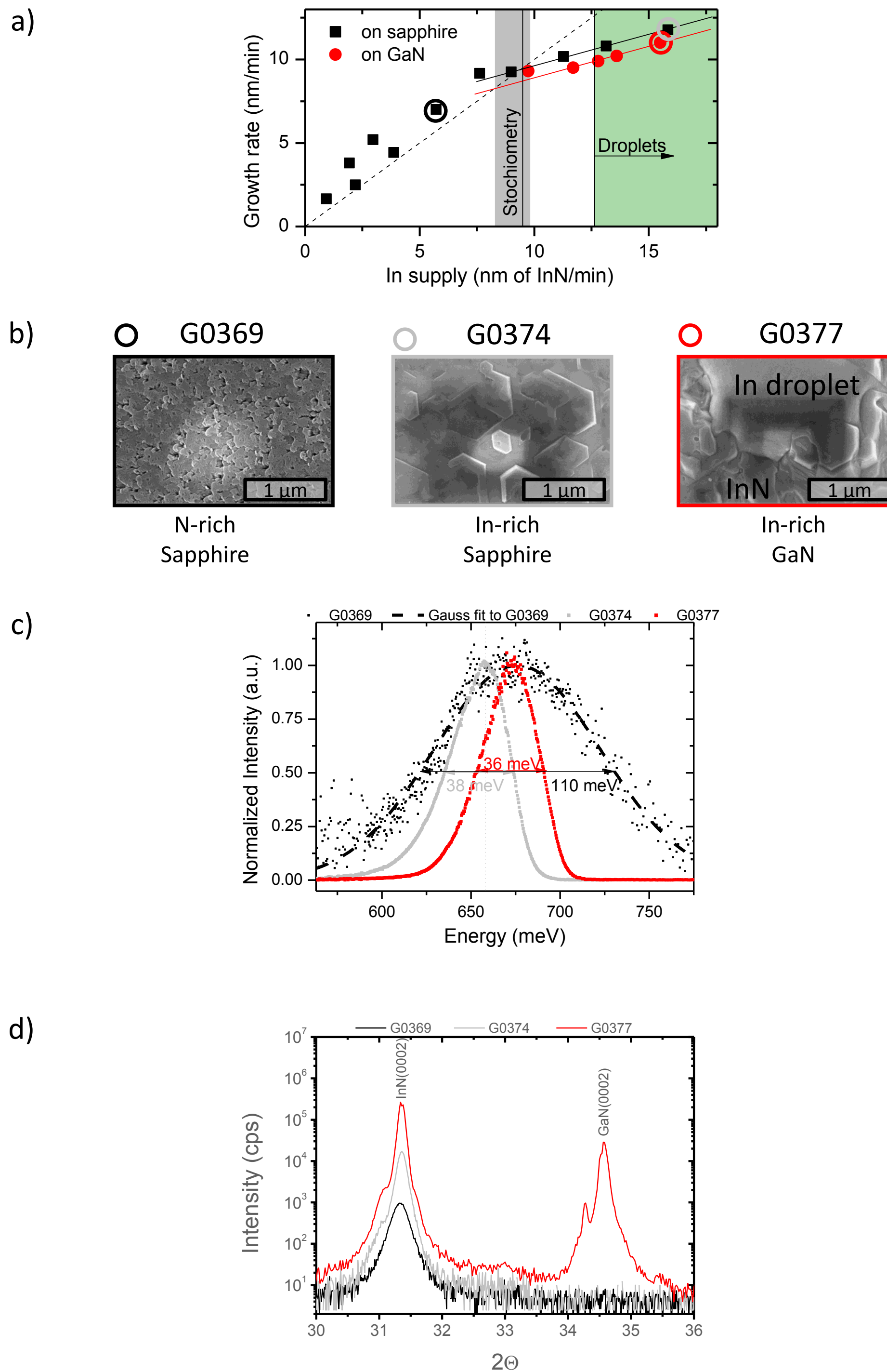

Figure 6.3.1.: *Three representative samples grown with a 1 step procedure without RHEED control. a) growth conditions, b) SEM images of the surface, c) photoluminescence spectra at 5K and d) XRD $\Theta - 2\Theta$ scans with the monochromatic Cu-K_α-line.*

FWHM of the rocking curve of the GaN template. This proves, that the crystal quality was strongly increased by reducing the lattice mismatch. This sample showed two additional peaks at about 34.6° and 33°. The first consisted of two contributions: A main peak at the position of GaN(0002) and a shoulder at 34.25. The second, at about 33°, could be an In (101) reflex or InN ($10\bar{1}1$). According to Yu *et al.* (2005), it is more likely that it is an InN($10\bar{1}1$) signal, because if it would be metallic In, other In reflexes would be also expected. Therefore, this peak at 33° indicated some random orientation of InN. This signal was four orders lower in intensity than the In(0002) peak and therefore the amount of randomly oriented material is assumed to be very little.

Raman spectroscopy of these layers shown in the PhD thesis of Jaime Segura (2009) are in agreement with these observations. Furthermore, Raman spectroscopy with a probing depth of about 40 nm showed no signals of strained InN or of other orientations. Therefore, strained and misoriented InN was probably at the interface of InN and GaN.

Photoluminescence measurements were performed at about $\lesssim$ 10 K to analyze the luminescence properties of the samples also by Jaime Segura. The samples were excited with an Ar^+ laser line of 514 nm and a power of $\sim$25 W/cm². The spectra of the same three representative samples are shown in figure 6.3.1 c). All spectra were characterized by a single peak in the infrared at about 0.7 eV. No other signals at higher energies were found. For all analyzed layer samples, the maximum of the peak varied between 0.66 and 0.68 eV. The N-rich grown sample showed a broad symmetric peak centered at 0.675 eV with a FWHM of about 110 meV. The In-rich grown samples showed a much narrower emission and the peaks were asymmetrically broadened. Their FWHM was comparably small with 35 meV(GaN) and 38 meV(sapphire). For further details see Segura-Ruiz (2009).

Non-degenerated semiconductors usually show spectra with sharp peaks for different transitions, such as band-to-band, free-to-bound and several excitonic peaks. Up to now, this has not been observed for InN, indicating that InN is always degenerated. Generally, this leads to PL-spectra with a single broad peak. Fu *et al.* (2006) analyzed PL spectra of InN layers with residual doping concentrations in the range of 3.5×10^{17}cm^{-3} to 5×10^{19}cm^{-3}. They explain the asymmetric broadening and blue shift by a combination of Kane's two band-model, band renormalization effect due to electron-electron interaction, electron-ionized impurity interaction and band tailing effect. In doing so, they fit the dependence of the energy of the maximum of the PL peaks and carrier concentration. Furthermore, Fu *et al.* (2006) observe an empirical dependence of the FWHM of the peaks on carrier concentration in the range of 1.2×10^{18}cm^{-3} to 5×10^{19}cm^{-3}. This dependence is given by $\log(\sigma) = 0.51\log(n) - 3.21$, with n the carrier concentration per cm³ and σ the FWHM of the peaks in meV. But it should be mentioned that for the sample with the lowest doping concentration of 3.5×10^{17}cm^{-3}, this empirical rule was significantly violated. A more theoretical study was published in 2009 by Moret *et al.*, supporting the results of Fu *et al.* The FWHM of 110 meV of the N-rich grown sample would correspond to a carrier concentration of 1×10^{19}cm^{-3} (Fu *et al.* (2006)) or 3×10^{18}cm^{-3}. For this high carrier concentration, the Burstein-Moss-shift should result in a PL peak position of 0.74 eV (Fu) or 0.7 eV (Moret), which is not in agreement with the observed 0.675 eV. This, in addition to the sample with low residual doping presented in the publication by Fu *et al.*, indicates that there are InN samples which do not follow this empirical rule. However, all studies on the PL of InN agree, that peaks around the assumed band gap of 0.67-0.68 eV near 0 K in combination with a low FWHM are indicators of high quality samples with low residual doping. Since all samples show emission in that range, their carrier concentration can be estimated to less than 2×10^{18}cm^{-3}. It is likely that the N-rich grown sample has the highest carrier concentration.

6.4. Interval growth

To increase the quality of the grown InN with a droplet-free surface, an interval approach was applied using reflection high energy electron diffraction (RHEED) to monitor the state of the surface.

6.4.1. RHEED of InN

RHEED allows one to monitor the state of a surface during MBE growth. In the Staib RHEED system, which was used for this study, electrons are accelerated with 14.5 kV under an angle of about 1-3° towards the substrate. The electrons are diffracted by atoms on the surface and detected on a screen. If the surface is 3D-structured (rough), a spotty pattern is observed. In contrast, 2D-surfaces (flat) result in a streaky pattern. A surface with a completely streaky pattern typically has an AFM rms surface roughness of less than 1 nm. According to the azimuthal orientation of the substrate, different interference conditions are found. For III-N in c-direction, diffraction along the high symmetry axes in a- and m- directions are of interest. The intensities of the spots are reduced by metal adlayers until the peaks completely disappear at a metal adlayer thickness of about 10 ML. Furthermore, RHEED detects surface reconstructions and it can be deduced from the different reconstructions whether the surface metal-terminated or nitrogen-terminated.

Two kinds of surface reconstructions were observed on c-plane InN: the 1×1 and $\sqrt{3} \times \sqrt{3}$. Due to geometric reasons, they are only distinguishable in the $[1\bar{1}00]$ direction. The $\sqrt{3} \times \sqrt{3}$ is a reconstruction of In and N atoms which appears under nitrogen rich conditions when little amounts of In are given to the surface. It reaches its highest intensity at an In coverage of 1/3 ML and is an indicator for In on the surface (Chen *et al.*, 2000). This reconstruction also appears if the sample temperature is high enough that the InN top-layer decomposes and releases its In to the surface.

This can be utilized to distinguish four temperature ranges. The first one is a low temperature range. Here, an 1×1-reconstruction forms under exposure to active nitrogen and remains if the N-shutter is closed. The second range is characterized by a 1×1-reconstruction under N-exposure and a slowly appearing $\sqrt{3} \times \sqrt{3}$-reconstruction due to decomposition if the N-exposure is stopped. The time it takes for the $\sqrt{3} \times \sqrt{3}$-reconstruction to appear can be used for further refinement of temperature determination. At higher temperatures, in the third temperature range, the behavior of the RHEED pattern is similar despite the fact that once the $\sqrt{3} \times \sqrt{3}$ is fully present, it starts to disappear due to further decomposition, which leads to higher metal coverages of the surface. In this temperature range, the time between stopping the N-exposure and the highest intensity of the stripes of the $\sqrt{3} \times \sqrt{3}$ can be used to characterize the temperature with higher accuracy. If the temperature is further increased to the fourth range, the $\sqrt{3} \times \sqrt{3}$ will only be present under N-exposure and immediately disappear when the N-exposure is stopped. In this temperature range, the decomposition of InN is so strong that the InN already decomposes under N-exposure. In theory, there should also be a fifth temperature range at even higher temperatures, in which the $\sqrt{3} \times \sqrt{3}$ cannot be observed, even under N-exposure.

6.4.2. RHEED-controlled interval growth

Semi-insulating GaN:Fe templates were used in order to perform Hall-measurements to reliably determine the concentration and mobility of the free-carriers in the InN layers. Specially designed mounting plates were used to enable RHEED-controlled growth. As mentioned in section 4.4.1, the choice of the substrate and mounting plate influences the relation of thermocouple to substrate temperature.

In addition, one faces the problem of growing the narrow band gap InN on top of a large gap substrate. This obviously changes the heat radiation adsorption during growth and again the relation of thermocouple and sample temperature. Therefore, a test sample was first grown to optimize the growth parameters. Specifically, about 200 nm of InN were grown under manually controlled In-rich conditions.

As mentioned previously, an interval growth method was chosen to combine the high crystal quality and smooth surface of In-rich growth with a droplet-free surface. In the presented interval method, each interval consists of three phases. In the first phase, In is given to the surface to ensure growth under In-rich conditions in the subsequent second phase of InN growth. In this second phase, In and

N are given simultaneously to the surface. In the final third phase, the sample is exposed to active nitrogen to consume excess In and, as such, suppress any droplet formation.

The growth parameters were optimized to conditions, under which a streaky InN $\sqrt{3}\times\sqrt{3}$ surface reconstruction appeared after exposure to active nitrogen, even on a surface with an initially spotty pattern. For this purpose, the thermocouple temperature was lowered by 50°C to 400°C. A nitrogen flux of 0.5 sccm and a plasma excitation power of 300 W (typically used for high quality GaN layer growth) was used with an In flux of 0.35 ML/s and a thermocouple temperature of 400°C. At this temperature, the $\sqrt{3}\times\sqrt{3}$ reconstruction appeared within 1s when N-exposure is stopped. This reconstruction is stable for more than 1 min.

About 3.5 ML of In were deposited during the first phase. This corresponded to a time of 10 s. For the second phase (simultaneous exposure to In and nitrogen), a duration of 7 min was found to be a good choice from GaN growth-experiments and was also adapted here. The length of the third phase was chosen to be 1 min. This ensures a complete consumption of excess In, because the RHEED pattern typically reaches its full constant intensity after about 30 s.

According to this optimization, a sample was grown with a thickness of about 1 μm to reduce the influence of the surface Fermi-level pinning and its resulting surface electron accumulation. The initial growth interval was manually controlled and the In flux was stopped several times during this nucleation period to monitor the nucleation behavior of InN on GaN. Figure 6.4.1 shows the switching of the In and N beams, the evolution of the RHEED intensity, as well as a selection of RHEED patterns along the $[11\bar{2}0]$ axis. These RHEED patterns showed that the initial GaN surface was flat and the grown material was relaxed to the lattice constant of InN after 10 s (3.5 ML) of In and 10 s of exposure to active nitrogen. The spotty pattern at this time indicates 3D island growth, the so-called Vollmer-Weber growth mode. During the subsequent 6.5 min, these islands coalesced to a smooth 2D layer, resulting in the streaky pattern observed after the initial growth interval.

Figure 6.4.2 shows the observed RHEED patterns along the $[1\bar{1}00]$ axis and the temporal evolution of their intensity at the beginning and end of a growth interval. The break in the graph of about 15 min includes a whole complete growth interval. During this break, the sample was rotated to avoid any inhomogeneity of flux distribution on the sample. A 1×1 reconstruction was observed during exposure to active nitrogen. Directly after the beginning of the In predeposition phase, the $\sqrt{3}\times\sqrt{3}$ reconstruction appeared for a short moment. With further deposition of In, it changed back to the 1×1 reconstruction, whereby its intensity continuously decreased. During the second phase of the growth interval, the screen stayed almost completely dark. The intensity of the diffraction pattern started to recover after 25 s of exposure to active nitrogen and saturated after a further 10-12 s. The surface during the recovery phase always showed the 1×1 reconstruction, but not the $\sqrt{3}\times\sqrt{3}$ reconstruction. Due to the rotation of the sample, a reliable comparison of the intensities before and after the break is not possible. During the whole growth time, however, no significant reduction in the intensity was observed. This shows that the surface roughness stayed constant throughout the growth.

In attempt to compensate for the increased heat absorption by InN, the thermocouple temperature was lowered from 400°C to 375°C with 1°C/min after 1 h of growth time. After the growth was finished, The sample was exposed several times to active nitrogen was given several times to the substrate until the $\sqrt{3}\times\sqrt{3}$ reconstruction, which appears due to decomposition, disappeared. This was carried out to avoid the formation of an In ad-layer.

The resulting layer was smooth, but did not show any terraces. Furthermore, the layer was unclosed and contained holes with a density of approximately 4.5×10^5 cm^{-2}.

AFM topology scans in figure 6.4.3 a) and b) showed a smooth layer, but with about 4.5×10^5 holes per cm². The holes were oval or round in shape, with a diameter of 60-120 nm. From the characterization of the substrate, it is known that the GaN layer contained about 5×10^5 threading dislocations per cm². This matches very well with the amount of holes in the layer. Therefore, it is likely that the InN did not grown on these dislocations under these conditions.

The surface of the layer between the holes was smooth. Steps of ML height were observed, but no

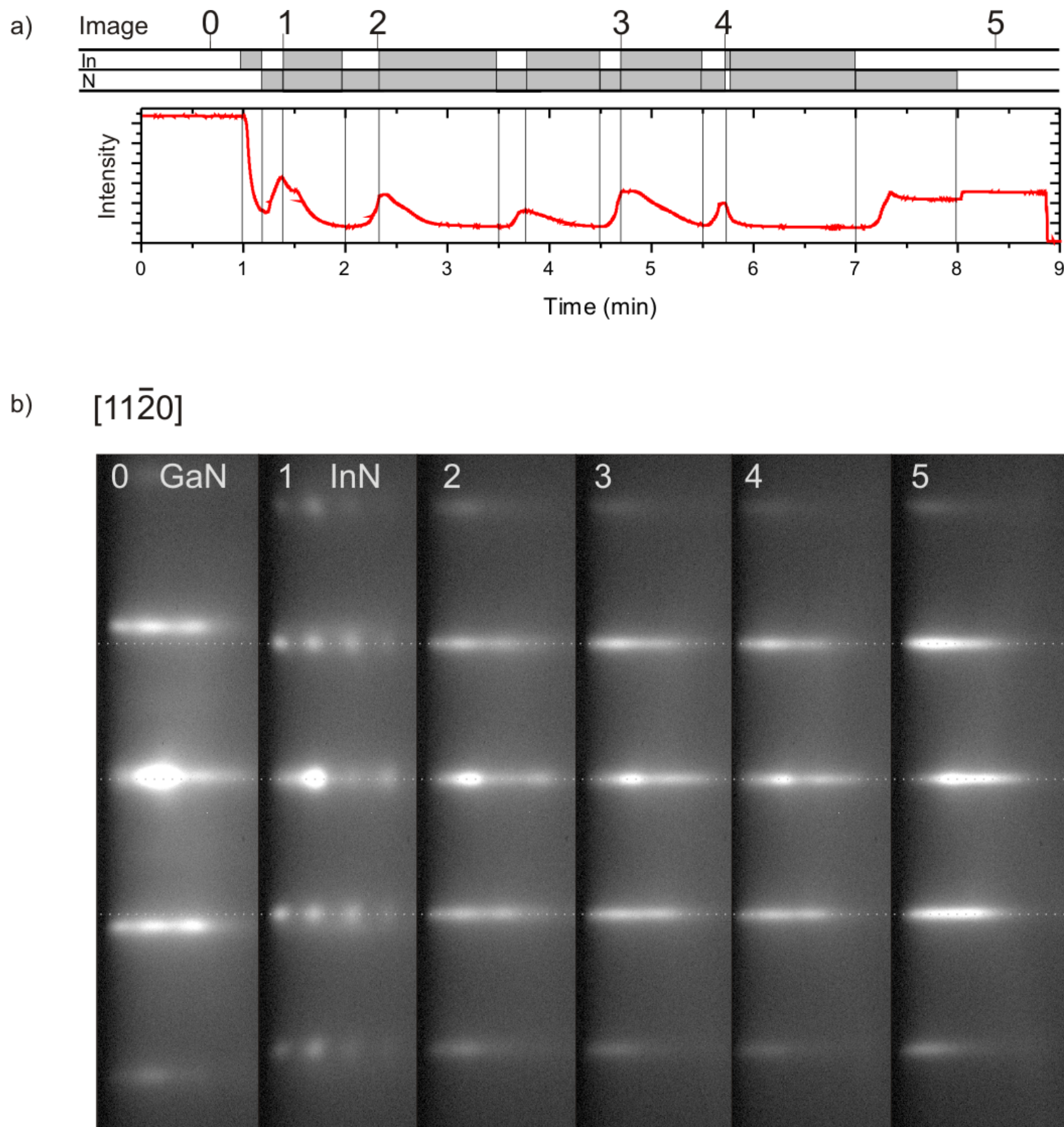

Figure 6.4.1.: *Initial layers of InN on a GaN template. a) The evolution of the intensity of RHEED intensity with time as well as In and N supply. b) Characteristic images of the RHEED pattern for the different stages of InN on GaN.*

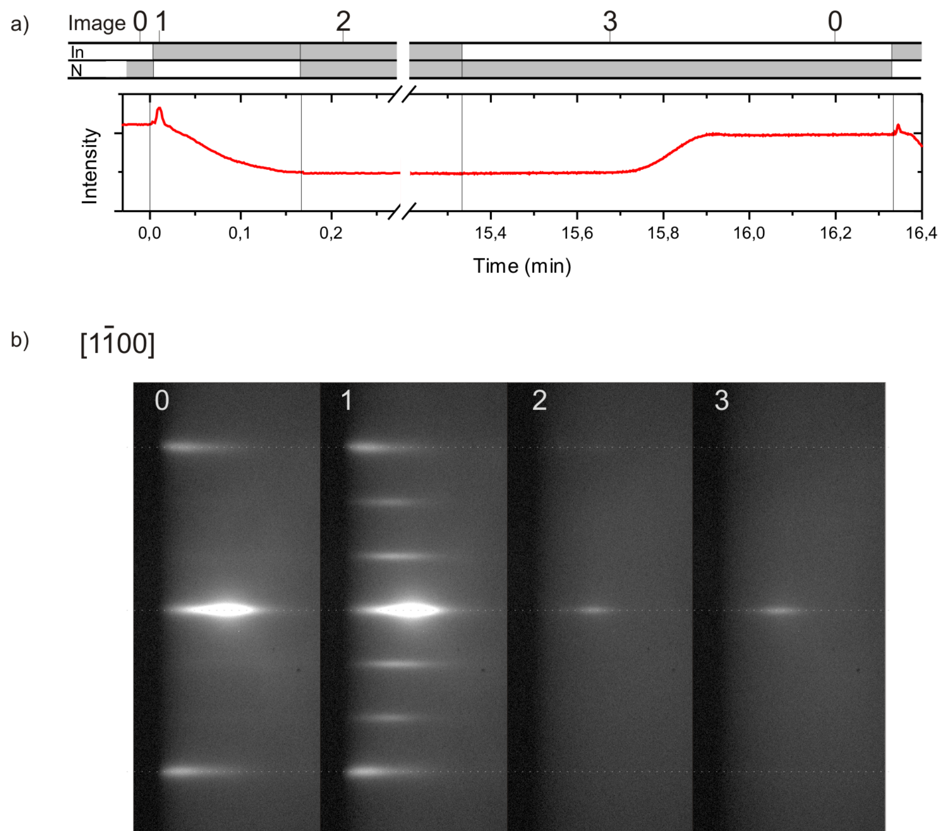

Figure 6.4.2.: *a) Typical evolution of the RHEED intensity during a growth loop. The break contains more than a complete loop. Furthermore, the change in intensity between the two points indicated with "0" is due to slightly different orientations of the sample. b) Typical corresponding RHEED patterns at the steps indicated by numbers in the images and time line.*

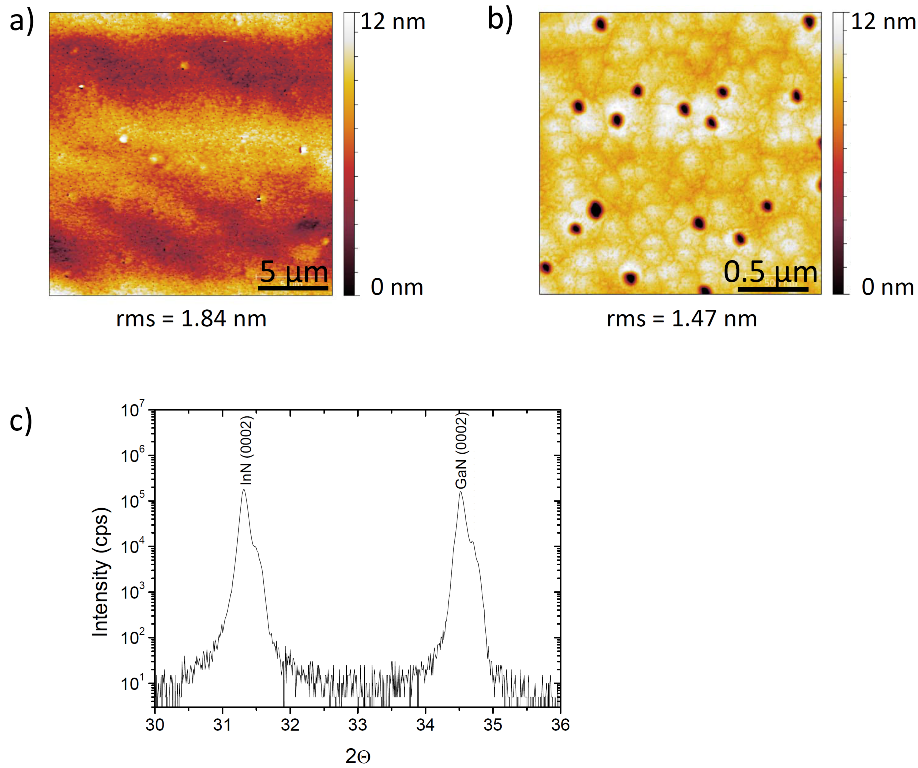

Figure 6.4.3.: *AFM topology at a) 400 µm² and b) 4 µm² areas, c) XRD Θ-2Θ scan.*

terraces were found. It could not be concluded from this postmortem characterization whether growth took place in a step flow or 2D-nucleation mode, since the substrate temperature after growth was so high that decomposition of the InN layer took place. The nitridation to compensate for the decomposition surely changed the surface. Even though the surface contained holes, the rms roughness values of 1.84 nm on 20×20 µm² and 1.47 nm on 2×2 µm² were relatively low. The rms roughness value was as low as 0.6-0.7 nm on areas without holes.

XRD $\Theta - 2\Theta$ scans in figure 6.4.3 c) in combination with rocking curves of the (0002) reflexes reveal that InN grew with a parallel alignment of the (0001) axis on the GaN. The FWHM of the rocking curve of the InN (0002) peak with 775 arcsec was the lowest observed value in this study indicating an improved orientation of the grown InN. It was only about double the value of the GaN (0002) rocking curve FWHM of 380 arcsec. This was almost as good as values obtained e.g. by Yoshikawa *et al.* (2010) or Knübel *et al.* (2009), who reached FWHM values of 200-540 arcsec.

Temperature-dependent Hall measurements in van-der-Pauw geometry were performed on two samples. One was the 1 µm thick sample grown by the interval approach on semi-insulating GaN:Fe and the other was a 8.8 µm thick sample grown also by an interval approach on sapphire with a thin GaN/AlN buffer layer.

Fehlberg *et al.* (2007) performed quantitative mobility spectrum analysis (QMSA) on multiple magnetic field Hall effect measurements of InN layers. By this method, two conductive channels were isolated: one surface or interface channel with sheet carrier density of around 3×10^{14} cm^{-2} and a mobility of about 600 cm²/(Vs) and a bulk channel with carrier concentration of about 10^{17} cm^{-3} and a mobility at room temperature of about 4000 cm²/(Vs). The only temperature dependent value of this channel was the mobility of the bulk contribution, which had a maximum at about 150 K. Because only single magnetic field Hall measurements were performed in this study, QMSA was not possible. However, it was possible to qualitatively reproduce the measured results under the assumption of two channels with constant carrier concentration and only one temperature-dependent mobility by using

the equations, e.g. given in Look & Molnar (1997). Assuming only one degenerate channel with constant carrier concentration and mobility, as done in Look & Molnar (1997), resulted in an unreasonable low carrier concentration in the bulk. Therefore, the exact values of carrier concentration and mobility could not be determined by single magnetic field Hall measurements shown in figure 6.4.4. The change in resistivity with temperature can be used for comparison to temperature-dependent resistivity changes of InN nanowires. In addition, the values determined by single magnetic field meausrements at room temperature are often used as figure of merit. The observed carrier concentration was about 1×10^{18} cm^{-3} with a mobility of 1000 cm²/(Vs) and the samples show a comparably low carrier concentration and high mobility compared to other high quality InN samples (Wu *et al.* (2004), Fehlberg *et al.* (2007)).

Assuming a surface sheet carrier concentration for the low mobility carriers of 3×10^{14} cm^{-2} as observed by Fehlberg *et al.* (2007), the bulk carrier concentration would be about 8×10^{17} cm^{-3} and the mobility about 2500 cm²/(Vs) for the 8.8 µm thick sample. For the 1µm thick sample, the bulk carrier concentration would be negative. Under the assumption of a lower surface sheet carrier concentration of 2.7×10^{13} cm^{-2}, as observed by Lu *et al.* (2003) by single magnetic field thickness dependent Hall measurements, the bulk electron concentration would be about 8×10^{17} cm^{-3} with a mobility of about 900 cm²/(Vs) at room temperature.

6.5. Conclusion

InN layers in (0001) direction were grown on sapphire with and without GaN buffer layer as a reference for InN nanowires. The growth rate limit given by the nitrogen supply was determined by the layer growth rate at stoichiometry. This limit was about 9.5 nm per minute, when the typical nitrogen conditions for nanowire growth of a nitrogen flux of $F_N = 1.5$ sccm and a plasma excitation power of $P_N = 450$ W were applied. This in combination with the atomic flux calibration of the metal sources enables the specification of the V:III ratio.

Furthermore, InN layers were grown using a state of the art interval growth method to obtain a droplet free surface under In-rich conditions, which are required for smooth surfaces. The samples showed a comparably low free carrier concentration of $\lesssim 1.3\times10^{18}$ cm^{-2} and a high mobility $\lesssim$ 1200 cm²/(Vs), as measured by single magnetic field Hall measurements at room temperature. The maxima of intensity of photoemission were centered at about 0.66 eV with a full width at half maximum down to 25 meV at low temperatures of $\leq 10\,K$. This further indicates a low carrier concentration. Therefore, the properties are comparable to other high quality samples reported in literature (compare Fu *et al.* (2006), Morkoc (2008) and Fehlberg *et al.* (2008)) and the layers are suitable as a reference system for the properties of nanowires.

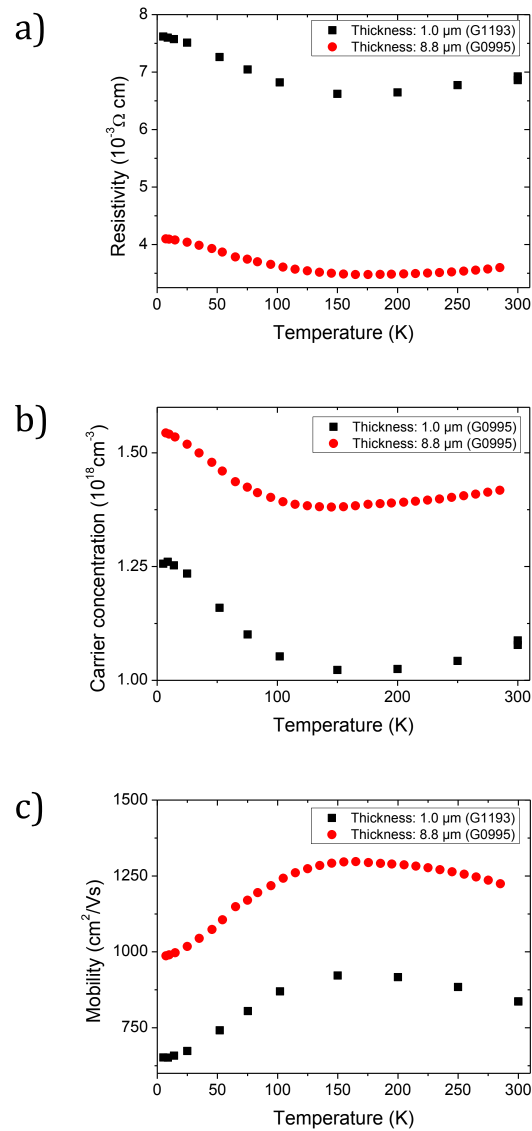

Figure 6.4.4.: *Results of Hall measurements in van-der-Pauw geometry. a) Resistivity, b) Carrier concentration, c) Mobility.*

7. Properties of InN nanocolumns

It was shown in the previous section that InN grown as layers is, so far, always a degenerate semiconductor. This might be due to growth on lattice mismatched substrates or a high residual unintentional doping. The growth of nanocolumns is a promising way to circumvent this problem, if a suitable lattice-matched substrate is lacking. In case of InN growth on silicon, the unavoidable formation of an amorphous silicon-nitride facilitates growth of strain free material without the introduction of defects. In addition, the change of growth conditions can affect the incorporation of impurities and may reduce residual background doping. Due to this fact, InN nanocolumns on silicon are auspicious to investigate intrinsic InN. However, nanowires have a high surface-to-volume ratio. Due to this fact, the properties can be controlled by effects originating from the surface. The following section is focused on the properties of InN nanocolumns grown on silicon to test how the properties of nanowires change compared to layers. The structural and chemical properties are probed by transmission electron microscopy (TEM), core-level X-ray photoemission spectroscopy (XPS) and Raman spectroscopy. The electronic properties are investigated by resistivity measurements, Raman spectroscopy, photoluminescence (PL) and photoluminescence excitation (PLE).

For this section, it has to be mentioned that it was developed in three parts. The first part about growth of InN nanowires (section 7.1) forms the base of the subsequent characterization and was part of my diploma thesis (Denker, 2007). The electrical and structural characterization, which builds the second part (section 7.2 - 7.4), began also in my diploma thesis and was continued in the framework of this thesis in collaboration with the diploma students F. Werner, F. Limbach, D. Ruttke, M. Carsten and the PhD student M. Gomez under my guidance. The third part about optical characterization (section 7.5) was developed in collaboration with the University of Valencia.

7.1. Self-organized growth of InN nanowires

In order to obtain InN nanocolumns for further characterization, various samples were grown with constant growth time and constant nitrogen plasma conditions on unstructured Si (111) in a self-organized way. Prior to growth the sample was heated to about 850°C to remove the native oxide. The resulting 7×7 reconstruction was used as an indicator for an oxygen free surface. The substrate temperature T_S for growth and the In flux were varied. In this way, five regimes with different morphologies were identified. These are summarized in figure 7.1.1. At a low substrate temperature of $T_s = 390$°C, the resulting morphology was columnar, but due to high density of nanocolumns almost layer-like. This is assigned to an increased nucleation probability and reduced diffusion length. At a higher substrate temperature of $T_S = 430$°C, the density of nanocolumns decreased and the structures showed a rounded cross section and tapering towards the top. At slightly higher temperatures, a bimodal distribution of length and size was observed. In this temperature range, an increasing number of long, round nanocolumns with a small diameter were found, while the rest of the nanocolumns on the sample were shorter with a much larger diameter. If the substrate temperature was further increased, the nanocolumns had a hexagonal cross section and broadened towards the top. These columns were well separated, which indicates a lowered nucleation probability and increased diffusion length of adatoms. This kind of nanocolumn morphology was also observed by Stoica *et al.* (2006), whereas the bimodal size distrubtion has not yet been reported by other groups. At a reduced In flux, the nanostructures were oblong, tilted and more extended and their density was lower. No column-like structures were observed when the substrate temperature was increased to over 465°C

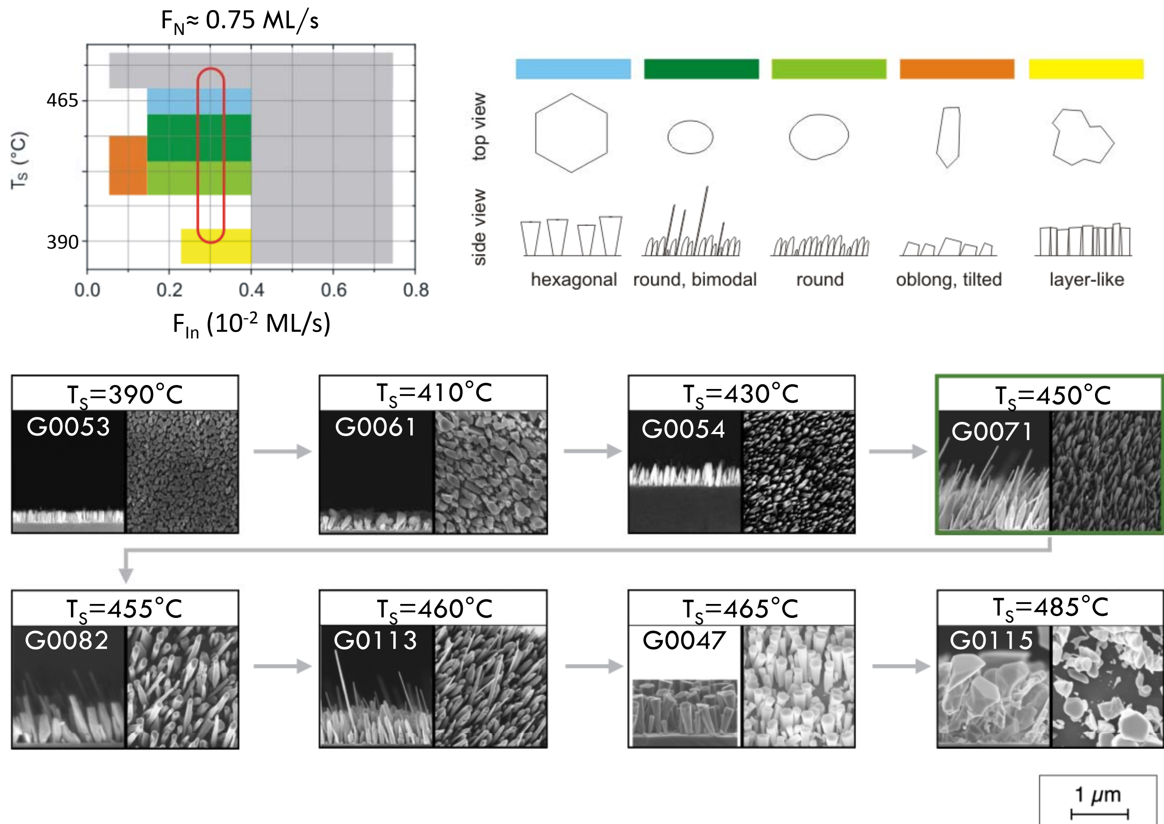

Figure 7.1.1.: *Morphologies obtained under varied metal flux and substrate temperature and constant growth time of 300 min and nitrogen conditions of* F_N *= 2 sccm and* P_N *= 500 W, which corresponds to a growth rate at stoichiometry of about 12.5 nm/min (Denker (2007) and Denker* et al. *(2008); substrate temperatures* T_S *and fluxes are given according to calibrations in section 4.4).*

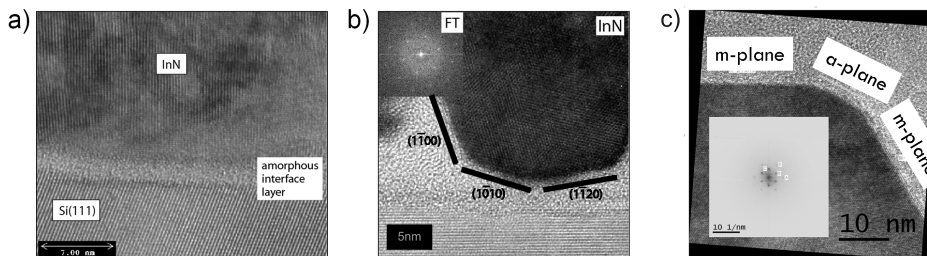

Figure 7.2.1.: *a) High resolution transmission electron microscopy Si/InN interface with a 2 nm thick amorphous Si_xN_y interlayer. Cross-section TEM of single InN columns in c-direction for b) long nanocolumn of the bimodal regime and c) for one that seems to be hexagonal in SEM (a) and b) adapted from Denker (2007)).*

or the metal flux over 0.74 nm/min. The longer wires of the bimodal growth regime are particularly interesting for the electrical characterization of single nanocolumns, since they are suitable for electrical measurements on single wires in four-point probe geometry. In this growth mode, nanocolumns were up to 2 µm long with an aspect ratio of up to 45. (Denker (2007) and Denker *et al.* (2008)).

7.2. Transmission electron microscopy (TEM)

Transmission electron microscopy perpendicular to the growth axis revealed, that the nanocolumns were single crystalline and showed a wurzite stacking sequence. Furthermore, only very few extended defects were found. Therefore, it is assumed that the nanowires were nearly free of extended defects aside from very few stacking faults.

An amorphous silicon nitride interlayer with a thickness of 2-3 nm was found at the interface of the silicon substrate and the InN nanowires, as shown in figure 7.2.1. This amorphous interlayer explains the missing epitaxial relation between the substrate and nanocolumns, which can be seen by the varying tilt of the nanowire's c-axis (i.e. its growth direction and the orientation of the sidewall facets). This missing relation was also confirmed by Gracing Incidence X-Ray Diffraction (Denker, 2007) for the directions perpendicular to the c-axis. This is in accordance with what is reported in literature by Grandal *et al.* (2007). For cross-sectional TEM of the nanowires, the nanowires were mechanically transferred to a silicon substrate with a native oxide by the "clean-room wipe"-technique. In a second step, the nanowires are covered by electron-beam-induced deposition of amorphous platinum to prevent damaging in the next step. In this step, a slice of the nanocolumn with the platinum and the substrate was cut by a focused beam of Ga-ions. This slice was then thinned by the Ga-ion beam to less than 30-40 nm to enable TEM.

Figure 7.2.1 b) and c) show a cross-sectional view in growth direction of two wires. The nanowire in figure 7.2.1 b) originated from a sample with the bimodal distribution of size and is a thin nanowire. In contrast to SEM, facetting was visible in TEM, but with rounded edges between the facets. The facets were identified as a- and m-plane facets. The other wire in figure 7.2.1 c) originated from a sample where the wires appeared hexagonal in the SEM. In TEM, these wires also showed a- and m-plane facets and are therefore not hexagonal, but dodecagonal. In contrast to the other nanowire, the edge between the facets were much sharper. The sizes of the facets were not regularly distributed. This reveals that the cross-section of these nanocolumns is not a equilibrium shape due to surface energy minimization, because any equilibrium shape would show a regular size distribution. Even though the shape was not an equilibrium one, it was close to one predicted by the Wulff-construction.

No signature of a surface oxide was observed by TEM imaging. To gain more information about the chemical composition, spatially resolved electron energy loss spectroscopy (EELS) in a TEM was

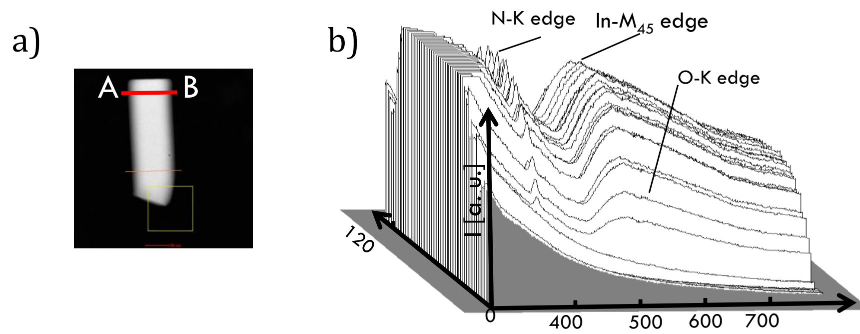

Figure 7.2.2.: *a) Scanning-TEM of the nanowire used for EELS; the scan across the nanowire is shown in red. b) The EELS spectra recorded at the different position of the scan (measurement done by R. Schneider).*

performed by Reinhard Schneider in Karlsruhe, Germany. Figure 7.2.2 shows EELS spectra recorded across the nanowire perpendicular to the growth axis. These spectra show the signal of the O-K edge at the nanowire sidewalls. This signal is low in intensity but significant, indicating some slight oxidation of the nanocolumns. From this it is concluded, that there is probably an oxide present, but its thickness is less than or equal 1 nm.

7.3. Surface oxidation of InN probed by XPS

In core-level X-ray photoemission spectroscopy (XPS), electrons in the core-levels of the probed material are excited by monochromatic X-rays. These excited electrons are then emitted due to the photoelectric effect. The energy of the emitted electrons is the excitation energy reduced by the work function of the material Φ_0 and the binding of its orbital E_B. The exact binding energy of a core level depends on the chemical shift due its environment and the valence state of the atom (Reinert & Huefner, 2005). Therefore, the energy of the emitted electrons allows to determine the species and the bond of the atom where it originates from. This is illustrated in figure 7.3.1. Due to the low penetration depth of 3±2 nm at an excitation energy of about 1 keV (Seah & Dench, 1979), this technique is ideally suited to investigate the chemical composition of a surface.

The here presented measurements were performed by M. Carsten using a monochromatic Al-K_α x-ray beam with an energy of 1486.6 eV is used for excitation in an UHV environment under an angle of 50° in order to obtain sufficient signal from the lateral sidewalls of the nanowires. The energy of the emitted electrons was detected by a 126 mm mean radius hemispherical energy analyzer with a multichannel electron detector. The measurement set-up is sketched in figure 7.3.2. The data were analyzed and interpreted by M. Carsten, F. Werner and A. Rizzi. See Carsten (2010) and Werner (2009) for further details.

To measure the chemical composition at the surface of InN nanowires, sample G0594 was exposed for one day to air after growth. After mounting the XPS system the specimen was heated to 120°C for 3h to desorb most of the water from the samples. This low annealing temperature was chosen to prevent decomposition.

The recorded spectra showed signals of In, N, O, Si and C. The carbon signal is typical for these kinds of measurements and originated at least partially from the measurement. This signal was used for calibration and normalization. Due to this calibration, the accuracy was estimated to ± 0.3 eV. To extract the constituent components, the peaks were fitted by Voigt functions and an adequate fitting for the background. The results for the In-3d, N-1s and O-1s peaks are shown in 7.3.3 b). The silicon

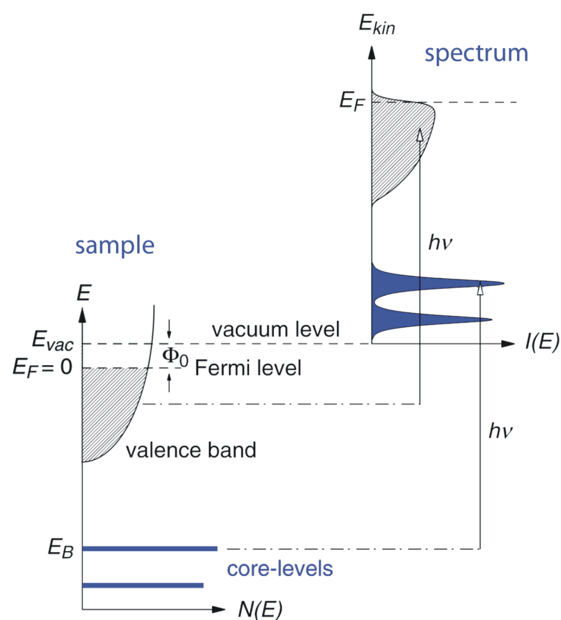

Figure 7.3.1.: *Sketch of the photoemission process in the single-particle picture. The left side shows the density of states for electrons in a sample and the right side shows the resulting emission spectra, which is shifted by the excitation energy $h\nu$ and broadened (Reinert & Huefner, 2005).*

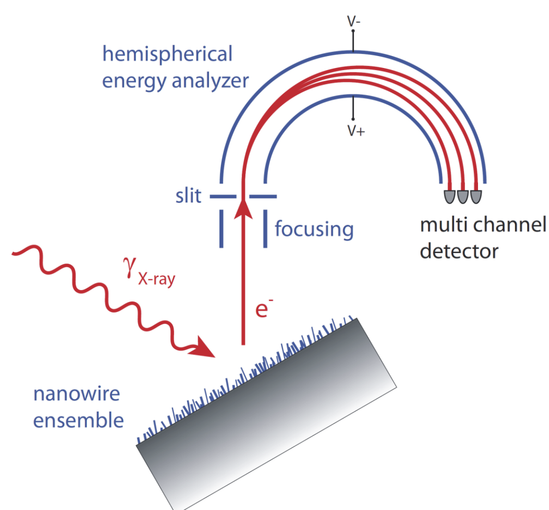

Figure 7.3.2.: *Schematic view of the experimental setup for XPS analysis of nanocolumns (Werner, 2009).*

Core-level	Binding energy [eV]	Chem. environment	Reference [eV]
In-3d$_{5/2}$	444.0	InN	443.7[1]; 440.0[2]
	445.0	In_2O_3	444.7[1,3]
N-1s	396.5	InN	396.4[2]
	397.7	SiN_x	397.5[3]
O-1s	530.7	In_2O_3	530.3[1]; 530.6[2]
	532.5	physisorbed O	532.0[1]; 532.2[2]

Table 7.3.1.: *Core-level binding energies for the considered compounds for the XPS analysis and their associated chemical environment ([1] from Piper* et al. *(2005), [2] from Veal* et al. *(2007), [3] from Moulder* et al. *(1995), compare also Werner (2009) and Carsten (2010)).*

signal originated from the substrate.

The N-1s core signal showed two distinct contributions which correspond to binding energies of 396.5 eV and 397.7eV. The lower one was assigned to In-N bonds (Veal *et al.*, 2007). The higher one was assigned to N-Si bonds in the SiN_x phase formed at the beginning of the growth.

The signal of the In-3d doublet clearly showed a contribution from two components. The signal at 444 eV was assigned to In-N bonds and the one at 445 eV to the In_2O_3 bonds (Piper *et al.*, 2005; Veal *et al.*, 2007).

The obtained signal was best fitted using two components at 530.7 and 532.5 eV. The component at 530.7 eV was associated with the In-O bond (Veal *et al.*, 2007), while the one at 532.5 eV was assigned to remaining physisorbed oxygen at the surface after the mild annealing. If the SiN_x would oxidize, the signal of a Si-0 bond would arise at 533 eV, very close to the one physisorbed oxygen and therefore would not contribute or become mixed up with signals from the In-O bonds.

These results clearly indicate not only, that InN surfaces oxidize, but also confirm that the outer 3 nm are not completely oxidized, which is in accordance with the TEM results. These XPS experiments showed that In_2O_3 and InN are present within the first 3 nm close to the surface. The exact nature of the oxide is hard to determine. It is reasonable to assume that the interface between the oxide shell and the nitrogen core is not completely abrupt and therefore different oxynitrides, as well as oxygen on a nitrogen site in an InN matrix, are expected. But their role cannot be revealed by this method. The In-O in InN would act as donors, which would lead to a surface accumulation layer of electrons.

7.4. Electrical measurements on single nanowires

This section shows the results of electrical measurements on single nanowires and also considers several technical aspects of contacting nanowire by e-beam lithography.

7.4.1. Contacting single nanowires

The first step of electrical measurements is processing electrical contacts to the specimen. In the case of MBE-grown InN nanowires, the specimen (i.e. the nanowires) are very small with a length of less than 2 µm. Therefore, the high resolution of e-beam lithography is needed to contact the nanowires. For e-beam lithography, the wires must be transferred to the surface of an insulating substrate.

Lithography

Lithography is a tool used to structure surfaces. A photo or e-beam sensitive resist is spin-coated onto the surface. By selective exposure and development, the resist can be structured and then be

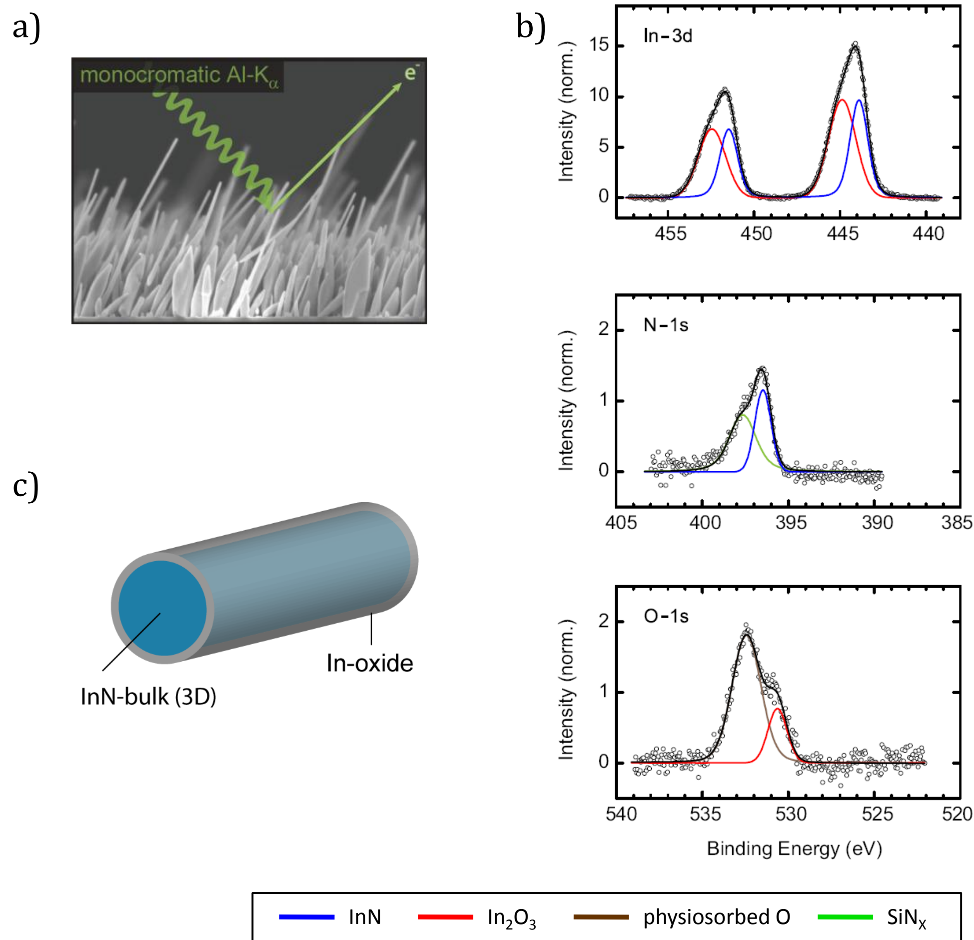

Figure 7.3.3.: *a) Sketch of XPS measurement. b) In-3d, O-1s, and N-1s core-level spectra (open circles) obtained under an emission angle of 50° and normalized to the intensity of the C-1s signal. The background is subtracted from the data (see Carsten (2010) for details). The black lines indicate the signals fitted with Voigt functions. The colored lines show the resultant single core-level contributions (Werner* et al.*, 2009). c) Model of the proposed nanowire structure: InN core with a thin native In_2O_3 shell.*

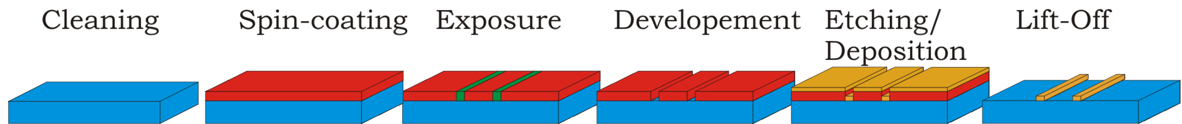

Figure 7.4.1.: *Illustration of a lithography step (Denker, 2007).*

used as a mask for further processes, such as etching, sputtering or metal deposition. The training courses of Raith, the company that manufactures e-beam lithography units, are recommended as a good introduction to lithography, whereas their manuals can be used as a reference book, but without claiming completeness. Furthermore, the technique itself is also well described in many textbooks, e.g. Waser (2003), Gerthsen & Vogel (1999) and Moreau (1988).

A lithography step consists, in general, of 6 steps as illustrated in figure 7.4.1.:

- Cleaning with solvents to remove any adsorbents or dirt
- Spin-coating of the e-beam or photo sensitive resist
- Exposure
- Development, depending on the resist, the exposed (positive resist) or unexposed (negative resist) parts of the resist are etched by an alkaline developer
- The processing step of etching and deposition
- Removing the residual resist and excess material from the deposition step

In the following, a brief summary of the experience of contacting nanowire is given. The kind of resist, positive or negative, is chosen according to the structure that should be written. It is better to choose a positive resist, if more resist should stay than be removed. Then the thickness of the resist is chosen according to etch intensity and thickness of the layer to deposit. For a pure etching step, the resist must be thick enough to be not completely removed after the etching. On the other hand, for deposition, the thickness of resist should be three times higher than the layer to deposit to ensure a good lift-off.

The exposure parameter must be optimized for each process. The minimum possible feature size depends mainly on the spot size of the electron beam. The spot size depends on the acceleration voltage, the working distance and the aperture. Furthermore, the proximity caused by electrons scattered in the substrate has to be regarded when structures are close to each other (≤ 1 µm). A higher acceleration voltage typically decreases the spot size, but increases the proximity effect. A higher working distance typically increases the spot size and the depth of sharpness. This is important when the position of exposure and the position where the beam is adjusted are not the same.

The exposure dose is specific for resist, resist thickness, developer and developing time and more or less scales with the inverse of the acceleration voltage. To determine the exposure dose test patterns, which are similar to the real ones, are exposed with varying dose (about two orders of magnitude in steps of 5-10% dose change). The best dose is the one at which the resist is completely removed at the exposed areas and the pattern size is only a little bigger (20-50 nm) than in the design.

The scanning step size should be chosen as one fifth of the minimum feature size. For the exposure the beam current must be adjusted by changing the aperture such that the beam speed is about 3-5 mm/s.

Positioning

To contact single nanowires, they must be transferred to an insulating substrate. This substrate needs to be structured to allow for the exact positioning of the nanowires, since they are randomly distributed

on the substrate after transfer. The field of view in SEMs used for e-beam lithography is limited to a maximum of 2×2 mm², but to 100×100 µm² for the highest possible resolution. Therefore, all structures are divided into writefields for exposure, whose sizes are limited by the size of the field of view. To expose a writefield, the center of this writefield is moved to the center of the field of view of the SEM by moving the stage. The structures in the writefield are then exposed with a fixed stage. If the structure size exceeds the size of writefield, the stage must be moved. Therefore, connected structures should be in the same writefield.

Typically, four coordinate systems are defined in e-beam lithography. The first one is the physical one given by the stage. This is used to control the stage movement with an accuracy of $\leq$1 µm. The second is given by the sample. Alignment of these two allows movement of the sample with an accuracy of about 1 µm. The third one is defined for a writefield on the sample and the fourth one is defined for a writefield for the microscope, i.e. for the scanning beam. Alignment of the latter two coordinate systems allows for positioning accuracy of $\leq$ 50-150 nm. The substrate needs to have markers to allow for reproducible alignment. Therefore, the prestructured insulating substrates have two kinds of markers. Big markers are located in the corners of the samples to align the coordinate systems of the stage and sample. Small markers are in every writefield of the sample to allow for the alignment of the writefield coordinate system of the beam to the writefield coordinate system of the sample.

To increase the processing time, the markers are usually written by optical lithography, as well as pads with a size of $\geq$ 100×100 µm². These pads are needed to connect the nano-sized contacts at the nanowires to micro-sized contacts, which can be connected by the needles of a micro-manipulator or by wire bonding to the macro-world.

The alignment itself is implemented as a coordinate transformation of 2D coordinate systems, which accounts for an offset of the origin (shift), linear correction of the length scales (zoom) and the angle of x and y axis (rotation). For the alignment of the first two coordinate systems ("sample-stage-alignment"), the stage must be driven to three markers whose positions are known. In the Raith software, the function "Adjust U,V,W" is used for this purpose. To utilizes this function, the positions must be entered, and, when the stage is at one marker, the position is read by the button "read". The software also allows the use of two of these coordinate systems: "global" and "local". This is important because the position in scanned images is always displayed in the "global" coordinate system. Furthermore, this function allows one to correct tilting of the sample, either by moving the stage or by correcting the working distance.

The alignment of the other two coordinate systems is carried out by scanning three areas defined in special layers of the design patterns (layer 61 or 63). In the manual mode, the results of the scanned images are displayed and then the center of the images must be marked by pressing "ctrl" and moving a cross-hair with the left mouse button to the center of the marker. For a good alignment, this step must be repeated several times, as shown in figure 7.4.3. It is also useful to reduce the scanned area step-by-step to about 1-2 µm². It should be mentioned that in the new Raith lithography software (version 6), it is necessary to increase the "point average" to at least 8, otherwise the scanned image is stretched in the x-direction.

Contacting

The important steps of contacting single nanowires are shown in figure 7.4.2. The substrate is shown in figure 7.4.2 a). The left image shows the whole sample with three markers close to the corners for the stage-sample-alignment and the center area with the writefields and contact pads. One of these writefields with its surrounding pads is shown in the center image. The right image shows the writefield with its markers and ends of the conductive paths to the big pads at higher magnification.

Figure 7.4.2 b) shows a photograph of the simple mechanical wire transfer process. In this step, the edge of a clean room wipe is gently dabbed at the sample with nanowires. In this way, nanowires

detach from the substrate and attach to the fibers of the wipe. In the second step, this edge is dabbed to the area where the wires should be transferred. Some nanowires then detach from the fibers and attach to the substrate by van-der-Waals forces that are strong enough to keep the wires at their positions until they are moved again with a wipe or are removed by an ultra-sonic bath. It was found that bigger wires (length $\geq$ 5µm and diameter $\geq$ 400 nm) are not bound strong enough to stay in position at during spin-coating with a rotation of 2000 rpm.

The left image in figure 7.4.2 c) shows a writefield with nanowires. The positions of nanowire suitable for contacting are marked in red. The center image shows the contacted nanowires and the right one shows the contacted nanowire at high magnification.

The fastest way to locate suitable wires, is first to scan all fields with a resolution of 2000 px $\times$2000 px (1 px $\hat{=}$ 50 nm) automatically and then check all images for promising wires. Their exact positions are determined in a second step using an accurate writefield alignment and taking magnified images of the wire. It must be ensured that the stage does not move for taking the images. A "point average $\geq$ 8" must be used when utilizing software version 6. The coordinates of the wires are always displayed in the "global" coordinate system. If the coordinates should refer to the writefield coordinates, the origin of the "global" coordinate system must be set to (0,0) when the stage arrives at the writefield. In this case, the "local" coordinate system can be used for moving the sample.

For the sake of completeness, it should be mentioned that there is a second writing strategy in e-beam lithography. In this strategy, a laser-interferometer-stage is needed. In this case, the stage can be moved with an accuracy of $\leq$ 20 nm and therefore a high positioning accuracy can be achieved with a fixed beam and moving stage. However, the measurement of the position of the nanowires requires a dense pattern of points written by e-beam lithography with the same strategy, which makes this approach less attractive.

Contacts

In the contacting process, an etching step is necessary to remove the insulating oxide layer. This step is also very crucial because the oxide must be removed, but the sputter intensity should be well adjusted. One must ensure that the insulating layer is removed but not all InN. Furthermore, the effective sputter rate depends on the geometry of the opening in the resist and angle of the sputter gun due to a strong shadowing effect cause the large sputter angle of 60°. Werner (2009) addressed this problem in detail in his diploma thesis. Figure 7.4.5 d) shows the effective sputter rate for a rotating sample in the center and edge of the opening. The geometry factor is defined by

$$\gamma = \sqrt{3}\frac{b}{h-d} \tag{7.4.1}$$

with b the width of the opening, h the thickness of the resist and d the wire diameter. It can be seen that for contacts of 100 nm width, a resist thickness of 480 nm and a wire diameter of 30 nm, the effective sputter rate is position-independent, but about 6 times lower than without any shadowing by the mask. This demonstrates why an exact quantification of an ideal sputter intensity is hard specify. Figure 7.4.5 a) shows a sputter intensity that is too high for large contacts, which leads to the formation of In islands. A sputter intensity that is too great for small contacts is hard to distinguish by SEM imaging.

The thickness of the metal layer should be more than half the wire diameter, but at least 50 nm, otherwise the metal on top of the nanowire has no contact to the conducting path on the substrate. This depicted in 7.4.5 b) in a FIB-prepared cross-sectional view. Ruttke (2010) addressed this problem in detail and found that 60-150 nm of metal layer thickness is a good choice. This thickness requires a resist thickness of about 450 nm.

The nanowires have a length of up to 1-2 µm. The minimum width of reproducible lines written

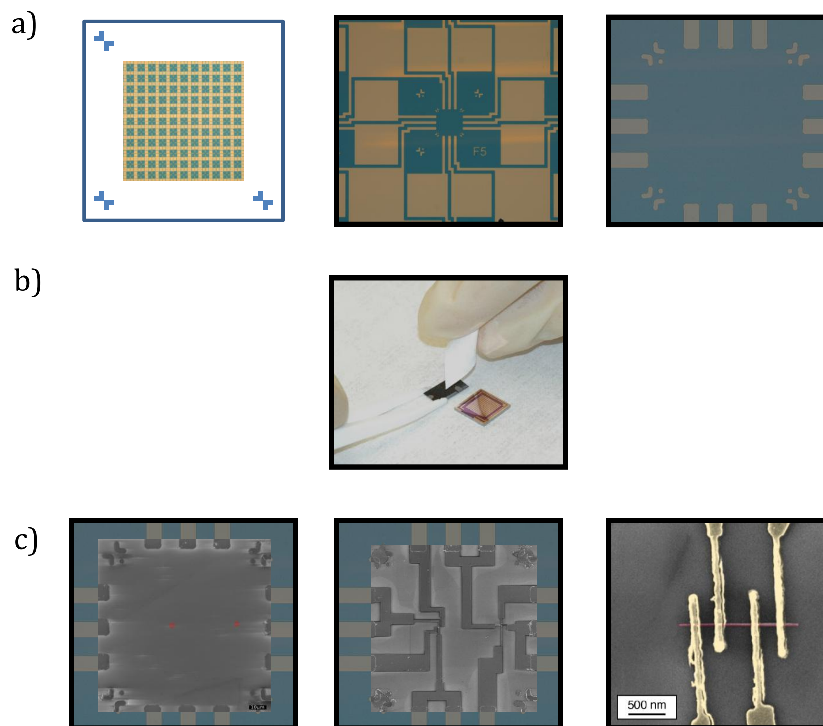

Figure 7.4.2.: *Overview of nanowire contacting processes: a) Prestructured insulating substrate with markers and contact pads of about 150×150 µm² (magnification increases from left to right), b) mechanical transfer of nanowires, c) locating and contacting by SEM and e-beam lithography.*

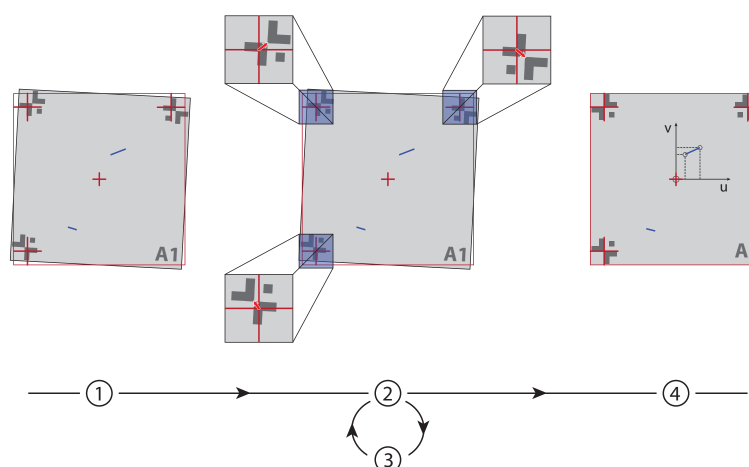

Figure 7.4.3.: *Writefield alignment procedure used in Raith lithography systems on prestructured samples (Werner, 2009).*

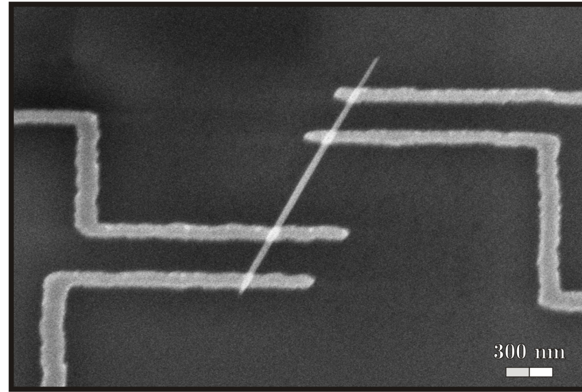

Figure 7.4.4.: *Contacted InN nanowire (Denker, 2007).*

by e-beam lithography is about 100 nm. The distance between the contacts should be larger than 150-200 nm. As mentioned above, the accuracy of locating the nanowire and positioning the contacts is limited to about 50-100 nm. Therefore, nanowires need to be at least 1000 nm (4×100 nm for contacts, 2×100 nm + 200 nm for separation, 2×100 nm for positioning uncertainty) long to place four contacts on it.

7.4.2. Electrostatic discharge, grid induced voltage peak-protection and bonding

Many nanowires become destroyed unintentionally during connection of the micro-size contacts onto the chip with the nanowires to macro-contacts and analysis of the contacted nanowire. In general, the destruction of nanowires can be based on two principles: Ohmic heating and spark discharge. The product of voltage and current per time is relevant for ohmic heating, whereas only voltage is important for spark discharge. The two processes are discussed briefly in the following section. It was found by experiment that a voltage peak of 1V (as measured by an oscilloscope) for several ns can be enough to destroy the nanowires.

The heat capacity of InN is $C_p = 43.886 + 8.194 \times 10^{-3}T{-}1.007 \times 10^{6}T^{-2} + 8.353 \times 10^{7}T^{-3}(JK^{-1}mol^{-1})$ according to Leitner *et al.* (2004). A nanowire with a radius of $r = 15$ nm and length of $L = 500$ nm would require a heating energy of about $1{\times}10^{-5}$ J to increase the its temperature from 0°C to its decomposition temperature of 500°C. The electrical current is 1 mA for a voltage of V = 1 V and a comparably low wire resistance R = 1000 Ω. In this case, a comparably long voltage pulse of 1 V for 2 µs would result in a ohmic heating of $5{\times}10^{-9}$ J, which is four orders too low to heat the wire to its decomposition temperature. A longer pulse length would be detected by the oscilloscope, but shorter and higher higher pulses could be damped by measurement setup. However, it is questionable if voltage peaks of several thousand volts are realistic. In addition, other effects of electrical transport would become important is this case. In particular, the breakdown voltage for electrodes with a distance smaller than 10 µm no longer adheres to the Paschen's law anymore (Hourdakis *et al.*, 2006) and can be as low as 80 V for 400 nm spacing. This limits the applied voltages to about 100 V. The electric field is for 500 nm spacing 2×10^{6} V/m per 1 V. In addition, the very short voltage pulses of several ns probably lead to non equilibrium transport situations. To understand the destruction of the nanowires, a details analysis of the system in a ns-time-scale would be required.

Counteractive measures

Despite the fact that the actual physical cause for nanowire destruction is still unclear, it is still necessary to protect the wires from such stress. Therefore, electrostatic discharge protection is fundamental, since the charging of persons can easily reach 30 kV and machines can also be charged. Electrical

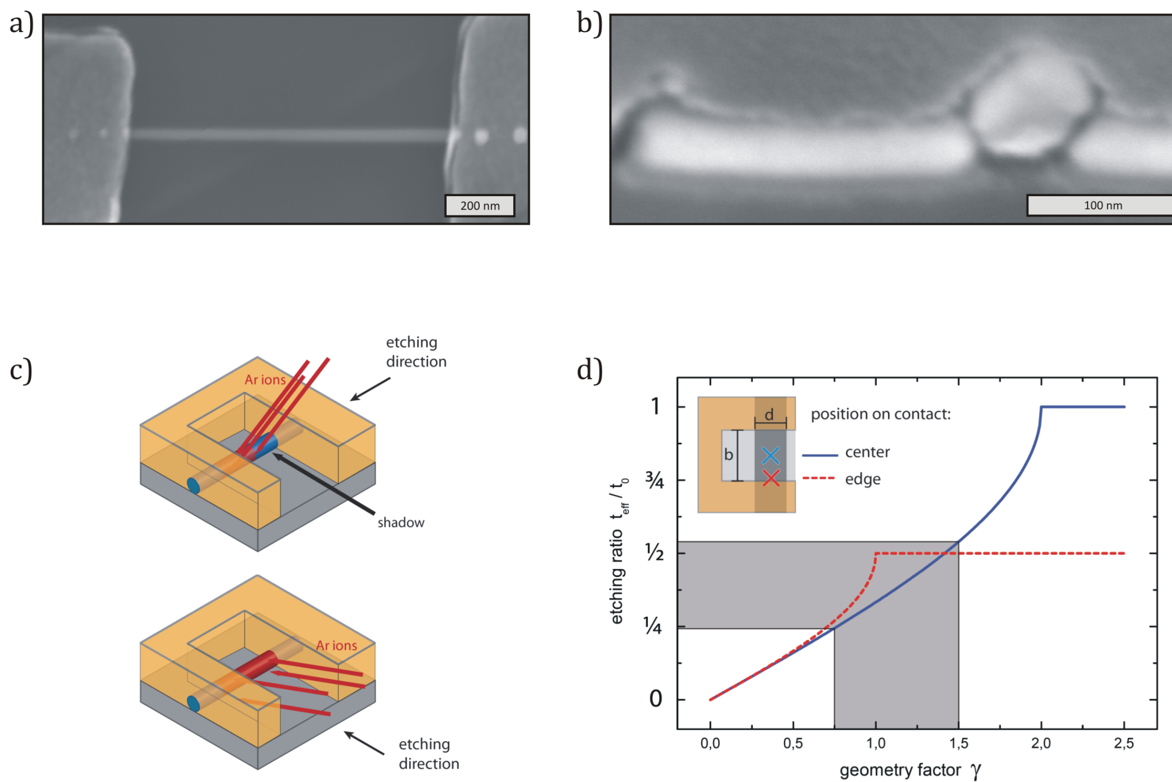

Figure 7.4.5.: *a) Too strong etch of nanowire, b) too thin metal contact layer, c) and d) influence of geometry on effective etching rates (a), b) from Ruttke (2010); c), d) from Werner (2009)).*

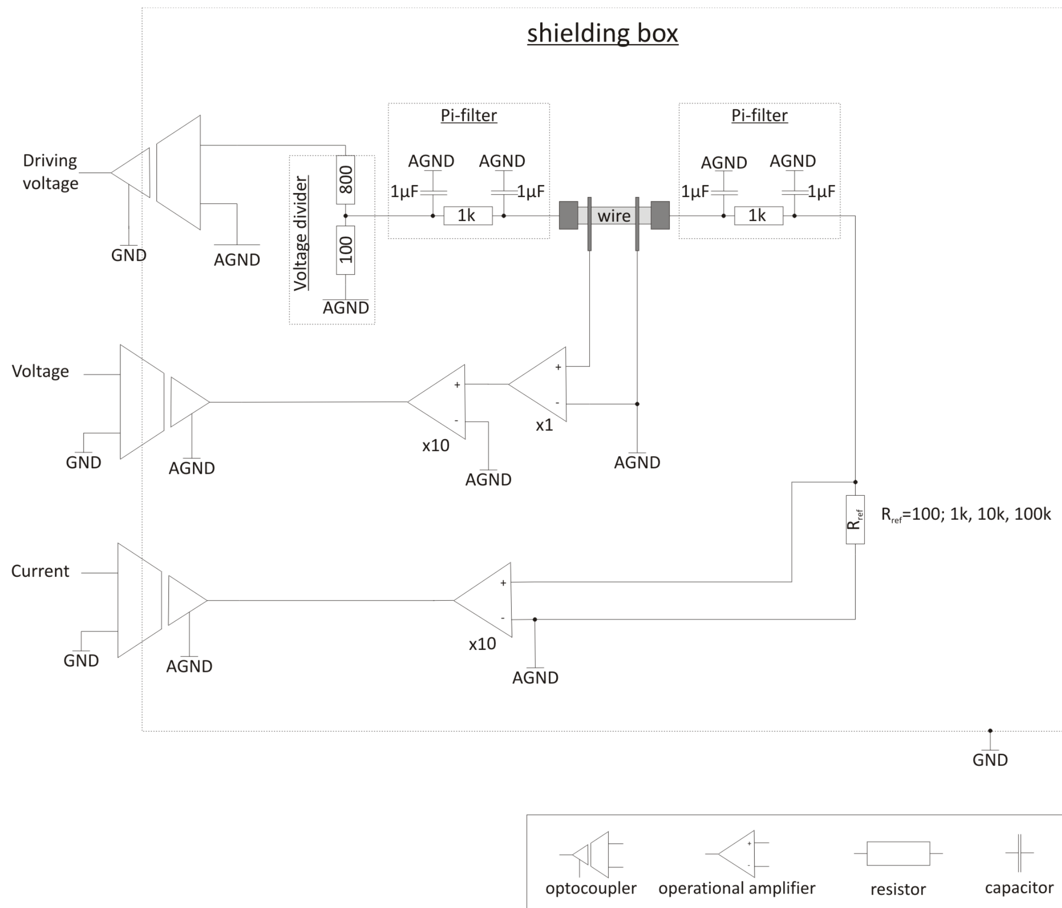

Figure 7.4.6.: *Schematic equivalent circuit diagram of the box used to measure IV-curves of nanowires and protect them from voltage peaks.*

grounding is essential to void such charging. Therefore, the machines and the operator should be grounded. In addition, a grounded conductive floor, conductive shoes, grounded bracelets, no insulation gloves and eventually high ohmic tweezers, as well as antistatic coats are recommended. Special attention must also be paid to chairs. Furthermore, the sample itself can be charged. Possible charges can be removed by an ionizing air blower, which emits positive and negative ions. The sample is neutralized by the attraction of charges of opposite sign. The balance of the ionized air blower gives the voltage at which the free floating metal plate can be maximally charged by the blower. The balance of the ion blower used here is $\pm$ 5 V, and can be further reduced to 0 by replacing the actual ion source by an alpha emitter.

When the sample is connect to the measurement setup, it must be ensured that no voltage peaks from the grid or induced by electromagnetic fields can reach the specimen. Therefore, loops in any cables have to be avoided, as well as any electrical switching. Surprisingly, mobile phones are found to be harmless. Of course, screened cables are required.

But theses measures are often not sufficient. Therefore the nanowire should be further protected by filters. The most simple way is to ground every connection to the nanowire with capacitors to ground. Here 10 nF capacitors proved to be a good choice and filter almost all signals with a frequency $\geq$ 100 kHz. Higher protection is gained by a specially designed filter box. A schematic sketch of this box is shown in figure 7.4.6. With this box, any connection to outside is electrically decoupled using opto-couplers. The box is battery-powered. The voltage for the voltage driven measurements is adjusted by a signal given to an opto-coupler and further reduced by a voltage divider. Furthermore,

Pi-filters protect the wire from high frequency signals. The current is determined by the voltage drop at a reference resistor and amplified, similar to the voltage drop at the nanowire. The outgoing connections do not need any filtering since opto-couplers allow only for signal propagation in one direction.

Bonding

Wire bonding between the micro-sized contacts of the chip on which the wire is connected and macro-sized contacts of the chip carrier is required to enable temperature-dependent measurements. In this process, a thin Al-wire of about 40 µm is pressed with defined force to the bond pads. Furthermore, ultrasound is used to increase the adhesion of the wire. In this process, two things can harm the nanowire. One is electrostatic discharge and the other is ultrasound itself. Therefore, for bonding, all of the above mentioned measures against electrostatic discharge should be applied and the power for ultrasound should be as low as possible.

7.4.3. Measurement geometries

Electrical conductivity

In classical theory, the electrical conductivity σ or its inverse, the resistivity ρ, is defined by:

$$j = \sigma E = \frac{1}{\rho} E \tag{7.4.2}$$

for j the current density and E the electric field. In general, these are vector quantities, but since the wire geometry allows only one direction of current flow, this can be neglected. The conductivity is the product of the carrier concentration n and their mobility μ. With semiconductors, one must account for the two types of charge carriers: electrons and holes. However, in InN, the concentration of electrons exceeds the concentration of holes by several orders of magnitude. Therefore, it is sufficient to assume that only electrons contribute to the conductivity:

$$\sigma \approx e n_e \mu_e \tag{7.4.3}$$

The mobility is defined as the derivative of the drift velocity with respect to the electric field and can regarded as constant for electric fields $\leq 10^6$ V/m $= \frac{100}{100}$ mV/nm (compare to figure 2.2.4). At higher electric fields, the mobility starts to saturate and then reduces. But the applied electric fields are typically below this limit.

In experiments, a voltage V is applied over a length L of a wire with radius r. The resulting electric field $E = V/L$ then causes a current $I = jA$, with A the cross-sectional area of the conductive channel. For InN nanowires, it is reasonable to assume two different conduction channels: one for the core with a low electron concentration and one for the shell with a high electron concentration.

For a cylinder of radius r, the conductivity σ_{3D} is given by:

$$\sigma_{3D} = \frac{I}{V} \frac{L}{\pi r^2} \tag{7.4.4}$$

There are two possibilities to account for the channel at the shell. One is to assume a hollow cylinder, but in this case, an assumption for the thickness is required. The other way is neglect the geometry and calculate a sheet conductivity.

For a hollow cylinder with outer radius r and thickness d, the conductivity is given by

$$\sigma_{2D^*} = \frac{I}{V} \frac{L}{\pi \left(r^2 - (r-d)^2 \right)} \tag{7.4.5}$$

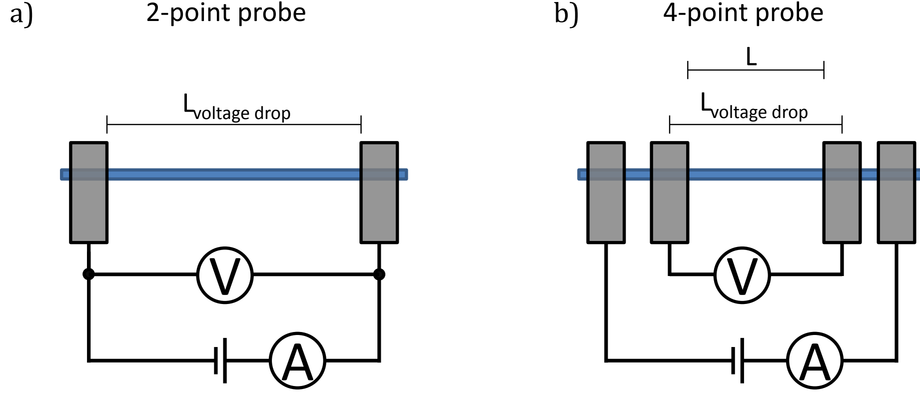

Figure 7.4.7.: *Schematic view a) of 2-point probe and b) 4-point probe measurement geometry. $L_{voltage\ drop}$ indicates the considered length for the voltage drop.*

whereas the sheet conductivity is given by

$$\sigma_{2D} = \frac{I}{V}\frac{L}{2\pi r} \tag{7.4.6}$$

In the measurements, both channels are connected in parallel. Therefore the two conductivities must be added. The resulting measured conductance is then:

$$\text{using sheet conductivity: } G = \frac{1}{R} = G_{3D} + G_{2D} = \frac{\pi\sigma_{3D}}{L}r^2 + \frac{2\pi\sigma_{2D}}{L}r \tag{7.4.7}$$

$$\text{using hollow cylinder assumption: } G = \frac{1}{R} = G_{3D} + G_{2D^*} = \frac{\pi\sigma_{3D}}{L}r^2 + \frac{\pi\sigma_{2D^*}}{L}\left(r^2 - (r-d)^2\right) \tag{7.4.8}$$

2-point probe and 4-point probe

I-V characteristics or resistivity can, in general, be measured in two different geometries, as shown in figure 7.4.7. In the simpler case, two probes (i.e. contacts) are used to apply the electric field, which induces the current, and to measure the voltage drop. This method suffers the problem that the measured resistance includes the contact resistances. If the specific contact resistance is constant, it is possible to remove the contribution of the contacts by calculation. But as shown in section 7.4.4.2, this is not the case for the preparation technique used for this thesis.

The other option is to process four contacts on the nanowire. In this case, the outer contacts are used to induce a current and the inner two to measure the voltage drop. As long as the contact resistances are much smaller than the internal resistance of the voltage measuring unit of several $G\Omega$, the influence of the contact resistances is negligible. Ideally, the size of the contacts are negligibly small compared to distance between them. Due to the small size of the wires, the contacts are only 2-10 times smaller. In this case, it must be regarded, which length has to be assumed to calculate the specific resistance from the voltage drop and current. The potential varies along the metal contact, but the conductive path connected to the contact is at a single potential. This potential is the average potential of the contact on the wire. Therefore, the conductive path (at which the potential is measured) is at the potential of the centers of the contacts and the distance between the contact centers has to be regarded for calculation of the specific resistance, as discussed in e.g. Denker (2007).

Furthermore, the contacts themselves provide a conductive channel in parallel to the wire and there-

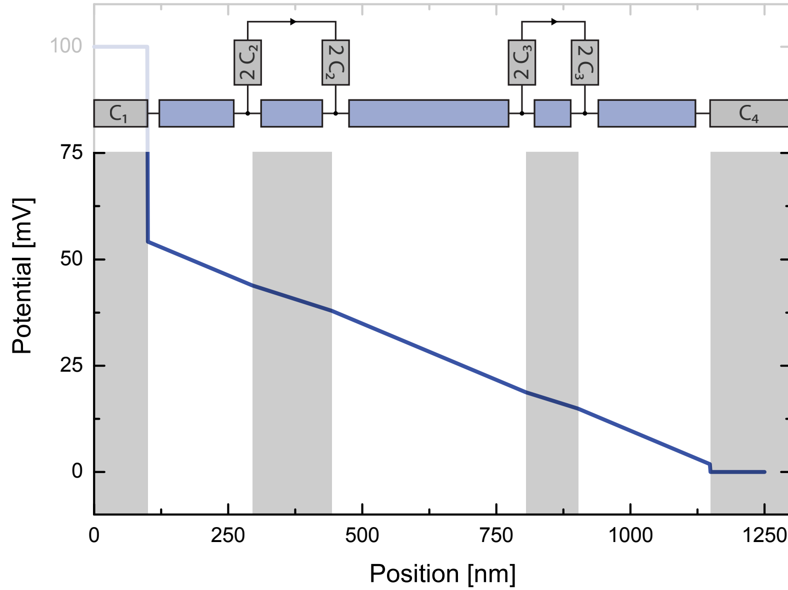

Figure 7.4.8.: *Voltage drop on a typical InN nanowire with a bias of 100 mV contacted in 4-point probe geometry (Werner, 2009).*

fore lower the resistance. The nanowire EB024/H5-1 was contacted in 4-point probe geometry. From resistivity measurements in all combinations of 2-point probe configurations, the specific contact resistances were determined. Since specific contact resistances are relatively high, the influence of the two inner contacts are low, as shown by Werner (2009) who calculated the voltage drop for a voltage of 100 mV at the outer contacts (figure 7.4.8) .

Transmission line method

The idea behind this method is to use contacts with the same resistance on different nanowires with equal diameter and vary the distance between the contacts. If the measured resistances are plotted versus the distance between the contacts, the slope is the resistance normalized by the length and the offset is twice the contact resistance. This method requires that the contact resistance is reproducible, which was not the case in this study (Limbach (2008) and Werner (2009)). Therefore, this method was not be applied.

Nanowire field effect transistor (NWFET)

In a field effect transistor, the carrier concentration can be modified by an external electric field induced by a gate voltage V_G. Figure 7.4.10 a) shows the corresponding equivalent circuit diagram. The measured current I_{SD} is then, within certain limits, linear to the applied gate voltage at a fixed source drain voltage, according to Wunnicke (2006):

$$I_{SD} = \mu \left(\frac{en_0 + CV_G}{L^2} \right) V_{SD} \tag{7.4.9}$$

with n_0 the carrier concentration without external electric field and C the capacitance of the

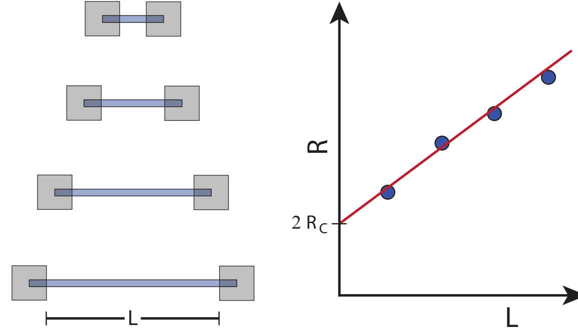

Figure 7.4.9.: *Schematic view of the transmission line method. R indicates the total resistance, R_C the resistance of a contact and L the length considered for the voltage drop (Werner, 2009).*

NWFET. The proportionality factor in this case is the mobility of the carriers and the kind of carriers determine the sign. In principle, this method is capable of determining the mobility in nanowires and identifying the type of majority carriers.

The transconductance is defined as the derivative of the source drain current with respect to gate voltage at a fixed source drain voltage

$$g_m = \frac{\partial I_{SD}}{\partial V_G}|_{V_{SD}=const} = \frac{\partial}{\partial V_G}\left[\mu\left(\frac{en_0 + CV_G}{L^2}\right)V_{SD}\right]_{V_{SD}=const} \tag{7.4.10}$$

$$\Rightarrow \mu = \frac{g_m L^2}{CV_{SD}} \tag{7.4.11}$$

The only unknown in this equation is the capacitance C of the NWFET.

All contacted nanowires are on a highly p-doped silicon substrate with 500 nm thick thermal oxide. The highly conductive p-type silicon can be used as a back gate, as illustrated in figure 7.4.10 b). Under the assumption of an infinitely long metallic nanowire, the capacitance for an embedded nanowire is given according to Wunnicke (2006) by

$$\frac{C}{L} = \frac{2\pi\varepsilon_0\varepsilon_r}{\text{arcosh}\left(\frac{R+h}{R}\right)} \tag{7.4.12}$$

with R the nanowire diameter, h the thickness of the the dielectric under the nanowire, i.e. oxide, ε_0 the vacuum permittivity and ε_r the relative permittivity. The assumption of a metallic nanowire is reasonable for a degenerate semiconductor with an estimated average carrier concentration $\geq 10^{18}$ cm^{-3}. If the wire is not embedded in the dielectric, the electric field is changed and therefore the capacitance. Figure 7.4.10 shows this difference. If the difference in the relative permittivity of the two media is low, as in the case of air and silicon dioxide, the use of an effective permittivity of $\varepsilon_r \approx 2.2$ is a good approximation (Wunnicke, 2006). This lowers the capacity of the NWFET by a factor of about 2 compared to an embedded one.

The wire is not infinitely long, so the influence of the contacts (which are approximately at 0 potential) must be taken into account. This problem was numerically treated by Khanal & Wu (2007) for an oxide thickness of 50 nm. Their 3D simulation of the electric field, figure 7.4.10 d), shows that this influence is not negligible for aspect ratios of the wire smaller than 100. The influence of the contacts can reduce the capacitance by a factor of up to 6. This means, that the contact geometry must be taken into account in order to reliably evaluate the transconductance measurements. For this purpose the capacitance of each NWFET must be modeled by solving the 3D Possion's equation numerically. But even this adjustment would neglect the fact that nanowires have a degenerate shell

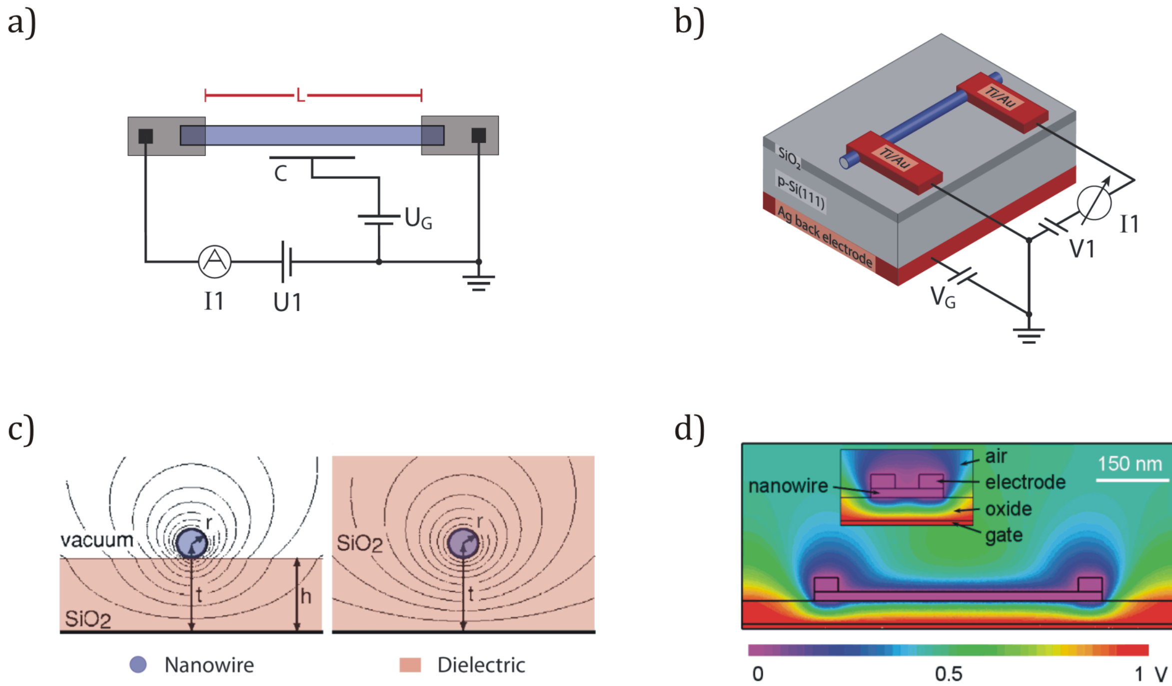

Figure 7.4.10.: *a) and b) schematic view of nanowire-FET measurements (Werner, 2009). c) Comparison of electric field between embedded and non-embedded nanowires (Wunnicke, 2006). d) Simulated electric field taking the influence of the contacts into account (Khanal & Wu, 2007).*

and an almost intrinsic or intrinsic core because NWFET mobility measurements always average over the complete nanowire. Due to this fact, it is only possible to extract the type of the majority carriers at this point. The conductance of the nanowires is reduced, when positive voltage is applied. This prooves that the majority carriers in InN nanowires are electrons. For further details on these measurements, see Limbach (2008) and Werner (2009).

7.4.4. Measurements

7.4.4.1. Measurement setups

All measurements at room temperature were performed in a Suss Microsystems Probe Station PM5 using an Agilent Technologies 4155C Parameter Analyzer and simple capacitors of 10 nF connected from the contact needles to the ground in order to protect the wire from high frequency signals.

The temperature-depend measurements were carried out in a Janis Research STVP-300T-MOD continuous flow He-cryostat using the filter unit described in section 7.4.2 in combination with a Keitley 2400 sourcemeter and two Keithley 2000/2010 multimeters. The combination of the filter unit and the Keithley source-and multimeters is also recommended for future measurements using the Suss Microsystems Probe Station.

7.4.4.2. Contact resistance

Ti/Au with thicknesses of 10 nm and 40-90 nm, respectively, were chosen to contact the nanowires, because all III-N without intentional doping are n-type and it is known that Ti/Au contacts form Ohmic contacts to n-type III-N. For the analysis of electrical measurements, knowledge about the kind of contact as well as the absolute values of resistance is essential. Figure 7.4.11 shows the log-

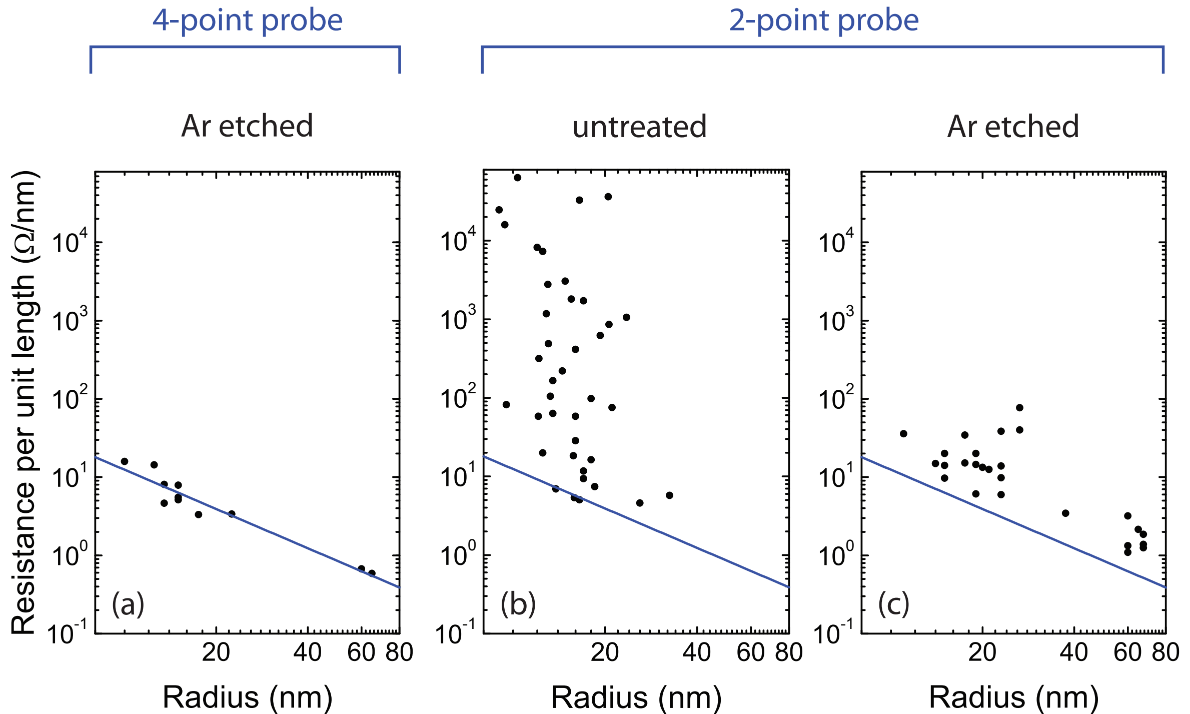

Figure 7.4.11.: *Resistance normalized to length as function of nanowire diameter. a) 4-point probe measurements with Ar sputtering, b) 2-point probe measurements with Ar sputtering and b) 2-point-probe without Ar sputtering (Werner, 2009).*

log plot of the measured normalized resistances R/L versus wire radius. The double logarithmic plot is suitable to test if there is a $R/L \propto r^{\beta}$ relation according to the 3D and 2D conduction model.

Without Ar sputtering prior to the deposition of the contact material, the observed normalized resistance varies by more than three orders of magnitude. This is probably due to the surface oxide of the nanowires. If Ar sputtering is used, this variation is reduced to almost one order of magnitude. The recorded resistances still do not show a clear $R/L \propto r^{\beta}$ dependence. But the resistances, including the contact resistances, are much lower than the internal resistance of the voltage measuring unit. This allows one to make reliable measurements in 4-point probe geometry. Using this geometry, the normalized resistance shows a clear $R/L \propto r^{\beta}$ dependence. This indicates that such a relation exits. Using this relation, it is possible to estimate the value of the contact resistances. The blue lines in figure 7.4.11 show this relation. Three wires with non-sputtered contacts show a very low contact resistance but the others vary about an order of magnitude. This behavior is typical for contacts with a tunnel barrier of varying thickness. This supports the model of an InN nanowire with a oxidized shell. The strong variation indicates in this case that oxide is not homogeneous. The thickness of tunnel barrier can be estimated to about 0-3 nm. But it should be noted, that possible residuals of the resists can also contribute to the barrier thickness.

The sputtered contacts show an Ohmic behavior in the range of $\pm$ 100-150 mV, figure 7.4.12 a). At higher voltages, the behavior becomes slightly non-ohmic because the voltage increases more than linear. The increase in resistance is 2.5%. This is ascribed to ohmic heating, which increases the phonon scattering, because at higher voltages, the wires typically decompose.

As already mentioned, the normalized resistances of wires with sputtered contacts vary by more than one order of magnitude. Using a wire with four contacts, it is possible to perform 4-point probe

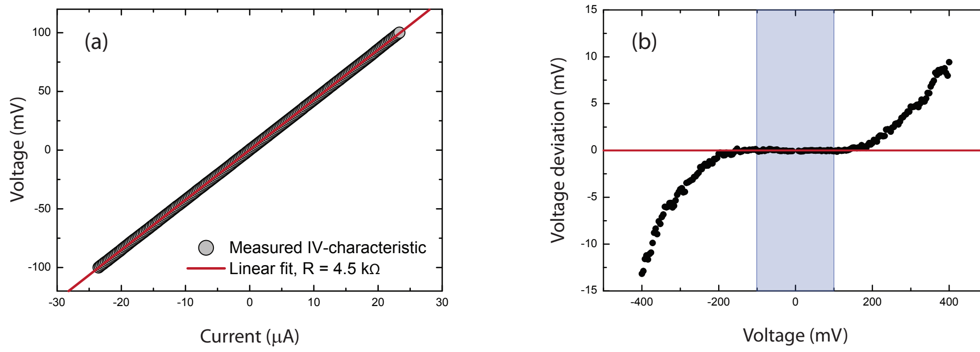

Figure 7.4.12.: *a) Ohmic I-V characteristic of a nanowire contacted with Ti/Au electrodes (-100 mV to 100 mV), b) deviation from ohmic behavior (-400 mV to 400 mV) (Werner, 2009).*

measurements and the transmission line method on one wire. The 4-point probe geometry can be used to determine the normalized resistance of the wire. In the case of the wire shown in figure 7.4.13 with a diameter of 30 nm, the normalized resistance is 5.1 Ω/nm. With this knowledge, 2-point probe measurements in all 6 possible arrangements allow one to calculate each contact resistance. This value increases from one side to the other: 130, 370, 590, 4500 Ω. The differences are assigned to variation in oxide thickness. Furthermore, this measurement enables the comparison of the results for the normalized resistivity obtained by the transmission line method and the one gained by 4-point probe measurements. A normalized resistance of 7.6 Ω/nm is deduced, if the results of all 6 2-point probe measurements are included. Using all measurements gained without using the high resistance contact 1, a value 5.1 Ω/nm is obtained. This is close to the value of the 4-point probe measurement, but still 20% higher. This reveals that only 4-point probe measurements are suitable to obtain reliable results for the resistance of InN nanowires. See also Limbach (2008), Werner (2009) and Werner *et al.* (2009).

7.4.4.3. Influence of the radius on conductivity

To investigate the electrical conductivity of InN nanowires, 10 of them were contacted in 4-point-probe geometry. As stated in section 7.4.3, two contributions with different r dependence are expected to contribute to the normalized conductance g_m under the assumption of a sheet conductivity for the shell contribution:

$$g_m = \frac{R}{L} = \frac{\pi}{\rho_{3D}} r^2 + \frac{2\pi}{\rho_{2D}} r \tag{7.4.13}$$

Plotting the double logarithm of g_m versus the nanowire radius r to determine the r dependence and the exponent β

$$g \propto r^{\beta} \tag{7.4.14}$$

allows an estimate of the contribution by the two expected channels, as shown in the inset in figure 7.4.14 a). According to this, β was found to be 1.6± 0.2. A value of 1 for β would be expected for pure shell conductivity and a value of 2 for pure bulk core conductivity (equation 7.4.13). Therefore, β = 1.6 ±0.2 indicates contributions from both channels, which proves the existence of a surface electron accumulation layer. However, the influence of the accumulation layer is less pronounced than reported by Chang *et al.* (2005) and Richter *et al.* (2008). It has to be regarded that the β exponent will increase for larger diameters since the relative contribution of the bulk will increase.

More quantitative information was gained by plotting the normalized conductance $g_m = R/L$ versus the nanowire radius (see figure 7.4.14 a)). From the results, the variables in equation 7.4.13 were

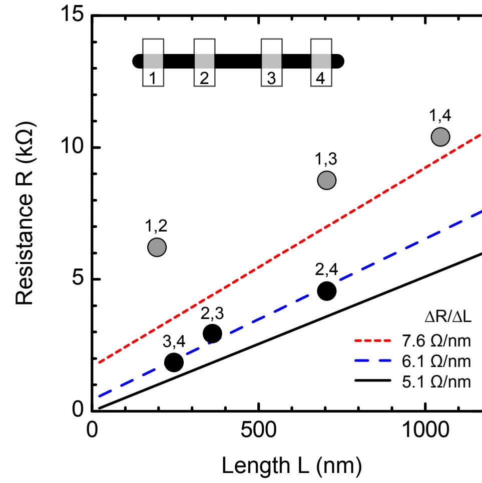

Figure 7.4.13.: *Resistances measured on a single wire with four contacts in the six different combinations of 2-point probe measurements as a function of length for the voltage drop. The red dotted line shows a linear fit to extract the contact resistance and the resistance of the wire regarding all combinations. The dashed blue line shows the linear fit if the contact with the highest resistance (contact 1) is neglected. The black straight line shows the resistance as function of wire length obtained from 4-point probe measurements (Werner* et al.*, 2009).*

determined to be $\rho_{3D} = (1.1 \pm 0.2) \times 10^{-3}$ Ωcm for the bulk resistivity and $\rho_{2D} = (820 \pm 150)$ Ω for the sheet resistivity of the surface accumulation layer. This bulk resistivity is one order higher compared to a detailed study of the conductance of layers perpendicular to the (0001) direction separating surface and bulk contribution (Fehlberg *et al.*, 2006). This difference can be mainly assigned to a difference in the electron concentration, which was as low as 1.5×10^{17} cm^{-3}, since such a large anisotropy for the conductance for different crystal directions is not expected. Assuming the same mobility, an average electron concentration of about 10^{18} cm^{-3} in the core channel was deduced. Previous studies from Chang *et al.* (2005) and Richter *et al.* (2008) neglected the surface conductivity and obtained a conductivity of $\approx 4 \times 10^{-4}$ Ωcm, which is in agreement with the result of this study where the average conductivity was $(4.6 \pm 0.8) \times 10^{-4}$ Ωcm.

These measurements reveal that the contribution of bulk and surface are equal at a diameter of (55 ± 15) nm and furthermore, that the contributions do not differ by more than an order of magnitude for the whole range of investigated diameters from 15 to 200 nm. In addition, the resistance anomaly of decreasing resistance with decreasing diameter below critical value as observed by Chang *et al.* (2005) could not be confirmed.

The other option to separate bulk and surface influence is, as mentioned in section 7.4.3, to assume a tube with certain thickness around a cylindrical core, resulting in the following r and d_{tube} dependence:

$$g = \frac{\pi}{\rho_{3D}} (r - d_{tube})^2 + \frac{\pi}{\rho_{2D^*}} \left(r^2 - (r - d_{tube})^2 \right) \tag{7.4.15}$$

This equation accounts for more details in the physical reality. But its additional free parameter, the thickness d_{tube}, is hard determine. Furthermore, there is no clear transition between the shell with its high electron concentration and the core with a lower one. From the simulations of the electron distribution, a value (4 ± 1) nm seems reasonable (compare Segura-Ruiz (2009)). Then, the bulk

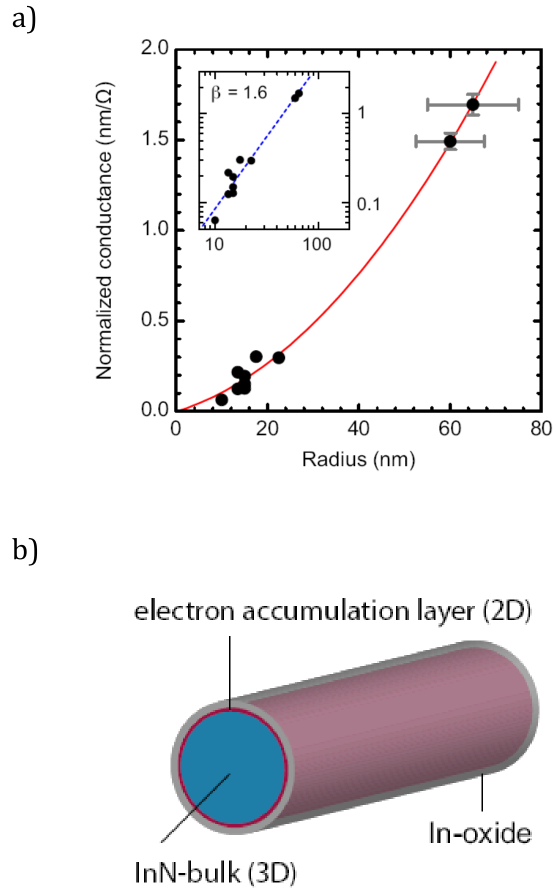

Figure 7.4.14.: *a) Normalized conductance g as a function of the nanowire radius r, obtained by 4-point measurements on 10 nanowires of different aspect ratios. The error bars of the thin wires are of the order of the symbol size and have not been plotted for clarity. The red line shows a parabola fitted to the data points to determine the resistivities of bulk and surface. The inset shows the same data points in logarithmic scale. The blue dashed line shows a power law fit to determine the β exponent 1.6 $\pm$ 0.2 in the relation $g \propto r^{\beta}$. b) Schematic view of the InN nanowire with an InN core, a In-oxide shell and a electron accumulation layer formed at the interface according to the electrical and photoemission measurements (Werner* et al., *2009).*

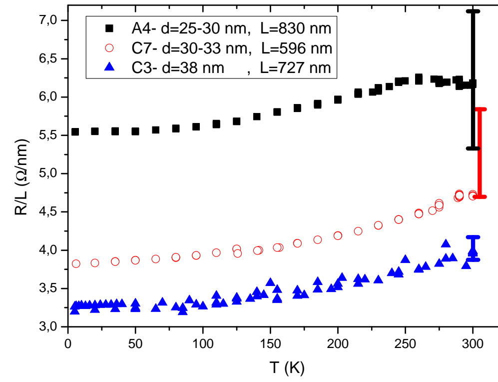

Figure 7.4.15.: *Normalized resistance R/L measured in 2-point probe configuration as a function of temperature. The bars at 300 K indicate the resistance calculated from size using $\rho_{3D} = 1.1 \times 10^{-3}\ \Omega cm$ and $\rho_{2D} = 820\ \Omega$.*

resistivity of the core is calculated to be $\rho_{3\text{D}} = (1.3 \pm 0.2) \times 10^{-3}\ \Omega cm$ and the resistivity of the shell to be $\rho_{2D^*} = (0.22 \pm 0.04) \times 10^{-3}\ \Omega cm$. This calculated ρ_{2D^*} is in agreement with the value $0.2 \times 10^{-3}\ \Omega cm$ for the electron accumulation layer formed at N-face layers according to Fehlberg *et al.* (2008). (Compare Werner *et al.* (2009) and Werner (2009)).

7.4.4.4. Temperature dependence

The wire consisted of a highly degenerate shell and a slightly degenerate core. PL and PLE measurements indicated, that this generally did not change at low temperatures. The peak energy and FWHM as function of temperature in figure 7.5.7 b) revealed that the carrier concentration increased with increasing temperature, but still indicated degeneracy, at least in the optical active region.

Recently, the experimental difficulties hindering temperature-dependent electrical measurements have been overcome by the measures described in section 7.4.2 and 3 wires were successfully measured in 2-point probe configuration. By comparing their resistance at room temperature with the range of resistances, that were calculated from the their length and diameter according to the previous section taking the uncertainty of size into account, it is found, that two are at the lower limit of this range, whereas the third in the middle of this range. Therefore, it can be concluded, that the contact resistances were low.

A decrease of resistance with decreasing temperature was observed for all samples. The overall change in resistance was 400-600 Ω. The resistance of the conductive path to wire should be lower than 50 Ω. Therefore, this metal-like behavior can ascribed to the wire under the assumption of negligible change in contact resistance. It can be seen in figure 7.4.15 that the normalized resistance changed for all wires in a similar way, but different from the behavior of layers. The absolute change is about 0.7-0.9 Ω/nm and relative change between 11 and 19%. For further analysis of these measurements, information about the carrier concentration inside the core and the shell would be needed, as well as a confirmation that the influence of change in contact resistance is negligible.

7.4.5. Conclusion

2- and 4-point probe electrical measurements on single InN nanowires contacted by e-beam lithography were carried out. Directly deposited contacts showed a strong variation in resistance up to several $G\Omega$, which indicated variation in the surface oxide thickness. The absolute value of the contact resistance as well as its variation was significantly reduced by Ar-sputtering prior to the deposition of the

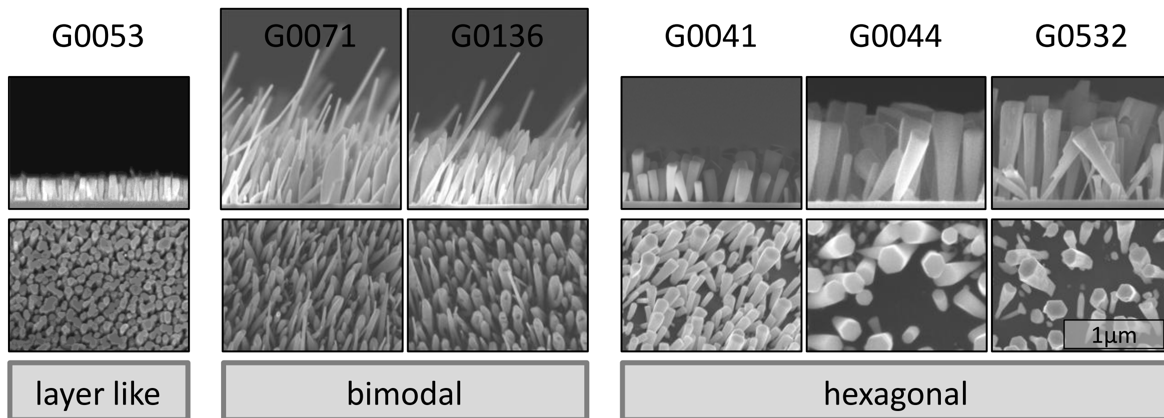

Figure 7.5.1.: *SEM images of the samples used for optical characterization sorted by morphology.*

contacts. A combination of 2- and 4-point probe measurements performed on single wires revealed, that only 4-point probe measurements were suitable to gain reliable information on the conductivity. NWFET measurements confirmed, that electrons were the majority carriers in InN nanowires. 4-point probe measurements on 10 nanowires with different radius revealed, that the conductance was dominated by two contributions originating from bulk and a surface accumulation layer. The bulk resistivity was found to be $\rho_{3D} = (1.1 \pm 0.2) \times 10^{-3}$ Ωcm, whereas the surface layer had a sheet resistivity of (820 ± 150) Ω. This implies that for a diameter of (55 ± 15) nm, the surface and bulk contributions were equal. This in combination with the observation of the surface oxide by XPS and TEM lead to the assumption that the surface accumulation layer was formed at the interface of the InN core and the oxide shell, as illustrated in figure 7.4.14 b).

7.5. Optical characterization of InN nanocolumns

In the previous section, the resistivity of the InN nanowires was determined. Hall measurements are typically used to gain more information about the carrier concentration and mobility, but are extremely challenging for nanowires. The analysis of photoluminescence (PL), photoluminescence excitation spectroscopy (PLE) and Raman-spectroscopy measurements allow one to estimate the carrier concentration. Furthermore, the electron distribution has been calculated to model the optical properties. This approach is used to estimate the background doping concentration and the density of surface states. In addition, the nature of the observed optical transition is identified.

The optical characterization in the remaining of this section has been performed within a collaboration with the University of Valencia, Spain, and the Instituto de Fisica, Gleb Wataghin-Unicamp in Campinas, Brasil. The characterization and interpretation was mainly done by J. Segura-Ruiz and his colleagues A. Sanchez-Molina, A. Garcia-Cristobal, M.I. Gomez-Gomez, N. Garro, A. Cantarero and F. Iikawa.

7.5.1. Qualitative evidence of electron accumulation by Raman-spectroscopy

Contrary to InN (0001) layers, InN (0001) nanocolumns showed further peaks in Raman-spectroscopy in backscattering configuration in addition to the allowed E_{2h} and A_1(LO)-modes at 488 cm^{-1} and 586 cm^{-1} (see figure 7.5.2). The high intensity peak centered at 519 cm^{-1} originated from the silicon substrate. Three peaks were ascribed to the A_1(TO) (447 cm^{-1}), E_1(TO) (476 cm^{-1}) and E_1(LO) mode (593 cm^{-1}) of InN. The narrow line width of the E_{2h} mode indicated high crystal quality.

Sample	Morphology	F_{In} (nm/min)	V:III ratio (F_N(sccm), P_N(W))	T_S (°C)	t (min)	d (nm)	h (nm)
G0041	hexagonal	0.27	≈ 31 (1.5, 400)	465	300	100	300
G0044	hexagonal	0.56	17 (1.5, 450)	465	300	100	360
G0053	layer-like	0.56	≈20 (2.0, 500)	392	300	55	230
G0071	bimodal	0.56	≈20 (2.0, 500)	446	300	80	500
G0136	bimodal	0.56	17 (1.5, 450)	446	300	90	470
G0532	hexagonal with defects	0.27	35 (1.5, 450)	465	400	150	900
G0374	layer on sapphire	15.8	0.6 (1.5, 450)	428	60		690

Table 7.5.1.: *Growth conditions, morphologies and average sizes of nanostructures used for optical characterization with F_{In} the In flux, F_N the nitrogen flux, P_N the nitrogen plasma excitation power, T_S the substrate temperature, t the growth time, d the nanowire diameter and h the height of the nanowires.*

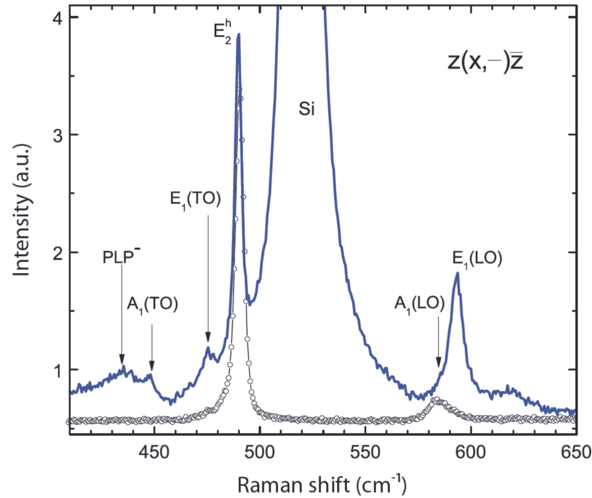

Figure 7.5.2.: *The blue line shows a Raman spectrum of an ensemble of InN nanowires with the frequencies of the phonon modes in comparison to the spectrum a high quality InN epilayer (black circles). The spectra were recorded in backscattering configuration at room temperature (Segura-Ruiz* et al.*, 2009).*

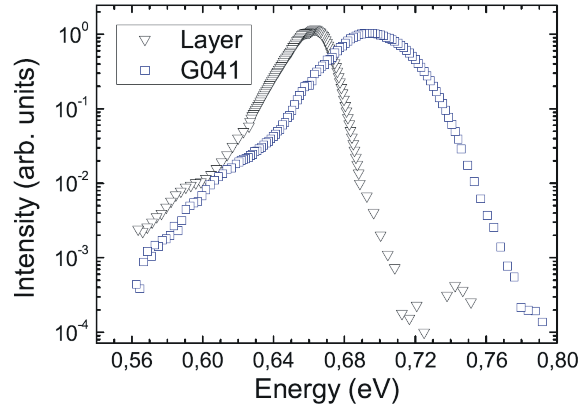

Figure 7.5.3.: *A normalized photoluminescence spectrum of nanowire ensemble (G0041; open squares) in comparison to a InN layer (G0374, open triangles). The spectra were recorded at 7 K and equal excitation conditions (Segura-Ruiz* et al., *2009).*

Their FWHMs were among the lowest reported values. This excluded the possibility that a minor material quality of the InN was responsible for the appearance of the additional modes. In addition, the tilt of the nanocolumns was not sufficient to explain this. Therefore, the additional peaks can only be explained by laser light scattered at the nanocolumns, which illuminated the nanowire lateral sidewalls (Lazić *et al.*, 2007). This conclusion is further supported by the observation that the change in relative intensities correlated with the aspect ratio of the nanowires (Segura-Ruiz, 2009). The position of the E_{2h} mode indicated that the nanowires were strain free ($\leq$0.1%).

Furthermore, an additional broad peak was observed at 435 cm^{-1}. For high quality samples, this peak is assigned to the PLP^{-} mode (Davydov *et al.*, 1999a,b; Chen *et al.*, 2005; Lazić *et al.*, 2007; Pomeroy *et al.*, 2007). The PLP^{-} indicates a high electron concentration and should imply damping of the LO modes. But this was not observed for the studied samples. Therefore, the observed spectra were explained by assuming that the nanowires consisted of two regions with a high and a low electron concentration. Furthermore, the broadening could be explained by a transition region of varying electron concentration, which indicated, that the regions must be inside one wire.

In conclusion, the results of Raman spectroscopy showed that the nanocolumns were strain free and of high crystal quality. Furthermore, the signature of an electron accumulation at the nanowire sidewall and core with a low carrier concentration was found.

See Segura-Ruiz (2009) and Segura-Ruiz *et al.* (2009) for further details.

7.5.2. First quantitative analysis based on Photoluminescence (PL)

The PL characteristics of InN nanowires differed from the characteristics of InN layers. The emission intensity varied by about one order of magnitude, but was in the range of high quality layers (compare to figure 7.5.3) and not reduced as sometimes observed (Shen *et al.*, 2006). The emission spectra were typically characterized by a single peak centered at 0.682-0.72 eV, which was blue-shifted compared to the band gap of InN of 0.67 eV. This blue shift as well as the broadening varied from sample to sample. In general, the smaller the FWHM of the PL peak, the higher the emission intensity.

Figure 7.5.4 shows the change in PL signal with excitation intensity of two representative samples. Generally, the peak broadened and blue shifted with excitation intensity because photoexcitation increased the carrier concentration. This was already sufficient to induce or increase the effect of band filling. Most of the samples showed a single peak, which blue-shifted and broadened with excitation intensity like G0071. This behavior was similar to layers with a carrier concentration of

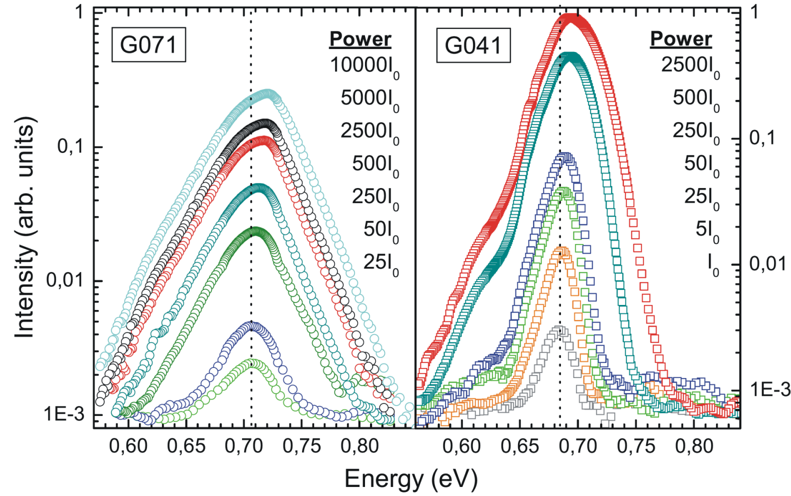

Figure 7.5.4.: *Change in PL spectra for two nanowire samples (left: G0071, right: G0041) with excitation power. The spectra were recorded at 7 K. I_0 corresponds to 14 mW/cm² (Segura-Ruiz, 2009).*

$n_e \geq 10^{18}$cm^{-3} (Klochikhin *et al.*, 2005). Therefore it was assumed that the optical active region in the nanowires had an electron concentration of $n_e \gtrsim 10^{18}$ cm^{-3}. At an excitation intensity of 14 mW/cm², sample G0041 showed a narrow peak with a single contribution at 0.685 eV with a low FWHM of 16 meV. If the excitation intensity was increased above 350 mW/cm², a second contribution arose and was identified as a LO-phonon replica. This replica was typically observed for samples with free carrier concentration in the 10^{17} cm^{-3} range. The comparably low FWHM of the PL peaks from 12 to 39 meV indicated a low doping concentration. 12 meV (G0532) was among the lowest values so far reported for FWHM of InN nanowires, which indicated a low free carrier concentration (Nguyen *et al.*, 2011). Furthermore, no direct relation between surface morphology and emission, and therefore electron concentration was found. This fact, in combination with the observation of oxidation of the nanowire surfaces, implied that the density of surface states was ruled by oxidation of the surface and not as often assumed (Nguyen *et al.*, 2011) by the surface stoichiometry. The sublinear dependence of the emission intensity on excitation intensity indicated a free-to-bound or donor-acceptor transition. Since it is well know that InN contains a lot of free electrons, a transition of free electrons to holes trapped at acceptors can be assumed. In general, the dependence of the characteristics of the PL spectra revealed that PL spectra of InN are only comparable if they are taken under the same excitation intensity. Conversely, the excitation energy has no observable influence, as shown in Segura-Ruiz (2009).

The observed PL and Raman spectra can be qualitatively explained by calculating the electron concentration for InN in the nanowire. Therefore, an analytical solution of the Thomas-Fermi-equation in the parabolic band approximation for layers was used according to Klochikhin *et al.* (2007). Under the assumption of bulk Fermi-level, which is located 10 meV below the conduction band minimum and a electron effective mass of $m_e^* = 0.25\ m_o$, which is much greater than the assumed effective mass of 0.042 m_0 to account for the non-parabolicity, the electron concentration is shown for different surface state densities in 7.5.5 a), with the resulting frequency of the PLP$^-$ mode in 7.5.5 b). The observed electron concentration was inhomogenous within the first nm close to the surface. The electron concentration of up to 10^{20} cm^{-3}, depending on the surface density, decreased by two orders of magnitude in the first 6-10 nm from the surface. Transferred to nanowires, this correlates to an electron rich shell and an low n_e in the nanowire core. According to this model, the position of the PLP$^-$ peaks implies according to this model an electron concentration of about 1×10^{19} cm^{-3} close

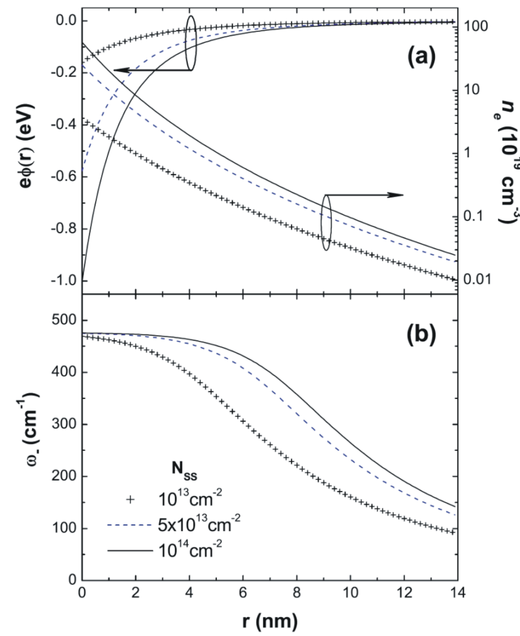

Figure 7.5.5.: *a) Calculated downward bending of the conduction-band minimum (left axis) and the corresponding electron distribution (right axis) with distance r from the nanowire surface for surface charge densities from 10^{13} to 10^{14} 1/cm². b) Corresponding change in the frequency of the PLP⁻ mode (Segura-Ruiz* et al.*, 2009).*

to the nanowire surface.

Figure 7.5.6 shows the calculated band bending for two different surface charge densities. The nanowire core, region (1), the electron concentration was low and holes tended to accumulate there due to the band bending. Close to the nanowire surface, a region with a strong band bending was found with a high electron concentration and marked with (2). If holes existed in this region, they would tend to drift immediately in the direction of the nanowire core. In region three, the transition region, holes trapped at acceptor states can exist for longer time due to a weaker electric field. These three regions have different probabilities of electron-hole recombination. Region (1) and (2) have a reduced recombination rate because photogenerated electrons (1) or holes (2) will directly drift out of region due to the strong electric field. The photogenerated holes show a spatial overlap with degenerate electrons only in transition region (3), and therefore this region should be the optically most active.

This band scheme presented in figure 7.5.6 explains the observed PL spectra. The blue shift of the PL emission is a result of the Burstein-Moss-shift taking place in the optically active region. The existence of holes to bound acceptors results in a breakdown of momentum conservation, and therefore all electrons can contribute to the emission. In this case, the maximum intensity of emission energy should be observed between the band gap energy and the absorption edge. According to figure 7.5.6, samples with higher surface state density should have a stronger blue shift and more pronounced broadening, as well as a reduced emission efficiency due to a smaller active region. This is in agreement with the obtained PL results.

The temperature dependence of the PL intensity is shown in figure 7.5.7 a) and can be fitted assuming two quenching mechanisms with scatter rates A and B, as well as activation energies E_1 and E_2 using the following formula according to Daly *et al.* (1995):

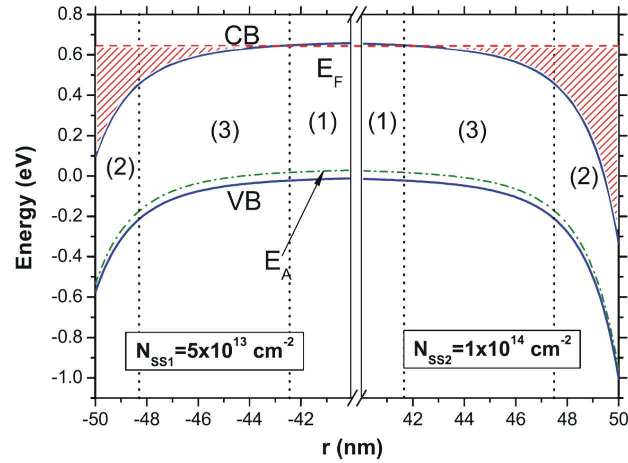

Figure 7.5.6.: *Calculated downward bending of the CBM and VBM in a nanowire with a radius of 50 nm close to its surface. On the left for a surface state density of N_{SS} of 5×10^{13} 1/cm² and on the right for 10^{14} 1/cm². According to the radiative recombination probability of electrons and holes, three different regions are indicated (Segura-Ruiz* et al., *2009).*

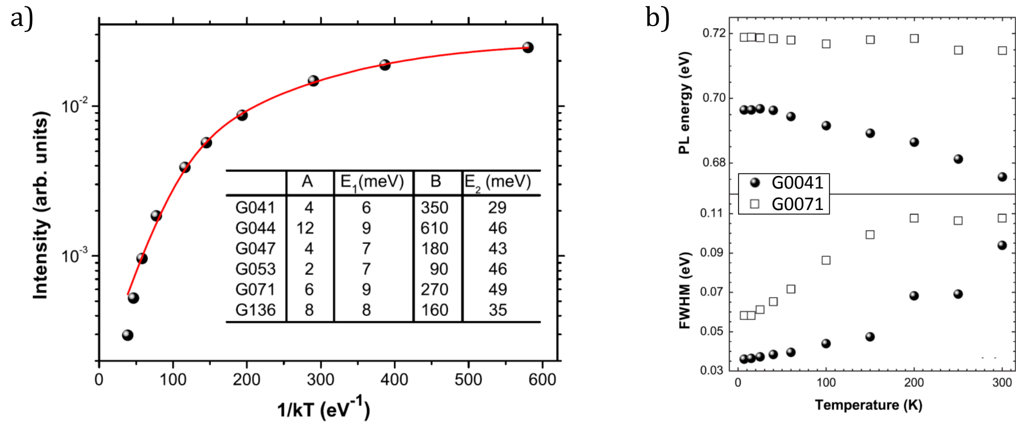

	A	E_1(meV)	B	E_2 (meV)
G041	4	6	350	29
G044	12	9	610	46
G047	4	7	180	43
G053	2	7	90	46
G071	6	9	270	49
G136	8	8	160	35

Figure 7.5.7.: *a) Integrated PL intensity of sample G0136 as a function of temperature in an Arrhenius plot and a fit according to equation 7.5.1 (solid line). The inset shows the values of the main parameters of equation 7.5.1 determined the best fit for several nanowire samples (Segura-Ruiz* et al., *2009). b) Change in energy of maximum emission intensity and FWHM of the PL emission as a function of temperature for two representative samples: G0041 (full circles) and G0071 (open squares). The spectra were recorded with an excitation power of 34.4 W/cm² (Segura-Ruiz* et al., *2009).*

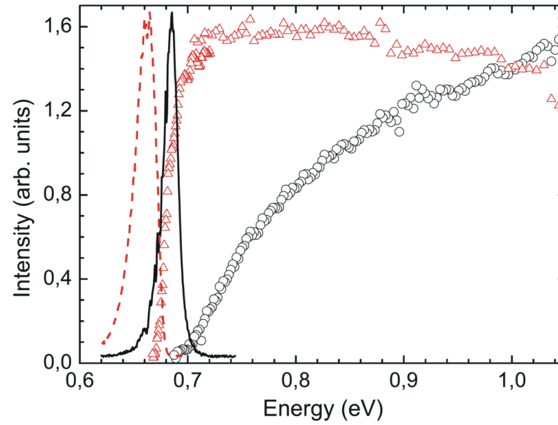

Figure 7.5.8.: *Comparison of PLE and PL spectra of a representative nanocolumns sample (G0041) with a high quality InN layer (G0374) at 7 K. The black solid line and open circles correspond to the PL and PLE spectra of nanowires, respectively, while the red dashed line and open triangles to the PL and PLE of the InN layer (Segura-Ruiz, 2009).*

$$I(T) = \frac{I_0}{1 + A\exp\left(\frac{E_1}{k_B T}\right) + B\exp\left(\frac{E_2}{k_B T}\right)} \quad (7.5.1)$$

The determined parameters are listed in figure 7.5.7 a). The activation energies of $\approx$ 7 meV and $\approx$ 30-50 meV are in good agreement with deep and shallow acceptor states reported by Arnaudov *et al.* (2004); Klochikhin *et al.* (2005). A third quenching mechanism with an activation energy of about 160$\pm$20 meV was found at higher temperatures. According to this, thermal delocalization of holes is responsible for the increase in non-radiative recombination.

The PL peak energy in figure 7.5.7 b) decreases with increasing temperature, but the red shift is significantly less than that of the band gap. This observation, in combination with a significant increase in the FWHM of the signal, originates from the fact that according to the above presented model, the photogenerated holes spread over a wider region and penetrate deeper into the region of higher free electron concentration at higher temperatures. Therefore, more recombination takes place in a region with higher electron concentration and results in the observation that the band filling effect partially compensates for the red shift of the band gap.

The results and conclusions of this section are described in more detail in Segura-Ruiz (2009) and Segura-Ruiz *et al.* (2009).

7.5.3. Quantitative analysis based on photoluminescence excitation spectroscopy (PLE)

PL and Raman spectroscopy sketched the first quantitative images of the carrier distribution inside the nanowires. Absorption experiments can be used to gain more information for samples on transparent substrates. In this case, photoluminescence excitation spectroscopy is used to obtain the absorption characteristics of the samples. In PLE experiments, the excitation and detection energies can be continuously scanned. PLE spectra are similar to absorption spectra within certain limits if the detection energy is fixed at an energy at which the sample emits light under excitation. This is limited if non-radiative recombination channels are involved, which is the case for InN when the detection energy is above 0.9 eV.

While InN layers showed no difference between absorption and emission peak energies, InN

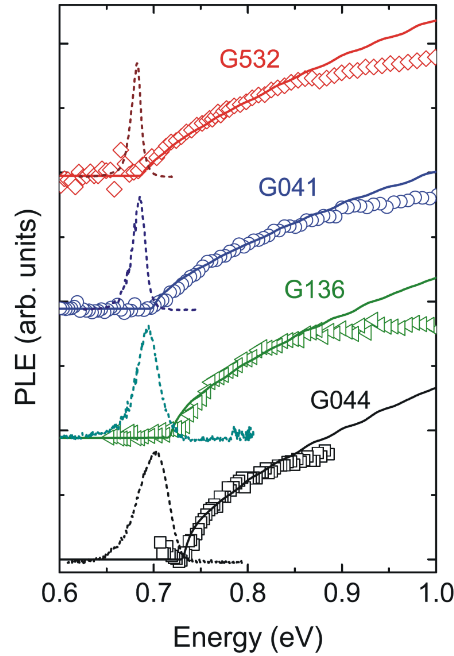

Figure 7.5.9.: *PL and PLE spectra of 4 different nanowire samples. (Dashed lines: PL; open symbols: PLE). The PLE spectra were detected at the PL peak energy of the different InN nanowire samples. Spectra are shifted along the vertical axis. The solid lines show the calculated absorption spectra with the best agreement with the experimental spectra (Segura-Ruiz, 2009).*

nanocolumns showed a clear blue shift (Stokes-Shift) of the absorption energy due to band-filling (see figure 7.5.8). Furthermore, layers showed a sharp rise of adsorption, whereas InN nanocolumns showed smooth and continuous rise.

The broadening of PL peaks in nanostructures is often associated with inhomogeneous size distribution. In this case, variation in the excitation energy would selectively excite certain nanostructures, leading to a narrowing of the PL peak. This not the case in the 0.72-1.03 eV range of excitation energy. Therefore, the line widths of the PL peaks correspond to their natural line width, i.e. homogeneous broadening.

The PLE spectra of the nanocolumns show a 45 meV variation in the absorption edge, as well as a difference in the slope of the PLE signal (see figures 7.5.9 and 7.5.10). Again, there was no correlation to the size of the nanostructures observed.

The PLE spectra were simulated based on the calculation of electron distribution within the nanowire. For this purpose, self-consistant solutions of the Schrödinger-Poisson equation system were numerically solved for an electron effective mass of $m_e^* = 0.07\ m_0$ and nanowire radius R , surface state density N_{SS} and doping concentration N_D as free parameters. For further details on these simulations, see Segura-Ruiz *et al.* (2010) or Segura-Ruiz (2009). Even if the value of the effective electron mass is not the assumed 0.042 m_0, the general result should not be affected. The calculation shows that the influence of size is almost negligible for nanowires with r $\geq$ 40 nm, which is typically the case for most of the nanowires. Therefore the PLE signal was simulated for different N_{SS} and N_D for a nanowire radius of 40 nm, as shown in figure 7.5.11. It was found, that the doping concentration N_D was correlated with the blue shift of the adsorption edge, while the surface state density N_{SS} was correlated with the slope of the PLE signal. By fitting the PLE spectra, it is now possible to determine N_{SS} and N_D independently. The results are shown in table 7.5.2, whereas the resulting fits are shown in figure 7.5.9. The exact values determined by this method are questionable because

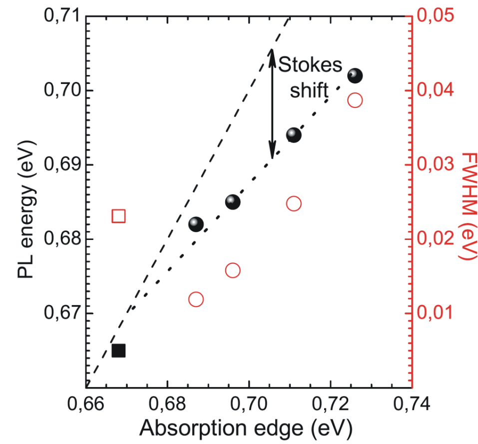

Figure 7.5.10.: *Energy (left axis - solid symbols) and FWHM (right axis - open symbols) of the PL peaks as function of the absorption edge for all studied samples. Circles represent samples with nanocolumns and squares correspond a layer sample. The deviation of the emission energy (indicated with a dotted line as visual guide) from the absorption edge energy (dashed line) corresponds to the Stokes shift (Segura-Ruiz, 2009).*

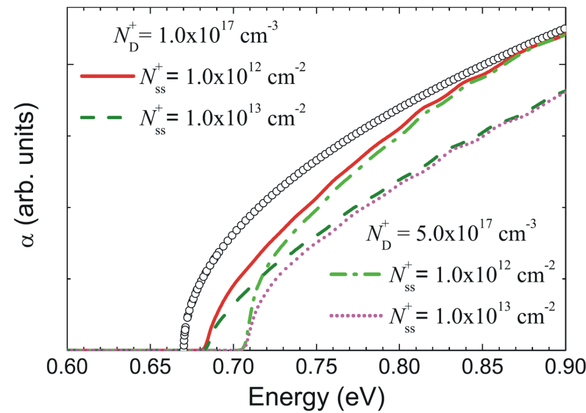

Figure 7.5.11.: *Calculated absorption spectra for InN. The open circles show the $E^{1/2}$ ideal dependence of the absorption for intrinsic bulk material. The other absorption spectra are calculated for a nanowire of 40 nm radius for two donor concentrations (N_D= 1.0$\times 10^{17}$ and 5.0 $\times 10^{17}$ cm^{-3}), and two densities of surface states (N_{SS}= 1.0$\times 10^{12}$ and 1.0$\times 10^{13}$ cm^{-2}) (Segura-Ruiz* et al., *2010).*

Sample	N_D (cm^{-3})	N_{SS} (cm^{-2})	N_D (cm^{-3})	N_{SS} (cm^{-2})
	r = 40 nm		r = 50 nm	
G0532	0.8×10^{17}	2.5×10^{13}	3.5×10^{17}	2.2×10^{13}
G0041	2.0×10^{17}	2.4×10^{13}	7.5×10^{17}	2.0×10^{13}
G0136	5.0×10^{17}	1.7×10^{13}	1.0×10^{18}	1.5×10^{13}
G0044	7.5×10^{17}	1.4×10^{13}	1.8×10^{18}	1.1×10^{13}

Table 7.5.2.: *Combinations of donor concentration N_D and density of surface states N_{SS} that provided the best agreement between experimental and theoretical spectra, assuming a nanowire radius of 40 nm and 50 nm (values for r = 40 nm from Segura-Ruiz* et al. *(2010) and r = 50 nm from Segura-Ruiz (2009)).*

of the sensitivity to wire diameter and assumed effective mass of 0.07 m_0. However, the observed trends as well as the range of electron concentration are trustworthy. The doping concentration was in the range of $3.5\times10^{17}-1.8\times10^{18}$ cm^{-3}. These comparably low values are similar to what is observed in high quality layers. It seems that the samples grown with a higher V:III ratio of $\approx$ 30 (G0532, G0041) had a lower doping concentration, but a higher surface state density N_{SS} of about 2×10^{13} cm^{-2}. In contrast, the samples grown with a lower V:III ratio of about $\approx$ 20 (G0136, G0044) showed a higher residual doping of 1-2$\times10^{18}$ cm^{-3}, but a lower surface state density of 1-1.5$\times10^{13}$ cm^{-2}. This indicates that the higher V:III ratio lowered the incorporation probability of the donors.

See Segura-Ruiz (2009) and Segura-Ruiz *et al.* (2010) for further details.

7.5.4. Conclusion

The position and FWHM of the E_{2H} peak in the Raman spectrum confirmed the high crystal quality of the InN nanowires observed with TEM imaging. The PL, Raman- and photoluminescence excitation-spectroscopy revealed a clear inhomogeneous electron distribution. The observed spectra are explained by calculating the electron distribution inside the nanowire under the assumption of a surface electron accumulation layer induced by donor-like surface states. According to this model, the donor concentration is in the range of $3.5\times10^{17}-2\times10^{18}$ cm^{-3} and surface state density in the range of 1-2$\times10^{13}$ cm^{-2}.

7.6. Discussion

The measurement of resistivity and estimation of electron concentration opens the possibility to estimate the charge carrier mobility using the following equation:

$$\mu_e = \frac{1}{n_e e \rho} \tag{7.6.1}$$

According to the electrical measurements, the surface sheet resistivity was (820 ± 150) Ω and the surface state density was estimated to be $10^{13}-10^{14}$cm^{-2} from PLE measurements. This would result in a mobility of 760-76 cm²/(Vs). This range includes the value of 500 cm²/(Vs) obtained for electron accumulation layers in layers (Fehlberg *et al.*, 2006). For the case that the thickness of the accumulation layer is taken into account, figure 7.6.1 shows the resulting carrier mobilities as a function of carrier concentration for the bulk and surface channels assuming an accumulation layer thickness of 4$\pm$1 nm. Assuming a surface state density of 1-2$\times10^{13}$cm^{-2} and a bulk electron density of 1-2$\times10^{8}$ cm^{-3} according to section 7.5.3 for nanowires grown under similar conditions, the electron density can be estimated to be about 5×10^{19} cm^{-3} for the surface accumulation layer

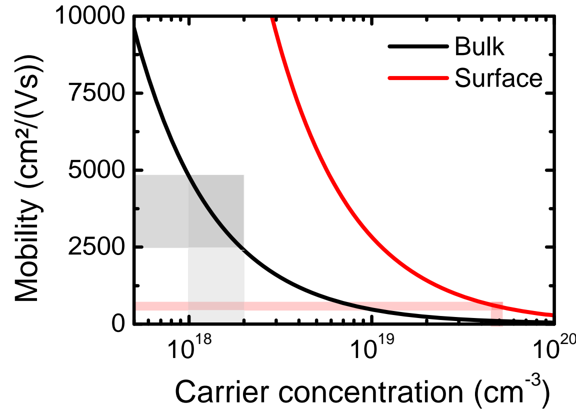

Figure 7.6.1.: *Carrier mobility as a function of carrier concentration for the bulk (core, $\rho_{3D} = (1.3 \pm 0.2) \times 10^{-3}$ Ωcm) and surface (shell, $\rho_{2D^*} = (0.22 \pm 0.04) \times 10^{-3}$ Ωcm) conduction channels assuming of an accumulation layer thickness of 4±1 nm.*

and to $\approx 1-2\times 10^{18}$ cm^{-3} for the a bulk electron concentration. These estimates were obtained by calculating of the electron distributions shown in Segura-Ruiz (2009). Under this assumption, the mobility would be in the range of 2400-4800 cm/(Vs) in the core and about 600 cm/(Vs) in the shell. These values are comparable to the values reported in literature for high quality layers. The bulk value is among the highest reported to-date.

The mobility determined by FET measurements was ≤ 100 cm²/(Vs). However, the influence of the contacts was neglected and can easily lead to an underestimation of the mobility by a factor of 6. It should be noted that the charge of the surface accumulation layer screens the electric field in NWFET measurements. This means that the majority of the probed electrons were close to the surface. Therefore, a re-evaluation of the NWFET measurements with simulation of the electric field, while taking the contacts into account, is favorable.

7.7. Conclusion

TEM and Raman spectroscopy confirmed the high crystal quality expected for nanowires. Measurements of chemical properties by XPS and STEM-EELS showed an In_2O_3 surface oxide formed at InN nanowires with a thickness about 1 nm or less. The strong variation in contact resistances further indicated that the thickness varied from wire to wire and also within single wires.

Concerning electrical properties, NWFET measurements proved that electrons were the majority carriers in InN nanowires. The existence of a surface accumulation layer was confirmed by the normalized resistance-diameter $R/L \propto r^{\beta}$ relation with $\beta = 1.6 \pm 0.2$, which was between the value expected for pure bulk conductivity $\beta = 2$ and pure surface sheet conductivity $\beta = 1$. Since the standard method of Hall measurements to determine the concentration and mobility of the charge carriers is challenging for nanowires, optical methods were used instead to determine the carrier concentration. Raman spectroscopy confirmed the existence of regions with a high and a low electron concentrations by the coexistence of the PLP$^-$ and LO-modes. A detailed analysis of PL and PLE results in combination with the calculation of the electron distribution, allowed us to estimate the donor concentration as well as the surface state density independently, which were in the range of $3.5\times10^{17} - 2\times 10^{18}$ cm^{-3} and 1-2$\times10^{13}$ cm^{-2}, respectively. A higher V:III ratio seems to lead to lower doping concentrations. The resulting carrier concentration opened the possibility to estimate the mobility inside the wire core to be in the range of 2400-4800 cm/(Vs) and about 600 cm/(Vs) in

the electron accumulation layer. This is in agreement with the reported mobilities for such carrier concentrations in layers, which indicates that all performed measurements and analysis are consistent with other reports on the mobility of InN.

The observation of a surface electron accumulation layer in combination with a surface oxide, suggests that donor-like states at the InN/InO interface induced a downward band-bending, since neither theoretical calculations predicted nor measurements on clean non-polar surfaces observed such band-bending. In conclusion, after exposure to air, the nanowires consist of an InN core with about an 1 nm or less thin indium oxide shell. It is suggested that donor-like states at the InN/InO interface induce the downward band-bending. The properties of these nanowires are then controlled by the density of induced donor-states at the indium oxide and nitride interface as well as the residual doping concentration of the core.

The core of the InN nanowires was characterized by a low carrier concentration in the range of of $3.5\times10^{17} - 2\times10^{18}$ cm^{-3} and a high electron mobility of about 2400-4800 cm/(Vs). This is comparable to the lowest observed carrier concentrations and highest mobilities reported for InN layers. Due to the low density of states in the conduction band, InN is already degenerated at this low carrier concentration. The influence of the surface accumulation of electrons on the electrical and optical properties was analyzed in detail and shown to have significant impact. Since this surface electron accumulation layer is probably not intrinsic for InN, it should be avoidable by a proper surface treatment.

8. InGaN nanocolumns

For most applications in LEDs and solar cells, the band of InN is too small and must be increased by replacing a fraction of the In atoms by Ga atoms. The resulting alloy $In_{1-x}Ga_xN$ is only thermodynamically stable at high temperatures, which would require an extremely high nitrogen vapor pressure to prevent decomposition of the material. For strained material the miscibility becomes higher, but the film thickness is limited in this case. If the material is grown in the standard growth direction, the c-direction, electrons and holes are spatially separated due to internal electric fields originating from its polar character. This is one of the main effects which significantly lower the efficiency of green LEDs (Schwarz & Scholz, 2011). Thus, there is high research activity on growth in the non-polar or semi-polar directions (ICNS, 2011).

Growth at low temperatures enables the synthesis of thermodynamically unstable alloy compositions. In this case, relaxation to thermodynamic equilibrium is kinetically hindered. However, this usually lowers the crystal quality drastically. Concerning this problem it is interesting that nanowires generally have a comparably high crystal quality and facilitate the growth of lattice mismatched heterostructures with a low concentration of defects due to their high surface-to-volume ratio and small diameter. Kikuchi *et al.* (2004) and Kishino *et al.* (2007) have previously demonstrated the successful growth of green, red and blue multiple-quantum-well InGaN-GaN LEDs by MBE. This indicates that MBE should be a suitable method for the growth of InGaN over the full compositional range.

The growth of $In_{1-x}Ga_xN$ nanowires over the full compositional range was demonstrated by Kuykendall *et al.* (2007) using Halide-CVD. But the In-rich material grown by this method showed a strong band filling effect, which indicates high unintentional doping. Previous, studies on MBE-growth of InGaN wires (Calleja *et al.* (2007), Vajpeyi *et al.* (2009), Wu *et al.* (2009), Goodman *et al.* (2011) and Limbach *et al.* (2011)) focused on the Ga-rich part of this alloy and the maximum observed In mole fractions is about 35%. To-date, MBE-growth of In-rich InGaN nanowires has been nearly unexplored and is therefore the focus of this study.

First, a set of samples was grown on Si(111) substrates with 60% Ga in the supplied metal to test whether phase separation occurred in the temperature range of 400-500°C. This range includes the typical growth temperatures for InN nanowires, which are limited to about 450°C. Three series with 7%, 13% and 26% Ga in the supplied metal were grown within the same temperature range to analyze morphology and composition, which were probed by X-ray diffraction (XRD) and photoluminescence (PL). In these three series, the observed Ga mole fraction in the nanowires was significantly lower than in the metal supply, which can be explained by a simple model of diffusion-induced growth.

8.1. Experimental conditions

Silicon substrates were chosen due to the property that an amorphous top-layer forms and therefore the nanowires are expected to be strain free. Therefore, no specific Ga concentration should be favored by a lower lattice mismatch. Prior to growth the sample was heated to about 850°C to remove the native oxide. The resulting 7×7 reconstruction was used as an indicator for an oxygen free surface. The growth conditions were similar to the ones of InN nanowires. The metal supply for In-rich samples was $1.7\text{-}1.8\times10^{15}$ $cm^{-2}min^{-1}$. This corresponded to about 0.55 nm/min, if all metal would form a compact III-N layer. The growth time for all samples was 200 min. Therefore, the overall amount of supplied metal corresponded to a 110 nm thick III-N layer. The Ga concentration in the supply x_{supply} was calculated by

$$x_{supply} = \frac{F_{Ga}}{F_{In} + F_{Ga}} \tag{8.1.1}$$

with F_{Ga} the Ga and F_{In} the In flux in atoms per area per time.

The conditions for the N-source were a nitrogen flux of $F_N = 1.5$ sccm and a plasma excitation power of $P_N = 450$ W. This corresponded to a III-N growth rate at stoichiometry of about 9.5 nm/min. The resulting V:III ratio was about 17 for the metal flux used for nanowire growth. Due to technical reasons, the nitrogen conditions were changed for the samples with 60% Ga of the metal supply to $F_N = 1.0$ sccm and $P_N = 400$ W, which corresponded to a growth rate at stoichiometry of about 6.3 nm/min. To maintain an equal V:III ratio, the metal supply was accordingly lowered to an overall amount of supplied metal that corresponded to a 75 nm thick III-N layer.

8.2. $In_{1-x}Ga_xN$ nanowires with x_{supply}=0.60

The observed structures were comparable for all applied substrate temperatures from 398°C to 502°C. The morphologies of the InGaN grown with 60% Ga in the metal supply shown in figure 8.2.1 a) were columnar, but the structures were so dense that they formed nearly a compact layer with a height of approximately 75 nm. This was equal to the expected thickness if the supplied metal formed a compact layer. This indicates that metal desorption was negligible. The diameters of the columns varied between 20 and 70 nm.

The $\theta - 2\theta$ XRD spectra in figure 8.2.1 b) using the Cu-K_α line show a broad peak at about $2\theta = 33°$, which is assigned to the (0002) reflex of $In_{1-x}Ga_xN$. The single broad peak indicates, that no phase separation occurred, but strong alloy fluctuation. Assuming Vegard's law, the lattice constants, deduced from the positions of the maxima of the peaks, allowed one to calculate a corresponding Ga mole fraction x_{wire}. The resulting fractions x_{wire} varied between 0.56 and 0.61, as shown in figure 8.2.1 d) and were close to Ga mole fraction of the supply x_{supply} of 0.60.

The samples showed emission in the visible range using photoluminescence (PL) at temperatures below 10 K, as shown in figure 8.2.1 c). The position of highest emission intensity varied between 1.49 eV and 1.58 eV with a FWHM of about 300-400 meV. Assuming a band bowing parameter b of 1.4 and a maximum emission intensity for PL of 0.69 eV for InN and of 3.42 for GaN, it was also possible to deduce the composition of the grown alloy. To compare the x_{wire} deduced from XRD and PL measurements, the resulting values of x are shown in figure 8.2.1 d) as functions of substrate temperature. The resulting mole fractions varied between those two methods by up to $\Delta x = 0.23$. In the case of PL, the excited electron hole pairs relax within a crystal to areas with lower band gap. Therefore, PL probes always the In-rich part of the crystals, whereas XRD averages over the whole volume of wires with the c-axis perpendicular to the surface. In addition, material with higher crystal quality is expected to contribute more to the peaks. The broad peak in the XRD $\theta - 2\theta$ scans, as well as the difference between the concentrations deduced from PL and XRD indicated that the material showed a high fluctuation in concentration, but no clear phase separation. These results confirmed that MBE is, in general, suitable for syntheses of $In_{1-x}Ga_xN$ over the entire compositional range at low temperatures of 400-500°C.

8.3. $In_{1-x}Ga_xN$ nanowires with x_{supply}=0.07, 0.13, 0.26

The morphology and sizes of all three series with lower percentages of Ga in the metal supply were similar to each other, but considerably different compared to the samples with $x_{supply} = 0.60$. Figure 8.3.1 a) shows the morphologies at different temperatures for a Ga mole fraction of $x = 0.07$, which is representative for all three series. For the sake of completeness, figure C.0.1 in the appendix shows the morphology of all three In-rich InGaN growth series. Hexagonal wires with an average length

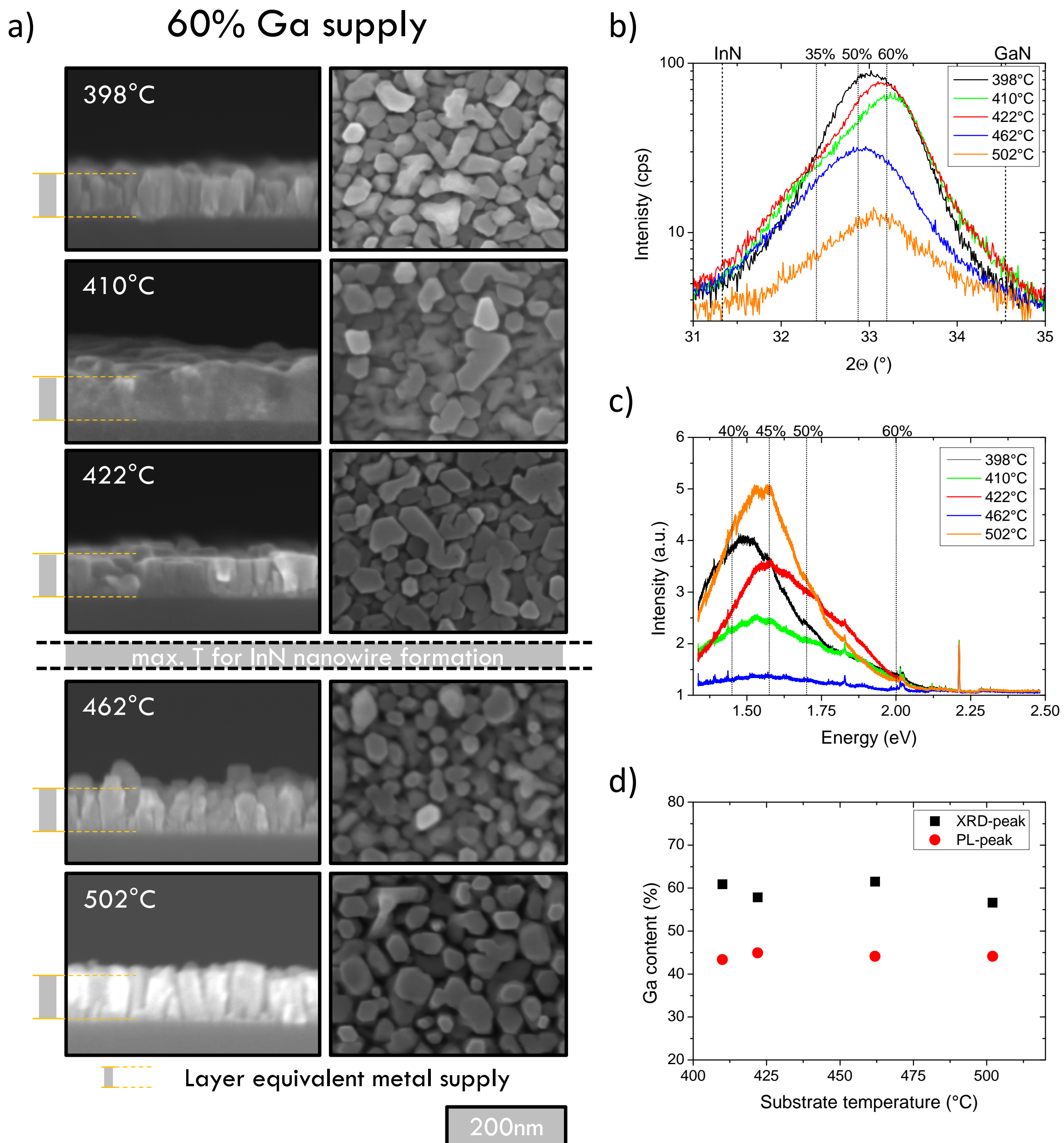

Figure 8.2.1.: *$In_{1-x}Ga_xN$ with $x_{supply} = 0.60$: a) SEM images of morphology; the gray bar and the yellow lines indicate the metal layer equivalent thickness. b) XRD $\theta - 2\theta$ scan of (0002) peak with Cu-K_α, c) PL spectra, d) deduced Ga mole fraction in the wire x_{wire}.*

between 250 nm and 1000 nm were observed, which was a multiple of the 110 nm, expected from the metal supply if all metal was incorporated into a compact III-N layer. This indicates diffusion-induced growth. Furthermore, the formation of a thin rough parasitic layer was observed. At temperatures below 450°C, the morphology, size and density of In-rich InGaN nanowires were comparable to pure InN ones, as shown in figure 8.3.2. In contrast to pure InN nanowires, the InGaN wires did not show the tendency of broadening to the top, which is probably due to Ga-related stabilization of the sidewall surfaces, as explained later. Furthermore, it was possible to grow InGaN wires at higher temperatures. At about 480-500°C, the shape of the columns changed, as shown in figure 8.3.1a). The upper part of the structures had a nearly hexagonal cross section with a diameter that abruptly increased close to the foot of the nanowires.

As shown in figure 8.3.1 b-d), the lengths increased from about 250 nm to 1000 nm with temperature and the diameters increased from about 20-30 nm to 500-600 nm. Conversely, the density decreased from 150-200 μm^{-2} to less than 1 μm^{-2}.

The XRD $\theta - 2\theta$ scans showed a main peak close to the (0002) peak of pure InN and signals of lower intensity which decreased in intensity with increasing angle. The intensity at the position of the GaN (0002) peak was at the level of the background noise. For the signal at higher angles, three different kinds of spectra were observed: a tail with continuously decreasing intensity up to the expected peak position for pure GaN(0002), a second peak at 32.4°, which corresponds to an $In_{1-x}Ga_xN$(0002) reflex with $x = 0.35$ and a superposition of both. Figure 8.3.3 a) shows three XRD $\theta - 2\theta$ scans which are representative for the three different kinds of spectra. Their appearances could not be assigned to certain growth conditions and could have also originated from slightly different measurement conditions. In conclusion, the XRD data is interpreted as follows. Most of the material had a lower Ga content than in the supply. The rest of the material had a varying concentration which amount decreased with decreasing Ga mole fraction and a preference for $x_{wire} = 0.35$.

Each PL spectra was characterized by a single peak. The maximum in luminescence intensity showed a clear redshift with increasing substrate temperature. However, the emission of the three series of In-rich InGaN nanowires lied within the emission range of pure InN nanowires. The values of Ga mole fraction x_{wire} in figure 8.3.4 were deduced using the same assumptions as for the Ga-richer InGaN wires. The values of the Ga mole fraction x_{wire} for the two probing methods showed good agreement, even though the PL peak was expected to show stronger variation due variations in the free carrier concentration as observed for pure InN nanowires. This indicates a relative homogenous Ga distribution within the nanowires. All series showed a significant reduction of the Ga content compared to the supply of a factor of about 3.5 to about 10. This reduction increased with substrate temperature.

In previous reports on Ga-rich InGaN nanowires, a reduction in In content was observed (e.g. Calleja *et al.*, 2007). These wires were grown at higher temperatures (> 600-650°C) which enabled In desorption. The reduction in In mole fraction in the wires compared to In mole fraction in the supply was explained by In desorption. However, in the present case of growth temperatures below 500°C, a reduction of the Ga mole fraction compared to mole fraction in the supply cannot be due to Ga desorption. First of all, significant metal desorption was not observed for the InGaN nanocolumns with $x = 0.60$ and is not expected in the temperature range of 400-500°C. In addition, the desorption rate of In should be significantly higher than of Ga and Ga should be preferentially incorporated due to the higher binding energy of GaN compared to InN. Therefore, the observed reduction of Ga content cannot be explained by desorption and it is supposed that it must be due to a different diffusion-behavior of In and Ga. In the following, it is discussed how different diffusion lengths change the Ga mole fraction inside the wires.

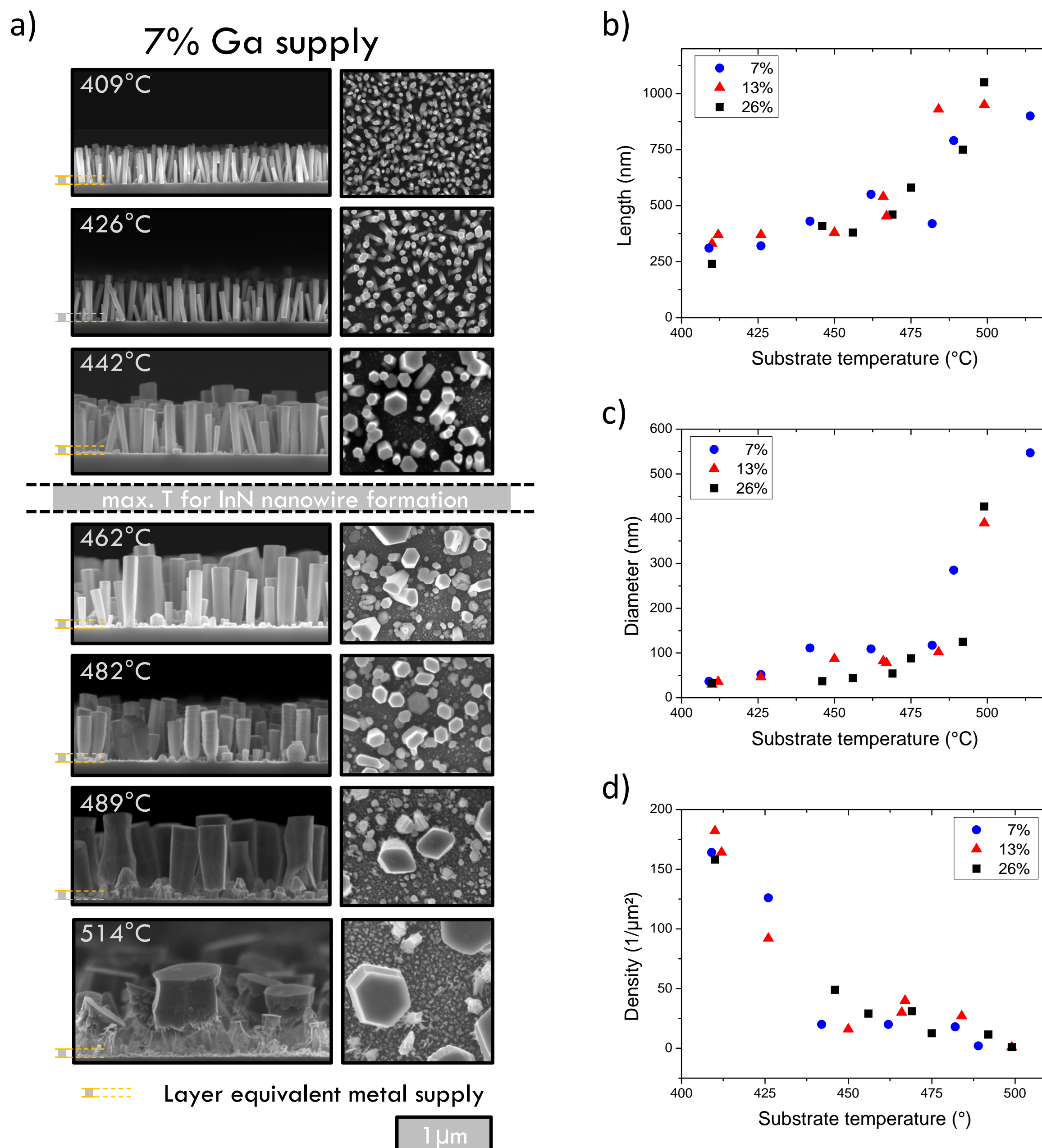

Figure 8.3.1.: *a) SEM images of morphology of $In_{1-x}Ga_xN$ nanowires with x=0.07 of supply. b) Length , c) diameter and d) density of $In_{1-x}Ga_xN$ nanowires for x_{supply}=0.07, 0.13, 0.26 as a function of substrate temperature.*

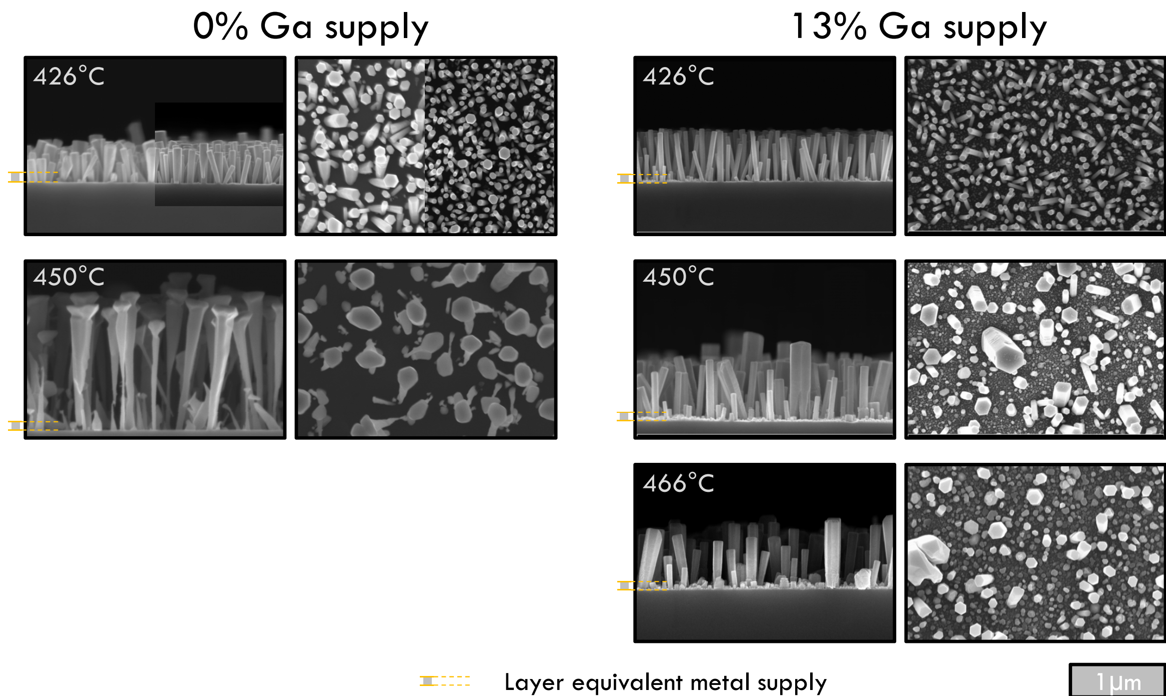

Figure 8.3.2.: *Comparison of morphology of InN and In-rich InGaN nanowires.*

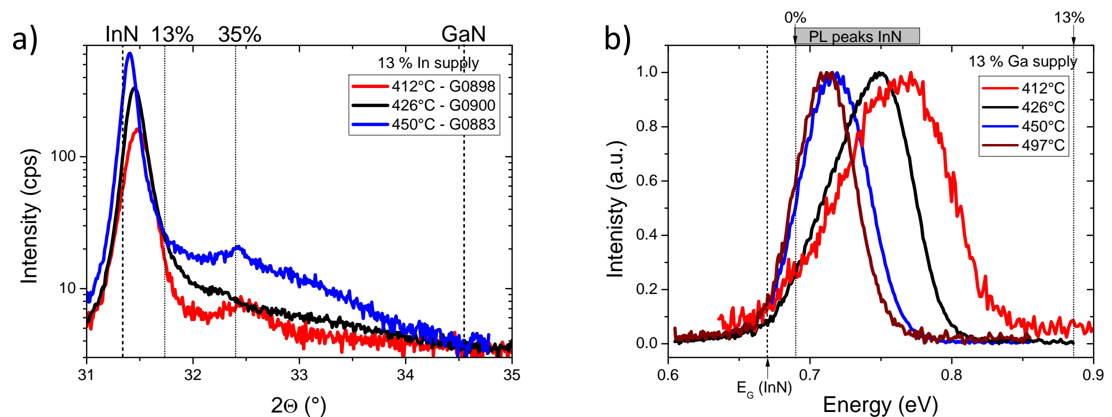

Figure 8.3.3.: *a) Representative XRD $\theta - 2\theta$ scans of the (0002) peak with Cu-K_α and b) normalized PL spectra for In-rich InGaN nanowires. The gray bar indicates the range of maxima in intensity of emission for pure InN.*

8.3.1. Growth rate model

Due to the high V:III ratio, only the limiting constituents, i.e. the metals, are regarded in the following. If metal desorption is negligible, all supplied metal remains on the sample and should be incorporated into a III-N alloy under the highly N-rich conditions. The higher growth rate of the nanowires G_{wire} compared to the growth rate G_{layer} expected for the case where all supplied metal forms a compact III-N alloy layer indicates a diffusion-induced growth mode.

If desorption is negligible, the diffusion length is only limited by incorporation. In this case, the mobility and incorporation probability determine the diffusion length. For GaN diffusion-induced self-organized nanowire growth on silicon temperatures above 620°C are needed, as shown by Meijers (2007), whereas 400°C are already high enough for InN to enable diffusion induced nanowire growth. At lower temperatures compact rough layers are formed. Since the growth temperature is more than 100-200°C below the minimum temperature for diffusion induced growth of GaN nanocolumns, it is reasonable to assume for Ga a negligible diffusion length on the substrate and on all facets of the nanowires. On the other hand, the substrate temperatures are well above the minimum for diffusion-induced growth of InN nanowires. Therefore, diffusion lengths of several µm can be assumed for In. This implies that Ga will more or less incorporate where it impinges, whereas most of the In will diffuse to positions which are energetically most favorable, which should be the top-facets as discussed in section 5.4. According to these assumptions, the following picture of the In-rich InGaN nanowire growth can be drawn. As an approximation, In adatoms can be regraded as mobile and Ga adatoms as immobile on the sample. The In adatoms agglomerate and start to form nuclei. These nuclei have a higher In mole fraction than as in the metal supply, since only the In diffused to the forming nuclei. The c-facet of these nuclei, which is typically the top-facet, acts as sinks for In adatoms and attracts In adatoms from their surrounding. Due to the high V:III ratio, all atoms that arrive at the a c-facts are incorporated there. These nuclei act as starting points for the wire growth. The atoms that incorporate in these wires are the In and Ga atoms from direct impingement and In atoms that diffused to the wire. The diffusing In atoms change the In-to-Ga ratio at the growing surface of the wires. Since the Ga adatoms are assumed to be immobile, they start to form a rough layer, which converts to III-N layer due the high V:III ratio and is not observed for pure InN nanowire growth. This rough layer lowers the diffusion length of In adatoms and some of the In adatoms incorporate in this rough parasitic layer, while most of In adatoms still diffuse to the top-facets of the wires. Ga atoms impinging on the sidewalls of the wires are expected to incorporate there. This should lead to a shell of the wires with a higher Ga mole fraction.

According to this picture, the species increasing the growth rate of the wires G_{wire} compared to the growth rate of the layer G_{layer} is only In. Therefore, the effective Ga:In ratio at the top-facet, where the crystals grow, is lowered compared to the ratio in the metal supply. Thus, the Ga:In ratio for atoms incorporated into wire is lowered and the Ga mole fraction of the wire x_{wire} decreases compared to the mole fraction of the supply x_{supply} by the factor by which the growth rate is increased.

$$\frac{G_{wire}}{G_{layer}} = \frac{x_{supply}}{x_{wire}} \tag{8.3.1}$$

Under the assumptions that all wires nucleate at the beginning of growth and that the growth rate is constant, the length of the nanowires divided by the growth time L_{wire}/t is equal to the growth rate G_{wire} or

$$x_{wire} = \frac{L_{layer}}{L_{wire}} x_{supply} \tag{8.3.2}$$

For the validation of this model, the different contribution of single wires to the signals in PL and XRD ensemble measurements must be considered. As a first approximation, the average composition, referred to the volume, determines the position of the (0002) peak in XRD $\theta - 2\theta$ scans and of the PL

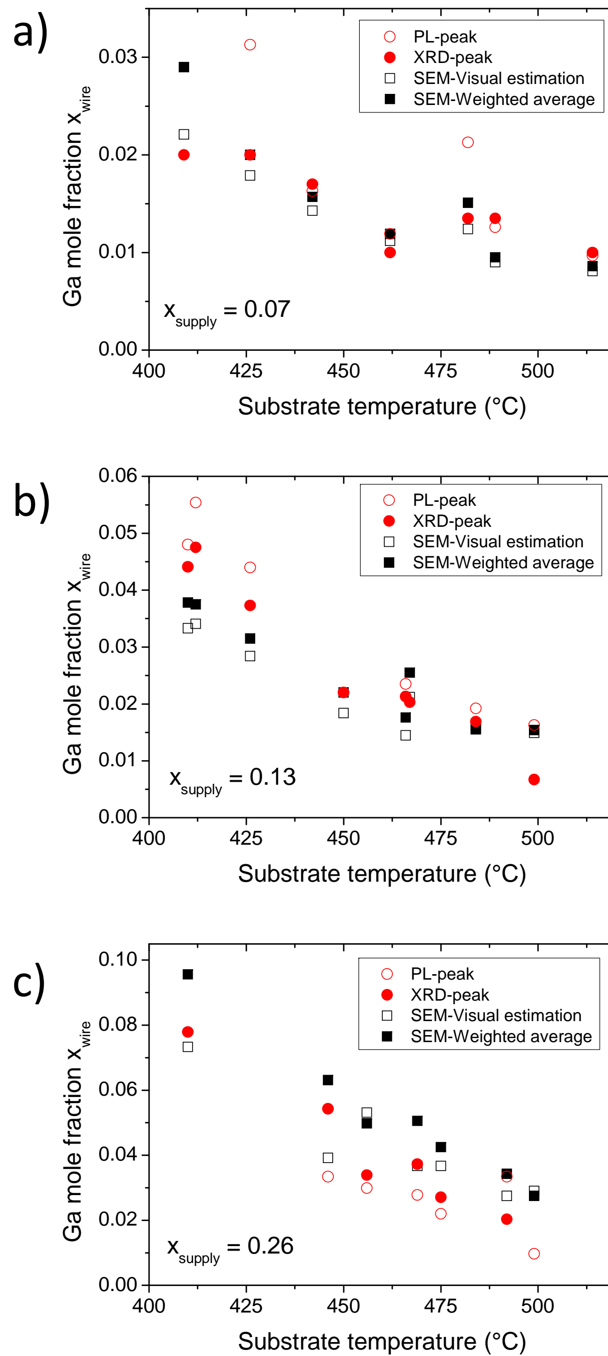

Figure 8.3.4.: *Deduced Ga mole fraction x_{wire} of $In_{1-x}Ga_xN$ from PL and XRD measurements, as well as predicted Ga mole fraction x_{wire} by growth rate model, for x_{supply} = (a) 0.07 , (b) 0.13, (c) 0.26 as a function of substrate temperature.*

peak. The thin parasitic layer is expected to have a minor contribution to both signals due to probably poor crystal quality. Therefore, the peak positions are assigned to the Ga mole fraction inside the wires. In addition, it has to be regarded for the PL peak, that PL probes the part of the wire with lower Ga mole fraction. Furthermore, it is assumed that all wires nucleated at the very beginning of growth and started to grow without any delay. As a first test, the average height of the nanowires was estimated by visual inspection of SEM side view images. This led to a relatively good agreement with the mole fractions deduced from the XRD and PL measurements, as shown in figure 8.3.4. A more reliable method is to weight the lengths of the wires according to their contribution to the total volume. This led to a volume weighted length of $L_{vol} = (V_{wire}/V_{all})\,L_{wire}$ with V_{wire} the volume of the wire and V_{all} the volume of all considered wires. The volume weighted average growth rate $\bar{L}_{vol}/t$ is then given by:

$$\bar{L}_{vol}/t = 1/t\sum_i L_{vol-i} = \frac{1}{tV_{all}}\sum V_{wire-i}L_{wire-i} \tag{8.3.3}$$

$$= \frac{1}{tV_{all}}\sum 2\pi r^2_{wire-i}L^2_{wire-i} \tag{8.3.4}$$

The sizes of wires were measured in SEM side view images at the centers of the samples. Only wires of the first row close to the cleaving edge were regarded to determine the size distribution of the nanowires. The deduced growth rates were comparable to the ones estimated by visual inspection. Here, values of x_{wire} showed slightly better agreement with the mole fractions deduced from PL and XRD measurements.

For the samples with $x_{supply} = 0.07,\ 0.13,\ 0.26$, the deduced values for x_{wire} from the growth rate model, XRD and PL were in good agreement.

8.4. Discussion

According to the above proposed model for In-rich InGaN nanowires, the position of the nanowires is defined by an initial nucleation process at the beginning of growth. In atoms diffuse to these nuclei and locally enhance the growth rate. The impinging Ga on the substrate leads to the formation of a Ga-rich rough parasitic layer because the nucleation barrier is lower or even absent for GaN. The tail to higher angles of the (0002) reflexes in the XRD $\theta - 2\theta$ and the additional peak at 32.4° indicates that there is $In_{1-x}Ga_xN$ with varying Ga mole fraction x which amount decreases with Ga mole fraction. According to the model, it is supposed that this material is mostly found on the substrate as parasitic layer.

Another aspect results from the proposed model. Ga atoms impinging on the sidewalls will incorporate there, while the In atoms will mostly diffuse to the nanowire top-facets. Consequently, there is a higher relative Ga concentration at the nanowire sidewalls, as found by nanoprobe X-ray fluorescence measurements by Segura-Ruiz *et al.* (2011).

The temperature at which pure InN nanowires can be grown is limited to $\leq$ 450°C. As can be seen in figure 8.3.2, the wires broaden to the top close to this upper temperature limit. Longer growth times or higher metal supply led to the similar results. This limits the maximum length for the InN nanowires. From the analysis of the evolution of the morphology with growth time (Denker, 2007), it is known that the diameters of the wires at their bottom became smaller when the broadening to the top set in. Therefore, it is assumed that the wires start to decompose at their bottom and the released In diffuses towards the top of the wire and incorporates there. This could be due to shadowing effects that screen the lower part of the wires from the active nitrogen flux, which is probably needed to stabilize the sidewall facets. In contrast, the In-rich InGaN nanowires showed constant diameters and the limit for nanowire formation was at higher temperatures and equal for all three series. Also, the shape of the structures close to this temperature limit were significantly different. The proposed model, as well as first measurements indicate a higher Ga content at the nanowire sidewalls. This

would stabilize the surfaces of the wires and hinder decomposition due to the higher binding in the Ga-richer alloy.

The assumption that all wires nucleated at the beginning of the growth and started to grow without any delay is probably not entirely correct because nucleation is observed during the first two hours of growth for InN nanowires with InGaN markers, as shown in the following section. This has two consequences. First of all, the growth rate is underestimated for the wires, which did not nucleate at the very beginning of growth. Secondly, if the growth rate decreases during growth as observed for InN nanowires in the following section, the Ga mole fraction would increase x_{wire} along the growth axis. In addition, further scenarios, which lead to a change in growth rate, could be possible according to Dubrovskii's diffusion growth model (Dubrovskii *et al.*, 2009b).

Even though the assumptions for this simple diffusion model neglect several aspects of diffusion-induced self-organized growth, it leads to a reliable estimation of the average Ga content inside the wires.

8.5. Conclusion

Four series of InGaN wires were grown at low temperatures of 400-500°C with Ga mole fractions form 0.07 to 0.6 and characterized by SEM, XRD and PL. The morphologies of the sample series with $x_{supply} = 0.60$ were comparable to columnar nearly compact layers. The heights of the columnar structures were equal to the thickness expected for layers, if all supplied metal would form a compact III-N layer. XRD and PL measurements indicated a Ga mole fraction x_{wire} close to the Ga mole fraction of the supply, but with fluctuation of $\pm$20-30%. However, no phase separation was observed. The synthesis of InGaN nanowires with a Ga mole fraction in the center of the immiscibility gap without phase separation indicates that MBE is generally suitable for the growth of InGaN nanowires over the entire compositional range.

To study the nearly unexplored MBE growth of In-rich InGaN nanowires, three sample series with a Ga mole fraction of 7%, 13 and 26% in the supplied metal were grown. Among these three sample series, the morphologies were similar. Below the critical temperature for pure InN nanowire growth of 450°C, they were also comparable to InN samples. However, the growth result was considerably different if compared to the samples with a Ga mole fraction of 0.60 in the supply. The substrates were only partially covered by nanowires and the heights of the nanowires were much larger than the thicknesses expected from the metal flux if a compact layer would be grown. The reduction of the relative Ga content in the nanowires deduced from PL and XRD measurements was quantitatively explained by a diffusion growth model under the assumption, that only In diffuses and Ga incorporates, where it impinged. Accordingly, In diffusion increased the growth rate of the nanowires and thereby lowered the Ga-to-In ratio inside the nanowires. Furthermore, this model qualitatively explains the formation of a thin parasitic rough layer, which was not observed for the growth of pure InN nanowires.

9. Growth rate monitoring with markers

In recent years, significant progress on understanding the mechanisms of nanowire growth has been achieved, but a consistent model that includes all aspects of self-organized formation of III-N nanocolumns is still lacking. When analyzing formation of nanowires, it is essential to monitor the growth rate as a function of time on single wires. Harmand *et al.* (2010) were the first to use an alternating supply to induce markers into the grown material for monitoring the growth rate. In this case, they used $InAs_{1-x}P_x$ with an alternating P mole fraction x. These markers were detectable by high angle annular dark field scanning transmission electron microscopy (HAADF-STEM) and enabled measurements of the instantaneous growth rate and total length of the nanowire at any time during growth. This allowed a detailed analysis of a single wire according to the diffusion growth model. Inspired by this work, Songmuang *et al.* (2010) and Galopin *et al.* (2011) adapted this idea for $Ga_{1-x}Al_xN$ nanowires. To transfer this concept to InN nanowires, $In_{1-x}Ga_xN$ markers were introduced into InN nanowires. First, the impact of the markers on morphologies and sizes was investigated. Second, the length-time dependence was determined by intensity oscillations in scanning transmission electron microscopy (STEM) images recorded under a high detection angle for single wires. The observed growth rate as a function of time can be explained by a simple diffusion growth model.

9.1. Growth of InN nanowires with $In_{1-x}Ga_xN$ markers

The InN nanowires with markers were grown under similar growth conditions as pure InN and InGaN nanowires on Si(111). Prior to growth the sample was heated to about 850°C to remove the native oxide. The resulting 7×7 reconstruction was used as an indicator for an oxygen free surface. The In and nitrogen supply was fixed to 0.56 nm/min and 9.5 nm/min, respectively, if a compact layer would be formed under stoichiometric conditions. The substrate temperature was set to 426°C, which was 25°C below the maximum temperature for self-organized formation of InN nanocolumns. The growth was initiated by one hour of pure InN growth. Subsequently, the growth continued with two hours of marker growth, which consisted of 24 units of 5 min. 15 min of InN growth followed thereafter. At the end of this growth, 6 of these 5 min marker units were grown. The 15 min pure InN growth was introduced to enable reliable determination of the growth direction of the wires. For each of the 5 min units, a small amount of Ga was added in the first two min. For the first sample, the Ga supply was lowered within the first sequence of markers from 12% of the metal supply to 4% to determine the detection limit of Ga in the TEM setup. The final six markers at the top contained 12% Ga in the metal supply. In the second sample, the Ga supply was constantly 4% of the metal supply for the markers.

9.1.1. Influence of the markers on morphology and size

Figure 9.1.1 shows SEM images of the morphology as well as a sketch of the growth sequence. Both samples were similar in the morphology, size and density of the nanowires. The wires had a nearly hexagonal cross-section with nearly constant diameter. The diameters and densities of the wires were similar to the ones of pure InN or In-rich InGaN nanowires within the typical variation for self-organized growth. See figure 9.1.1. The average height of the wires with markers was 510 nm, as determined by visual estimation. The average length of the wires without markers was estimated to

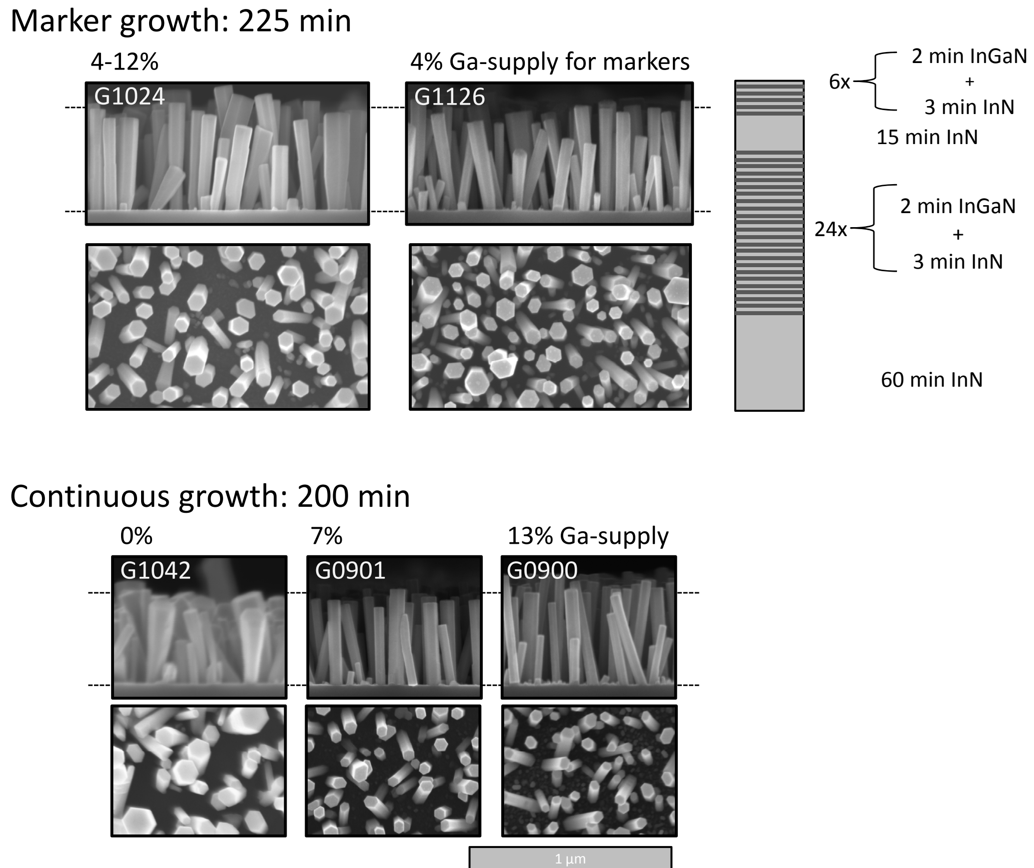

Figure 9.1.1.: *a) Morphology of InN nanowires with InGaN markers and a sketch of the growth procedure. b) InN and InGaN nanowires shown for comparison. The dashed lines indicate the estimated average height as determined by visual inspection.*

be 450 nm. Regarding the slightly different growth times, the average growth rate for all samples was about 2.25 nm/min. This was four times higher than the growth rate, expected for the case where all metal would form a compact III-N layer. Resultantly, the Ga concentration in the markers should be about 1-3%. Thus, the introduction of markers did not change the sizes or morphology of the nanowires significantly which indicates a minor or even negligible influence on the growth.

9.2. Marker detection by transmission electron microscopy

The nanowires were mechanically transferred to a copper grid covered with a thin carbon foil to allow for TEM. The markers were detected by scanning transmission electron microscopy (STEM) in a Philips CM200-FEG-UT operated at 200 kV. A small camera length and an annular dark field detector were chosen for a high angle of electron detection to obtain an elemental sensitive z-contrast. The distortion of the STEM images was corrected by comparison with TEM images. Intensity profiles along the nanowire growth axis were used to determine the length-time dependence of single wires. The maxima in these profiles were then assigned to the center of the InGaN markers.

9.3. Length-time dependence

Figure 9.3.1 shows STEM images of three wires of the sample with varying Ga supply and the deduced length as a function of growth time. The first two investigated wires nucleated almost 60 min after the start of the growth. This indicates that the nucleation of nanowires was not a single process within the first minutes of growth, but rather a process that took place over a longer time scale.

Concerning the length as a function of time, it is first noticeable that the growth rates were nearly constant and equal. “Wire 2” had a constant growth rate of 1.90 ± 0.01 nm/min. Upon closer examination, the length as a function of time for the other two wires was found to be only piecewise linear. A change in the slope from 2.63 ± 0.10 nm/min to 1.91 ± 0.01 nm/min at about 96 min of growth time was observed for “wire 1”. For the longer “wire 3”, a change in slope from 1.86 ± 0.04 nm/min to 1.63 ± 0.02 nm/min at about 120 min of growth time was observed. The extrapolation using the growth rate observed after 60 min to 100 min would result in a wire length of 27 ± 4 nm at time equals zero. Therefore, it is assumed that the growth rate also changed in the first hour of growth.

This behavior can be understood by assuming negligible In desorption and no significant parasitic layer growth. The diffusion length on the substrate is then practically infinite. Therefore, the nanowires cannot be regarded as separated and an overlap of their collection areas, as well as exchange of material among each other has to be assumed. The extension of all markers over the whole cross section indicates negligible radial growth. In this case, the only sinks for adatoms are the growing surfaces, i.e. the top-facets of the nanowires. The formation of a new nuclei or nanowire is equal to an abrupt increase in the growing surface area. This implies, that the impinging atoms must be spread on more growing surface area and the adatom concentration on the top-facets is lowered. This leads to an abrupt decrease in the growth rate. The abrupt change in the growth rate indicates, that the nanowires “collect” their atoms in an area close to the nanowire. Otherwise, single changes would not be visible and the growth rate would decrease continuously with the density of nanowires. The relative change of the growth rates were about 27% and 13%, indicating an increase of the collecting area by about this value. Assuming a single nucleation process responsible for this change, as well as equal diameters for all wires, the change in amount of nanowires in the collection area of the investigated wires would be 25% for adding one to 4 wires and 12.5% for adding one to 8 wires. For a more detailed analysis, it would therefore be necessary to analyze the length-time function of a set of nanowires with regard to their spatial distribution and tilting angles.

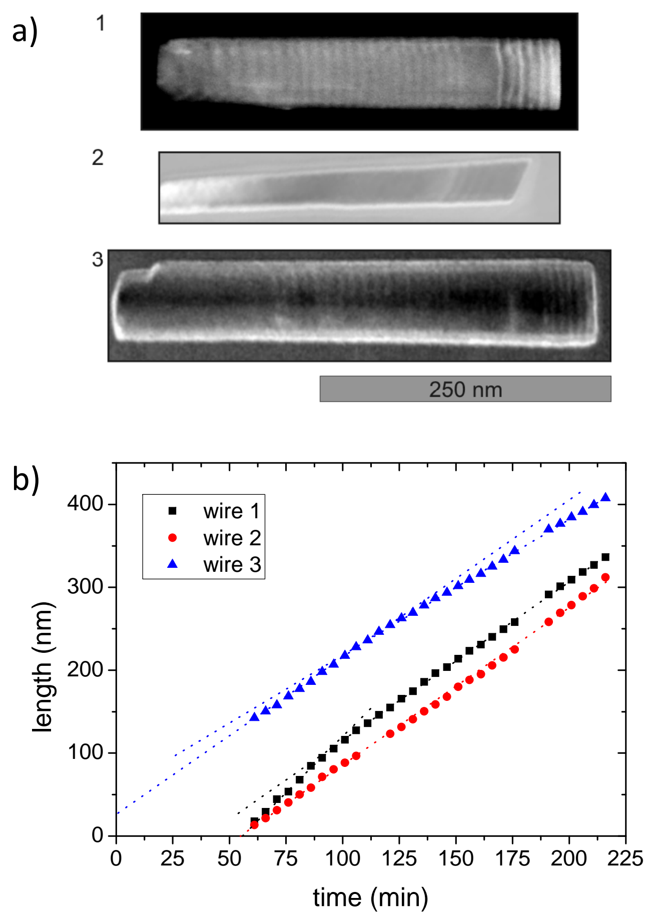

Figure 9.3.1.: *a) STEM images of the investigated wires. b) Length versus time diagram deduced from markers. The dotted lines indicate linear fits of the stepwise constant growth rate.*

9.4. Conclusion

InN nanowires with InGaN markers were successfully grown at a typical substrate temperature for InN nanocolumns. This enabled the monitoring of their length as a function of time to gain a further insight into their growth mechanisms. The morphologies, as well as sizes and densities, were similar to pure InN or In-rich InGaN nanowires. This indicates that the additional Ga had a minor influence on the growth. Nucleation of nanocolumns started from the beginning of growth and new wires formed at least during the first two hours, because not all wires showed the complete sequence of markers. The observed growth rate was nearly equal for the investigated wires. This was assigned to the fact, that no In desorbed and the adatom concentration on the top-facets was nearly independent of the nanowire length and diameter. On closer examination the growth rate was found to be piecewise constant. This is assigned to nucleation taking place close to the investigated nanowires during growth. The observation of 1-2 changes of the growth rate in the wires instead of a continuous change indicates, that every few nanowires were in the collection area the growing wires. The relative change of the growth rate indicates that the collection area of a nanowire contained about 4-9 nanowires.

10. Selective area growth: A way to control nucleation and growth

Selective area growth (SAG) is the control over nucleation by structuring the surface of the substrate in such a way that the areas of nucleation are predefined. SAG can be used for Epitaxial Layer Overgrowth (ELOG) and position-controlled growth of nanostructures. The only difference is the shape of the growing structures. In particular, SAG can allow the growth of ordered arrays of single nanocolumns. The random uncontrolled nucleation in self-organized growth of III-N nanowires led to variations in size, properties, distribution and for InGaN wires to variation of Ga content. In the case of ordered arrays, the growth conditions for each nanowire are equal, which reduces the variation in length and diameter. This is required for most device applications because the properties of the nanowires are mainly controlled by surface-to-volume ratio. Furthermore, an equal growth rate of the wires would lead to equal incorporation of Ga in the InGaN nanowires. Possible equal changes of the growth rates could than be compensated by adjusting the Ga supply. This would enable the growth of homogeneous InGaN nanowires by MBE. The use of SAG has been shown to reduce the variation of Ga concentration in InGaN/GaN multiple quantum well nanowire LEDs (Sekiguchi *et al.*, 2008). In the case of InN, the nanowires start to decompose at the bottom at a certain point in growth. Thus, the maximum length of InN nanowires by MBE is limited. If the wires exceed a certain length, the active nitrogen beam is geometrically screened at the bottom of the nanowires by their neighbors. It is supposed, that active nitrogen is needed to stabilize the sidewalls of the wires. Reducing the density of nanowires by SAG could reduce this screening effect and allow the growth of longer wires. The following section gives an introduction to selective area growth and demonstrates the successful SAG of InN on Si.

For this section, it has to be mentioned that the experiments were performed in collaboration with the diploma students S. Huels and B. Landgraf under my guidance.

10.1. General aspects of selective area growth

The areas of nucleation are predefined for SAG by structuring the surface of the substrate. This means that two kinds of regions are needed. The growth rate or nucleation must be enhanced on one region relative to the other. In the ideal case material grows only on one of the regions. There are several technical methods for SAG of nanocolumns.

The most common method is the use of particles, which locally enhance the growth rate, as illustrated in figure 10.1.1 a). The diameter and position are then defined by the particle. The growth techniques are typically precursor-based, but not limited to these. The growth of ordered arrays of nanocolumns was demonstrated for various material systems with various growth techniques (Fan *et al.*, 2006). But all particle-based approaches suffer the general problem, that the particle itself is generally a source of impurities and can increase the amount of stacking faults, as in the case GaN by MBE with Ni-particles (Chèze *et al.*, 2010).

Another method to achieve position-controlled growth is to cover the substrate with a mask, which suppresses nucleation. Holes in the mask then act as nucleation centers, as shown in figure 10.1.1 b). The inverse is also possible. In this case, the material of the nanowire needs to have a low nucleation rate on the substrate, whereas the areas for nucleation must be modified to increase the nucleation rate. This can be done by the deposition of a different material or by modifying the surface by sputtering,

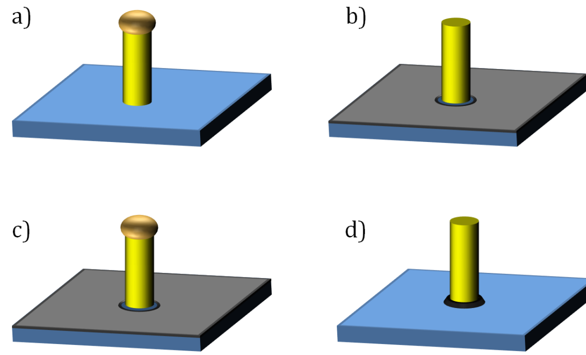

Figure 10.1.1.: *Different approaches for position-controlled growth of nanowires. a) Positioning of catalyst, b) mask with opening, c) mask and catalyst, d) defined nucleation site by a particle on the substrate.*

as depicted in figure 10.1.1 d). In the latter case, the rougher surface in the holes, their curvature or a combination of both, increase the nucleation probability; this was shown for InN with MBE by Araki *et al.* (2009). In principle, it is also possible to combine these approaches, like the one with masks and the one with particles as in figure 10.1.1 c).

The advantage of the pure mask or nucleation spot approach is the absence of the particle and the above mentioned problems related to it. In contrast to the particle, masks for SAG need to be inert and stable, which drastically reduces the risk of contamination. Therefore, the mask approach and definition of nucleation spots are the most promising techniques to maintain high quality and purity in MBE samples.

Precursor-based techniques, such as MOCVD and CBE, offer some advantages for SAG compared to MBE. This is mainly due the fact that “in CVD techniques [...] the selectivity is mainly governed by the much lower gas phase reactivity and higher desorption on masked dielectric layer as compared to the semiconductor surface”(Hertenberger *et al.*, 2010). But MBE allows the growth of material with higher purity, which is of high interest especially for InN. Also, an important advantage of MBE is abrupt switching in supply, which is necessary for heterostructures with sharp interfaces . But similar to the case InAs, SAG of InN by MBE is challenging because two possible SAG promoting mechanisms, selective reactivity and desorption, are practically excluded due to the direct supply of the constituents and low growth temperature. Therefore, it is expected that SAG of InN by MBE can only be realized based on a diffusion mechanism.

Despite the interest in InN nanowires, reports on SAG by MBE are rare. Only Araki *et al.* (2009) reported position controlled-growth of nanowires on a focused ion beam-structured GaN template with holes. Additionally, Kamimura *et al.* (2010) showed ELOG by MBE of InN on sapphire using Molybdenum masks. Reports of SAG of single wires on other substrates are lacking. Therefore, this study focuses on SAG of InN on Si, due to its technical importance and the option to obtain high quality III-N on a low cost substrate. SAG was shown with Ti masks on Si(111) by Kishino *et al.* (2008) and Kishino *et al.* (2009) for GaN, where the chemical processes of growth are similar, but the metal desorption rate at typical growth temperature is higher. Recently, it was shown that SiN_x (Bertness *et al.*, 2010) and SiO_x (Schumann *et al.*, 2011 and Gotschke *et al.*, 2011) are also suitable mask materials for GaN growth on AlN-buffered Si(111). For other related In-V materials, the reports on SAG by MBE are also rare. Even though Hertenberger *et al.* (2010) recently showed successful SAG of single nanowire arrays by SiO_x masks on Si(111), this is not directly transferable to growth of InN, since during MBE of III-nitrides an amorphous layer on the Si is formed, but not during MBE of III-arsenides.

10.1.1. Mechanisms of SAG in the mask approach

During SAG, two temporal phases should be regarded. The first one is the formation of the initial nuclei. When all holes are filled with nuclei, the second phase of nanowire growth begins.

As shown in section 5.3, nucleation is a complex function of the substrate properties, nitrogen and In flux, as well as temperature and time. In the case of SAG, this problem gets even more complex because of the spatial inhomogeneity of the substrate. Therefore, the general physical processes are analyzed to gain insight into the mechanisms of SAG. The nucleation probability J depends linear on the adatom concentration and exponentially on the nucleation barrier ΔG Markov (1995):

$$J \propto N_{adatom} \exp\left(-\frac{\Delta G}{k_B T}\right) \tag{10.1.1}$$

The growth is initiated by starting the impingement of atoms of the material to grow. Since the growth of nanowires takes place under nitrogen-rich conditions and nitrogen cannot accumulate on the surface, only the limiting constituent (In) is regarded in the following. Once the atoms are adsorbed at the surface, these adatoms can diffuse, accumulate, incorporate and desorb. Due to the low growth temperature of InN, desorption of In is unlikely and the In adatom density on the surface will increase with time. Temperature and impingement rates are equal all over the sample. According to equation 10.1.1, one way to achieve selective nucleation could be to lower the adatom concentration on the mask compared to inside the holes. For this purpose, the chemical potential for the adatoms inside the holes must be decreased compared to on the mask such that the adatoms will diffuse to the holes and by this, increase the nucleation probability there. Therefore, the diffusion barrier on the mask needs to be low enough and the temperature high enough to allow sufficient diffusion. A second mechanism could rely on the fact that the nucleation probability depends exponentially on the nucleation barrier. As shown in equation 5.3.7, the nucleation barrier is given as follows:

$$\Delta G_{cr} = \frac{4}{27}\frac{k_{surf}^3}{\Delta\mu^2} \tag{10.1.2}$$

with $k_{surf} \propto \sqrt[3]{\sigma_{ci+}}$. According to this relation, there are two options to increase the nucleation barrier and nucleation rate. One is to increase the interface energy σ_{ci+}. Therefore, inert materials are desirable as masks since they typically form weaker bonds to other materials, which implies a lower adhesion to the growing material or higher interface energy. The other option is to decrease the supersaturation $\Delta\mu$. The impingement rate from the vapor and temperature is fixed by the growth conditions for the whole sample and accordingly the rate of the forward reaction. However, the mask could increase the decomposition rate, if it would have a catalytic effect on the decomposition reaction. This would be equal to reducing the supersaturation on the mask.

Even though both effects lower the nucleation probability, nucleation will take place if there is no process which limits the adatom concentration. Either a directed adatom flux to holes or growing nanowire is needed or desorption, which increases with the adatom concentration. In the case of desorption, there is an equilibrium adatom concentration (e.g. Markov (1995) or Dubrovskii *et al.* (2009b)). If this equilibrium adatom concentration is sufficiently low, nucleation is suppressed. Without desorption, the adatom concentration increases continuously with time. In this case, a directed adatom diffusion flux to the holes or nanowires is required to reduce the adatom concentration and suppress nucleation. Therefore, a sufficient mobility of the adtoms, as well as a lower chemical potential for atoms on the growing surface as on the mask, are needed. However, the atom concentration increases with the distance from the holes or nanowires and the adatom concentration will be sufficiently high to induce nucleation after an certain deposition time in a certain distance. Therefore, the density of holes must be high enough that the adatom concentration between the nuclei is always too low for nucleation.

In typical growth experiments, the supply rates of the constituents are kept constant and the tem-

perature is varied. An increase in temperature increases the decompostion rate and thereby lowers the supersaturation $\Delta\mu$ and enhances diffusive mobility of adatoms. At lower temperatures, the supersaturation is higher, according to section 4.3, and the diffusion mobility is reduced, so nucleation on the mask and holes is expected. With increasing temperature, the diffusive mass transport increases and supersaturation will become lower, resulting at a certain temperature in a lowered nucleation probability on the mask compared to inside the holes. Therefore, an increase in selectivity is expected with increasing temperature.

After the initial nucleation process, the second phase of nanowire growth begins. The growth can be described according to the diffusion model of Dubrovskii, but with a little modification. In the model of Dubroskii, the diffusion length is limited by incorporation and desorption. For InN growth, desorption is not expected and single atoms cannot incorporate into the mask due to the nucleation barrier. However, In atoms can agglomerate and form a new nuclei on the mask, which is the starting for a new wire. Therefore, this model is limited to the case that spacing between the holes is small enough that no nucleation on the mask can be observed, because the case of changing wire density is not regarded in the diffusion growth model. Furthermore, the diffusion growth model can be used to model the adatom concentration profile, i.e. the increase in adatom concentration with distance from the nanowire, which can provide information of the inset of nucleation.

Nucleation inside the holes can differ from the nucleation obtained by growth without the mask. First of all, the maximum footprint size of the nuclei is limited by the hole size of mask. When the hole size is comparable to the inverse density of nuclei forming without the mask, formation of multiple nucleation centers will take place in one hole. In the case of epitaxial growth, the nuclei can coalesce to one. But in the case of textured growth, as in InN on Si, this leads to the growth of several nanocolumns in one opening, since coalescence is hampered due to the different orientation of the crystals. The density of InN nanowires on Si is approximately 200 μm^{-2}, thus the inverse density or area per nanowire is about 70×70 nm^2. Therefore, the maximum hole sizes in a mask for position controlled growth of single wires on Si substrates must be smaller 70 nm in diameter. Furthermore, it should be regarded that the III:V ratio on the top-facets is changed by diffusion of In. Thus, the nitrogen supply has to be adjusted that the conditions are still nitrogen rich at the top-facets to favor the columnar growth.

10.1.2. InN - SAG: Choice of mask material and growth conditions

According to the previous section, the mask material should have low adhesion to InN, low diffusion barrier and high chemical potential for In adatoms. Furthermore, the choice of the mask material underlies some technical restrictions for the MBE process. It should be temperature-stable so that the structure does not change at the elevated growth temperatures. In addition, the vapor pressure of the material needs to be nearly zero so not to contaminate the growth chamber. Lastly, the material should be stable to exposure of molecular beams of the constituents, otherwise it will change its chemical composition during growth. These demands are typically fulfilled by temperature-stable materials with passivated surfaces. Typical temperature-stable surface passivations are the formation of an oxide or nitride.

Silicon nitride and oxide are typically used for SAG or ELOG. SiO_2 evaporates at temperatures of 715°C-850°C under UHV conditions depending on the oxide preparation (Ishizaka & Shiraki, 1986). At the growth temperature of GaN, decomposition of the mask and subsequent incorporation of O in the GaN can reduce its quality. Furthermore, bare silicon reacts with the activated nitrogen under the growth conditions for GaN and InN nanowires to silicon nitride and can be regarded as stable. However, silicon nitride cannot be used as mask material on bare silicon and a buffer layer such as AlN must be used (Bertness *et al.*, 2010), otherwise the whole substrate would consist of silicon nitride.

But there are much more auspicious materials for SAG since any temperature-stable material with

a low vapor pressure and good passivated surface could be suitable. Furthermore, various compounds of carbon are inert and temperature stable. Accordingly, the oxides and nitrides of, for example, Si, Ge, Ti, Mo, W, Ta and Pd are auspicious, as well as their carbides. For this study, Si(111) with native oxide was chosen as the substrate due to its technological importance. Pure carbon was tested as the mask material, as well as Ti due the successful SAG of single GaN nanowire arrays by Kishino *et al.* (2009). Finally, Mo was also chosen due its chemical stability and UHV compability.

The growth conditions used for the SAG samples were similar to the ones of self-organized growth (P_N = 400-450 W and F_N = 1.0-1.5 sccm, which corresponds to a growth rate at stoichiometry of 6-9.5 nm/min and a metal supply of 0.37-0.56 nm/min). The growth duration was lowered to one hour to reduce possible nucleation on the mask. To not destroy the mask on the sample the degassing temperature prior to growth was lowered to about 560°C. Therefore, the native surface oxide of the Si substrates was not removed.

10.2. Selective area nucleation by carbon masks

Motivated by the observation that e-beam exposure in the SEM can reduce the nucleation probability on Si with a native oxide, arrays of rings were intentionally exposed with varying exposure time. The e-beam of the SEM cracks organic compounds in the residual gas in the microscope chamber, which then releases carbon to the surface (Djenizian *et al.* (2001)). This process is known as electron beam-induced deposition (EBID). Special precursors are usually used to increase and control the concentration the carbon containing compounds in the residual gas. The film thickness obtained without intentional introduction of precursors is very thin and mainly depends on the exposure time and residual gas pressure, as well as its composition. Since the composition of the residual gas is uncontrolled the given conditions can only be used as guidelines. With an exposure time of about 15 min/µm², an acceleration voltage of 20 kV and 30 µm aperture, selective nucleation was observed, but there was no formation of nanorods or columns in the openings, as shown in figure 10.2.1 a). Because of the extremely long exposure time, a pulsed laser deposition (PLD) carbon mask structured by e-beam lithography in a lift-off process was used for further experiments. Selectivity was also observed with these samples, as shown in figure 10.2.1 b). But the InN that grew inside the opening did not had the shape of nanocolumns. In the figurative language of nanostructures the morphology could be called “cauliflower”-like. It seems that some material diffused from the mask to nanostructures and hindered the formation of nanocolumns. Therefore, this approach was suitable for selective nucleation, but not for position-controlled growth of InN nanocolumns (see Huels (2008) for further details).

10.3. Selective area growth by Molybdenum and Titanium masks

Four Si samples were structured with Mo and Ti patterns by e-beam lithography (as shown in figure 10.3.1) to test the suitability of Ti and Mo as mask materials. Without drying the sample, intensive acetone and propanol rinse was used to remove residuals of the resist directly after lift-off. After the lift-off, the samples were exposed to air.

Clean Mo and Ti thin films form a surface oxide in air. XPS measurements by Carsten (2010) showed that the oxides of Mo start to decompose at about 500°C in vacuum. When active nitrogen is introduced into the chamber, the signal of pure Mo vanishes and a signal of MoN_x arises. This happens already when the nitrogen plasma is switched on and the shutter is still closed. The surface of clean Mo masks will consist of a mixture of MoO_x and MoN_x when the growth process is initiated by opening the shutters. Mo- and Ti- patterns were deposited on the same samples close to each other to ensure that the growth temperature were equal for both patterns. In addition, the substrates were prepared in parallel to avoid any difference in the preparation process. The thickness of the metal

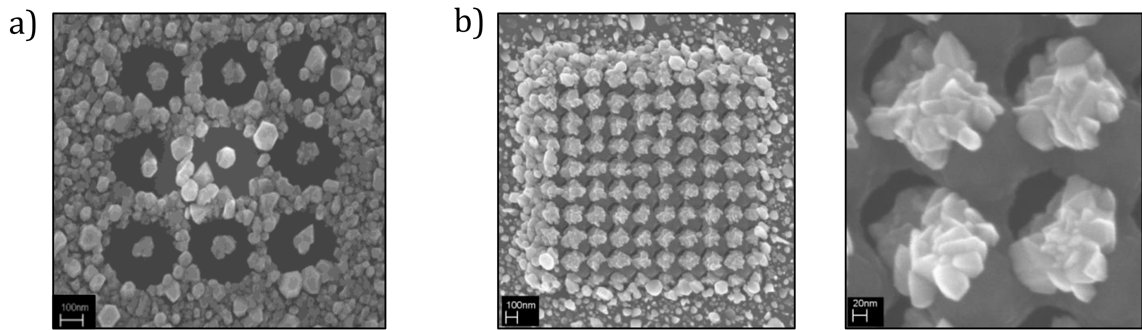

Figure 10.2.1.: *Selective nucleation using different carbon masks: a) carbon mask by electron beam-induced deposition (EBID-C) with an exposure time of about 16 min/μm^2) on sample G0342, b) carbon mask by pulsed laser deposition (PLD-C) of 50 nm thickness on sample G0351. The growth conditions were a metal supply of 0.37 nm/min, a substrate temperature of 454°C and nitrogen conditions of P_N = 400 W and F_N = 1.0 sccm, which corresponds to a growth rate at stoichiometry of 6 nm/min (Huels, 2008).*

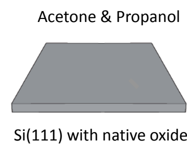

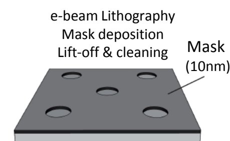

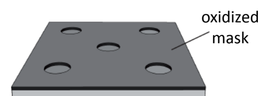

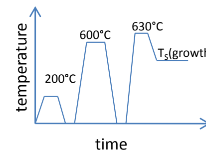

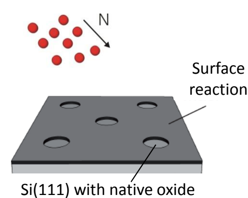

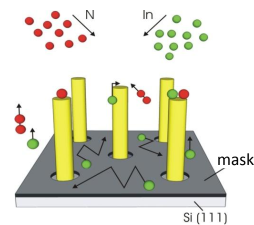

Figure 10.3.1.: *Preparation steps for SAG samples. The degassing temperature is given as thermocouple values. The last temperature step of 630°C thermocouple temperature corresponds to 560°C of the substrate.*

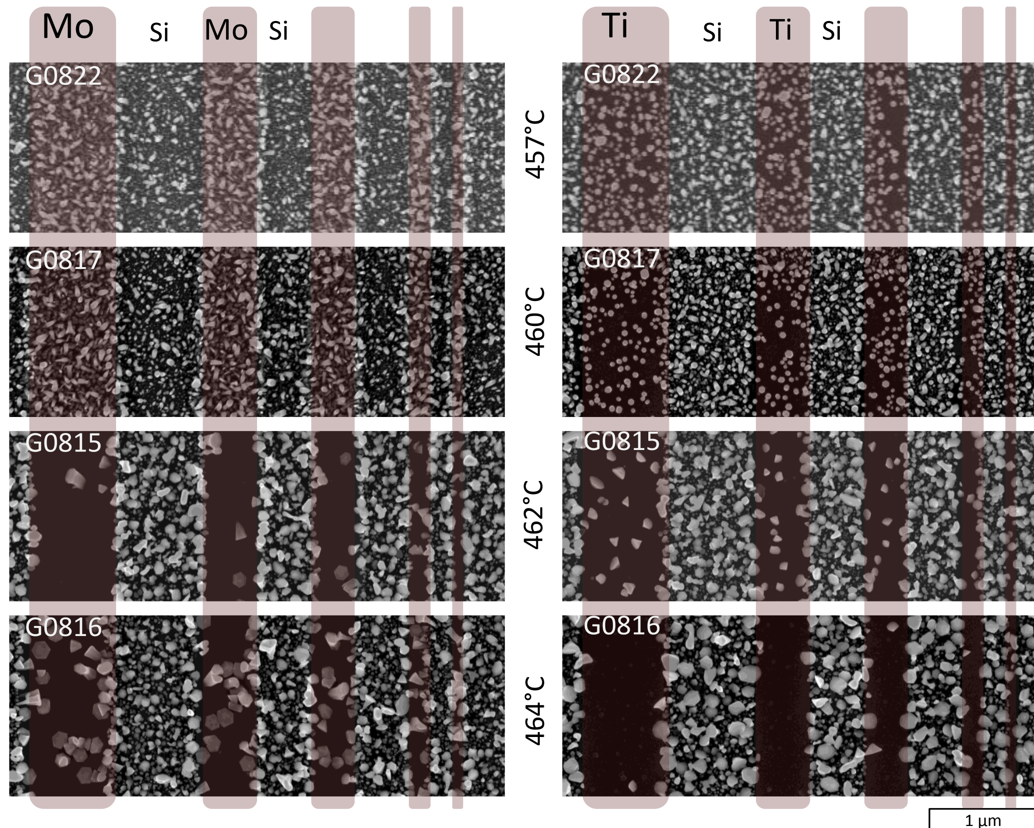

Figure 10.3.2.: *SEM images of (a) titanium and (b) molybdenum stripes on Si (111) after the growth of InN at different temperatures. Growth conditions are P_N = 450 W and F_N = 1.5 sccm, which corresponds to a growth rate at stoichiometry of 9.5 nm/min and a metal supply of 0.56 nm/min.*

films was about 10 nm. Former experiments showed that the layer thickness, roughness or thickness has a minor influence on the growth, as shown in Landgraf (2009).

Figure 10.3.2 shows the nanostructure distribution and morphology after growth at four different temperatures, above and below the critical temperature above which InN does not form nanowires. The temperature steps were narrow with 2-3°C. To allow such small steps, particular attention was paid to equal mounting and temperature ramping. Even though the absolute values are probably not reliable, the sequence of the temperatures should be reliable, as indicated by the following. Nanowire growth was observed on the two samples with lower growth temperatures (457°C and 460°C) at free Si with native oxide, whereas formation of unordered InN was found for the two grown at higher temperatures (462°C and 464°C). Therefore, maximum temperature for InN nanowire formation was between 460-462°C. This is in agreement with other experiments in section 8 within the error of the absolute temperature. Furthermore, this reveals again how critical temperature is for the growth of InN nanowires.

The growth on Ti masks showed a clear trend. The nucleation density decreased with increasing temperature. The nucleation density in the depicted temperature range was always lower than on the substrate and decreased continuously from 175 via 85 and 16 to $\leq$1 µm^{-2}. For successful position controlled growth of single wires, the minimum density of nanowires on the larger mask areas should be less than the density of positions for nanowires to avoid unintentional nucleation. The minimum density was about 85 µm^{-2} for nanowire formation. This is very close to the maximum density of holes achievable by e-beam lithography of about 25-100 µm^{-2}. With FIB, hole densities of up to 400

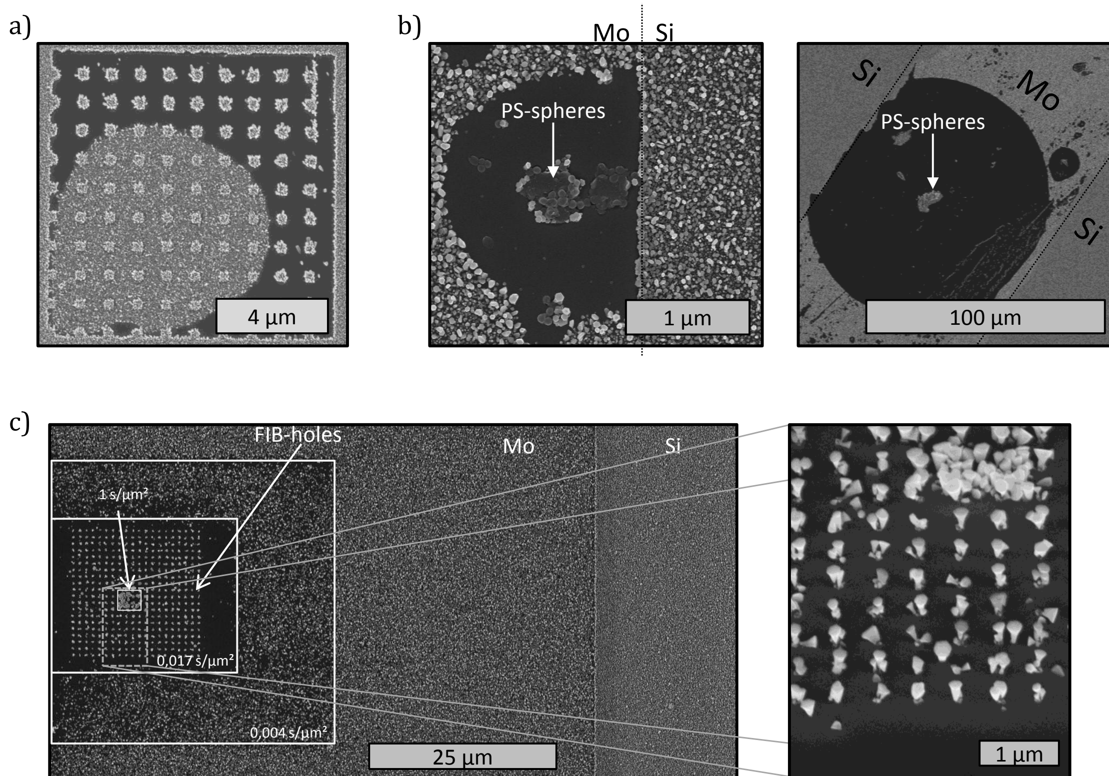

Figure 10.3.3.: *Patterns with partial SAG: on (a) a single Mo structure and (b) close to PS-nanospheres . c) FIB structured sample after growth with e-beam exposure times. The "baseball bat" morphology of the nanowires is shown in the high magnification image taken under an angle of 45°.*

μm^{-2} could be reached, but then the distance between the wires is extremely limited. Furthermore, even thin lines of Ti with 100 nm width were not free of nucleation, which indicates that Ti is not an ideal mask material for SAG of InN.

The nuclei density on the Mo mask did not show a clear trend. Below the critical temperature for InN nanowire formation, the density of nanowires on substrate and mask were comparable. It seems that the amount of grown InN was even higher on the mask. Above the critical temperature, the density of nuclei decreased abruptly to a very low value and then increased again with temperature. In addition, another test sample showed a high selectivity at a significantly lower temperature of 446°C. This observations indicate that either the temperature was not the control parameter for selectivity on Mo masks or the temperature was not well controlled. An insufficient control over temperature is highly unlikely by the observation of selectivity and non-selectivity within one structure with a size of about 10×10 µm², as shown in figure 10.3.3 a). Furthermore, polystyrene (PS) nanospheres, which were used for beam adjustment in the e-beam lithography process, were surrounded by circular areas free of nucleation with a size up to 100 µm in diameter (as shown in figure 10.3.3 b)), whereas the growth on the substrate was unchanged.

PS is a polymer of the hydrocarbon-monomer C_8H_8. PS with a long chain length or high molecular weight is solid, whereas PS with a lower molecular weight is liquid or even volatile. If PS is heated, the polymer starts to decompose. The precise temperature behavior depends on the production process. Gausepohl (1996) summarized the research results on thermal decomposition of PS in vacuum. Below 250°C, the molecular weight reduces moderately and there are no considerable amounts of

volatile products. Above 300°C, the reduction of molecular weight and amount of volatile products increase dramatically. At temperature above 500°C, considerable amounts products of decomposition, which are smaller than the styrene monomer (mostly other hydrocarbons), appear. At temperatures of 420°C, 99% of the initial PS should be decomposed to volatile products Madorsky & Straus (1948). During the sample preparation, the substrates are heated to 560°C. During this process, the PS should decompose into styrenes with lower molecular weight. A fraction of the PS will decompose to a liquid intermediate product. This fraction can probably wet the surface in circular regions around the former PS-spheres. During the further heating to the final degassing temperature of 560°C, this liquid fraction should further decompose into hydrocarbons with lower molecular weight. Thus, it is unlikely that the surface was covered by PS prior to the growth. It is more likely that a little amount of hydrocarbons remained on the surface or modified it. Therefore, a hydrocarbon-related surface modification of the Mo mask can be responsible for the selectivity in the growth InN.

To further validate this hypothesis, Mo masks on Si with native oxide were structured with a hole pattern with a FIB and subsequently exposed with an electron beam which is known to deposit small amounts of carbon on the molybdenum mask. For short exposure times, it could be possible that the hydrocarbon of the residual gas are not completely decomposed and thin layers of hydrocarbon are deposited instead of a carbon layer, as observed by Djenizian *et al.* (2001). For the deposition, an acceleration voltage of 10 kV and 30 µm aperture were used to crack the residual gas in the FIB chamber. To investigate the effect of different amounts of hydrocarbon or carbon, the exposure time was varied on different areas on the same sample. An exposure time of 4 ms/µm² significantly reduced the nucleation density on the Mo mask, as shown in figure 10.3.3 c) and an exposure time of 17 ms/µm² was sufficient to nearly completely suppress any nucleation on the mask, whereas an exposure of 1s/µm² increased the nucleation probability even further than on unexposed Si. If Mo and Si areas were exposed simultaneously, it was observed that an exposure time, that was sufficient to suppress the nucleation on Mo mask, left the nucleation on the Si nearly unchanged. Furthermore, the exposure time by e-beam to suppress nucleation on Molybdenum masks was much shorter than needed in the carbon mask on Si approach with about 15 min/µm². From these results, it is concluded that very little amount of hydrocarbon or C, which modify the surface of the Mo mask reduce the nucleation and if the amount is sufficient to form carbon layers the nucleation probability is increased. Therefore, it is supposed that only a hydrocarbon-related surface modification of the Mo mask is responsible for the selectivity and not carbon layers on the Mo mask.

Several steps and parameters were varied in order to identify the step inducing the necessary surface modification. But none of them were able to intentionally reproduce this surface modification. Intentional underexposure was used to test if residual resist under the metal film could be responsible. Drying of acetone, propanol and propanol with a little of PMMA-Acetone solution on the pattern was applied to test if the contamination could originate from the final cleaning process, but did not lead to the desired result. Samples with HF-dip or O-plasma cleaning to remove any surface contamination support the observation that clean Mo or MoO_x does not work and that hydrocarbon-related surface modification is needed for SAG.

Although the responsible process in e-beam lithography was not identified, several samples, namely G0662, G0777, G1062, G1071, G1089, showed the desired selectivity. Experiments with EBID-C obtained a similar behavior. This reveals that this approach, in principle, is suitable for SAG of InN on Si with native oxide. Figure 10.3.4 shows the growth result of G0662. On this sample, the hole size was reduced from 1200 nm, to 600 nm to 120-150 nm to 60-90 nm. In patterns with a hole size of 60-90 nm, most of the holes were occupied by one or two nanorods. This agrees with the estimation of 70 nm for the maximum diameter hole in masks on Si substrates for position controlled growth of single nanowires. This reveals that Mo masks with the hydrocarbon-related surface modification are suitable for position-controlled growth of single wires, if the holes size are small enough to suppress multiple nucleation in one hole.

PL with an excitation area of about 1µm² on selectively grown InN nanowires showed similar spec-

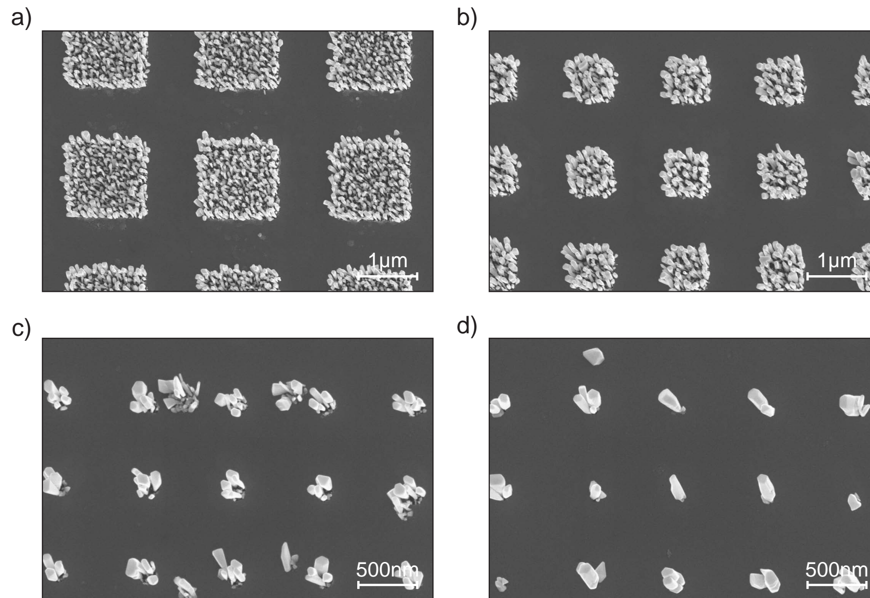

Figure 10.3.4.: *Selective area growth on a molybdenum mask with different hole diameters (G0662) (Landgraf, 2009).*

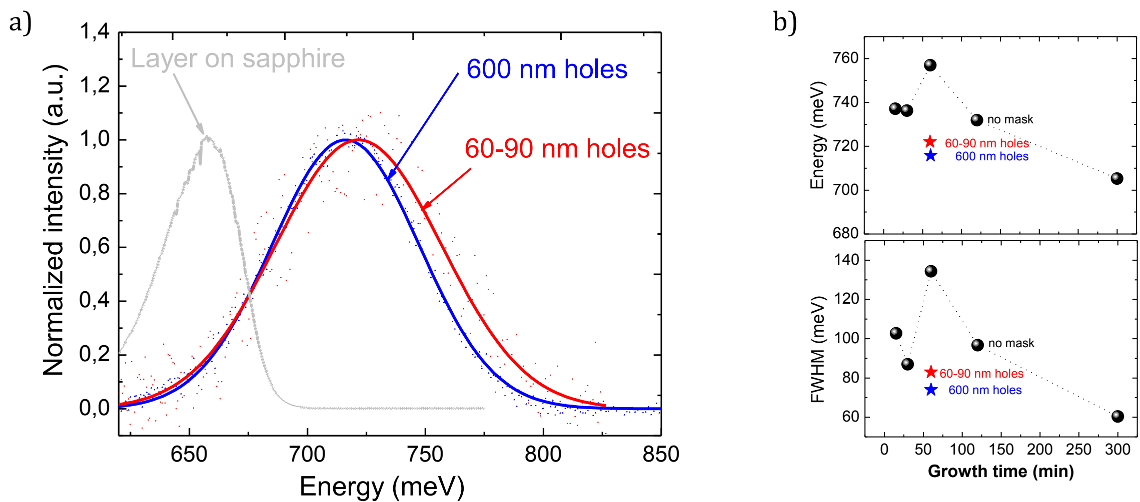

Figure 10.3.5.: *a) Photoluminescence spectra of InN nanorods by selective area growth with a molybdenum mask with different hole diameters and of a layer for comparison. b) Energies of maximum intensity and FWHM of InN nanorods by selective area growth with a molybdenum and self-organized grown samples with different growth times.*

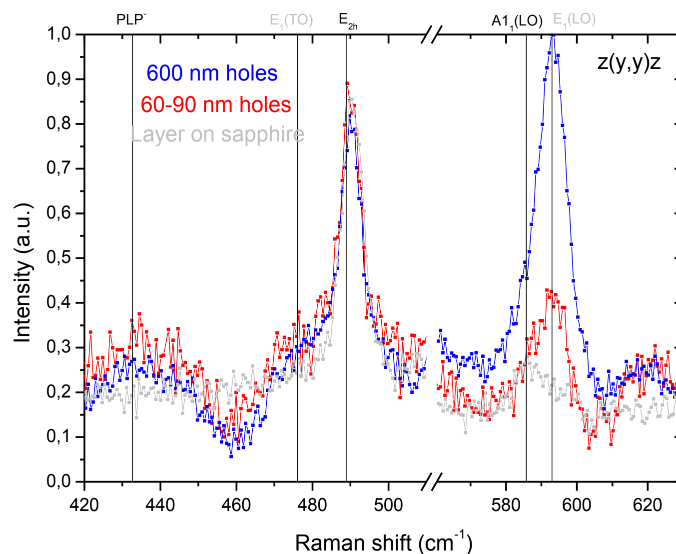

Figure 10.3.6.: *Raman spectra of InN nanorods by selective area growth on a molybdenum mask with different hole diameters and a layer. The Si peak 519 cm^{-1} of nanowire samples is fitted and subtracted for better comparison to the layer.*

tra to those of self-organized grown samples. Figure 10.3.5 a) shows two spectra of sample G0662: One for a 600 nm hole and one for a 60-90 nm, which were characterized by a single peak at about 0.72 eV and a FWHM of 75-85 meV. The hole size showed minor influence. The obtained values of energies of maximum intensity and FWHM were higher compared to layers or nanowires samples with 300 min growth time. But comparison to samples with varying growth time at equal substrate temperature reveal, that they are even lower or at least comparable to samples with shorter growth times (see figure 10.3.5 b)). This shows that the luminescence properties were not negatively influenced by the mask. Furthermore, Raman spectroscopy indicated a high crystal quality comparable to self-organized grown nanowires by a narrow E_{2h} mode signal.

10.4. Conclusion

Carbon, titanium and molybdenum were tested for suitability as masks for SAG of InN on Si with a native oxide. Carbon masks were shown to be suitable for selective nucleation, but not for position-controlled growth of nanowires since the nanostructures were more cauliflower-like. This is assigned to carbon diffusing from the mask to the nanostructures, which hindered the formation of nanocolumns. The nucleation probability on Ti masks was lower than on Si, but not sufficiently low to allow growth of ordered arrays of single nanocolumns with a periodicity larger than about 50-100 nm. Mo masks with a surface modification showed high selectivity. The origin and nature of this modification is unclear. Close to the hydrocarbon polymers spheres, areas free of nucleation were found. Furthermore, short e-beam exposure, which is known to result in ultra-thin carbon or hydrocarbon coating, also suppressed the nucleation on the mask. Therefore, it is assumed that this surface modification was probably related to hydrocarbon. Spatially resolved X-ray fluorescence (XRF), X-ray Absorption Near Edge Structure (XANES), Raman backscattering (RBS), XPS or Auger electron spectroscopy (AES) measurements would be needed to identify the nature of this surface modification on the small structures after growth. Mo masks with this surface modification showed areas free

of nucleation $> 50 \times 50\ \mu m^2$ at temperatures below the maximum temperature for InN nanowire growth. Experiments with ordered arrays proved, that this approach is suitable for position-controlled growth of single InN nanowires. Raman spectroscopy and PL revealed that the high crystal quality and good luminescence characteristics of self-organized growth, are maintained for SAG by Mo masks.

11. Conclusion

InN and InGaN nanowires were investigated to gain a deeper understanding of the electronic properties of InN nanowires and growth mechanisms of InN and InGaN nanowires.

As a reference, InN layers were grown using a state-of-the-art interval growth method. Their properties were comparable to other high quality samples reported in literature and were suitable as a reference system for investigating the properties of nanowires.

The high crystal quality expected for nanowires was confirmed by Raman scattering spectroscopy, as well as by transmission electron microscopy (TEM) parallel and perpendicular to their growth axis. Furthermore, measurement of chemical properties by X-ray photoemission spectroscopy (XPS) and scanning TEM-electron energy loss spectroscopy (EELS) showed that a surface oxide formed at InN nanowires with a thickness about 1 nm or less.

First of all, nanowire-field effect transistor (NWFET) measurements proved, that electrons were the majority carriers in InN nanowires. However, the influence of the contacts hindered reliable determination of charge carrier mobilities. The electrical resistivity of single MBE-grown InN nanowires was determined for the first time without the effects of contacts resistances in four-point probe measurements. The existence of a surface accumulation layer was confirmed by the normalized resistance-diameter relation. Further, since the standard method using Hall measurements to determine the concentration and mobility of the charge carriers is challenging for nanowires, optical methods of analysis were used instead. Raman scattering spectroscopy confirmed the existence of regions with different carrier concentrations within the nanowires by the coexistence of modes which indicated a high and low electron concentration. The donor concentration and surface state density were independently deduced by the detailed analysis of photoluminescence (PL) and PL-excitation (PLE) results in combination with calculation of the electron distribution. These were determined to be in the range of $3.5\times10^{17} - 2\times10^{18}$ cm^{-3} and 1-2$\times10^{13}$ cm^{-2}, respectively. A higher V:III ratio seemed to lead to lower donor concentrations. Using the resulting carrier concentration, the mobility at room temperature was estimated to be in the range of 2400-4800 cm^2/(Vs) inside the wire core and about 600 cm^2/(Vs) in the electron accumulation layer. This is in agreement with the reported mobilities for such carrier concentrations in layers. In literature, neither theoretical calculations predict nor measurements observed electron accumulation on clean non-polar surfaces. Therefore, it is suggested that donor-like states at the InN/InO interface caused a downward band-bending leading to an electron accumulation at the nanowire sidewall surfaces. The properties of these nanowires were controlled by the density of donor-states induced at the indium oxide and nitride interface, as well as the concentration of residual donors in the core. The carrier concentrations in the core are among the lowest and the mobilities the highest reported in literature. This indicates, that the InN nanowire cores were of high quality and with low residual doping. To expand the outstanding properties of the InN nanowire core to the whole wire, a proper surface treatment to suppress the electron accumulation must be found.

For most applications in light emitting diodes (LED) and solar cells, the band gap of InN is too small and must be increased by adding Ga. The high crystal quality typical for nanowires makes the growth of InGaN in the form of nanowires attractive, since InGaN is generally defect-rich due its limited miscibility and high lattice mismatch to most substrates.

Therefore, InGaN wires were grown at low temperatures of 400-500°C with different Ga mole fractions. The general suitability of MBE for synthesis of InGaN nanowires over the whole compositional range was confirmed by the growth nanowires with an In to Ga ratio of about 1:1 in the

center of the immiscibility gap. X-ray diffraction (XRD) and PL measurements indicate a fluctuation of the Ga mole fraction by ±20-30%, but no phase separation. The morphologies of these samples were similar to porous columnar layers and the substrate surfaces were nearly completely covered by InGaN.

To further study the nearly unexplored MBE-growth of In-rich InGaN nanowires, three sample series with a Ga mole fraction from 7% to 26% in the supplied metal were grown. The morphologies were comparable among the series and below the critical temperature for pure InN nanowire growth at 450°C, as well as to samples without Ga supply. But the growth was significantly changed compared to the series with a Ga mole fraction of about 1:1. The substrates were only partially covered by nanowires and they were much longer than expected from the metal flux, if it would be grown as a compact layer. This indicates diffusion-induced nanowire growth. The reduction of the relative Ga content in the nanowires deduced from PL and XRD measurements was quantitatively explained by a diffusion growth model under the assumption that only In diffused and Ga incorporated, where it impinged. Accordingly, In diffusion increased the growth rate of the nanowires and therefore lowered the effective Ga-to-In ratio at the growing surface. The Ga distribution inside single wires is the focus of the current research activity by M. Gomez and J. Segura.

To gain further insight into the nucleation and growth processes of InN and In-rich InGaN nanowires, the concept of monitoring the evolution of growth rate for single nanowires by introducing markers was adapted. For this purpose, InN nanowires with InGaN markers were grown at a typical temperature for InN growth to monitor their length as a function of time. Their morphologies, as well as their size and density, were similar to pure InN or In-rich InGaN nanowires. Nanocolumns started to grow from the very beginning, but additional wires formed at least during the first two hours of growth, since not all wires showed the complete sequence of markers. The observed growth rate was nearly constant and equal for the investigated wires. This was assigned to the fact, that no In desorbed and the adatom concentration on the top-facets was nearly independent of the nanowire length and diameter. Furthermore, the wires showed discrete reductions in the growth rate. This was assigned to nucleation taking place close to the investigated nanowires during growth.

The random uncontrolled nucleation of nanowires led to variations in size, properties, distribution and, for InGaN, to variation in Ga content. Hence, control over nucleation is essential to obtain nanowires with exact control of properties. Therefore, several mask materials to suppress nucleation were tested and position-controlled growth of nanowires could be demonstrated by an approach based on molybdenum masks.

In conclusion, this thesis addressed some fundamental questions about InN and the growth of InN and InGaN nanowires. In particular, a consistent picture of electron concentration and distribution, as well as their impact on conductivity was developed with regard to surface modifications. Furthermore, In-rich InGaN nanowires were successfully synthesized and important aspects of their growth were understood. Furthermore, the first steps towards position- and size-controlled growth of single InN nanowires were achieved.

Appendix

A. List of abbreviations

BEP	beam equivalent pressure
DFT	density-functional theory
CBM	conduction band minimum
CBE	chemical beam epitaxy
CVD	chemical vapor deposition
EELS	electron energy loss spectroscopy
ELOG	epitaxial layer overgrowth
FIB	focused ion beam
FET	field effect transistor
FWHM	full width at half maximum
HAADF-STEM	high-angle annular dark-field scanning transmission electron microscopy
HVPE	hydride vapor phase epitaxy
LD	laser diode
LED	light emitting diode
MBE	molecular beam epitaxy
ML	monolayer
MOCVD	metalorganic chemical vapour deposition
NWFET	nanowire field effect transistor
PID	proportional-integral-derivative
PL	photoluminescence spectroscopy
PLE	photoluminescence excitation spectroscopy
PLP	coupled plasmon-LO-phonon
QMSA	quantitative mobility spectrum analysis
Raman spectroscopy	Raman scattering spectroscopy
RHEED	reflection high energy electron diffraction
RT	room temperature

SAG	selective area growth
SEM	scanning electron microscopy
STEM	scanning tunneling electron microscopy
TEM	tunneling electron microscopy
UHV	ultra high vacuum
VBM	valence band minimum
VLS	vapor-liquid-solid
XPS	X-ray photoelectron spectroscopy
XRD	X-ray diffraction
YSZ	Yttria-stabilized zirconia

B. List of experimental setups

MBE: Veeco “GEN II” MBE system with a Veeco “UNI-bulb RF” nitrogen plasma source and metal effusion cells

SEM: Zeiss Leo Supra 35

Electron beam lithography: Raith eline-system and Zeiss Leo Supra 35 with a Raith Elphy lithography control unit

FIB: Nova NanoLab 600

TEM: Philips CM200-UT FEG (H. Schumann and A. Urban, University of Göttingen)

XPS: Custom-build XPS system with a monochromatic Al-K_{α} X-ray source and 126 mm mean radius hemispherical energy analyzer with a multichannel electron detector (M. Carsten, University of Göttingen)

XRD: Bruker AXS D8 Advance Diffractometer with a monochromatic Cu-K_{α} X-ray source and Yttrium Aluminum Perovskite activated by Ce3+ (YAP:Ce) scintillation crystal detector

PL: PL-setup pf the University of Valencia (Spain) with an Ar^{+}-laser for excitation, a He-cryostat to control the temperature of the sample (7K-300K) and a 0.19 m monochromator with a 600 groove/mm grating with an InGaAs photodiode (cutoff wavelength of 2.2 µm) for detection of the emitted light

PLE: PLE-setup of the University of Campinas (Brazil) with a tunable monochromatic light source (50 W tungsten halogen lamp dispersed with a single grating monochromator, focal distance 1 m and grating of 600 groove/mm), liquid-He cryostat (T$\approx 6K$) for sample cooling, a double monochromator with a focal distance of 0.75-m with gratings of 600 grooves per millimeter and an InAs detector for the detection of emitted light

Raman spectroscopy: Micro-Raman scattering setup of the University of Valencia (Spain) with a 514.5 nm line from an Ar+ laser focused by a 100x microscope objective for excitation of the sample at room temperature in back-scattering configuration and a Jobin Yvon T64000 triple spectrometer with a liquid-nitrogen-cooled charge coupled device for detection of the scattered light

Electrical measurements at room temperature: Suss Microsystems Probe Station PM5 with an Agilent Technologies 4155C Parameter Analyzer and simple capacitors of 10 nF connected from the contact needles to the ground in order to protect the wire from high frequency signals

Electrical measurements as a function of temperature: Janis Research STVP-300T-MOD continuous flow He-cryostat with the filter unit described in section 7.4.2, with a Keitley 2400 sourcemeter and two Keithley 2000/2010 multimeters

C. InGaN nanowire morphologies

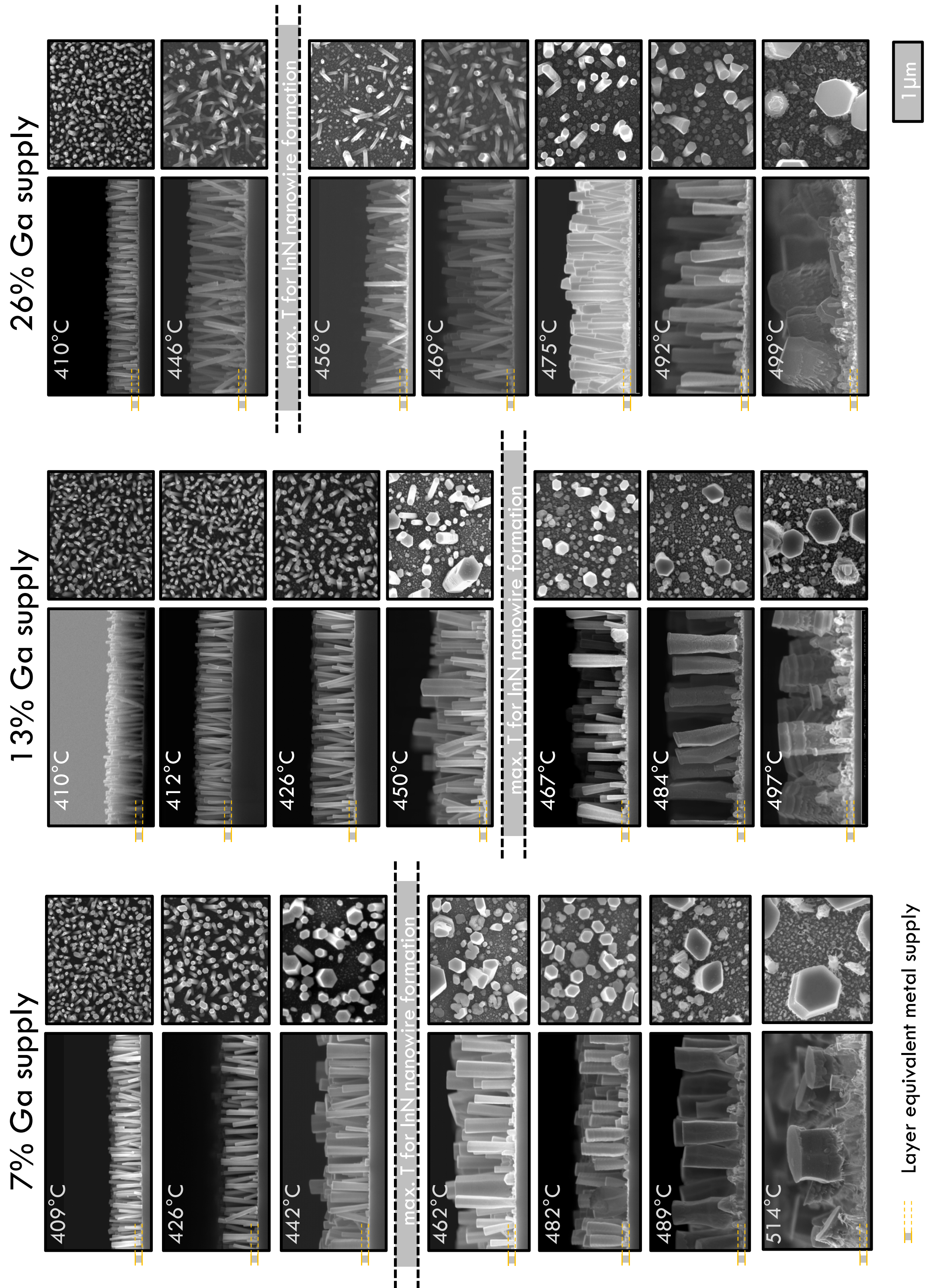

Figure C.0.1.: *Morphologies of the three In-rich InGaN nanowire growth series*

D. Equilibrium nucleation

The in section 5.3 presented model for nucleation enables the calculation of the nucleation rate depending on the growth conditions. The aim of this part of the appendix is to deduce the nucleation rate depending on the growth conditions, in particular on the control parameters of MBE growth. The variables of following equations were already introduced in section 5.3.

D.1. Nucleation rate for vapor deposition with desorption

To calculate the nucleation rate for vapor deposition with desorption, an expression for the impingement rate of building units to a nucleus of critical must be found. As shown, i.e in Markov (1995), the equilibrium concentration of adatoms with an impingement rate F to the substrate and an adatom life time of

$$\tau_s = \frac{1}{\nu} e^{E_{des}/k_B T} \tag{D.1.1}$$

the density of adatoms is approximated by

$$N_1 \approx n_s = F\tau_s = \frac{F}{\nu} e^{E_{des}/k_B T} \tag{D.1.2}$$

Assuming a diffusion towards the nuclei of $j_S = D_S \nabla n_s \approx D_s \frac{n_s}{a} = Fae^{(E_{des}-E_{diff})/k_B T}$ with the diffusion constant $D_S = a^2 \nu e^{E_{diff}/kT}$ and accounting only for the diffusive impingement to critical nuclei the impingement rate of atoms towards a critical nuclei is given by the relation

$$\omega_{cr} = \underbrace{6a_{edge\ cr}}_{\text{periphery of footprint}} \underbrace{Fae^{(E_{des}-E_{diff})/k_B T}}_{\text{diffusion flux to nuclei}} \tag{D.1.3}$$

with

$$a_{edge\ cr} = \frac{2}{3} \sqrt[3]{\frac{2}{3\sqrt{3}}} \sqrt[3]{\frac{\sigma_m}{\sigma_{c+} + \sigma_{ci}}} \sqrt[3]{v_c} \left(\frac{k_{surf}}{\Delta\mu_{vc}} \right) \tag{D.1.4}$$

Now the nucleation rate

$$J = \omega_{cr} n_s \Gamma e^{-\Delta G_{cr}/k_B T} \tag{D.1.5}$$

can be calculated using

$$n_{cr} = \frac{8}{27} \left(\frac{k_{surf}}{\Delta\mu_{vc}} \right)^3 = \underbrace{\frac{8}{27} \left(6\sqrt[3]{\frac{2}{3\sqrt{3}}} + \sqrt[3]{\frac{2}{3}\sqrt{3}} \right)^3}_{\approx 47.01} v_c^3 \sigma_m^2 \left(\sigma_{c+} + \sigma_{ci} \right) \frac{1}{\Delta\mu^3} \tag{D.1.6}$$

and

$$\Delta G_{cr} = \frac{4}{27} \frac{k_{surf}^3}{\Delta\mu^2} = \underbrace{\frac{4}{27} \left(6\sqrt[3]{\frac{2}{3\sqrt{3}}} + \sqrt[3]{\frac{2}{3}\sqrt{3}} \right)^3}_{\approx 23.50} v_c^2 \sigma_m^2 \left(\sigma_{ci+} \sigma_{c+} \right) \frac{1}{\Delta\mu^2} \tag{D.1.7}$$

This leads to:

$$J = \underbrace{\underbrace{6a_{edge\ cr}}_{\text{periphery of footprint}} \underbrace{Fae^{(E_{des}-E_{diff})/k_BT}}_{\text{Diffusion flux to nuclei}}}_{\omega_{cr}} \underbrace{\frac{F}{\nu}e^{E_{des}/k_BT}}_{n_s} \underbrace{\frac{3}{4}\sqrt{\frac{1}{\pi k_BT}}\frac{\Delta\mu^2}{k_{surf}^{3/2}}}_{\Gamma} e^{-\frac{4}{27}\frac{k_{surf}^3}{\Delta\mu^2}/k_BT} \tag{D.1.8}$$

$$J = 6\frac{2}{3}\sqrt[3]{\frac{2}{3\sqrt{3}}}\sqrt[3]{\nu_C}\frac{a}{\nu}\frac{3}{4}\sqrt{\frac{1}{\pi k_BT}}\sqrt[3]{\frac{\sigma_m}{\sigma_{c+}+\sigma_{ci}}}\frac{\Delta\mu}{k_{surf}^{1/2}}F^2 e^{\left((2E_{des}-E_{diff})-\frac{4}{27}\frac{k_{surf}^3}{\Delta\mu^2}\right)\frac{1}{k_BT}} \tag{D.1.9}$$

or

$$J = c_1\frac{a}{\nu}\sqrt{\frac{1}{\pi k_BT}}\sqrt{\frac{1}{(\sigma_{c+}+\sigma_{ci})}}\Delta\mu F^2 e^{\left((2E_{des}-E_{diff})-c_2\frac{\nu_c^2\sigma_m^2(\sigma_{ci+}\sigma_{c+})}{\Delta\mu^2}\right)\frac{1}{k_BT}} \tag{D.1.10}$$

with $c_1 = 3\sqrt[3]{\frac{2}{3\sqrt{3}}}\left(6\sqrt[3]{\frac{2}{3\sqrt{3}}}+\sqrt[3]{\frac{2}{3}\sqrt{3}}\right)^{-1/2} \approx 0.94$ and $c_2 = \frac{4}{27}\left(6\sqrt[3]{\frac{2}{3\sqrt{3}}}+\sqrt[3]{\frac{2}{3}\sqrt{3}}\right)^3 \approx 23.50$.

Now, the nucleation rate of III-N growth under N-rich conditions with desorption can calculated as a function of substrate temperature and fluxes using the relations of section 4.1. The equation for J is rewritten with F replaced by the limiting flux F_{In}.

$$J = \overbrace{c_1\frac{a}{\nu}\sqrt{\frac{1}{\pi k_B}}\sqrt{\frac{1}{(\sigma_{c+}+\sigma_{ci})}}}^{=c'_!} T^{-1/2}\Delta\mu(F_N,F_{In},T)\, F_{In}^2 e^{\left(\overbrace{(2E_{des}-E_{diff})/k_B}^{=c'_2}-\frac{\overbrace{c_2\nu_c^2\sigma_m^2(\sigma_{ci+}\sigma_{c+})/k_B}^{=c_{3'}}}{\Delta\mu(F_N,F_{In},T)^2}\right)\frac{1}{T}} \tag{D.1.11}$$

$$\Leftrightarrow J = c'_1\ T^{-1/2}\Delta\mu(F_N,F_{In},T)\, F_{In}^2 e^{\left(c'_2-\frac{c'_3}{\Delta\mu(F_N,F_{In},T)^2}\right)\frac{1}{T}} \tag{D.1.12}$$

$$\text{with } \Delta\mu = \Delta\mu_{N-rich}^{vs}(F_{In},F_N,T) \approx k_BT\ \ln\frac{F_{In}}{F_{0In}(F_{0N},T)}$$

$$\text{or } \Delta\mu = \Delta\mu_{N-rich}^{vs}(F_{In},F_N,T) \approx E_a\ \ln\left(\frac{A}{F_{In}}\right) - E_a\ \ln\left(e^{-E_a/k_BT}-\frac{F_N}{A}\right)$$

This leads to following expression for the nucleation rate

$$\Rightarrow J(F_N,F_{In},T) = E_a c'_1\ T^{-1/2}\left(\ln\left(\frac{A}{F_{In}}\right)-\ln\left(e^{-E_a/k_BT}-\frac{F_N}{A}\right)\right) F_{In}^2 e^{\left(c'_2-\frac{c'_3/E_a^2}{\left(\ln\left(\frac{A}{F_{In}}\right)-\ln\left(e^{-E_a/k_BT}-\frac{F_N}{A}\right)\right)^2}\right)\frac{1}{T}} \tag{D.1.13}$$

D.2. Nucleation rate for vapor deposition without desorption

Similar to the case of nucleation rate for vapor deposition with desorption, it is possible to derive a time depend steady state approximation for the nucleation rate if no desorption occurs. The only factor that changes in the equation is the adatom density which now becomes time depend

$$n_s(t) = Ft \tag{D.2.1}$$

with F the impinging flux and t the time. From this the following expression for the rate of im-

pingement to a nucleus of critical size follows.

$$\omega_{cr}(t) = j_s \underbrace{6a_{edge\ cr}}_{\text{periphery}} = 6a_{edge\ cr}(D_s \nabla n_s) \approx 6a_{edge\ cr} D_s \frac{n_s}{a_{diff}} \tag{D.2.2}$$

With $a_{edge\ cr}$ as

$$a_{edge\ cr} = \frac{2}{3}\sqrt[3]{\frac{2}{3\sqrt{3}}}\sqrt[3]{\frac{\sigma_m}{\sigma_{c+}+\sigma_{ci}}}\sqrt[3]{v_C}\left(\frac{k_{surf}}{\Delta\mu_{vc}}\right) \tag{D.2.3}$$

it follows

$$\Rightarrow \omega_{cr}(t) \approx 4\sqrt[3]{\frac{2}{3\sqrt{3}}}\sqrt[3]{\frac{\sigma_m}{\sigma_{c+}+\sigma_{ci}}}\sqrt[3]{v_C}\left(\frac{k_{surf}}{\Delta\mu_{vc}}\right) F t a_{diff} \nu e^{-E_{diff}/k_b T} \tag{D.2.4}$$

Γ, n_{cr}, a_{cr} and ΔG_{cr} do not change compared to the case with desorption and are therefore as following

$$\Delta G_{cr} = \frac{4}{27}\frac{k_{surf}^3}{\Delta\mu^2} = \underbrace{\frac{4}{27}\left(6\sqrt[3]{\frac{2}{3\sqrt{3}}}+\sqrt[3]{\frac{2}{3}\sqrt{3}}\right)^3}_{\approx 23.50} v_c^2 \sigma_m^2 (\sigma_{ci+}\sigma_{c+}) \frac{1}{\Delta\mu^2} \tag{D.2.5}$$

$$\Gamma = \sqrt{\frac{\Delta G_{cr}}{3\pi k_B T}}\frac{1}{n_{cr}} = \frac{3}{4}\sqrt{\frac{1}{\pi k_B T}}\frac{\Delta\mu^2}{k_{surf}^{3/2}} \tag{D.2.6}$$

$$n_{cr} = \frac{8}{27}\left(\frac{k_{surf}}{\Delta\mu_{vc}}\right)^3 = \underbrace{\frac{8}{27}\left(6\sqrt[3]{\frac{2}{3\sqrt{3}}}+\sqrt[3]{\frac{2}{3}\sqrt{3}}\right)^3}_{\approx 47.01} v_c^3 \sigma_m^2 (\sigma_{c+}+\sigma_{ci}) \frac{1}{\Delta\mu^3} \tag{D.2.7}$$

This enables the calculation of the nucleation rate $J(t)$

$$J(t) = \omega_{cr}(t) n_s(t) \Gamma e^{-\Delta G_{cr}/k_B T} \tag{D.2.8}$$

$$J(t) = \underbrace{4\sqrt[3]{\frac{2}{3\sqrt{3}}}\sqrt[3]{\frac{\sigma_m}{\sigma_{c+}+\sigma_{ci}}}\sqrt[3]{v_C}\left(\frac{k_{surf}}{\Delta\mu_{vc}}\right) F t a_{diff} \nu e^{-E_{diff}/k_b T}}_{\omega_{cr}} \underbrace{Ft}_{n_s} \underbrace{\frac{3}{4}\sqrt{\frac{1}{\pi k_B T}}\frac{\Delta\mu^2}{k_{surf}^{3/2}}}_{\Gamma} e^{-\overbrace{\frac{4}{27}\frac{k_{surf}^3}{\Delta\mu^2}}^{\Delta G_{cr}}/k_B T} \tag{D.2.9}$$

$$\Rightarrow J(t) = 3\sqrt[3]{\frac{2}{3\sqrt{3}}}\sqrt[3]{\frac{\sigma_m}{\sigma_{c+}+\sigma_{ci}}}\sqrt[3]{v_C}(Ft)^2 a_{diff} \nu e^{-E_{diff}/k_b T}\sqrt{\frac{1}{\pi k_B T}}\frac{\Delta\mu}{k_{surf}^{1/2}} e^{-\frac{4}{27}\frac{k_{surf}^3}{\Delta\mu^2}/k_B T} \tag{D.2.10}$$

$$\Rightarrow J(t) = c_1 (Ft)^2 a_{diff} \nu \sqrt{\frac{1}{\pi k_B T}}\sqrt{\frac{1}{\sigma_{c+}+\sigma_{ci}}}\Delta\mu e^{-\left(E_{diff}+c_2\frac{v_c^2\sigma_m^2(\sigma_{ci+}\sigma_{c+})}{\Delta\mu^2}\right)\frac{1}{k_B T}} \tag{D.2.11}$$

with $c_1 = 3\sqrt[3]{\frac{2}{3\sqrt{3}}}\left(6\sqrt[3]{\frac{2}{3\sqrt{3}}}+\sqrt[3]{\frac{2}{3}\sqrt{3}}\right)^{-1/2} \approx 0.94$ and $c_2 = \frac{4}{27}\left(4+\sqrt{3}\right)^3 \approx 27.9$.

Now, the nucleation rate for III-N growth under N-rich conditions without desorption can be given as a function of the substrate temperature and the fluxes. The equation J is rewritten with F replaced

by the limiting flux F_{In}

$$J(t) = \overbrace{c_1 a_{diff} \nu \sqrt{\frac{1}{\pi k_B}} \sqrt{\frac{1}{\sigma_{c+} + \sigma_{ci}}}}^{c_1''} T^{-1/2} \Delta\mu(F_N, F_{In}, T) \, (Ft)^2 \, e^{-\left(\overbrace{E_{diff}/k_B}^{c_2''} + \frac{\overbrace{c_2 \nu_c^2 \sigma_m^2 \left(\sigma_{ci+} \sigma_{c+}\right)/k_B}^{c_3''}}{\Delta\mu(F_N, F_{In}, T)^2}\right)\frac{1}{T}} \tag{D.2.12}$$

$$\Rightarrow J(t) = c_1'' \, T^{-1/2} \Delta\mu(F_N, F_{In}, T) \, (Ft)^2 \, e^{-\left(c_2'' + \frac{c_3''}{\Delta\mu(F_N, F_{In}, T)^2}\right)\frac{1}{T}} \tag{D.2.13}$$

$$\text{with } \Delta\mu^{ls}_{N-rich}(T, F_N) \approx \frac{\Delta s_m}{T_e(F_N)} (T - T_e(F_N))$$

$$\text{or } \Delta\mu^{ls}_{N-rich}(T, F_N) \approx \Delta s_m \frac{k_B T}{E_a} \ln\left(\frac{A}{F_N}\right) - \Delta s_m$$

This leads to following expression for the nucleation rate:

$$\Rightarrow J(t, F_N, F_{In}, T) = c_1'' \Delta s_m \, T^{-1/2} \left(\frac{k_B T}{E_a} \ln\left(\frac{A}{F_N}\right) - 1\right) (Ft)^2 \, e^{-\left(c_2'' + \frac{c_3''}{\left(\Delta s_m \frac{k_B T}{E_a} \ln\left(\frac{A}{F_N}\right) - \Delta s_m\right)^2}\right)\frac{1}{T}} \tag{D.2.14}$$

E. Nitrogen spectra

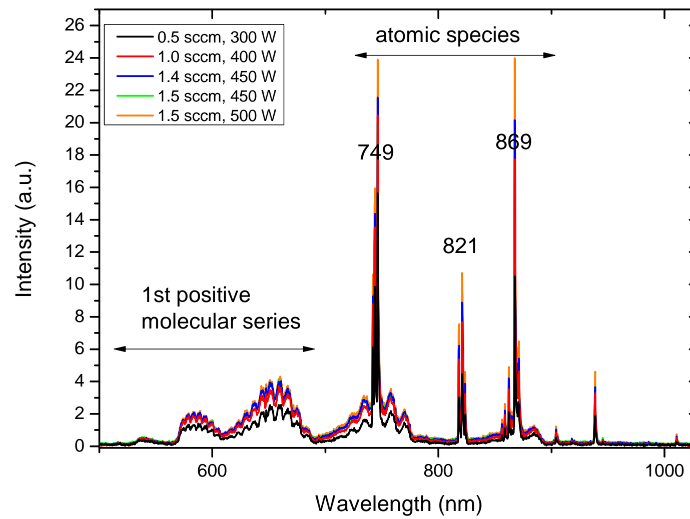

Figure E.0.1.: *Emission spectra of the Veeco "UNI-Bulb RF" nitrogen plasma source at several typical operation conditions*

F. Curriculum vitae

Lebenslauf

Name: Christian Denker

Geburtsdatum: 4.8.1980
Geburtsort: Oldenburg (Oldb)
Staatsangehörigkeit: deutsch
Familienstand: ledig

Anschrift: Untere-Masch-Straße 4,
37073 Göttingen
E-mail: Christian.Denker@gmx.de

Bildungsweg

9/2007-11/2011
Promotion, Fachrichtung Physik
Georg-August-Universität, Göttingen
IV. Physikalisches Institut, Halbleiterphysik
„InN and In-rich InGaN Nanocolumns by Molecular Beam Epitaxy"

9/2001-7/2007
Diplom, Fachrichtung Physik
Georg-August-Universität, Göttingen
Diplomarbeit am IV. Physikalischen Institut, Halbleiterphysik
„InN Nanodähte durch Selbstorganisation in der Molekularstahlepitaxie"

8/1997-6/2000
Allgemeine Hoschschulreife
Berufsbildende Schulen II der Stadt Oldenburg
Fachgymnasium Technik

8/1993-7/1997 Altes Gynmasium Oldenburg
8/1991-6/1993 Orientierungstufe am Flötenteich
8/1987-7/1991 Grundschule Ohmstede

Berufliche Tätigkeiten

Wissenschaftlicher Mitarbeiter
9/2007-10/2011
Georg-August-Universität, Göttingen
IV. Physikalisches Institut, Halbleiterphysik
Forschung und Lehre

Studentische Hilfskraft
1/2005-12/2006 DLR_School_Lab, Göttingen
3/2002-7/2002 Georg-August-Universität Göttingen, Tutorium für Physik II

Zivildienst
9/2000-7/2001 AWO Kinder- und Jugendhaus „TREFF – Hasport", Delmenhorst

G. List of publications

- J. Segura-Ruiz, G. Martinez-Criado, J. A. Sans, R. Tucoulou, P. Cloetens, I. Snigireva, C. Denker, J. Malindretos, A. Rizzi, M. Gomez-Gomez, N. Garro and A. Cantarero
  „*Direct observation of elemental segregation in InGaN nanowires by X-ray nanoprobe*"
  Physica Status Solidi Rapid Research Letters 1, 1-4 (2011)

- A. Cantarero, A. Cros, N. Garro, M.I. Gómez-Gómez, A. García, M.M .de Lima, B. Daudin, A. Rizzi, C. Denker and J. Malindretos
  „Optical properties of nitride nanostructures"
  Annalen der Physik, 523 (1-2), 51-61 (2011)

- J. Segura-Ruiz, A. Molina-Sánchez, N. Garro, A. García-Cristóbal, A. Cantarero, F. Iikawa, C. Denker, J. Malindretos, and A. Rizzi
  „Inhomogeneous free-electron distribution in InN nanowires: Photoluminescence excitation experiments"
  Physical Review B, 82, 125319 (2010)

- J. Segura-Ruiz, N. Garro, A. Cantarero, C. Denker, J. Malindretos and A. Rizzi
  „Optical studies of MBE-grown InN nanocolumns: Evidence of surface electron accumulation"
  Physical Review B, 79, 115305-115309 (2009)

- F. Werner, F. Limbach, M. Carsten, C. Denker, J. Malindretos and A. Rizzi
  „Electrical Conductivity of InN Nanowires and the Influence of the Native Indium Oxide Formed at Their Surface"
  Nano Letters 9(4), 1567-1571 (2009)

- J. Segura-Ruiz, N. Garro, A. Cantarero, F. Iikawa, C. Denker, J. Malindretos and A. Rizzi
  "Optical properties of InN nanocolumns: Electron accumulation at InN non-polar surfaces and dependence on the growth conditions"
  Physica Status Solidi (c), 6, (S2), S553–S556 (2009)

- J. Segura-Ruiz, N. Garro, A. Cantarero, C. Denker, F. Werner, J. Malindretos and A. Rizzi
  "Photoluminescence and Raman spectroscopy of MBE-grown InN nanocolumns"
  Physica Status Solidi (c), 5 (6), 1678–1681, (2008)

- C. Denker, J. Malindretos, F. Werner, F. Limbach, H. Schuhmann, T. Niermann, M. Seibt and A. Rizzi
  „Self-organized growth of InN-nanocolumns on p-Si(111) by MBE"
  Physica Status Solidi (c), 5 (6), 1706-1708 (2008)

List of Figures

2.1.1 Comparison of zincblende and wurzite crystal structure. a) Unit cells, b) stacking sequences of wurzite structure in the (0001) direction and zincblende in the (111) direction, c) wurzite unit cell with important planes, d) first Brillouin zone for wurzite crystals showing points of high-symmetry and directions according to the Koster notation. Figures c) and d) are taken from Segura-Ruiz (2009). 4

2.1.2 Calculated frequencies of the $PLP^{\pm}$ modes in InN as function of electron concentration (Segura-Ruiz, 2009 and Lazic, 2008). 5

2.1.3 Equilibrium vapor pressure of nitrogen and metals over III-N semiconductors (adapted from Wang & Yoshikawa (2004)). Vertical and horizontal lines indicate typical nitrogen pressures and growth temperatures used in MBE. 6

2.2.1 Calculated band structures of a) InN (Mahboob *et al.*, 2004) and b) GaN (Fritsch *et al.*, 2003). E_{FS} denotes the Fermi-level stabilization energy. 7

2.2.2 a) Burstein-Moss-shift (Walukiewicz *et al.*, 2004) and b) increase of effective mass with electron concentration (Rinke *et al.*, 2009) for InN (Symbols represent experimental data and solid lines calculations). 7

2.2.3 Temperature dependence of InN band gap as reflected in the absorption edge and photoluminescence of a thick layer (7.5 µm) layer and photoluminescence of nanocolumns. 8

2.2.4 a) The empirical rule $m_e^* = 0.06\ E_g$ for several semiconductors (adapted from Nag (2003)). b) The simulated electron drift velocity depending on electric field. For "InN revised", $E_g = 0.75\ eV$ and $m_e^* = 0.045\ m_e$ were used and for "InN traditional", $E_g = 1.9\ eV$ and $m_e^* = 0.11\ m_e$ (O'Leary *et al.*, 2010). 9

2.2.5 On the left, the dependence of the band gap on In concentration in AlInN and InGaN alloys is shown. On the right, the band offset for these alloys are shown as deduced from a valence band offset for InN/GaN of 1eV (taken from Walukiewicz *et al.* (2004)). 10

2.2.6 a) Sketch of the observed band bending at the c-plane surfaces for n-type InN and GaN. b) The calculated density of states of bulk and surface of polar and non-polar surfaces (Segev & van de Walle (2006) and Segev & Van de Walle (2007)). 11

2.3.1 a) Overview of quantum structures and their density of states (Buhro & Colvin (2003); Waser (2003)), b) Sketch of increase of band gap with diameter (Buhro & Colvin, 2003), c) Calculated increase of lowest quantized energy level in a quantum well with infinite barrier height depending on its thickness (Compare also Denker (2007)). . . . 12

2.4.1 a) Nanowire solar cell and sensor on one chip (Tian *et al.*, 2009), b) InN nanowire p-i-n solar cell on silicon (Nguyen *et al.*, 2011), c) InGaN nanowire LEDs on silicon (Kikuchi *et al.*, 2004) , d) tunable quantum dots made of InAs nanowires (Fasth *et al.*, 2005). 13

3.3.1 Calculated phase diagram compared to experimental data. The solid line indicates the binodal curve and the dashed one the spinodal (Stringfellow, 2010). 18

4.0.1 a) Sketch of an MBE system. b) Image of the "Veeco GEN II" MBE system, in the inset the source flange with cryo shield, cells and shutters is shown. 20

4.1.1 p-T phase diagram of a) GaN Newman (1997), b) sketch of metastable growth model of Newman (1997) and c) InN with marked MBE window. The grey area indicates the conditions, under which InN is unstable according to Newman (1997) and Onderka *et al.* (2002). 20

4.4.1 Sketch of sample holder and heater with thermocouple and pyrometer for temperature measurement. 23

4.4.2 a) and c) Assembly of the sample holder for 1x1cm² and 2" samples, b) difference between a original retainer plate from Veeco and the home build one, d) mounting plates for five 1x1cm² samples and one 1/4 of 2" sample. 24

4.4.3 Substrate temperature measured by a "Ircon modline 3" 3V-13C10 as a function of the thermocouple temperature. 25

4.4.4 a) Thermocouple and substrate temperature as a function of time for a two inch silicon substrate with a clear over shot of the substrate temperature if the thermocouple temperature is changed , b) deviation of substrate temperature from the equilibrium value as a function of time for cooling down to a thermocouple temperature of 400, 450, 500°C with 10°C/min. (The temperature was measured by a "Ircon Modline 3, 3W-08C02" pyrometer). 26

4.4.5 Flux of the effusion cells: a) Flux from In, Ga and Al cells in monolayers (ML) (half c-lattice spacing) per second, if all metal incorporated into a compact III-nitride layer, b-d) Flux in $\frac{1}{cm^2\, s}$, $\frac{nm}{s}$ and $\frac{c}{s} = \frac{ML}{s}$ for b) In, c) Ga and d) Al (data from January the 11th to 13th, 2011) 27

4.4.6 a) Sketch of nitrogen plasma source (adapted from Franke (2009)), b) Image of a Veeco "UNI-Bulb RF" plasma source with matching unit and power supply (Veeco, 2009) , c) Picture of an aperture plate, d) Typical optical emission spectrum of an Veeco "UNI-Bulb RF" plasma source (Veeco, 2009) 29

5.2.1 a) Illustration of the Wulff construction for the aspect ratio of free III-nitrides nanowires, b) the effect of increasing interface energy on the equilibrium shape for crystals on a foreign substrate. 34

5.2.2 Surface energy calculations for GaN a) (0001), b) $(10\bar{1}0)$ and c) $(11\bar{2}0)$ from Segev & Van de Walle (2007) and Northrup & Neugebauer (1996) 35

5.2.3 Equilibrium cross section of GaN nanowires in c-direction deduced by the Wulff rule. 36

5.2.4 Equilibrium cross section of InN nanowires in c-direction deduced by the Wulff rule. 36

5.2.5 Ratios of the m- and a-plane facet lengths for the equilibrium cross section for wurzite nanowires growing in c-direction deduced by the Wulff rule as a function of the specific surface energy ratio. The equilibrium conditions given by Wulff rule were numerically calculated for some discrete values. 37

5.5.1 Illustration of the geometry and the different contributions for nanowire growth by MBE. 42

6.1.1 Growth rate of InN as function of Indium supply under nitrogen flux of 1.5 sccm and activation power of 450 W. The black dashed line has a slope of one. The growth rate under nitrogen rich conditions is increased due to the porosity of the grown material. The red and black lines are visual guidelines for the increment of the growth rate as a function of metal supply under metal rich conditions. The intersection of the dashed line and the straight lines enable estimation of the stoichiometric point. The stoichiometry was determined to be at ca. 9.5 nm/min In supply. Its estimated uncertainty is indicated by the gray area. InN droplet formation is observed on samples grown with a metal higher than ca. 12.5 nm/min, indicated by the green area. The 1x1 cm² samples were grown using the original Veeco 1x1 cm² holder at a heater temperature of T_{thermo} = 450°C. 48

6.2.1 Surface morphology of InN samples grown on sapphire under different III:V ratios. The images show representative results of optical, scanning electron and atomic force microscopy. AFM measurements of G0368 and G0371 were not carried out because no meaningful results could be observed due to high porosity. 50

6.3.1 Three representative samples grown with a 1 step procedure without RHEED control. a) growth conditions, b) SEM images of the surface, c) photoluminescence spectra at 5K and d) XRD $\Theta - 2\Theta$ scans with the monochromatic Cu-K_α-line. 51

6.4.1 Initial layers of InN on a GaN template. a) The evolution of the intensity of RHEED intensity with time as well as In and N supply. b) Characteristic images of the RHEED pattern for the different stages of InN on GaN. 55

6.4.2 a) Typical evolution of the RHEED intensity during a growth loop. The break contains more than a complete loop. Furthermore, the change in intensity between the two points indicated with “0” is due to slightly different orientations of the sample. b) Typical corresponding RHEED patterns at the steps indicated by numbers in the images and time line. 56

6.4.3 AFM topology at a) 400 µm² and b) 4 µm² areas, c) XRD Θ-2Θ scan. 57

6.4.4 Results of Hall measurements in van-der-Pauw geometry. a) Resistivity, b) Carrier concentration, c) Mobility. 59

7.1.1 Morphologies obtained under varied metal flux and substrate temperature and constant growth time of 300 min and nitrogen conditions of F_N = 2 sccm and P_N = 500 W, which corresponds to a growth rate at stoichiometry of about 12.5 nm/min (Denker (2007) and Denker *et al.* (2008); substrate temperatures T_S and fluxes are given according to calibrations in section 4.4). 62

7.2.1 a) High resolution transmission electron microscopy Si/InN interface with a 2 nm thick amorphous Si_xN_y interlayer. Cross-section TEM of single InN columns in c-direction for b) long nanocolumn of the bimodal regime and c) for one that seems to be hexagonal in SEM (a) and b) adapted from Denker (2007)). 63

7.2.2 a) Scanning-TEM of the nanowire used for EELS; the scan across the nanowire is shown in red. b) The EELS spectra recorded at the different position of the scan (measurement done by R. Schneider). 64

7.3.1 Sketch of the photoemission process in the single-particle picture. The left side shows the density of states for electrons in a sample and the right side shows the resulting emission spectra, which is shifted by the excitation energy $h\nu$ and broadened (Reinert & Huefner, 2005). 65

7.3.2 Schematic view of the experimental setup for XPS analysis of nanocolumns (Werner, 2009). 65

7.3.3 a) Sketch of XPS measurement. b) In-3d, O-1s, and N-1s core-level spectra (open circles) obtained under an emission angle of 50° and normalized to the intensity of the C-1s signal. The background is subtracted from the data (see Carsten (2010) for details). The black lines indicate the signals fitted with Voigt functions. The colored lines show the resultant single core-level contributions (Werner *et al.*, 2009). c) Model of the proposed nanowire structure: InN core with a thin native In_2O_3 shell. 67

7.4.1 Illustration of a lithography step (Denker, 2007). 68

7.4.2 Overview of nanowire contacting processes: a) Prestructured insulating substrate with markers and contact pads of about 150×150 µm² (magnification increases from left to right), b) mechanical transfer of nanowires, c) locating and contacting by SEM and e-beam lithography. 71

7.4.3 Writefield alignment procedure used in Raith lithography systems on prestructured samples (Werner, 2009). 71

7.4.4 Contacted InN nanowire (Denker, 2007). 72

7.4.5 a) Too strong etch of nanowire, b) too thin metal contact layer, c) and d) influence of geometry on effective etching rates (a), b) from Ruttke (2010); c), d) from Werner (2009)). 73

7.4.6 Schematic equivalent circuit diagram of the box used to measure IV-curves of nanowires and protect them from voltage peaks. 74

7.4.7 Schematic view a) of 2-point probe and b) 4-point probe measurement geometry. $L_{voltage\ drop}$ indicates the considered length for the voltage drop. 76

7.4.8 Voltage drop on a typical InN nanowire with a bias of 100 mV contacted in 4-point probe geometry (Werner, 2009). 77

7.4.9 Schematic view of the transmission line method. R indicates the total resistance, R_C the resistance of a contact and L the length considered for the voltage drop (Werner, 2009). 78

7.4.10 a) and b) schematic view of nanowire-FET measurements (Werner, 2009). c) Comparison of electric field between embedded and non-embedded nanowires (Wunnicke, 2006). d) Simulated electric field taking the influence of the contacts into account (Khanal & Wu, 2007). 79

7.4.11 Resistance normalized to length as function of nanowire diameter. a) 4-point probe measurements with Ar sputtering, b) 2-point probe measurements with Ar sputtering and b) 2-point-probe without Ar sputtering (Werner, 2009). 80

7.4.12 a) Ohmic I-V characteristic of a nanowire contacted with Ti/Au electrodes (-100 mV to 100 mV), b) deviation from ohmic behavior (-400 mV to 400 mV) (Werner, 2009). 81

7.4.13 Resistances measured on a single wire with four contacts in the six different combinations of 2-point probe measurements as a function of length for the voltage drop. The red dotted line shows a linear fit to extract the contact resistance and the resistance of the wire regarding all combinations. The dashed blue line shows the linear fit if the contact with the highest resistance (contact 1) is neglected. The black straight line shows the resistance as function of wire length obtained from 4-point probe measurements (Werner *et al.*, 2009). 82

7.4.14 a) Normalized conductance g as a function of the nanowire radius r, obtained by 4-point measurements on 10 nanowires of different aspect ratios. The error bars of the thin wires are of the order of the symbol size and have not been plotted for clarity. The red line shows a parabola fitted to the data points to determine the resistivities of bulk and surface. The inset shows the same data points in logarithmic scale. The blue dashed line shows a power law fit to determine the β exponent 1.6 ± 0.2 in the relation $g \propto r^{\beta}$. b) Schematic view of the InN nanowire with an InN core, a In-oxide shell and a electron accumulation layer formed at the interface according to the electrical and photoemission measurements (Werner *et al.*, 2009). 83

7.4.15 Normalized resistance R/L measured in 2-point probe configuration as a function of temperature. The bars at 300 K indicate the resistance calculated from size using $\rho_{3D} = 1.1 \times 10^{-3}\ \Omega cm$ and $\rho_{2D} = 820\ \Omega$. 84

7.5.1 SEM images of the samples used for optical characterization sorted by morphology. . 85

7.5.2 The blue line shows a Raman spectrum of an ensemble of InN nanowires with the frequencies of the phonon modes in comparison to the spectrum a high quality InN epilayer (black circles). The spectra were recorded in backscattering configuration at room temperature (Segura-Ruiz *et al.*, 2009). 86

7.5.3 A normalized photoluminescence spectrum of nanowire ensemble (G0041; open squares) in comparison to a InN layer (G0374, open triangles). The spectra were recorded at 7 K and equal excitation conditions (Segura-Ruiz *et al.*, 2009). 87

7.5.4 Change in PL spectra for two nanowire samples (left: G0071, right: G0041) with excitation power. The spectra were recorded at 7 K. I_0 corresponds to 14 mW/cm² (Segura-Ruiz, 2009). 88

7.5.5 a) Calculated downward bending of the conduction-band minimum (left axis) and the corresponding electron distribution (right axis) with distance r from the nanowire surface for surface charge densities from 10^{13} to 10^{14} 1/cm². b) Corresponding change in the frequency of the PLP^{-} mode (Segura-Ruiz *et al.*, 2009). 89

7.5.6 Calculated downward bending of the CBM and VBM in a nanowire with a radius of 50 nm close to its surface. On the left for a surface state density of N_{SS} of 5×10^{13} 1/cm² and on the right for 10^{14} 1/cm². According to the radiative recombination probability of electrons and holes, three different regions are indicated (Segura-Ruiz *et al.*, 2009). 90

7.5.7 a) Integrated PL intensity of sample G0136 as a function of temperature in an Arrhenius plot and a fit according to equation 7.5.1 (solid line). The inset shows the values of the main parameters of equation 7.5.1 determined the best fit for several nanowire samples (Segura-Ruiz *et al.*, 2009). b) Change in energy of maximum emission intensity and FWHM of the PL emission as a function of temperature for two representative samples: G0041 (full circles) and G0071 (open squares). The spectra were recorded with an excitation power of 34.4 W/cm² (Segura-Ruiz *et al.*, 2009). 90

7.5.8 Comparison of PLE and PL spectra of a representative nanocolumns sample (G0041) with a high quality InN layer (G0374) at 7 K. The black solid line and open circles correspond to the PL and PLE spectra of nanowires, respectively, while the red dashed line and open triangles to the PL and PLE of the InN layer (Segura-Ruiz, 2009). . . . 91

7.5.9 PL and PLE spectra of 4 different nanowire samples. (Dashed lines: PL; open symbols: PLE). The PLE spectra were detected at the PL peak energy of the different InN nanowire samples. Spectra are shifted along the vertical axis. The solid lines show the calculated absorption spectra with the best agreement with the experimental spectra (Segura-Ruiz, 2009). 92

7.5.10 Energy (left axis - solid symbols) and FWHM (right axis - open symbols) of the PL peaks as function of the absorption edge for all studied samples. Circles represent samples with nanocolumns and squares correspond a layer sample. The deviation of the emission energy (indicated with a dotted line as visual guide) from the absorption edge energy (dashed line) corresponds to the Stokes shift (Segura-Ruiz, 2009). 93

7.5.11 Calculated absorption spectra for InN. The open circles show the $E^{1/2}$ ideal dependence of the absorption for intrinsic bulk material. The other absorption spectra are calculated for a nanowire of 40 nm radius for two donor concentrations (N_D= 1.0×10^{17} and 5.0×10^{17} cm^{-3}), and two densities of surface states (N_{SS}= 1.0×10^{12} and 1.0×10^{13} cm^{-2}) (Segura-Ruiz *et al.*, 2010). 93

7.6.1 Carrier mobility as a function of carrier concentration for the bulk (core, $\rho_{3D} = (1.3\pm0.2)\times10^{-3}\ \Omega cm$) and surface (shell, $\rho_{2D^*} = (0.22\pm0.04)\times10^{-3}\ \Omega cm$) conduction channels assuming of an accumulation layer thickness of 4±1 nm. 95

8.2.1 $In_{1-x}Ga_xN$ with x_{supply} = 0.60: a) SEM images of morphology; the gray bar and the yellow lines indicate the metal layer equivalent thickness. b) XRD $\theta-2\theta$ scan of (0002) peak with Cu-K_α, c) PL spectra, d) deduced Ga mole fraction in the wire x_{wire}. 99

8.3.1 a) SEM images of morphology of $In_{1-x}Ga_xN$ nanowires with x=0.07 of supply. b) Length , c) diameter and d) density of $In_{1-x}Ga_xN$ nanowires for x_{supply}=0.07, 0.13, 0.26 as a function of substrate temperature. 101

8.3.2 Comparison of morphology of InN and In-rich InGaN nanowires. 102

8.3.3 a) Representative XRD $\theta-2\theta$ scans of the (0002) peak with Cu-K_α and b) normalized PL spectra for In-rich InGaN nanowires. The gray bar indicates the range of maxima in intensity of emission for pure InN. 102

8.3.4 Deduced Ga mole fraction x_{wire} of $In_{1-x}Ga_xN$ from PL and XRD measurements, as well as predicted Ga mole fraction x_{wire} by growth rate model, for x_{supply} = (a) 0.07 , (b) 0.13, (c) 0.26 as a function of substrate temperature. 104

9.1.1 a) Morphology of InN nanowires with InGaN markers and a sketch of the growth procedure. b) InN and InGaN nanowires shown for comparison. The dashed lines indicate the estimated average height as determined by visual inspection. 108

9.3.1 a) STEM images of the investigated wires. b) Length versus time diagram deduced from markers. The dotted lines indicate linear fits of the stepwise constant growth rate. 110

10.1.1 Different approaches for position-controlled growth of nanowires. a) Positioning of catalyst, b) mask with opening, c) mask and catalyst, d) defined nucleation site by a particle on the substrate. 114

10.2.1 Selective nucleation using different carbon masks: a) carbon mask by electron beam-induced deposition (EBID-C) with an exposure time of about 16 $min/\mu m^2$) on sample G0342, b) carbon mask by pulsed laser deposition (PLD-C) of 50 nm thickness on sample G0351. The growth conditions were a metal supply of 0.37 nm/min, a substrate temperature of 454°C and nitrogen conditions of P_N = 400 W and F_N = 1.0 sccm, which corresponds to a growth rate at stoichiometry of 6 nm/min (Huels, 2008). 118

10.3.1 Preparation steps for SAG samples. The degassing temperature is given as thermocouple values. The last temperature step of 630°C thermocouple temperature corresponds to 560°C of the substrate. 118

10.3.2 SEM images of (a) titanium and (b) molybdenum stripes on Si (111) after the growth of InN at different temperatures. Growth conditions are P_N = 450 W and F_N = 1.5 sccm, which corresponds to a growth rate at stoichiometry of 9.5 nm/min and a metal supply of 0.56 nm/min. 119

10.3.3 Patterns with partial SAG: on (a) a single Mo structure and (b) close to PS-nanospheres . c) FIB structured sample after growth with e-beam exposure times. The "baseball bat" morphology of the nanowires is shown in the high magnification image taken under an angle of 45°. 120

10.3.4 Selective area growth on a molybdenum mask with different hole diameters (G0662) (Landgraf, 2009). 122

10.3.5 a) Photoluminescence spectra of InN nanorods by selective area growth with a molybdenum mask with different hole diameters and of a layer for comparison. b) Energies of maximum intensity and FWHM of InN nanorods by selective area growth with a molybdenum and self-organized grown samples with different growth times. 122

10.3.6 Raman spectra of InN nanorods by selective area growth on a molybdenum mask with different hole diameters and a layer. The Si peak 519 cm^{-1} of nanowire samples is fitted and subtracted for better comparison to the layer. 123

C.0.1 Morphologies of the three In-rich InGaN nanowire growth series 134

E.0.1 Emission spectra of the Veeco "UNI-Bulb RF" nitrogen plasma source at several typical operation conditions 140

List of Tables

2.1.1 Lattice constants of III-nitrides (Morkoc, 2008). 4

2.1.2 Phonon modes of AlN, GaN, and InN (in cm^{-1}) without the silent B_1 modes (Cantarero *et al.* (2011), Garro *et al.* (2008) and Segura-Ruiz *et al.* (2009)). 5

2.1.3 Comparison of binding energies and formation enthalpies of InN, GaN and AlN (Lax, 1967; Stampfl & Van de Walle, 1999, and references therein), as well as calculated energy differences between wurzite and zincblende phases ΔE_{wz-zb} (Yeh *et al.*, 1992). 6

3.2.1 Lattice parameter and mismatch of possible substrates for InN and GaN in (0001) direction. The mismatch calculated by $f = (a_{Layer} - a_{substrate})/a_{substrate}$. Constants from Morkoc (2008); Chen *et al.* (2002). (* a* is the corresponding lattice constant to the a lattice constant of the wurzite structure; ** see Morkoc (2008) for details). . . . 17

4.4.1 Material and ion gauge geometry specific constant C_i from calibration samples for deposition rate calculation from beam flux monitor ion gauge pressure $P_{display}$ and cell temperature T_{cell}. The values in brackets refer to standard deviation of the measurements. The constant C_{Ga} from thickness measurements is overestimated due to the porous structure of the GaN grown under cold and nitrogen rich conditions 27

7.3.1 Core-level binding energies for the considered compounds for the XPS analysis and their associated chemical environment ([1] from Piper *et al.* (2005), [2] from Veal *et al.* (2007), [3] from Moulder *et al.* (1995), compare also Werner (2009) and Carsten (2010)). 66

7.5.1 Growth conditions, morphologies and average sizes of nanostructures used for optical characterization with F_{In} the In flux, F_N the nitrogen flux, P_N the nitrogen plasma excitation power, T_S the substrate temperature, t the growth time, d the nanowire diameter and h the height of the nanowires. 86

7.5.2 Combinations of donor concentration N_D and density of surface states N_{SS} that provided the best agreement between experimental and theoretical spectra, assuming a nanowire radius of 40 nm and 50 nm (values for r = 40 nm from Segura-Ruiz *et al.* (2010) and r = 50 nm from Segura-Ruiz (2009)). 94

Bibliography

1997. *Ircon- Modline 3 Infrafra Thermometer - Installation and Operation Manual*. Revision a, august 1997 edn.

2011. *9th International Conference on Nitride Semiconductors, Glasgow*.

Anderson, P. A., Swartz, C. H., Carder, D., Reeves, R. J., Durbin, S. M., Chandril, S., & Myers, T. H. 2006. Buried p-type layers in Mg-doped InN. *Applied Physics Letters*, **89**(18), 184104.

Araki, T, Fukuoka, D., Tamiya, H., Harui, S, Yamaguchi, T., Miyake, H., Hiramarsu, K., & Nanishi, Y. 2009. Fabrication of position-controlled InN nanocolumns by ECR-MBE. *Proc. of SPIE Vol*, **7216**, 72160N–1.

Arnaudov, B., Paskova, T., Paskov, PP, Magnusson, B., Valcheva, E., Monemar, B., Lu, H., Schaff, WJ, Amano, H., & Akasaki, I. 2004. Energy position of near-band-edge emission spectra of InN epitaxial layers with different doping levels. *Physical Review B*, **69**(11), 115216.

Bertness, K.A., Sanders, A.W., Rourke, D.M., Harvey, T.E., Roshko, A., Schlager, J.B., & Sanford, N.A. 2010. Controlled Nucleation of GaN Nanowires Grown with Molecular Beam Epitaxy. *Advanced Functional Materials*, **20**(17), 2911–2915.

Broxtermann, Daniel. 2011. *2-dimensional electron gases by molecular beam epitaxy of III-N heterostructures*. Ph.D. thesis, IV. Physikalisches Institut, Georg-August-Universität Göttingen.

Bugajski, M., & Lewandowski, W. 1985. Concentration-dependent absorption and photoluminescence of n-type InP. *Journal of Applied Physics*, **57**(2), 521–530.

Buhro, W.E., & Colvin, V.L. 2003. Semiconductor nanocrystals: shape matters. *Nature materials*, **2**(3), 138–139.

Caetano, C., Teles, L. K., Marques, M., Dal Pino, A., & Ferreira, L. G. 2006. Phase stability, chemical bonds, and gap bowing of $In_xGa_{1-x}N$ alloys: Comparison between cubic and wurtzite structures. *Phys. Rev. B*, **74**(Jul), 045215.

Calleja, E., Ristic, J., Fernandez-Garrido, S., Cerutti, L., Sánchez-García, M. A., Grandal, J., Trampert, A., Jahn, U., Sanchez, G., Griol, A., & Sanchez, B. 2007. Growth, morphology, and structural properties of group-III-nitride nanocolumns and nanodisks. *physica status solidi (b)*, **244**(8), 2816–2837.

Cantarero, A., Cros, A., Garro, N., Gómez-Gómez, M.I., García, A., de Lima, M.M., Daudin, B., Rizzi, A., Denker, C., & Malindretos, J. 2011. Optical properties of nitride nanostructures. *Annalen der Physik*, **523**(1-2), 51–61.

Carsten, Michael. 2010. *Photoemissionspectroskopie an Gruppe III Nitrid basierten Schichten und Nanostrukturen*. Diploma thesis, IV. Physikalisches Institut der Georg-August-Universität Göttingen.

Chang, C.Y., Chi, G.C., Wang, W.M., Chen, L.C., Chen, K.H., Ren, F., & Pearton, SJ. 2005. Transport properties of InN nanowires. *Applied Physics Letters*, **87**, 093112.

Chen, C.H., Wakiya, N., Shinozaki, K., & Mizutani, N. 2002. Effects of thermal coefficient and lattice constant mismatches on mosaic dispersion of heteroepitaxial YSZ/Si (001) thin films. *Journal of Physics D: Applied Physics*, **35**, 151.

Chen, H., Feenstra, R.M., Northrup, J.E., Zywietz, T., Neugebauer, J., & Greve, D.W. 2000. Surface structures and growth kinetics of InGaN (0001) grown by molecular beam epitaxy. *Journal of Vacuum Science & Technology B: Microelectronics and Nanometer Structures*, **18**, 2284.

Chen, J.W., Chen, Y.F., Lu, H., & Schaff, W.J. 2005. Cross-sectional Raman spectra of InN epifilms. *Applied Physics Letters*, **87**, 041907.

Chèze, C., Geelhaar, L., Trampert, A., Brandt, O., & Riechert, H. 2010. Collector Phase Transitions during Vapor-Solid-Solid Nucleation of GaN Nanowires. *Nano Letters*, **10**(9), 3426–3431.

Chèze, C., Geelhaar, L., Brandt, O., Weber, W.M., Riechert, H., Münch, S., Rothemund, R., Reitzenstein, S., Forchel, A., Kehagias, T., *et al.* 2010. Direct comparison of catalyst-free and catalyst-induced GaN nanowires. *Nano Research*, **3**(7), 528–536.

Consonni, V., Hanke, M., Knelangen, M., Geelhaar, L., Trampert, A., & Riechert, H. 2011. Nucleation mechanisms of self-induced GaN nanowires grown on an amorphous interlayer. *Phys. Rev. B*, **83**(3), 035310.

Curless, J.A. 1985. Molecular beam epitaxy beam flux modeling. *Journal of Vacuum Science & Technology B: Microelectronics and Nanometer Structures*, **3**(2), 531–534.

Daly, E. M., Glynn, T. J., Lambkin, J. D., Considine, L., & Walsh, S. 1995. Behavior of $In_{0.48}Ga_{0.52}P/(Al_{0.2}Ga_{0.8})_{0.52}In_{0.48}P$ quantum-well luminescence as a function of temperature. *Phys. Rev. B*, **52**(Aug), 4696–4699.

Davydov, V.Y., Emtsev, V.V., Goncharuk, I.N., Smirnov, A.N., Petrikov, V.D., Mamutin, V.V., Vekshin, V.A., Ivanov, S.V., Smirnov, M.B., & Inushima, T. 1999a. Experimental and theoretical studies of phonons in hexagonal InN. *Applied physics letters*, **75**, 3297.

Davydov, V.Y., Klochikhin, A.A., Smirnov, M.B., Emtsev, V.V., Petrikov, V.D., Abroyan, I.A., Titov, A.I., Goncharuk, I.N., Smirnov, A.N., Mamutin, V.V., *et al.* 1999b. Phonons in Hexagonal InN. Experiment and Theory. *physica status solidi (b)*, **216**(1), 779–783.

Denker, C. 2007. *InN-Nanodräthe durch Selbstorganisation in der Molekularstrahlepitaxy*. Diploma thesis, IV. physikalisches Instiut, Georg-August-Universität Göttingen.

Denker, C., Malindretos, J., Werner, F., Limbach, F., Schuhmann, H., Niermann, T., Seibt, M., & Rizzi, A. 2008. Self-organized growth of InN-nanocolumns on p-Si(111) by MBE. *physica status solidi (c)*, **5**(6), 1706–1708.

Djenizian, T., Santinacci, L., & Schmuki, P. 2001. Electron-Beam Induced Nanomasking for Metal Electrodeposition on Semiconductor Surfaces. *Journal of The Electrochemical Society*, **148**(3), C197–C202.

Drago, M. 2006. *MOVPE growth of InN analyzed by in-situ spectroscopic ellipsometry*. Ph.D. thesis, TU Berlin.

Dubrovskii, V. G., Sibirev, N. V., Cirlin, G. E., Soshnikov, I. P., Chen, W. H., Larde, R., Cadel, E., Pareige, P., Xu, T., Grandidier, B., Nys, J.-P., Stievenard, D., Moewe, M., Chuang, L. C., & Chang-Hasnain, C. 2009a. Gibbs-Thomson and diffusion-induced contributions to the growth rate of Si, InP, and GaAs nanowires. *Phys. Rev. B*, **79**, 205316.

Dubrovskii, V. G., Sibirev, N. V., Cirlin, G. E., Bouravleuv, A. D., Samsonenko, Yu. B., Dheeraj, D. L., Zhou, H. L., Sartel, C., Harmand, J. C., Patriarche, G., & Glas, F. 2009b. Role of nonlinear effects in nanowire growth and crystal phase. *Phys. Rev. B*, **80**(20), 205305.

Ebert, Ph., Schaafhausen, S., Lenz, A., Sabitova, A., Ivanova, L., Dähne, M., Hong, Y.-L., Gwo, S., & Eisele, H. 2011. Direct measurement of the band gap and Fermi level position at InN($11\bar{2}0$). *Applied Physics Letters*, **98**(6), 062103.

Elsner, J., Haugk, M., Jungnickel, G., & Frauenheim, Th. 1998. Theory of Ga, N and H terminated (0 0 0 1)/($0\ 0\ 0\ \bar{1}$) surfaces. *Solid state communications*, **106**(11), 739–743.

Fan, H.J., Werner, P., & Zacharias, M. 2006. Semiconductor Nanowires: From Self-Organization to Patterned Growth. *Small*, **2**(6), 700–717.

Fasth, C., Fuhrer, A., Björk, M.T., & Samuelson, L. 2005. Tunable double quantum dots in InAs nanowires defined by local gate electrodes. *Nano Lett*, **5**(7), 1487–1490.

Fehlberg, T. B., Umana-Membreno, G. A., Nener, B. D., Parish, G., Gallinat, C. S., Koblmüller, G., Rajan, S., Bernardis, S., & Speck, J. S. 2006. Characterisation of Multiple Carrier Transport in Indium Nitride Grown by Molecular Beam Epitaxy. *Japanese Journal of Applied Physics*, **45**(41), L1090–L1092.

Fehlberg, T. B., Koblmüller, G., Umana-Membreno, G. A., Gallinat, C. S., Nener, B. D., Speck, J. S., & Parish, G. 2008. Multiple carrier transport in N-face indium nitride. *physica status solidi (b)*, **245**(5), 907–909.

Fehlberg, T.B., Umana-Membreno, G.A., Gallinat, C.S., Koblmüller, G., Bernardis, S., Nener, B.D., Parish, G., & Speck, J.S. 2007. Characterisation of multiple carrier transport in indium nitride grown by molecular beam epitaxy. *physica status solidi (c)*, **4**(7), 2423–2427.

Franke, E. 2009. *Entwicklung einer optischen Prozesskontrolleinheit für Stickstoff Plasmaquellen*. Bachelor thesis, IV.Physikalisches Institut der Georg-August-Universität Göttingen.

Fritsch, D., Schmidt, H., & Grundmann, M. 2003. Band-structure pseudopotential calculation of zinc-blende and wurtzite AlN, GaN, and InN. *Phys. Rev. B*, **67**(23), 235205.

Fu, S.P., Chen, T.T., & Chen, Y.F. 2006. Photoluminescent properties of InN epifilms. *Semiconductor science and technology*, **21**, 244.

Gallinat, C. S., Koblmüller, G., & Speck, J. S. 2009. The role of threading dislocations and unintentionally incorporated impurities on the bulk electron conductivity of In-face InN. *Applied Physics Letters*, **95**(2), 022103.

Gallinat, C.S., Koblmüller, G., Brown, J.S., & Speck, J.S. 2007. A growth diagram for plasma-assisted molecular beam epitaxy of In-face InN. *Journal of Applied Physics*, **102**, 064907.

Galopin, E., Largeau, L., Patriarche, G., Travers, L., Glas, F ., & Harmand, J. C. 2011. Morphology of self-catalyzed GaN nanowires and chronology of their formation by molecular beam epitaxy. *Nanotechnology*, **22**(24), 245606.

Garro, N., Cros, A., García-Cristóbal, A., & Cantarero, A. 2008. *Optical and vibrational properties of self-assembled GaN quantum dots*. Elsevier Science.

Gausepohl, H. 1996. *Polystyrol*. Kunststoff- Handbuch. Neuausgabe. Hanser.

Geelhaar, L., Chèze, C., Weber, W. M., Averbeck, R., Riechert, H., Kehagias, Th., Komninou, Ph., Dimitrakopulos, G. P., & Karakostas, Th. 2007. Axial and radial growth of Ni-induced GaN nanowires. *Applied Physics Letters*, **91**(9), 093113.

Gerthsen, C., & Vogel, H. 1999. *Gerthsen Physik*. Vol. 21. Gerthsen Physik, XXI, Springer-Verlag Berlin Heidelberg New York. Also Springer-Lehrbuch.

Givargizov, EI. 1975. Fundamental aspects of VLS growth. *Journal of Crystal Growth*, **31**, 20–30.

Goodman, K. D., V., Protasenko. V., Verma, J., Kosel, T. H., Xing, H. G., & Jena, D. 2011. Green luminescence of InGaN nanowires grown on silicon substrates by molecular beam epitaxy. *Journal Applied Physics*, **109**(8), 084336.

Gotschke, T., Schumann, T., Limbach, F., Stoica, T., & Calarco, R. 2011. Influence of the adatom diffusion on selective growth of GaN nanowire regular arrays. *Applied Physics Letters*, **98**(10), 103102.

Gradečak, S., Qian, F., Li, Y., Park, H.G., & Lieber, C.M. 2005. GaN nanowire lasers with low lasing thresholds. *Applied Physics Letters*, **87**, 173111.

Grandal, J., Sánchez-García, MA, Calleja, E., Luna, E., & Trampert, A. 2007. Accommodation mechanism of InN nanocolumns grown on Si (111) substrates by molecular beam epitaxy. *Applied physics letters*, **91**(2), 021902–021902.

Grille, H., Schnittler, C., & Bechstedt, F. 2000. Phonons in ternary group-III nitride alloys. *Physical Review B*, **61**(9), 6091–6105.

Guo, W., Zhang, M., Banerjee, A., & Bhattacharya, P. 2010. Catalyst-Free InGaN/GaN Nanowire Light Emitting Diodes Grown on (001) Silicon by Molecular Beam Epitaxy. *Nano Letters*, **10**(9), 3355–3359.

Harmand, J.-C., Glas, F., & Patriarche, G. 2010. Growth kinetics of a single $InP_{1-x}As_x$ nanowire. *Phys. Rev. B*, **81**(23), 235436.

Herman, M.A., & Sitter, H. 1996. *Molecular beam epitaxy: fundamentals and current status*. second, revised and updated edn. Springer series in material science 7. Springer Berlin.

Hersee, S. D., Fairchild, M., Rishinaramangalam, A. K., Ferdous, M. S., Zhang, L., Varangis, P. M., Swartzentruber, B. S., & Talin, A. A. 2009. GaN nanowire light emitting diodes based on templated and scalable nanowire growth process. *Electronics Letters*, **45**(1), 75 – 76.

Hertenberger, S., Rudolph, D., Bichler, M., Finley, J. J., Abstreiter, G., & Koblmüller, G. 2010. Growth kinetics in position-controlled and catalyst-free InAs nanowire arrays on Si(111) grown by selective area molecular beam epitaxy. *Journal of Applied Physics*, **108**(11), 114316.

Ho, I., & Stringfellow, G.B. 1996. Solid phase immiscibility in GaInN. *Applied physics letters*, **69**, 2701.

Hofmann, T., Chavdarov, T., Darakchieva, V., Lu, H., Schaff, WJ, & Schubert, M. 2006. Anisotropy of the Γ-point effective mass and mobility in hexagonal InN. *physica status solidi (c)*, **3**(6), 1854–1857.

Hollermann, H. 2010. *Der Einfluss verschiedener Stickstoffspezies auf das GaN-Wachstum mittels Molekularstrahlepitaxie*. Bachelor thesis, IV. Physikalisches Institut der Georg-August-Universität Göttingen.

Honke, T., Fujioka, H., Ohta, J., & Oshima, M. 2004. InN epitaxial growths on Yttria stabilized zirconia (111) step substrates. *Journal of Vacuum Science & Technology A: Vacuum, Surfaces, and Films*, **22**(6), 2487–2489.

Hourdakis, E., Simonds, B. J., & Zimmerman, N. M. 2006. Submicron gap capacitor for measurement of breakdown voltage in air. *Review of Scientific Instruments*, **77**(3), 034702.

Huels, S. 2008. *Selective Nucleation of Indium Nitride on Silicon - An Investigation of Substrate Patterning Techniques*. Diploma thesis, IV. Physikalisches Institut der Georg-August-Universität Göttingen.

Ishizaka, A., & Shiraki, Y. 1986. Low Temperature Surface Cleaning of Silicon and Its Application to Silicon MBE. *Journal of The Electrochemical Society*, **133**(4), 666–671.

Jones, R. E., Yu, K. M., Li, S. X., Walukiewicz, W., Ager, J. W., Haller, E. E., Lu, H., & Schaff, W. J. 2006. Evidence for p-Type Doping of InN. *Phys. Rev. Lett.*, **96**(12), 125505.

Joyce, T.B., & Bullough, T.J. 1993. Beam equivalent pressure measurements in chemical beam epitaxy. *Journal of crystal growth*, **127**(1-4), 265–269.

Kamimura, J., Kishino, K., & Kikuchi, A. 2010. Dislocation reduction via selective-area growth of InN accompanied by lateral growth by rf-plasma-assisted molecular-beam epitaxy. *Applied Physics Letters*, **97**(14), 141913.

Karpov, S Y. 1998. Suppression of phase separation in InGaN due to elastic strain. *MRS Internet J Nitride Semicond Res*, **3**(1998), 16.

Khanal, D. R., & Wu, J. 2007. Gate Coupling and Charge Distribution in Nanowire Field Effect Transistors. *Nano Letters*, **7**(9), 2778–2783.

Kikuchi, A., Kawai, M., Tada, M., & Kishino, K. 2004. InGaN/GaN multiple quantum disk nanocolumn light-emitting diodes grown on (111) Si substrate. *Jpn. J. Appl. Phys*, **43**, L1524–L1526.

King, P.D.C., Veal, T.D., Kendrick, C.E., Bailey, L.R., Durbin, S.M., & McConville, C.F. 2008. InN/GaN valence band offset: High-resolution x-ray photoemission spectroscopy measurements. *Physical Review B*, **78**(3), 33308.

Kishino, K., Kikuchia, A., Sekiguchia, H., & Ishizawaa, S. 2007. InGaN/GaN nanocolumn LEDs emitting from blue to red. *Proc. of SPIE*, **64730**, 64730T–1.

Kishino, K., Hoshino, T., Ishizawa, S., & Kikuchi, A. 2008. Selective-area growth of GaN nanocolumns on titanium-mask-patterned silicon (111) substrates by RF-plasma-assisted molecular-beam epitaxy. *Electronic letters*, **44**(13), 2.

Kishino, K., Sekiguchi, H., & Kikuchi, A. 2009. Improved Ti-mask selective-area growth (SAG) by rf-plasma-assisted molecular beam epitaxy demonstrating extremely uniform GaN nanocolumn arrays. *Journal of Crystal Growth*, **311**(7), 2063 – 2068.

Klochikhin, A.A., Davydov, V.Y., Emtsev, V.V., Sakharov, A.V., Kapitonov, V.A., Andreev, B.A., Lu, H., & Schaff, W.J. 2005. Acceptor states in the photoluminescence spectra of n-InN. *Physical Review B*, **71**(19), 195207.

Klochikhin, A.A., Davydov, V.Y., Strashkova, I.Y., Brunkov, P.N., Gutkin, A.A., Rundinsky, M.E., Chen, H.Y., & Gwo, S. 2007. Band bending of n-InN epilayers and exact solution of the classical Thomas-Fermi equation. *Physica status solidi. Rapid research letters(Print)*, **1**(4), 159–161.

Knübel, A., Aidam, R., Cimalla, V., Kirste, L., Baeumler, M., Leancu, C.-C., Lebedev, V., Wallauer, J., Walther, M., & Wagner, J. 2009. Transport characteristics of indium nitride (InN) films grown by plasma assisted molecular beam epitaxy (PAMBE). *physica status solidi (c)*, **6**(6), 1480–1483.

Koley, G., & Zhihua, C. 2008 (oct.). InN nanowire based sensors. *Pages 118 –121 of: Sensors, 2008 IEEE.*

Kuykendall, T., Ulrich, P., Aloni, S., & Yang, P. 2007. Complete composition tunability of InGaN nanowires using a combinatorial approach. *Nature Materials*, **6**(12), 951.

Lai, W.J., Li, S.S., C.C., Lin, Kuo, C.C., Chen, C.W., Chen, K.H., & Chen, L.C. 2010. Near infrared photodetector based on polymer and indium nitride nanorod organic/inorganic hybrids. *Scripta Materialia*, **63**(6), 653 – 656.

Lan, ZH, Wang, WM, Sun, CL, Shi, SC, Hsu, CW, Chen, TT, Chen, KH, Chen, CC, Chen, YF, & Chen, LC. 2004. Growth mechanism, structure and IR photoluminescence studies of indium nitride nanorods. *Journal of Crystal Growth*, **269**(1), 87–94.

Landgraf, B. 2009. *Selectives Wachstum von InN Halbleiter-Nanodrähten*. Diplomarbeit, IV. Physikalisches Institut der Georg-August-Universität Göttingen.

Landré, O., Bougerol, C., Renevier, H., & Daudin, B. 2009. Nucleation mechanism of GaN nanowires grown on (111) Si by molecular beam epitaxy. *Nanotechnology*, **20**(41), 415602.

Law, M., Greene, L.E., Johnson, J.C., Saykally, R., & Yang, P. 2005. Nanowire dye-sensitized solar cells. *Nature Materials*, **4**(6), 455–459.

Lax, E. 1967. *Taschenbuch für Chemiker und Physiker-BD. 1: Makroskopische physiklaisch-chemische Eigenschaften*. 3. neu bearb. aufl. edn. Springer Berlin Heidelberg.

Lazic, S. 2008. *Optical properties of nitride semiconductors structures*. Ph.D. thesis, Universidad autonoma de Madrid.

Lazić, S., Gallardo, E., Calleja, J.M., Agulló-Rueda, F., Grandal, J., Sánchez-Garcia, M.A., Calleja, E., Luna, E., & Trampert, A. 2007. Phonon-plasmon coupling in electron surface accumulation layers in InN nanocolumns. *Physical Review B*, **76**(20), 205319.

Leitner, J., Marsík, P., Sedmidubský, D., & Ruzicka, K. 2004. High temperature enthalpy, heat capacity and other thermodynamic functions of solid InN. *Journal of Physics and Chemistry of Solids*, **65**(6), 1127 – 1131.

Limbach, F., Gotschke, T., Stoica, T., Calarco, R., Sutter, E., Ciston, J., Cusco, R., Artus, L., Kremling, S., Höfling, S., Worschech, L., & Grützmacher, D. 2011. Structural and optical properties of InGaN–GaN nanowire heterostructures grown by molecular beam epitaxy. *Journal of Applied Physics*, **109**(1), 014309.

Limbach, Friederich. 2008. *Electrical charaterization of InN-Nanowires*. Diplomarbeit, IV.Physikalisches Institut der Georg-August-Universität Göttingen.

Look, D. C., & Molnar, R. J. 1997. Degenerate layer at GaN/sapphire interface: Influence on Hall-effect measurements. *Applied Physics Letters*, **70**(25), 3377–3379.

Lu, H., Schaff, W.J., Eastman, L.F., & Stutz, C. E. 2003. Surface charge accumulation of InN films grown by molecular-beam epitaxy. *Applied Physics Letters*, **82**(11), 1736–1738.

Madorsky, S., & Straus, S. 1948. Pyrolytic fractionation of polystyrene in a high vacuum and mass spectrometer analysis of some of the fractions. *Journal of research of the National Bureau of Standards*, **40**, 417–425.

Mahboob, I., Veal, T. D., Piper, L. F. J., McConville, C. F., Lu, Hai, Schaff, W. J., Furthmüller, J., & Bechstedt, F. 2004. Origin of electron accumulation at wurtzite InN surfaces. *Phys. Rev. B*, **69**(20), 201307.

Markov, I. 1995. *Crystal growth for beginners - Fundamentals of nucleation, crystal growth and nucleation*. World Scientific Publishing Co. Pte. Ltd., Singapore. ISBN 981-02-1531-2.

Meijers, R. 2007. *Growth and Characterisation of Group-III Nitride-based Nanowires for Devices*. Ph.D. thesis, Rheinisch-Westfälische Technische Hochschule Aachen.

Mi, Z., & Chang, Y.L. 2009. III-V compound semiconductor nanostructures on silicon: epitaxial growth, properties, and applications in light emitting diodes and lasers. *Journal of Nanophotonics*, **3**(031602), 031602.

Moreau, W.M. 1988. *Semiconductor Lithography: Principles, Practices, and Materials*. Plenum Press New York.

Moret, M., Ruffenach, S., Briot, O., & Gil, B. 2009. The determination of the bulk residual doping in indium nitride films using photoluminescence. *Applied Physics Letters*, **95**, 031910.

Morkoc, H. 2008. *Handbook of Nitride Semiconductors and Devices, Materials Properties, Physics and Growth*. Vch Verlagsgesellschaft Mbh.

Moss, T.S. 1985. Relations between the Refractive Index and Energy Gap of Semiconductors. *physica status solidi (b)*, **131**(2), 415–427.

Moulder, J.F., Stickle, W.F., Sobol, P.E., & Bomben, K.D. 1995. *Handbook of X-ray Photoelectron Spectroscopy. Eden Prairie: Physical Electronics*. Physical Electronics.

Nag, B.R. 2003. On the band gap of indium nitride. *physica status solidi (b)*, **237**(2), R1–R2.

Neugebauer, J., Zywietz, T.K., Scheffler, M., Northrup, J.E., Chen, H., & Feenstra, R.M. 2003. Adatom kinetics on and below the surface: the existence of a new diffusion channel. *Physical review letters*, **90**(5), 56101.

Newman, N. 1997. The energetics of the GaN MBE reaction: a case study of meta-stable growth. *Journal of Crystal Growth*, **178**(1-2), 102–112.

Nguyen, H. P. T., Chang, Y.-L., Shih, I., & Mi, Z. 2011. InN p-i-n Nanowire Solar Cells on Si. *Selected Topics in Quantum Electronics, IEEE Journal of*, **17**(4), 1062–1069.

Northrup, John E., & Neugebauer, J. 1996. Theory of GaN $(10\bar{1}0)$ and $(11\bar{2}0)$ surfaces. *Physical Review B*, **53**(16), 478–480.

O'Leary, S.K., Foutz, B.E., Shur, M.S., & Eastman, L.F. 2010. The sensitivity of the electron transport within bulk wurtzite indium nitride to variations in the crystal temperature, the doping concentration, and the non-parabolicity coefficient: an updated Monte Carlo analysis. *Journal of Materials Science: Materials in Electronics*, **21**(3), 218–230.

Onderka, B., Unland, J., & Schmid-Fetzer, R. 2002. Thermodynamics and phase stability in the In–N system. *Journal of materials research*, **17**(12), 3065–3083.

Pearton, S.J., Kang, B.S., Gila, B.P., Norton, D.P., Kryliouk, O., Ren, F., Heo, Y.W., Chang, C.Y., Chi, G.C., Wang, W.M., *et al.* 2008. GaN, ZnO and InN nanowires and devices. *Journal of Nanoscience and Nanotechnology*, **8**(1), 99–110.

Piper, L.F.J., Veal, T.D., Walker, M., Mahboob, I., McConville, C.F., Lu, H., & Schaff, W.J. 2005. Clean wurtzite InN surfaces prepared with atomic hydrogen. *Journal of Vacuum Science & Technology A: Vacuum, Surfaces, and Films*, **23**(4), 617–620.

Pomeroy, J.W., Kuball, M., Swartz, C.H., Myers, T.H., Lu, H., & Schaff, W.J. 2007. Evidence for phonon-plasmon interaction in InN by Raman spectroscopy. *Physical Review B*, **75**(3), 035205.

Reinert, F., & Huefner, S. 2005. Photoemission spectroscopy - from early days to recent applications. *New Journal of Physics*, **7**, 97.

Richter, T., Bloemers, C., Lueth, H., Calarco, R., Indlekofer, M., Marso, M., & Schaepers, T. 2008. Flux quantization effects in InN nanowires. *Nano letters*, **8**(9), 2834–2838.

Rinke, P., Scheffler, M., Qteish, A., Winkelnkemper, M., Bimberg, D., & Neugebauer, J. 2009. Band gap and band parameters of InN and GaN from quasiparticle energy calculations based on exact-exchange density-functional theory. *Applied Physics Letters*, **89**(16), 161919.

Ruth, V., & Hirth, J.P. 1964. Kinetics of Diffusion-Controlled Whisker Growth. *The Journal of Chemical Physics*, **41**, 3139.

Ruttke, D. 2010. *Kontaktierung und Transportmessungen von einzelnen InN-Nanodräthen*. Diplomarbeit, IV. Physikalisches Institut der Georg-August-Universität Göttingen.

Saitoh, H., Utsumi, W., & Aoki, K. 2008. Decomposition of InN at high pressures and temperatures and its thermal instability at ambient conditions. *Journal of Crystal Growth*, **310**(2), 473–476.

Sanchez-Garcia, M.A., Calleja, E., Monroy, E., Sanchez, F.J., Calle, F., Muñoz, E., & Beresford, R. 1998. The effect of the III/V ratio and substrate temperature on the morphology and properties of GaN- and AlN-layers grown by molecular beam epitaxy on Si(1 1 1). *Journal of Crystal Growth*, **183**(1-2), 23 – 30.

Sardar, K., Deepak, F.L., Govindaraj, A., Seikh, M.M., & Rao, C.N.R. 2005. InN Nanocrystals, Nanowires, and Nanotubes. *Small*, **1**(1), 91–94.

Schumann, T., Gotschke, T., Limbach, F., Stoica, T., & Calarco, R. 2011. Selective-area catalyst-free MBE growth of GaN nanowires using a patterned oxide layer. *Nanotechnology*, **22**, 095603.

Schwarz, U., & Scholz, F. 2011. Rosige Aussichten für grünes Licht. *Physik Journal der Deutschen Physikalischen Gesellschaft*, **2**, 21–26.

Seah, MP, & Dench, WA. 1979. Quantitative electron spectroscopy of surfaces. *Surface and Interface Analysis*, **1**(2).

Segev, D., & van de Walle, CG. 2006. Origins of Fermi-level pinning on GaN and InN polar and nonpolar surfaces. *EPL (Europhysics Letters)*, **76**, 305.

Segev, David, & Van de Walle, Chris G. 2007. Electronic structure of nitride surfaces. *Journal of Crystal Growth*, **300**(1), 199 – 203. First International Symposium on Growth of Nitrides - ISGN-1.

Segura-Ruiz, J. 2009. *Electronic and Vibrational States of InN and GaInN Nanocolumns*. PhD-Thesis, Universidad de Valencia, Departamento de Física Aplicada y Electromagnetismo.

Segura-Ruiz, J., Garro, N., Cantarero, A., Denker, C., Malindretos, J., & Rizzi, A. 2009. Optical studies of MBE-grown InN nanocolumns: Evidence of surface electron accumulation. *Phys. Rev. B*, **79**(11), 115305.

Segura-Ruiz, J., Molina-Sánchez, A., Garro, N., García-Cristóbal, A., Cantarero, A., Iikawa, F., Denker, C., Malindretos, J., & Rizzi, A. 2010. Inhomogeneous free-electron distribution in InN nanowires: Photoluminescence excitation experiments. *Phys. Rev. B*, **82**(12), 125319.

Segura-Ruiz, J., Martinez-Criado, G., Denker, C., Malindretos, J., & Rizzi, A. 2011. Elemental distribution in InGaN nanowires studied by synchrotron radiation nanoprobe. *E-MRS proceedings*, **to be published**, 2011.

Sekiguchi, H., Kishino, K., & Kikuchi, A. 2008. Ti-mask Selective-Area Growth of GaN by RF-Plasma-Assisted Molecular-Beam Epitaxy for Fabricating Regularly Arranged InGaN/GaN Nanocolumns. *Applied Physics Express*, **1**(12), 124002.

Shen, C.H., Chen, H.Y., Lin, H.W., Gwo, S., Klochikhin, AA, & Davydov, V.Y. 2006. Near-infrared photoluminescence from vertical InN nanorod arrays grown on silicon: Effects of surface electron accumulation layer. *Applied Physics Letters*, **88**, 253104.

Songmuang, R., Landré, O., & Daudin, B. 2007. From nucleation to growth of catalyst-free GaN nanowires on thin AlN buffer layer. *Applied Physics Letters*, **91**, 251902.

Songmuang, R., Ben, T., Daudin, B., González, D., & Monroy, E. 2010. Identification of III-N nanowire growth kinetics via a marker technique. *Nanotechnology*, **21**(29), 295605.

Stampfl, C., & Van de Walle, C.G. 1999. Density-functional calculations for III-V nitrides using the local-density approximation and the generalized gradient approximation. *Physical Review B*, **59**(8), 5521–5535.

Stoica, T., Meijers, R., Calarco, R., Richter, T., & Lüth, H. 2006. MBE growth optimization of InN nanowires. *Journal of crystal growth*, **290**(1), 241–247.

Stringfellow, G.B. 2010. Microstructures produced during the epitaxial growth of InGaN alloys. *Journal of Crystal Growth*, **312**(6), 735–749.

Swartz, C.H., Durbin, S.M., Anderson, P.A., Carder, D., Reeves, R.J., Chandril, S., Myers, T.H., Kennedy, V.J., & Ahrenkiel, S.P. 2008. Mg doping of InN and the use of yttrium-stabilised zirconia substrates. *physica status solidi (c)*, **5**(2), 508–510.

Tabata, A., Teles, L.K., Scolfaro, L.M.R., Leite, J.R., Kharchenko, A., Frey, T., As, D.J., Schikora, D., Lischka, K., Furthmuller, J., *et al.* 2002. Phase separation suppression in InGaN epitaxial layers due to biaxial strain. *Applied physics letters*, **80**(5), 769–771.

Terentjevs, A., Catellani, A., Prendergast, D., & Cicero, G. 2010. Importance of on-site corrections to the electronic and structural properties of InN in crystalline solid, nonpolar surface, and nanowire forms. *Phys. Rev. B*, **82**(Oct), 165307.

Tian, B., Zheng, X., Kempa, T.J., Fang, Y., Yu, N., Yu, G., Huang, J., & Lieber, C.M. 2007. Coaxial silicon nanowires as solar cells and nanoelectronic power sources. *Nature*, **449**(7164), 885–889.

Tian, B., Kempa, T.J., & Lieber, C.M. 2009. Single nanowire photovoltaics. *Chemical Society Reviews*, **38**(1), 16–24.

Vajpeyi, A. P., Ajagunna, A. O., Tsagaraki, K., Androulidaki, M., & Georgakilas, A. 2009. InGaN nanopillars grown on silicon substrate using plasma assisted molecular beam epitaxy. *Nanotechnology*, **20**(32), 325605.

Van de Walle, C.G., Lyons, J.L., & Janotti, A. 2010. Controlling the conductivity of InN. *physica status solidi (a)*, **207**(5), 1024–1036.

Veal, T.D., King, P.D.C., Jefferson, P.H., Piper, L.F.J., McConville, C.F., Lu, H., Schaff, W.J., Anderson, P.A., Durbin, S.M., Muto, D., *et al.* 2007. In adlayers on c-plane InN surfaces: A polarity-dependent study by x-ray photoemission spectroscopy. *Physical Review B*, **76**(7), 075313.

Veeco, Instruments Inc. 2009. *UNI-Bulb RF Plasma Source for Nitrogen and Hydrogen*.

Vilkotskii, V.A., Domanevskii, D.S., Kakanakov, R.D., Krasovskii, V.V., & Tkachev, V.D. 1979. Burstein-Moss effect and near-band-edge luminescence spectrum of highly doped indium arsenide. *physica status solidi (b)*, **91**(1), 71–81.

Wagner, R.S., & Ellis, W.C. 1965. The vapor-liquid-solid mechanism of crystal growth and its application to silicon. *Trans. Metall. Soc. AIME*, **233**, 1053–1064.

Walukiewicz, W. 1989. Amphoteric native defects in semiconductors. *Applied physics letters*, **54**(21), 2094–2096.

Walukiewicz, W. 2001. Intrinsic limitations to the doping of wide-gap semiconductors. *Physica B: Condensed Matter*, **302-303**, 123 – 134.

Walukiewicz, W., Li, S.X., Wu, J., Yu, K.M., Ager, J.W., *et al.* 2004. Optical properties and electronic structure of InN and In-rich group III-nitride alloys. *Journal of Crystal Growth*, **269**(1), 119–127.

Wang, Jianli, Bai, Dongmei, Tang, Gang, Wu, X.S., & Gu, Mingqiang. 2011. Stable structure and effects of oxygen on InN (1010) and (1120) surfaces. *Journal of Crystal Growth*, **327**(1), 233–236.

Wang, X., & Yoshikawa, A. 2004. Molecular beam epitaxy growth of GaN, AlN and InN. *Progress in Crystal Growth and Characterization of Materials*, **48**, 42–103.

Wang, X., Che, S.-B., Ishitani, Y., & Yoshikawa, A. 2008. Hole mobility in Mg-doped p-type InN films. *Applied Physics Letters*, **92**(13), 132108.

Waser, R. 2003. *Nanoelectronics and Information Technology*. Wiley-VCH Verlag GmbH & Co. KGaA, Weinheim.

Werner, F. 2009. *Electrical characterization of single InN-Nanowires*. Diplomarbeit, IV. Physikalisches Institut der Georg-August-Universität Göttingen.

Werner, F., Limbach, F., Carsten, M., Denker, C., Malindretos, J., & Rizzi, A. 2009. Electrical Conductivity of InN Nanowires and the Influence of the Native Indium Oxide Formed at Their Surface. *Nano Letters*, **9**(4), 1567–1571. PMID: 19290610.

Wright, A.F. 1997. Basal-plane stacking faults and polymorphism in AlN, GaN, and InN. *Journal of Applied Physics*, **82**(10), 5259–5261.

Wu, C.-L., Lee, H.-M., Kuo, C.-T., Chen, C.-H., & Gwo, S. 2008. Absence of Fermi-Level Pinning at Cleaved Nonpolar InN Surfaces. *Phys. Rev. Lett.*, **101**(10), 106803.

Wu, J., Walukiewicz, W., Li, S.X., Armitage, R., Ho, J.C., Weber, E.R., Haller, E.E., Lu, H., Schaff, W.J., Barcz, A., *et al.* 2004. Effects of electron concentration on the optical absorption edge of InN. *Applied physics letters*, **84**, 2805.

Wu, K.M., Pan, Y., & Liu, C. 2009. InGaN nanorod arrays grown by molecular beam epitaxy: Growth mechanism structural and optical properties. *Applied Surface Science*, **255**(13-14), 6705 – 6709.

Wunnicke, O. 2006. Gate capacitance of back-gated nanowire field-effect transistors. *Applied Physics Letters*, **89**(8), 083102.

Yamaguchi, T., & Nanishi, Y. 2009. Indium Droplet Elimination by Radical Beam Irradiation for Reproducible and High-Quality Growth of InN by RF Molecular Beam Epitaxy. *Applied physics express*, **2**(5), 051001.

Yamashita, T., Tomita, T., & Sakurai, T. 1987. Calculations of Molecular Beam Flux from Liquid Source. *Japanese Journal of Applied Physics*, **26**(Part 1, No. 7), 1192–1193.

Yeh, C.-Y., Lu, Z. W., Froyen, S., & Zunger, A. 1992. Zinc-blende–wurtzite polytypism in semiconductors. *Phys. Rev. B*, **46**(16), 10086–10097.

Yoshikawa, A., Wang, X., Ishitani, Y., & Uedono, A. 2010. Recent advances and challenges for successful p-type control of InN films with Mg acceptor doping by molecular beam epitaxy. *physica status solidi (a)*, **207**(5), 1011–1023.

Yoshizawa, M., Kikuchi, A., Fujita, N., Kushi, Ko., Sasamoto, H., & Kishino, K. 1998. Self-organization of GaN/$Al_{0.18}Ga_{0.82}N$ multi-layer nano-columns on (0001) Al_2O_3 by RF molecular beam epitaxy for fabricating GaN quantum disks. *Journal of Crystal Growth*, **189-190**, 138 – 141.

Yu, K.M., Liliental-Weber, Z., Walukiewicz, W., Shan, W., Ager, J.W., Li, S.X., Jones, R.E., Haller, E.E., Lu, H., & Schaff, W.J. 2005. On the crystalline structure, stoichiometry and band gap of InN thin films. *Applied Physics Letters*, **86**(7), 071910–071910.

Acknowledgments

This thesis is the result of about four years of research and would have been impossible without the advice, support or just presence of some people whom I would like to thank gratefully:

- Prof. Dr. Angela Rizzi, for giving me the opportunity to continue the interesting work on III-N nanowires of my diploma thesis in the frame work of a PhD thesis and for the constant support, excellent guidance and helpful discussions during these years; as well as for the friendly atmosphere in the group
- Prof. Dr. Alois Krost, for the problemless commitment to be the second corrector of this thesis
- Dr. Jörg Malindretos, for his patience and excellent mentoring, as well as for becoming a good friend
- Prof. Dr. Rainer G. Ulbrich, Prof. Dr. Michael Seibt and Dr. Martin Wenderoth, for their critical comments and wise suggestions
- Sönke Hüls, for the collaboration on the selective area growth with carbon masks
- Friederich Limbach, Florian Werner and Dominik Ruttke, for the excellent collaboration on the electrical measurements of single InN nanowires and friendship
- Boris Landgraf, for the amicable collaboration on the selective area growth with Mo and Ti masks and for being a good friend
- Arne Urban, for TEM imaging, FIB sample preparation, as well as for the fruitful discussions
- Henning Schumann, for TEM imaging
- Martin Röver, Dong-Du Mai, Daniel Broxtermann, Marco Bertelli, Amilcar Bedoya and Christian Zube for the discussions, help and nice time at the IV. physikalisches Institut
- The group of Andres Cantarero at University of Valencia, in particular Jaime Segura-Ruiz for the Raman spectroscopy, PL, PLE of InN and their interpretation, Maria Isabel Gomez Gomez for Raman spectroscopy, PL, XRD of InGaN, assistance for electrical measurements as a function of temperature, F. Iikawa for opportunity for J. Segura to perform PLE measurements and Nuria Garro, as well as Andres Cantarero who guided and supervised all the work on the optical characterization. It was a really nice time with you in the nanoLicht project
- Thomas Lehman, Rasit Kösker and Andrea Smandzik, for their technical and mental support
- Nicole Yee, for the native speaker proof reading
- Katharina Suck, für den liebvollen Rückhalt und die großartige Unterstützung bei dieser Arbeit. Danke, dass Du immer für mich da warst!
- Meinen Eltern, die mir viel Kraft geben haben und mich während des Studiums und der Doktorarbeit immer unterstützt haben